Proteoglycan Regulation Of Cell Shape And Adhesion

A Mechanical Study Using The Atomic Force Microscope

Thomas Michael Kennelly

Department of Physics & Astronomy

University of Sheffield

This thesis is submitted for the degree of

Doctor of Philosophy

October 2018

I would like to dedicate this thesis to my loving parents,

Michael and Tracey Kennelly,

for their constant and unwavering support.

Declaration

I hereby declare that except where specific reference is made to the work of others, the contents of this thesis are original and have not been submitted in whole or in part for consideration for any other degree or qualification in this, or any other university. This thesis is my own work and contains nothing which is the outcome of work done in collaboration with others, except as specified in the text and Acknowledgements.

Thomas Michael Kennelly

October 2018

Acknowledgements

First and foremost I would like to thank my parents, Michael and Tracey Kennelly, and my sister, Hannah, who's continued support has kept me going though the hardest and most gruelling periods of this PhD project. Throughout the frequent sleepless nights working in the laboratory, being able to pick up the phone and speak to my family helped to somewhat alleviate the stress and pressure of the PhD experience and I am forever grateful for their understanding and caring nature. I would also like to thank my girlfriend, Maysoon Mehdi, for her support and reassurance throughout the latter stages of this project and who kept me smiling in the most stressful of times. Furthermore, I would like to thank my supervisors, Prof. Mark Geoghegan and Prof. Eva Qwarnstrom for their guidance and academic support throughout my PhD.

I would like to thank Prof. Yi Cao and Dr. Yiran Li for allowing me to travel to Nanjing University (*Nanjing, China*) to work in their lab, for teaching me the methods of surface modification (in order to exhibit functional proteins at the apex of AFM tips) used throughout this work and for making arrangements to ensure that my trip was both enjoyable and informative. I would also like to thank Dr. Nicole Töpfner at the University of Cambridge (*Cambridge, UK*) for taking time out of her busy schedule to conduct real-time deformability cytometry measurements with me. Additionally, I would like to thank the Department of Physics and Astronomy (*University of Sheffield, Sheffield, UK*) for funding my PhD studentship and for providing the financial support which allowed me to travel to conferences.

I would also like to thank the people who worked alongside me in both the Department of Physics & Astronomy and Department of Infection, Immunity & Cardiovascular Disease at the University of Sheffield: Latifah Alfhaid, Markus Ariaans, Jozraureliano De Asturias, Emer Atkinson, Stephanie Berg, Jamie Blakeman, Jonathan Burns, Ellie Dougherty, Ben Freestone, Amy Hall, Linda Kay, Ana Lorena, Martin McAllister, Calum Macdonald, Rob Masters, Matt Mears, Nic Mullin, Andy Nichols, David Owen, Kishan Patel, Fabio Pontecchiani, Dave Price, David Rhodes, Tom Routledge, Andriy Samokhin, Sarah Smith, Spyridon Sovatzoglou, Michael Stringer, Jamie Taylor, Raveen Tank, Mike Weir and David Woodward. In particular I would like to thank Mr. Jamie Blakeman for allowing me to use his macro for force-curve analysis, Dr. Nic Mullin for all his technical knowledge and troubleshooting related to AFM use alongside Dr. Andy Nichols, Dr. Sarah Smith, Dr. Linda Kay and Dr. Markus Ariaans for their aid in any biological issues I encountered.

Abstract

Proteoglycans (PGs), biomolecules comprised of a core protein which exhibit sulphated glycosaminoglycan chains, are prevalent within bodily tissues and have been found to regulate a large number of cellular mechanisms. PGs are primarily located at the cell surface or in the extracellular matrix (ECM) and interact with structural proteins such as fibronectin (FN). The present study utilised the atomic force microscope (AFM) to characterise the interaction between FN and both syndecan-4 (a heparan sulphate PG [HSPG]; SDC4) and decorin (an ECM PG; DCN) alongside cell surface adhesion receptor integrin $\alpha_5\beta_1$ ($\alpha_5\beta_1$). Revealed energy barriers suggest that the SDC4-FN bond is able to withstand substantial deformation whereas the DCN-FN bond is much more brittle. The character of the $\alpha_5\beta_1$-FN bond depends on external loading (deformable under low loading and brittle under high loading conditions).

Interleukin-1 (IL-1) receptor (IL-1RI) signalling is a central regulatory component of the innate immune system and inflammatory response. IL-1RI co-receptor Toll-like and IL-1 receptor regulator (TILRR) is a cell surface HSPG which amplifies pro-inflammatory signalling upon association with the receptor complex. Furthermore, TILRR controlled activation of IL-1RI has previously been shown to induce changes in cell shape due to cytoskeletal rearrangement and reduce cell contact with the ECM at focal adhesions. Using the AFM this study reports a significant reduction in the strength of binding between HeLa cells and FN due to increased TILRR expression and is indicative of weakened adhesion with the ECM. In addition, a significant reduction in elastic modulus was observed due to TILRR controlled activation of IL-1RI which is consistent with cytoskeletal alterations.

Table of contents

List of figures

List of tables

Nomenclature

Roman Symbols

$\Delta F_{\text{baseline}}$	hydrodynamic shift in approach and retraction curve baselines
ΔG	thermodynamic energy of adhesion
A_{RTDC}	projected surface area of cell
C	concentration of cells
c	y-intercept
C_{RTDC}	cell circularity
D_{RTDC}	cell deformation
E	Young's modulus
E_{r}	reduced modulus
E_{sample}	Young's modulus of sample
E_{tip}	Young's modulus of probe
E_{HM}	energy of harmonic oscillator
F	force

f_{m}	molecular vibration frequency
F_{rupture}	rupture force
F_{chain}	elastic restoring force on polymer chain
F_{hydro}	hydrodynamic drag force
g_{n}	acceleration due to gravity
G_i	integral gain
G_p	proportional gain
k	spring constant
k_{B}	Boltzmann's constant
k_{eff}	effective spring constant
$k_{\mathrm{off}}(F)$	force-driven dissociation rate
k_{off}^{0}	equilibrium dissociation rate
L_{c}	contour length
L_{p}	persistence length
m	mass
m_{fit}	gradient of linear fit
m_{dilution}	dilution factor
N	number of cells
n_{cell}	number of cells counted

P	area under Lorentzian curve
p_{HM}	momentum of harmonic oscillator
p_{chamber}	proportion of hemocytometer chamber counted
P_{RTDC}	cell perimeter
R	radius of spherical indenter
r	loading rate
T	temperature
V	volume
v	velocity
v_{square}	volume of hemocytometer region counted
x	deflection
x_{sep}	end-to-end separation distance of polymer chain
z	piezo z-position / height
z_{sep}	tip-sample separation

Greek Symbols

χ_{B}	width of energy barrier
δ	indentation depth
κ	bending stiffness
ν	Poisson's ratio

ν_{sample}	Poisson's ratio of sample
ν_{tip}	Poisson's ratio of probe
ω_0	resonant angular frequency
θ	half-angle
φ	signal error

Acronyms / Abbreviations

$\alpha_5\beta_1$	integrin $\alpha_5\beta_1$
AFM	atomic force microscope/microscopy
APTES	(3-aminopropyl)triethoxysaline
CD14	cluster of differentiation 14
cDNA	complementary deoxyribonucleic acid
CS	chondroitin sulfate
CSPG	chondroitin sulfate proteoglycan
DCN	decorin
DMEM	Dulbecco's modified Eagle's medium
DMSO	dimethyl sulfoxide
DNA	deoxyribonucleic acid
DS	dermatan sulfate
DSMFS	dynamic single molecule force spectroscopy

ECM	extracellular matrix
EDTA	ethylenediaminetetraacetic
EV	empty vector
FCS	foetal calf serum
FGFR	fibroblast growth factor receptor
FN	fibronectin
FS	force spectroscopy
GAG	glycosaminoglycan
GDP	guanosine diphosphate
GFP	green fluorescent protein
GTP	guanosine triphosphate
GUI	graphical user interface
HA	hyaluronic acid
Hep	heparin
HS	heparan sulfate
HSPG	heparan sulfate proteoglycan
IκBα	inhibitor of κB
Ig	immunoglobulin
IKK	inhibitor of κB kinase

IKKα	inhibitor of κB kinase subunit-α
IKKβ	inhibitor of κB kinase subunit-β
IL-1	interleukin-1
IL-1A	interleukin-1 antagonist
IL-1R	interleukin-1 receptor
IL-1RAP	interleukin-1 receptor accessory protein
IL-1RI	interleukin-1 receptor type I
IL-1RII	interleukin-1 receptor type II
IL-8	interleukin-8
IPA	isopropanol
IRAK	interleukin-1 receptor-associated kinase
KS	karatan sulfate
LB	Luria broth
MAD	median absolute deviation
Mal	maleimide
MFP	molecular force probe
MIDAS	metal ion-dependent adhesion site
MLCT	microlever cantilever
MyD88	myeloid differentiation primary response protein 88

NEMO	NF-κB essential modulator
NF-κB	nuclear factor κ-light-chain-enhancer of activated B cells
NHS	*N*-hydroxysuccinimede
OBL	Olympus BioLever
OLS	optical level sensitivity
PAMP	pathogen-associated molecular pattern
PBS	phosphate-buffered saline
PBS−	PBS absent magnesium and calcium ions
PEG	polyethylene glycol
PG	proteoglycan
PI3K	phosphoinositide 3-kinase
PRR	pattern recognition receptor
PS	penicillin-streptomycin
PUNIAS	Protein Unfolding and Nano-Indentation Analysis Software
RGD	arginylglycylaspartic acid
RHD	Rel homology domain
RNA	ribonucleic acid
rpm	revolutions per minute
RTDC	real-time deformability cytometry

SAM	self-assembled monolayer
SD	standard deviation
SDC4	syndecan-4
SEM	standard error of the mean
siRNA	small interfering ribonucleic acid
ssRNA	single-stranded ribonucleic acid
TAB	transforming growth factor-β activated kinase binding protein
TAD	transactivation domain
TAK	transforming growth factor-β activated kinase
TGF-β	transforming growth factor-β
TGF-βR3	transforming growth factor-β receptor III
TILRR	Toll-like and interleukin-1 receptor regulator
TIR	Toll/interleukin-1 receptor
TIRAP	Toll/interleukin-1 receptor domain containing adaptor protein
TLR	Toll-like receptor
TRAF6	tumour necrosis factor receptor-associated factor 6
WLC	worm-like chain

Chapter 1

Background and Theory

1.1 Rationale for the Present Study

Many biological responses are propagated and regulated through the initiation of signalling cascades (see *Section 1.2.9*; Gabay et al., 2010). The inflammatory mechanism is initiated in response to injury or infection and is primarily regulated by the activation of the transmembrane interleukin-1 receptor, type I (IL-1RI; see *Section 1.2.4*; Weber et al., 2010). The Toll-like and interleukin-1 receptor regulator (TILRR) is a cell surface proteoglycan (PG) which acts as an IL-1RI co-receptor and amplifies its signalling by association with both the receptor complex and with extracellular fibronectin (FN; Vallés et al., 1999; Zhang et al., 2012). It has been shown that the TILRR induced amplification of IL-1RI has significant effects on both cell structure and shape (Zhang et al., 2010). Additionally, cell attachment to the extracellular matrix (ECM) seems to be affected by the activation of IL-1RI under conditions designed to potentiate TILRR expression at the cell surface (see *Section 1.2.8*; Qwarnstrom et al., 1991). It seems clear that understanding the mechanical properties of the system (both the binding properties of the cell with ECM components and the elastic properties of cells due to rearrangements of the internal structure) are crucial in fully appreciating the biological significance of the response. This study aims to investigate these physical

properties of the TILRR amplified activation of IL-1RI alongside similar PG interactions with FN using the atomic force microscope (AFM). The AFM is an excellent tool to use in such biophysical applications as it allows for the extraction of quantitive data (including both the force of rupture between desired biomolecules and the elastic modulus of a sample surface) from living samples in an aqueous environment such as eukaryotic cells in growth media (see *Section 1.3* and *Section 2.4*; Parot et al., 2007; Putman et al., 1994).

1.2 Inflammation, Cell Signalling and Proteoglycans

1.2.1 Adaptive and Innate Immunity

At one point or another in life, every human being will experience an infection. It is a consequence of the world, that is so of living organisms, in which we live. In a broad sense, infection is the introduction of pathogenic material, disease causing microorganisms that gain nourishment from colonising us as a host, into the body and we rely on our immune system to rid us of the threat (Nicholson, 2016). Generally the immune response is separated into two classifications; adaptive immunity which relies on prior recognition of specific antigens (substances capable of triggering immune responses) via specialised immune cells, and innate immunity which instead relies on the recognition of specific molecular motifs associated with infectious agents that are absent from the body under normal conditions (Chaplin, 2010). In the scientific community these are commonly referred to as pathogen-associated molecular patterns (PAMPs; Mogensen, 2009). The adaptive immune system, a relatively recent development in evolutionary terms, is only present in vertebrates and cartilaginous fish and despite being by far the most efficient method of eliminating pathogens, is a relatively slow process, taking days to develop (Dempsey et al., 2003). Comparatively, the innate immune response is evolutionarily ancient, highly conserved from a time in history before the divergence of plants and animals and is present in virtually all known living multicellular organisms (Alberts et al., 2002). It is often described as the body's first line of defence against infection (with the exception of external physical barriers such as the skin) due to its rapid response, being able to detect and react to pathogenic attack in just a matter of minutes or hours (Hoffmann et al., 1999). In fact, it is still such an essential mechanism in the early recognition of infectious agents and the initiation of appropriate responses that significant defects in the innate immune system of any given organism will lead to severe immunodeficiency and ultimately fatality.

While the immune system is split into two categories, it would be incorrect to describe innate and adaptive immunity as two separate and non-interacting entities. There is much interplay and crosstalk between the two, each aiding the other in the cooperative detection and destruction of invasive and infectious materials (Getz, 2005). It is generally accepted that the adaptive immune system evolved alongside an already functional and well established innate immune system at a time when vertebrates first came into existence in order to provide suitable immunological protection for more complicated organisms (Boehm, 2012). However, the adaptive response to infection cannot function on its own and significant evidence suggests that complications in the innate immune system result in a functional failure of the adaptive immune response. In fact, the two are so intertwined that cells specific to the innate immunological response are capable of presenting antigens to those more suited to mechanisms of the adaptive immune system, which in turn will often exhibit receptors on their surface which are functionally relevant to the innate immune system (Turvey and Broide, 2010).

The adaptive response relies heavily on the ability to recognise a familiar antigen (one that the host has previously been infected with) and recognition is often specific to that particular pathogen (Moresco et al., 2011). In contrast, the innate immune system does not rely on prior exposure to a particular infection and so both the mechanism of pathogen detection and the nature of the response are much more general. Once a pathogen has breached the outer barriers of the body, PAMPs are bound by pattern recognition receptors (PRRs) at the cell surface (Beutler, 2004). PAMPs allow the body to discriminate between native and foreign material quickly and effectively due to their absence in any healthy eukaryotic tissue. In fact, PAMPs are so highly conserved in pathogenic organisms that a single structural motif can allow for the detection of a huge number and variety of infectious microbes. PAMPs can vary significantly in structure between pathogenic invaders (examples including proteins, membrane components, ribonucleic acids [RNAs] etc.), but always include integral features

of the microbe as not to be susceptible to significant variability (Moresco et al., 2011). Each PRR is specific to a single or small selection of PAMPs but their highly conserved nature makes the innate immune response a highly effective and elegant system despite its low specificity.

1.2.2 Mechanisms of Inflammation

Upon the detection of PAMPs by PRRs at sites of infection or tissue injury the inflammatory response is rapidly initiated, often within a matter of minutes (Shephard, 2001). Broadly, it is split up into two stages termed acute and chronic. Acute inflammation consists of the five cardinal signs: *rubor* (reddening), *calor* (heat), *tumor* (swelling), *dolor* (pain) and *functio laesa* (loss of function) and is usually a relatively short lived process (Celsus, 0025; Tracey, 2006). Injury, infections and toxins disrupt the natural homeostasis (the regulation and maintenance of key variables to achieve equilibrium and stability of the internal environment) of cells and acute inflammation can be considered as a response to pathogen-induced perturbations to restore homeostasis at the cellular level (Chovatiya and Medzhitov, 2014). Chronic activation of inflammatory mechanisms however can last significantly longer and have been shown to contribute to the pathogenesis of diseases such as cancer and atherosclerosis (Coussens and Werb., 2002; Tuttolomondo et al., 2012). Atherosclerosis has been reported to be the principle cause of strokes, heart attacks and gangrene (Lusis, 2000). Furthermore it is the leading cause of vascular disease and is currently the biggest killer in America, with predictions by the World Health Organisation indicating that it could be the biggest killer globally in a number of years (Hansson et al., 2006). In short, atherosclerosis is the aberrant clogging of arteries and development of plaques due to endothelial dysfunction which is mediated by pro-inflammatory molecules (Berliner et al., 1995). This is largely due to contributions from runaway Toll/interleukin-1

receptor (TIR) signalling (see *Section 1.2.3*, *Section 1.2.4* and *Section 1.2.5*; Kleemann et al., 2015; Libby et al., 2009).

Inflammatory responses are primarily propagated, regulated and amplified by TIR signalling (Sims and Smith, 2010). Following PAMP detection by Toll-like receptors (TLRs; see *Section 1.2.3*), PRRs which are a members of the TIR superfamily, activation of nuclear factor κ-light-chain-enhancer of activated B cells (NF-κB) results in the release of pro-inflammatory cytokines from the cell (Takeda et al., 2003). Cytokines, from the Greek *cyto* - meaning cell and *kinos* - meaning movement, are small messenger proteins which are secreted from parent cells and diffuse through the extracellular matrix (the scaffold space between individual cells onto which they are anchored; ECM). They act to permit communication between cells by interacting with specific cell surface receptors which induce intracellular signalling cascades and often the release of further cytokines (Zhang and An, 2009). In this way, cytokine-receptor binding can induce a very rapid amplification of biological activity. Of particular importance in the context of pro-inflammatory signalling are members of the interleukin-1 (IL-1) and IL-1 receptor (IL-1R) families (see *Section 1.2.4*) which act as central mediators of the innate immune and inflammatory responses (Garlanda et al., 2013).

1.2.3 Toll-like Receptor System

By far the most widely studied PRRs within the body are the TLRs which were named after being identified as a human Toll homologue following genetic comparison by Medzhitov et al. (1997). Toll was discovered by Nüsslein-Volhard and Wieschaus (1980) inside the common fruit fly, *Drosophia Melanogaster*, and reportedly takes its name from Nüsslein-Volhard's outburst of *"das ist ja toll!"* upon its discovery which translates from German as *"that is great!"* (Nüsslein-Volhard et al., 1985). Initially, Toll was studied for its involvement in establishing the dorsal-ventral axis in developing embryos and it was only much later that it was shown to exhibit anti-fungal immunogenic properties. Similarly, TLRs exhibit a

wide variety of immunological importance and are responsible for the detection of a large proportion of all infectious agents. In fact the TLR system has been shown to be able to recognise all known pathogens (Moresco et al., 2011). Unlike Toll however, TLRs have no developmental role and function solely in immunity. In humans, a total of ten TLRs have been identified termed TLR1 to TILR10. Structurally, they are type I transmembrane proteins containing distinct extracellular and intracellular regions, the latter of which is the highly conserved TIR homology domain. This region is predominantly identical across all TLRs and is also found in IL-1RI. Functionally, it responsible for the development of the immune response by initiation of signalling cascades (Takeda et al., 2003).

The TLR extracellular domain is responsible for interaction with PAMPs and as such varies somewhat between members of the family. Broadly however, their extracellular structure is dominated by leucine-rich repeats, hydrophobic motifs which allow TLRs to form complexes with PAMP containing substances. Extracellular regions of TLRs are shaped like curved solenoids and can exhibit binding sites on both the convex and concave sides in hydrophobic pockets (see *Figure 1.1*; Moresco et al., 2011). With the exception of TLR1, TLR2 and TLR6, all TLRs form homodimers upon ligand binding in order to permit both the binding interaction itself and to initiate downstream signalling by undergoing conformational changes in the TIR domain. TLR1 and TLR6 instead both form heterodimers with TLR2. The TLR1/TLR2 complex is responsible for the detection of triacylated lipopeptides prevalent in mycoplasma and Gram-negative bacteria alongside peptidoglycan which resides outside of the plasma membrane on all bacteria (Kawai and Akira, 2010). The TLR2/TLR6 complex is responsible for the detection of diacylated lipopeptides present in Gram-positive bacteria and in mycoplasma (Moresco et al., 2011). TLR3 is responsible for the detection of double-stranded RNA in the cell endosome (internal membrane bound vesicles) and as such is associated with the detection of viral infections (Alexopoulou et al., 2001; Kawai and Akira, 2010). TLR4 is primarily responsible for the detection of lipopolysaccharide (endotoxin)

which is prevalent on a number of infectious agents and also detects alternatively spliced variants of bodily proteins which are produced in response to injury (Okamura et al., 2001; Yoshimura et al., 1999). TLR5 associates with bacterial flagellin and TLR7 is activated by single-stranded RNA (ssRNA), thereby recognising ssRNA viruses (Crozat and Beutler, 2004; Hayashi et al., 2001). Finally, TLR9 is activated by single stranded CpG deoxyribonucleic acid (DNA) present in a variety of bacteria while the ligands for TLR8 and TILR10 remain unknown (Moresco et al., 2011; Rutz et al., 2004).

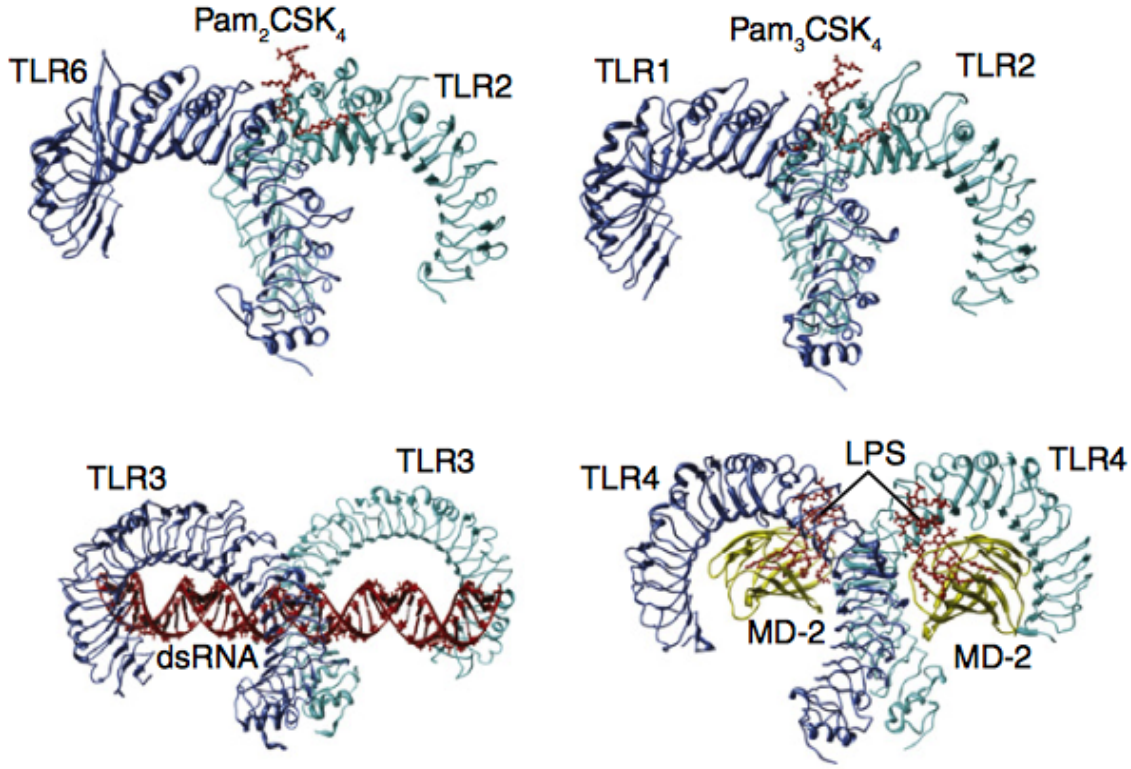

Fig. 1.1 Model structures of the extracellular regions of the TLR6/TLR2, TLR1/TLR2, TLR3/TLR3 and TLR4/TLR4 complexes displaying the LRR solenoid structures. The location of ligand binding is indicated in each complex. Reprinted from Current Biology, 21/13, Moresco et al., Toll-like receptors, R488-R493, Copyright (2011), with permission from Elsevier.

1.2.4 Interleukin-1 Receptor System

Members of the IL-1 and IL-1R families are central regulators of inflammation (Gabay et al., 2010; Garlanda et al., 2013). IL-1 stimulus and subsequent activation of IL-1R results in the production and secretion of many pro-inflammatory cytokines such as interleukin-8 (a protein responsible for attracting various immune cells to the site of injury; IL-8; Elliott et al., 1998; Martin et al., 1994; Robson et al., 1995; Romero et al., 1989). In humans the IL-1/IL-1R system consists of three ligands, IL-1α, IL-1β and IL-1 antagonist (IL-1A), and two receptors, type I (IL-1RI) and type II (IL-1RII) alongside IL-1R accessory protein (IL-1RAP; Garlanda et al., 2013). Structurally both IL-1Rs are transmembrane proteins and contain extracellular regions which are characterised by three antibody (immunoglobulin; Ig) domains (O'Neill, 2008). These domains permit the ligand-binding functionality of the receptors. The IL-1RI is $\backsim$ 80 kDa and contains the intracellular TIR domain (See *Section 1.2.5*) where as IL-1RII contains only a small cytoplasmic domain and is $\backsim$ 60 kDa in size (Garlanda et al., 2013; McMahan et al., 1991). Signal transduction and NF-κB activation (see *Section 1.2.9*) occurs only by association of IL-1α or IL-1β with IL-1RI (Sims et al., 1993). Interaction of ligands with IL-1RII does not permit downstream signalling and in this way IL-1RII functions as a negative regulator of IL-1 signalling responses (see *Figure 1.2*; Peters et al., 2013). In addition to ligand binding, association of IL-1RAP with IL-1RI is required for signal transduction. IL-1RAP, a $\backsim$ 65 kDa transmembrane protein, does not bind IL-1 directly but, following recruitment to the IL-1/IL-1RI complex, induces conformational changes in the intracellular TIR domain and permits subsequent association of adaptor proteins (see *Section 1.2.9*; Greenfeder et al., 1995; Sims and Smith, 2010). Both IL1α and IL-1β are $\backsim$ 17 kDa in size and while binding to IL-1RI with comparable affinity, result in somewhat separate functions (Afonina et al., 2015). IL-1A does not induce signalling upon binding with IL-1RI and, with similarity to IL-1RII, acts as a negative regulator of the system (Garlanda et al., 2013; Symons et al., 1995).

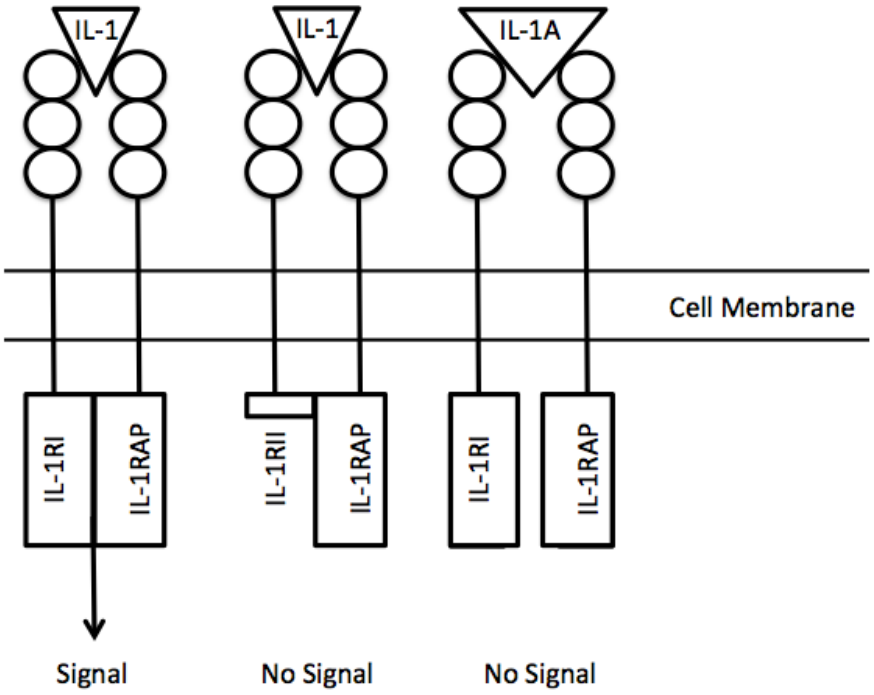

Fig. 1.2 IL-1 signalling components at the receptor level. IL-1 binds to the Igs in the IL-1R extracellular domain. Signal is permitted following IL-1 association with the IL-1RI complex but is blocked by IL-1A and IL-1RII.

1.2.5 Toll/Interleukin-1 Receptor Homology Domain

All members of the TIR superfamily contain the homologous intracellular TIR domain. It is highly conserved between all members and permits signalling cascades following TLR association with corresponding PAMPS and IL-1RI association with IL-1α or IL-1β. Upon ligand binding and receptor dimerisation (TLR/TLR or IL-1RI/IL-1RAP), the formed complex induces conformational changes in the TIR domain which allow association of TIR domain containing, intracellular adaptor proteins such as myeloid differentiation primary response protein 88 (MyD88; Gay and Gangloff, 2007). The mechanism of adaptor association to the complex is dependent on the receptor system. In the canonical NF-κB pathway (see *Section 1.2.9*) MyD88 is able to associate directly with the IL-1RI receptor complex however, in the case of TLR4 induced pro-inflammatory signalling the intermediate molecule TIR domain containing adaptor protein (TIRAP) is required. TIRAP, containing

a negatively changed surface TIR domain, primarily acts as a bridge, and allows for the association by proxy of the positively charged TIR domains of the receptor complex and MyD88 (Moresco et al., 2011; Takeda et al., 2003). Association of adaptor proteins permit the propagation of the signal which subsequently results in the translocation of NF-κB to the cell nucleus (Kenny and O'Neill, 2008; Martin and Wesche, 2002).

1.2.6 Co-Receptors in Cell Signalling

Cell signalling is generally induced by ligand binding with receptors at the cell surface. Often these signals are regulated by the association of co-receptors to the primary receptor complex. The extracellular region of the primary receptor contains the required molecular motifs to permit specific ligand binding but often the cytoplasmic domain is either not sufficient to permit signal propagation unaided or has a higher signalling potential than that induced by just the ligand. Co-receptors (following binding with appropriate ligands and structural proteins) associate with the primary receptor and induce conformational changes to the intracellular domain of the resulting complex. This then allows for the recruitment of adaptor proteins which transmit signals into the inner regions of the cell via association of further components such as kinases (enzyme molecules responsible for the phosphorylation and subsequent modification of their binding partners; Mak, 2005). Several types of biomolecules with co-receptor functionality have been identified, including proteins and PGs, and these have been shown to bind with a variety of extracellular ligands such as cytokines and ECM components. Examples of co-receptors include cluster of differentiation 14 (CD14) which associates with the TLR4 dimer complex in the detection of LPS, syndecan-4 (SDC4), a PG which regulates fibroblast growth factor receptors (FGFRs) and transforming growth factor-β (TGF-β) receptor III (TGF-βR3; commonly referred to as betaglycan), a PG which regulates TGF-β signalling (Elfenbein and Simons, 2010, 2013; Mythreye and Blobe, 2010).

1.2.7 Proteoglycans

PGs and glycosaminoglycans (GAGs) are subsets of biomolecules produced and secreted by virtually all mammalian cells and have a vital role in a wide variety of immunological and signalling processes within the body. These can range from tissue repair and inflammatory regulation to mechanical interactions with the ECM (Jackson et al., 1991). Structurally, PGs consist of a protein core or anchor onto which a variety of GAG chains are are attached and all PG molecules are characterised by which of these attached carbohydrate chains they exhibit. GAG's themselves are linear in structure and consist of repeating disaccharide domains which broadly contain a hexosamine (*N*-acetylglucosamine or *N*-acetylgalactosamine) and (with the exception of karatan sulfate [KS] which instead contains galactose) a hexuronic acid (D-gluronic acid or L-iduronic acid; Gandhi and Mancera, 2008). GAG's are categorised by both the structure and composition of these repeating units and are divided into the heparin (Hep) / heparan sulfate (HS), chondroitin sulfate (CS) / dermatan sulfate (DS), KS or hyaluronic acid (HA) families with each being responsible for specific sets of bodily processes. Primarily, all GAG's act to bind with other molecules to induce some biological or mechanical effect and, with the exception of HA, exhibit a negative charge of differing strength due to variations in the degree of sulfation between different GAG types, variations between chains of the same family and variations between different domains within each chain (Gulati and Poluri, 2016).

The amino sugar contained within the repeated disaccharides of Hep, HS and HA is *N*-acetyl-D-glucosamine which has lead to the broad categorisation of these three GAG types as glucosaminoglycans (Gulati and Poluri, 2016). Generally, Hep and HS are considered to be two variations on the same type of carbohydrate chain with Hep containing a higher density of negative charge due to a composition of uniformly sulfated domains. HS instead contains repeated sulfated units interspaced with non-sulfated units (Capila and Linhardt, 2002; Xu and Esko, 2014). Hep is most notably known for its properties as an anti-coagulant

by inducing conformational changes within inhibitor molecules that prevent the formation of fibrin in blood, but it is theorised that its original role within the mammalian body was involved in protection from bacterial attack (Page, 2013). Not only is Hep the most sulfated of the GAGs but it is also the biomolecule containing the highest negative charge density that has currently been identified (Weiss et al., 2017). HS is generally found in PG form as a cell surface or transmembrane receptor and, upon ligand binding, and often associates with other receptor complexes to amplify downstream effects including, but not limited to, inflammatory regulation, cellular growth and differentiation, wound repair and interaction with the ECM (Lin, 2004; Sarrazin et al., 2011). One such HS PG (HSPG), with particular relevance to this thesis is SDC4.

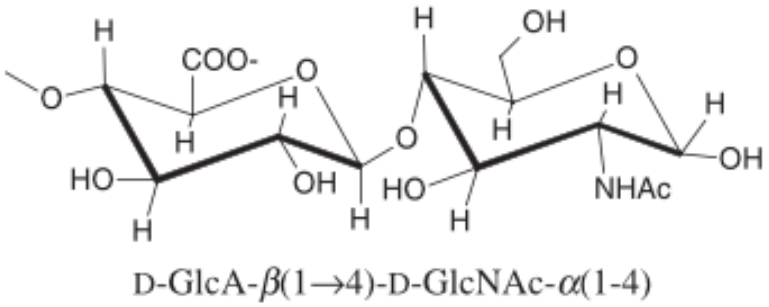

Fig. 1.3 Disaccharide repeating units of ECM/cell surface HS GAGs (D-glucoronic acid & D-glucosamine). Reprinted with permission from Chemical Biology & Drug Design, 72/6, Gandhi and Mancera, The structure of glycosaminoglycans and their interactions with proteins, 455-482, Copyright (2008) Wiley.

SDC4 is a member of the syndecan family of HSPGs alongside syndecans 1, 2 and 3 which are grouped due to their origination from a single ancestral gene. They are all type I transmembrane proteins which act as co-receptors and as such, couple with primary receptors in order to illicit a cellular response (Mythreye and Blobe, 2010). Each of these proteins contain a N-terminal extracellular domain, onto which the HS GAGs that are responsible for binding are attached, a hydrophobic transmembrane domain, containing a GxxxG dimerisation motif to allow for association with primary receptors, and a C-terminal cytoplasmic domain which is highly conserved across the syndecan family (see *Figure 1.4*;

Liu et al., 2015; Prakash et al., 2011). While the other members of the syndecan family are located in specific tissue types, SDC4 seems to be expressed ubiquitously which is possibly due to the wide variety and high versatility of its effects, including the mediation of cellular proliferation, migration, adhesion, endocytosis and mechanotransduction (Elfenbein and Simons, 2013; Kimata et al., 2007). It has also been shown to be the only syndecan which is consistently expressed at focal adhesions (Fears and Woods, 2006; Woods and Couchman, 2001). SDC4 is the smallest member of the family with a molecular weight of $\backsim$ 20 kDa and binds a variety extracellular molecules including soluble growth factors and ECM proteins (Simons and Horowitz, 2001; Tkachenko et al., 2005). Extracellular FN is one such component and association primarily occurs via the SDC4 HS chain with the HepII binding domain located at FN repeats III_{12} to III_{14} (see *Section 1.2.10*) which seems to be governed by a cluster of basic residues at III_{13} (Bloom et al., 1999).

CS and DS are always found in the form of PGs and essentially differ only in their patterns of sulfation and their localisation within the body, DS PGs being prevalent in the skin and connective tissues while CS PGs (CSPGs) mainly reside within the central nervous sytem (Gulati and Poluri, 2016; Habuchi et al., 2004; Silbert and Sugumaran, 2002). In fact, before being an accepted GAG in its own right, DS was previously considered a subclass of the CS group known as CS-B. Both CS and DS contain *N*-acetyl-D-galactosamine as the repeated amino sugar and as such (alongside KS) fall into the galactosaminoglycan categorisation of GAG molecules (Gandhi and Mancera, 2008). DS PGs primarily function in the provision of structural integrity to tissues, including contributions to the tensile strength of skin, by interaction with ECM proteins such as collagen (Elefteriou et al., 2001; Trowbridge and Gallo, 2002). CSPGs by contrast predominantly affect axons and have a role in cellular growth, plasticity and migration (Dyck and Karimi-Abdolrezaee, 2015). Decorin (DCN) is a CSPG with significant relevance to this thesis.

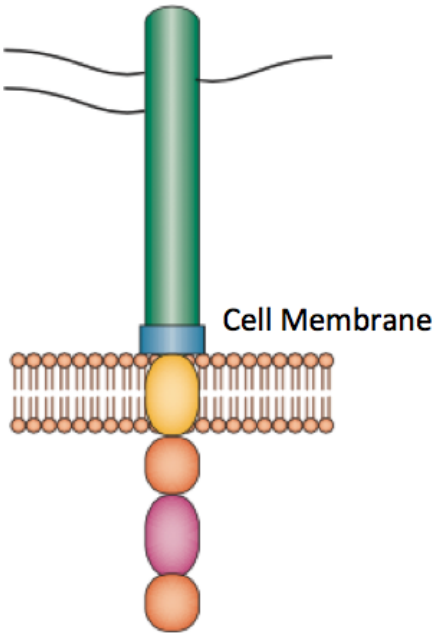

Fig. 1.4 A schematic diagram depicting the structure of SDC4. HS chains (black lines) are attached to the extracellular region of the protein core (green). A shedding region (blue) allows for the release of the extracellular domain as a negative regulator of signalling mechanisms. The highly conserved transmembrane region (yellow oval) facilitates attachment to the cell surface. The intracellular domain is made up of two domains which are conserved across all members of the syndecan family (orange circles) and one region specific to SDC4 (red oval). Adapted with permission from Nature Reviews Rheumatology, 9/1, Pap and Bertrand, Syndecans in cartilage breakdown and synovial inflammation, 43-55, Copyright (2013) Macmillan Publishers Limited.

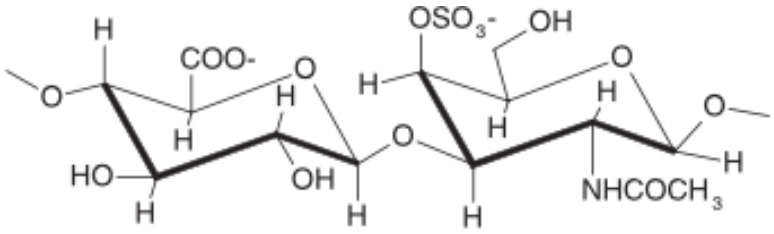

D-GlcA-β(1$\rightarrow$ 3)-D-GalNAc4S-β(1$\rightarrow$ 4)

Fig. 1.5 Disaccharide repeating units of CS GAGs (D-glucoronic acid & D-galactosamine). Reprinted with permission from Chemical Biology & Drug Design, 72/6, Gandhi and Mancera, The structure of glycosaminoglycans and their interactions with proteins, 455-482, Copyright (2008) Wiley.

DCN (structurally and functionally similar to biglycan) is a small leucine-rich PG, approximately 90 to 130 kDa in size, and is composed of a $\backsim$ 40 kDa protein core and a single $\backsim$ 50 kDa CS chain (despite the molecule containing three possible GAG attachment sites; Schaefer and Iozzo, 2008; Zhu et al., 2008). Unlike SDC4 and other HSPGs described above, DCN is not a membrane spanning proteoglycan but instead resides within the ECM (Feidler and Eble, 2009). As such it functions as a structural molecule by binding various extracellular components such as collagen and FN (in fact DCN takes its name from its tendency to decorate collagen fibres), but also has significant relevance in signalling, specifically in cell immunity, growth and morphogenesis (Boskey and Robey, 2013; Seidler, 2012). The molecule itself is shaped like an arch with a β-sheet on the concave surface and α-helecies on the convex side (see *Figure 1.6*). A central cavity is made up of leucine-rich repeats which permit binding (Weber et al., 2001). The CS GAG is located at the N-terminus edge and seems to be responsible for binding with adjacent ECM fibrils Additionally, a number of cysteine residues are positioned on the convex rear and three *N*-linked oligosaccharides reside near the C-terminus (Schönherr et al., 1995). Studies have suggested that both the attached CS GAG and the core DCN protein itself have both signalling and structural functions and have indicated that both may contribute to its binding with extracellular FN (Schmidt et al., 1991; Seidler, 2012).

1.2.8 Toll-like and Interleukin-1 Receptor Regulator

TILRR is an IL-1RI co-receptor and functions to potentiate signals induced by association of IL-1 and IL-1RI at the receptor level (Zhang et al., 2012, 2010). Amplification of IL-1 signalling following ligand binding with IL1-RI is induced by association of TILRR with the receptor complex. This is dependent on TILRR binding with extracellular FN. Inhibition of IL-1RI/TILRR association in the presence of FN which did not contain Hep binding sites (sites were deleted) identified TILRR as a HSPG which interacts with FN via its exposed

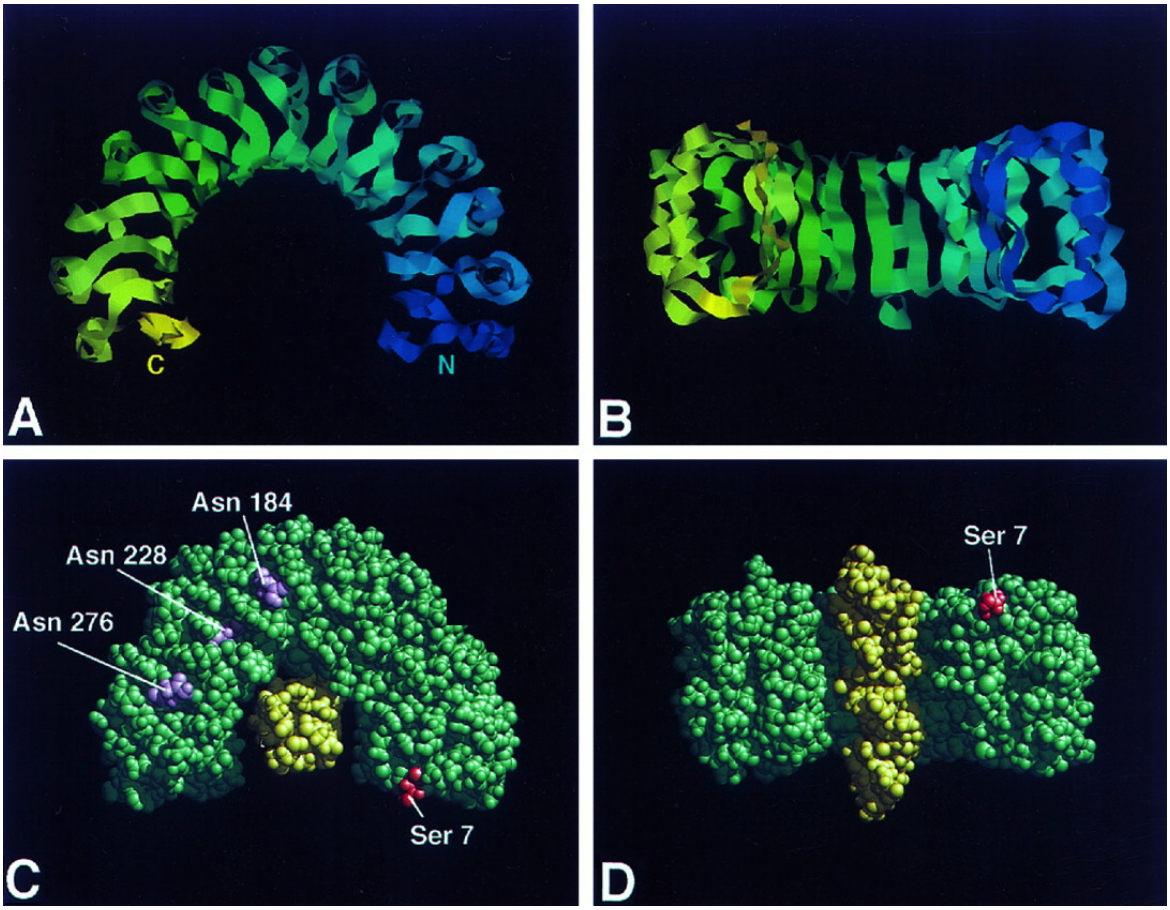

Fig. 1.6 The Model structure of human DCN is shown from two viewpoints illustrating the β-sheet on the concave surface and the α helices on the convex side (**A**, **B**). Model images constructed from individual residues illustrate DCN (green) *decorating* a collagen molecule (yellow; **C**, **D**). GAG (Ser 7) and *N*-linked oligosaccharide (Asn 184, Asn 228 and Asn 276) attachment sites are labeled clearly in red and purple respectively. Reprinted from the Journal of Biological Chemistry, 271/50, Weber et al., Model structure of decorin and implications for collagen fibrillogenesis, 31767-31770, Copyright (1996) American Society for Biochemistry and Molecular Biology.

HS chains (Vallés et al., 1999). Similarly, incubation with heparinase yielded the same inhibitory effect. Studies using a green fluorescent protein (GFP)-tagged TILRR variant have demonstrated its localisation at the cell surface (see *Figure 1.7a*) which supports its identified function (Zhang et al., 2010). Structurally, TILRR contains a core protein which is $\backsim$ 70 to $\backsim$ 80 kDa in size and is anchored to the cell membrane via a lectin binding domain. The core protein also contains an arginylglycylaspartic acid domain (integrin binding domain; Arg-Gly-Asp; RGD), multiple *N*-linked glycosylation sites and a Calx-β motif (see *Figure 1.7b*; Erickson and Wynshaw-Boris, 2016). It also contains two GAG attachment sites, one of which is located at the exposed N-terminal end of the protein and facilitates attachment of the functional HS chain. Recently, TILRR has been demonstrated to have a role in disease. Studies of TILRR *in vivo* have revealed low levels of expression in healthy tissue however, significantly higher expression has been identified within atherosclerotic plaques. It has been reported that blocking TILRR reduces both vascular inflammation and atherosclerotic plaque development, with lesions instead exhibiting characteristics of stable plaques (Samokhin et al., 2014; Smith et al., 2017).

1.2.9 Signal Transduction

The inflammatory mechanism is governed by the transcription factor NF-κB family of proteins. Found to be present in almost all cell types, they are characterised by the inclusion of a Rel homology domain (RHD) binding motif at the N-terminus. Upon NF-κB activation, the RHD permits both dimerisation and binding to DNA which in turn allows for signal transduction and pro-inflammatory functionality (Zheng et al., 2011). Inactive NF-κB resides in the cell cytoplasm bound to the 37 kDa inhibitor of κB (IκBα). IκBα interacts with NF-κB at the RHD and induces conformational changes such that the RHD is inaccessible to further interaction (Krappmann and Scheidereit, 1997). The mammalian NF-κB family is highly conserved and consists of five members, RelA, RelB, c-Rel, p105/p50 and p100/p52 (see

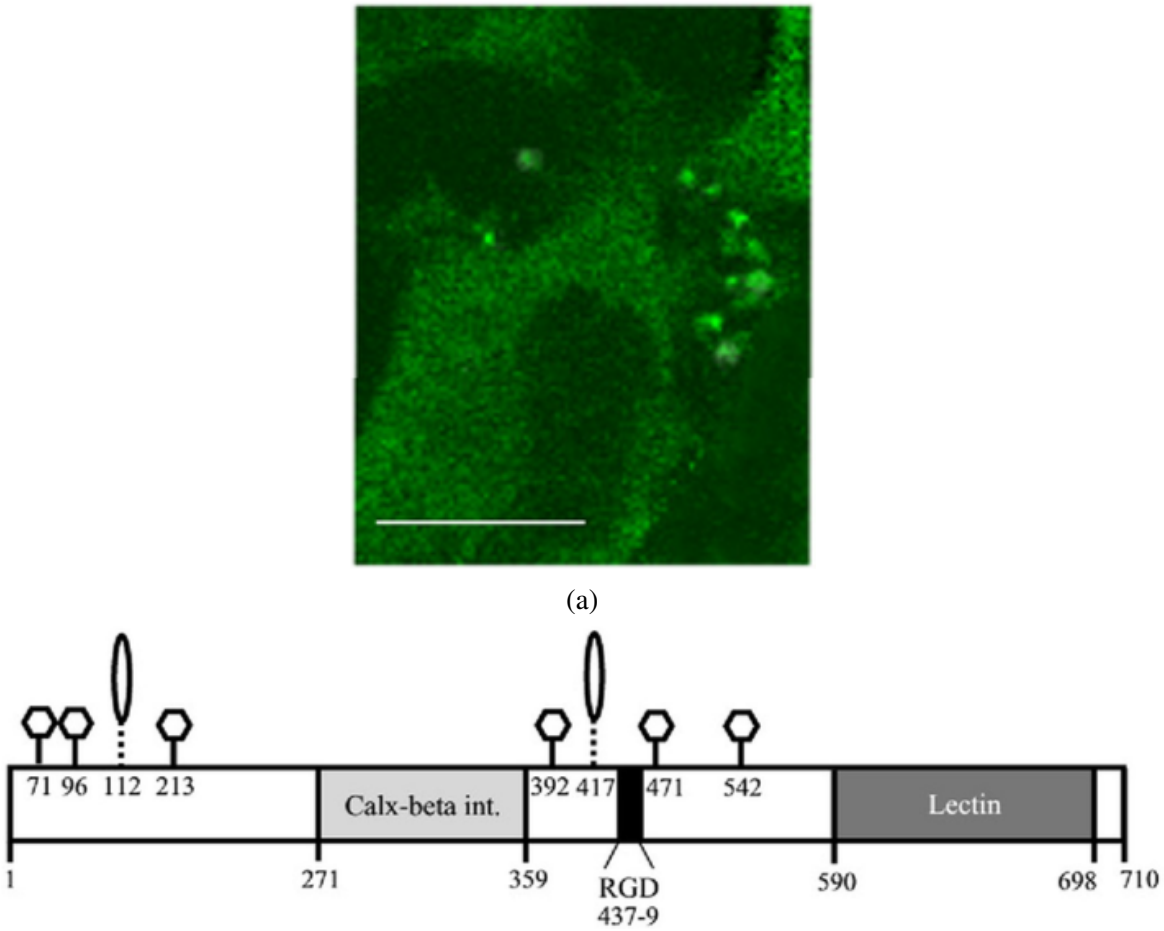

(a)

(b)

Fig. 1.7 A confocal micrograph of HeLa cells transfected with an EGFP-TILRR construct (a). Localisation of TILRR at the cell surface is clear. Scale bar: 3 μm. A schematic diagram of the structural components of the TILRR protein core (b). A GPI anchor is located in the lectin domain at the C-terminus and a RGD motif is located near the the centre of its length. The positions of GAG attachments sites (ovals) and *N*-linked glycosylation sites (hexagons) are indicated. Reprinted from the Journal of Biological Chemistry, 285/10, Zhang et al., TILRR, a novel IL-1RI co-receptor, potentiates MyD88 recruitment to control Ras-dependent amplification of NF-κB, 7222-7232, Copyright (2010) American Society for Biochemistry and Molecular Biology.

Figure 1.8; Lindström and Bennett, 2005). RelA, RelB and c-Rel all contain transactivation domains (TADs) at the C-terminus which are required for the initiation of DNA transcription. By comparison, p100 and p105 along with IκBα contain repeated ankyrin motifs which prevent translocation of inactive NF-κB and both p105/p50 and p100/p52 variants to the nucleus, subsequently blocking signal propagation. Activated NF-κB (following cleavage of p105/p50 into p50 and p100/p52 into p52 under mechanisms of activation) is composed of heterodimers of family members linked at the RHD. The p52/RelA variant of NF-κB is the most widely studied and results from the degradation of IκBα. The p50/p52 dimer acts as a negative regulator of the system by binding with active sites but inducing no signal propagation due to the absence of TADs (Hoesel and Schmid, 2013; May and Ghosh, 1997).

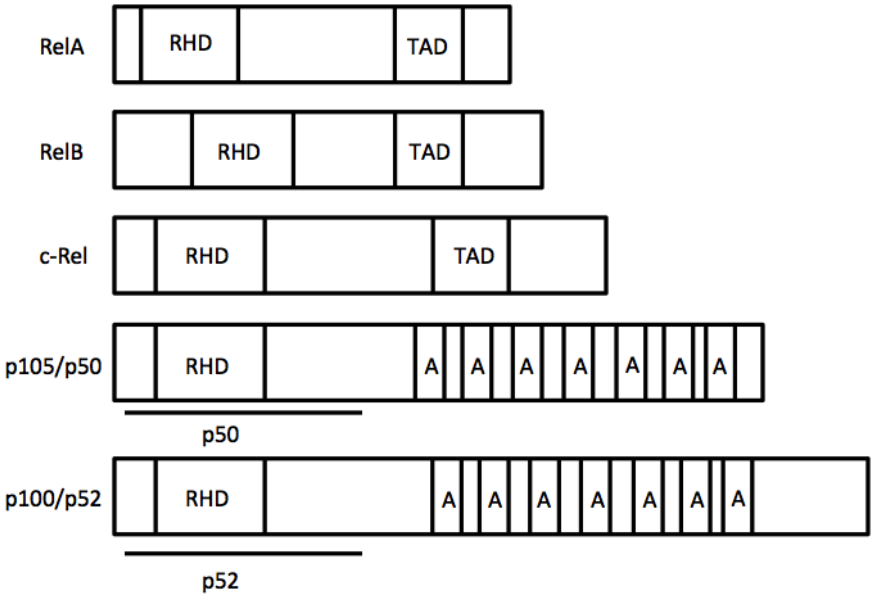

Fig. 1.8 Members of the human NF-κB family. The presence and positions of RHDs, TADs and ankyrin motifs (A) are indicated for each.

Following activation of the IL-1RI receptor complex by binding IL-1, intracellular signalling cascades are initiated through the cytoplasmic TIR domain. IL-1 signalling can be split into two categories termed the canonical and non-canonical pathways. Both pathways activate NF-κB and result in the production and secretion of pro-inflammatory cytokines from the parent cell. IL-1 induced NF-κB signalling is summarised in *Figure 1.9*. The

canonical pathway is characterised by association of adapter protein MyD88 with the TIR domain of the activated IL-1RI complex. Following this, members of the interleukin-1 receptor-associated kinase (IRAK) family are recruited to the intracellular TIR/MyD88 complex (Weber et al., 2010). IRAK4 is the first to associate via a N-terminal death domain that interacts directly with MyD88. IRAK4 has been shown to be of great significance immunologically with studies reporting that deficiency results in an inability to respond to TLR2, TLR4 and TLR9 associated pathogens (Suzuki et al., 2012). Following IRAK4 association with MyD88, IRAK1 is recruited to the complex and subsequent phosphorylation allows for the introduction of tumour necrosis factor receptor-associated factor 6 (TRAF6; Weber et al., 2010). TRAF6 is responsible for the transduction of the inflammatory signal from the TIR domain of the IL-1RI complex to the inner regions of the cell. Following phosphorylation via association with IRAK1, the TRAF6/IRAK1 complex dissociates from the TIR domain and associates with TGF-β-activated kinase (TAK)1, TAK binding protein (TAB)1 and TAB2. The TAK1/TAB complex then associates with the IκB kinase (IKK) complex which is comprised of IKK subunit-α (IKKα), IKK subunit-β (IKKβ) and NF-κB essential modulator (NEMO). Upon association of the two complexes via TAK1 and NEMO, the activated IKK degrades IκBα via IKKα and IKKβ thereby releasing NF-κB. Activated NF-κB is then free to translocate to the nucleus and propagate pro-inflammatory signals (Gabay et al., 2010).

Non-canonical NF-κB signalling, as induced by IL-1RI activation, does not involve recruitment of adaptor MyD88. Instead, phosphoinositide 3-kinase (PI3K), via its p85 regulatory subunit, associates directly with the receptor complex (Reddy et al., 1997). Activation of PI3K results in the phosphorylation of the serine/threonine kinase, Akt (Sizemore et al., 1999). Phosphorylated Akt subsequently activates IKKα which then phosphorylates RelA and permits translocation of NF-κB to the nucleus and therefore the propagation of pro-inflammatory signals (Bai et al., 2009). The activation of Akt and subsequent release

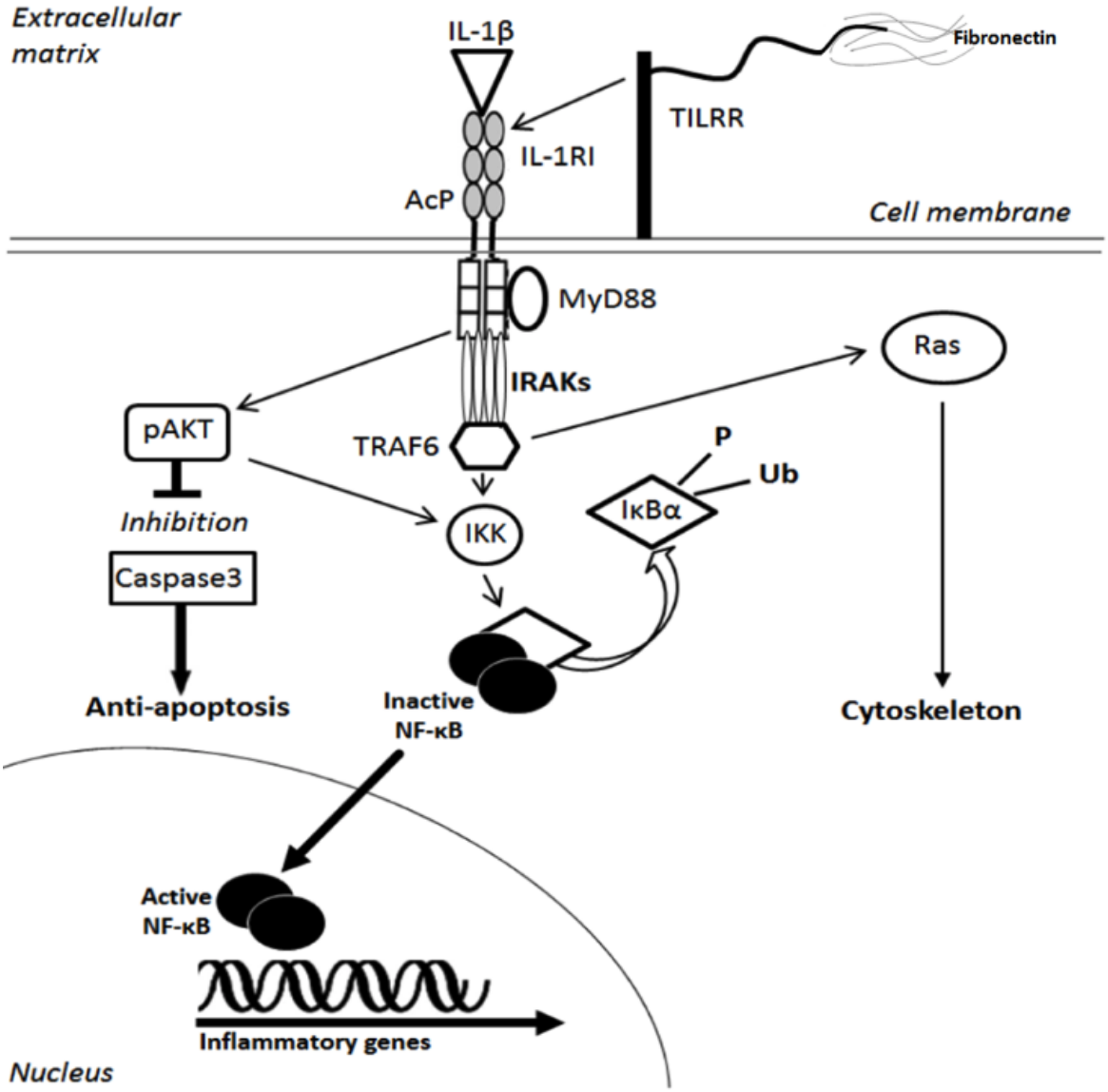

Fig. 1.9 The canonical and non-canonical signalling pathways initiated by IL-1β association with IL-1RI and amplified by co-receptor TILRR. Key signalling components and cellular effects are indicated. Adapted from PLoS One, 10/6, Rhodes et al. (2015), Computational modelling of NF-κB activation by IL-1RI and Its co-Receptor TILRR, predicts a role for cytoskeletal sequestration of IκBα in inflammatory signalling, e0129888.

of NF-κB also have inhibitory effects on caspase-3 which results in anti-apoptotic effects on cells. In this way, non-canonical NF-κB signalling as induced by IL-1RI activation has pronounced effects on cell survival and longevity (Zhang et al., 2004a, 2012).

Under conditions which potentiate TILRR association with the IL-1RI complex (or more specifically in the presence of extracellular FN), studies have shown that the activation of IL-1RI results in pronounced changes in cell shape and dramatically disorganises the cytoskeletal structure (see *Figure 1.10*; Zhu et al., 1998). In the absence of FN these changes were not observed suggesting its requirement in their induction. Similarly, under the same conditions IL-1 was shown to affect cell contact with the dish at focal adhesions (see *Figure 1.11*), inferring an effect on binding with the ECM which is induced by phosphorylation and redistribution of talin (a structural protein which facilitates the attachment between the cell cytoskeleton and adhesion receptors on the cell surface; Qwarnstrom et al., 1991). Zhang et al. (2010) demonstrated that these mechanical effects on cells require TILRR amplification of IL-1RI (blocking TILRR under IL-1 saturation inhibited these changes while increased expression of TILRR caused cells to exhibit them under endogenous levels of IL-1; see *Figure 1.12*) and that they result from activation of Ras. As a member of the small GTPase family along with Rac and Rho, Ras acts to hydrolyse guanosine triphosphate (GTP) and plays a significant role in the control of cell function, structure and signalling. In short GTPases act as molecular switches following association of GTPase activation proteins and the phosphorylation of guanosine diphosphate (GDP) into GTP via guanine nucleotide exchange factors. Ras then permits the conversion of GTP back to GDP via hydrolysis. This switching nature between GDP and GTP results in the activation of multiple kinases which subsequently induce a variety of downstream effects and cellular processes. Ras has been reported to control the organisation and structure of the cell cytoskeleton and aberrant function has been shown to have a significant role in cancer (Choi and Helfman, 2014; Goodsell, 1999; Prendergast and Gibbs, 1993).

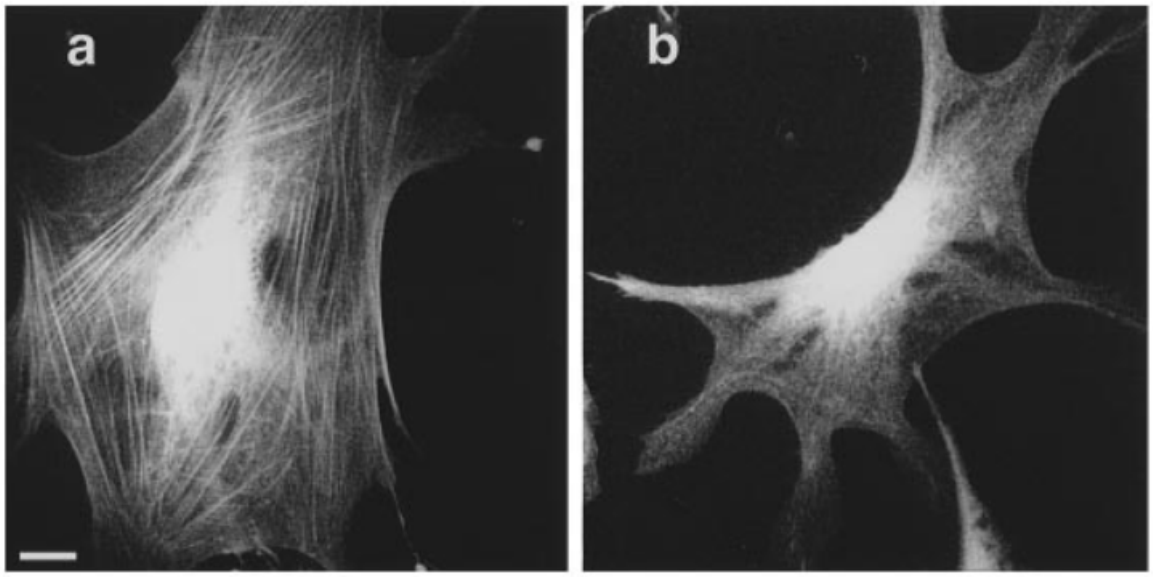

Fig. 1.10 Confocal microscopy images of fibroblast cells with FITC-phalloidin staining of the actin cytoskeleton plated on FN-coated plates (10 μgml^{-1}) for 2 hours. Prior to IL-1 stimulation cells displayed ordered actin filaments with regular cell morphology and a well defined cytoskeleton (a). Stimulating with 1nM IL-1β for 30 minutes significantly disrupted the cytoskeletal structure resulting in a pronounced change in cell shape. Cells plated absent FN did not exhibit structural changes under IL-1 stimulation. Reprinted with permission from the Biochemical Journal, 330/2, Zhu et al., Regulation of interleukin 1 signalling through integrin binding and actin reorganization: disparate effects on NF-κB and stress kinase pathways, 975-981, Copyright (1998) Portland Press.

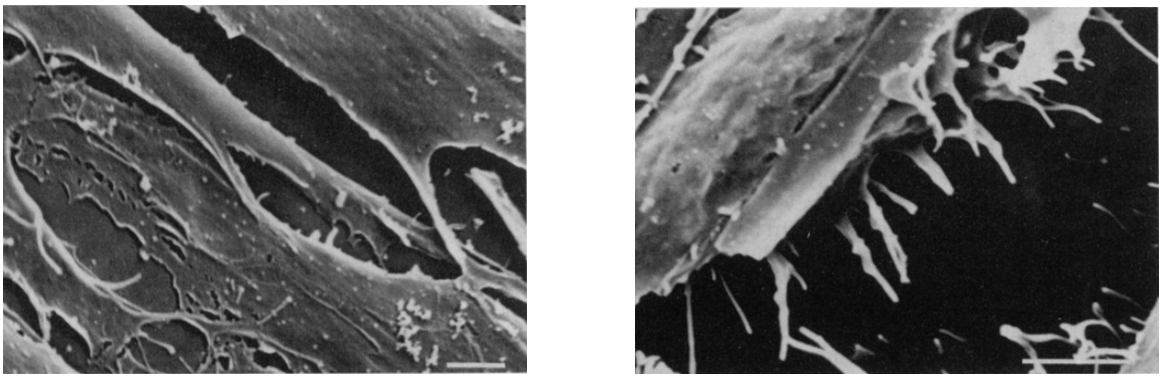

(a) (b)

Fig. 1.11 Scanning electron microscopy images of control cells (a) and cells following 15 minutes of IL-1β stimulation (b). A partial loss of cell contact can be observed following IL-1β stimulation when compared with control cultures which show clear attachment. Scale bars: 2 μm. Reprinted with permission from the Proceedings of the National Academy of Sciences of the United States of America, 88/4, Qwarnstrom et al., Interleukin 1β induces rapid phosphorylation and redistribution of talin: a possible mechanism for modulation of fibroblast focal adhesion, 1232-1236, Copyright (1991) National Academy of Sciences of the United States of America.

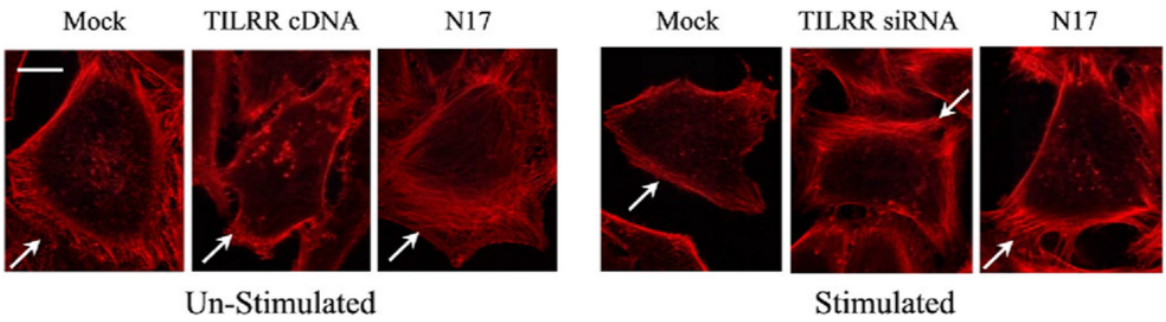

Fig. 1.12 Confocal microscopy images demonstrating significant changes in the cell shape and cytoskeleton (actin filaments were stained with rhodamine-tagged phalloidin) following 1 hour stimulation with 1 nM IL-1β when compared with control cultures. These changes were also observed in unstimulated cultures (under endogenous levels of IL-1) with increased TILRR expression (using complementary DNA [cDNA]). Reductions in extended processes can be observed by comparing regions highlighted with arrows between cultures. Furthermore, both blocking TILRR (with small interfering RNA [siRNA]) and Ras (with dominant negative N17) inhibits these mechanical effects and demonstrates that they are induced through activation of Ras GTPase and require TILRR amplification of IL-1RI. Scale bars: 2 μm. Reprinted from the Journal of Biological Chemistry, 285/10, Zhang et al., TILRR, a novel IL-1RI co-receptor, potentiates MyD88 recruitment to control Ras-dependent amplification of NF-κB, 7222-7232, Copyright (2010) American Society for Biochemistry and Molecular Biology.

1.2.10 The Extracellular Matrix in Cell Signalling

The ECM offers a space for cytokines and other biological molecules to travel between tissue components and bind with nearby cells in order to induce a wide variety significant effects. In addition to this, it is responsible for the structural arrangement and mechanical properties of the cell system it permeates (Yue, 2014). The composition of the ECM varies greatly with tissue types but in general is composed of water, minerals, PGs and fibrous (rod-like) proteins alongside the aforementioned ligand molecules (Järveläinen et al., 2009). ECM macromolecules have been shown have significant biological functions, modulating many cellular events including differentiation, migration, proliferation, adhesion and even survival (Daley et al., 2008). Disturbances in the ECM are linked with a large number of diseases, including atherosclerosis, which is indicative of its relevance in the regulation of heathy tissues and cellular homeostasis (Glorieux, 2008; Humphrey et al., 2014; Katsuda and Kaji, 2003; Nakashima et al., 2008; Wight and Merrilees, 2004). There are a huge number of fibrous proteins contained within the ECM but by far the most prevalent are collagens which make up 30% of the entire protein mass of multicellular organisms and are largely responsible for the structural stability of connective tissues (Järveläinen et al., 2009; Shoulders and Raines, 2009). FN is another structurally important, fibrous component of the ECM and has been described by some as *"biological glue"*. It has crucial applications in cellular attachment and migration and, due to its significant relevance in this thesis, will be described in detail along with is primary cell surface receptor, the $\alpha_5\beta_1$ integrin ($\alpha_5\beta_1$; Carsons, 1989; Yue, 2014).

FN is a large and complicated protein which exists naturally as a soluble 440 kDa dimer and is expressed by a wide variety of cell types (Mosher and Furcht, 1981). It can be found in both the ECM and blood plasma in high abundance. The dimer is covalently linked by a pair of disulfide bonds near the C-terminus of each $\backsim$220 kDa monomer (Bingham and Potts, 2010; Pankov and Yamada, 2002). The monomers themselves are composed

of three types of repeated domain structures which are termed type I, type II and type III FN repeats respectively (see *Figure 1.13*). Type I and type II repeats each containin four cysteine residues, involved in disulfide-bond loops, and consist of $\backsim$ 45 and $\backsim$ 60 amino acids respectively. Type III repeats by contrast do not contain disulfide bonds, some may however contain free sulfhydryl groups, and are approximately 90 amino acids in length (Proctor, 1987). The FN monomer consists of twelve type I repeats, two type II repeats and 15 - 17 type III repeats (where variations are due to alternative splicing). The type III extradomain (EIII)A and EIIIB, located between FN III_{11} to FN III_{12} and FN III_7 to FN III_8 respectively, have a variable presence in naturally produced FN dimers and the inclusion or exclusion of these regions seem to have significant relevance in injury and tissue repair (White and Muro, 2011). Similarly a variable V-domain between FN III_{14} and FN III_{15} can be partially included, fully included or excluded completely from the molecule and seems to be species specific. In humans five V variants have been identified and this domain has been reported to have a significant role in the spreading and motility of cancerous cells (Kapila et al., 1997; Pankov and Yamada, 2002).

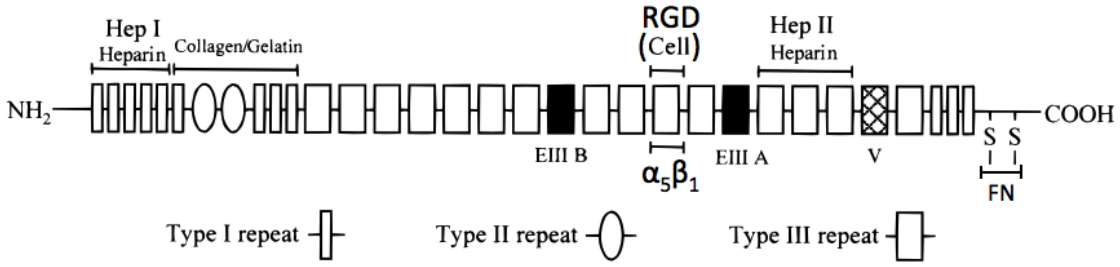

Fig. 1.13 Repeating domain structures of FN monomers with the location of the HepI and HepII binding domains, RGD motif and FN dimerisation site indicated. Variable splice regions are included and the position of the interaction with $\alpha_5\beta_1$ is noted. The repeats are counted from N-terminus to C-terminus as normal. Adapted with permission from Biochemistry, 39/12, Lin et al., Imaging and mapping heparin-binding sites on single fibronectin molecules with atomic force microscopy, 3192-3196, Copyright (2000) American Chemical Society.

FN monomers contain a large quantity of binding sites for ECM components and cell surface receptors. These include, but are not limited to, integrins, collagen, gellatin, fibrin and Hep/HS. FN can interact with Hep via two different binding sites, HepI and HepII (in actuality there is a HepIII binding site in FN but this will not be considered further). The HepII binding site is located between FN III_{12} and FN III_{14} and is considered the high affinity site (Mahalingam et al., 2007; Woods et al., 2000a,b). Furthermore, the HepII domain has been shown to result in the destabilisation and disassembly of the actin cytoskeleton in human trabecular meshwork cells (White and Muro, 2011). The HepI domain by contrast is considered the weaker binding site and is located between FN I_1 and FN I_5. Integrins, including $\alpha_5\beta_1$, bind with FN at the well characterised RGD domain in FN III_{10} which contains specific integrin-binding pockets. The RGD sequence is well conserved across species and is an integral component in the adhesion of cells to the ECM, allowing for the mediation of differentiation, growth, migration and apoptosis through the integrins and the cytoskeleton (Ruoslahti, 1996). A synergy site in FN III_9 is involved in the interaction with $\alpha_5\beta_1$ by binding with the α_5 monomer and a separate integrin binding domain, possibly associating with $\alpha_5\beta_1$, has been reported incorporating FN I_1 to FN I_9 and FN II_1 to FN III_2 which may induce different downstream signals than those induced by the RGD domain (Mao and Schwarzbauer, 2006; Pankov and Yamada, 2002; Tomasini-Johansson et al., 2007).

$\alpha_5\beta_1$, as indicated above, is a heterodimeric protein containing a $\backsim$ 160 kDa α_5 and a $\backsim$ 130 kDa β_1 subunit. Like all integrins, $\alpha_5\beta_1$ is a transmembrane receptor and possesses a horseshoe-like structure with both α and β units connected to the cell surface (Schaffner et al., 2013). The intracellular domain is comprised of the C-termini of both monomers and the tail of the β_1 subunit is linked to the actin cytoskeleton via intermediate proteins talin and vinculin at focal adhesions (Campbell and Humphries, 2011; Gu and Taniguchi, 2004). The extracellular N-terminus of each subunit is joined together at the centre of the horseshoe structure and forms a head which is responsible for ligand binding. As aforementioned, the

α_5 subunit interacts with the FN synergy site and β_1 binds with the RGD domain at its metal ion-dependent adhesion site (MIDAS; Zhang and Chen, 2012). $\alpha_5\beta_1$ structure and RGD binding is illustrated in *Figure 1.14*. Association of $\alpha_5\beta_1$ with FN governs ECM assembly, mediates FN fibrillogenesis and promotes cell survival (Schwarzbauer and Sechler, 1999; Takagi et al., 2003; Zhang et al., 1995b). With the integrin primary function being in both cell attachment and the transmission of external stimuli into cell, it is most prevalent at the cell edge and at focal adhesions (Teckchandani et al., 2009; Wozniak et al., 2004). The link between integins and the cytoskeleton allows cells to detect perturbations and stresses from external stimuli and provides a mechanism for the cell to respond to the surrounding environment (Bershadsky et al., 2003). These actin-integrin connections also allow for the extension of the leading edge and disassembly of focal adhesions at the cell rear under migration (Huttenlocher and Horwitz, 2011). Furthermore, it has been shown that $\alpha_5\beta_1$ has the capacity to induce NF-κB activity through activation of GTPases (Klein et al., 2002).

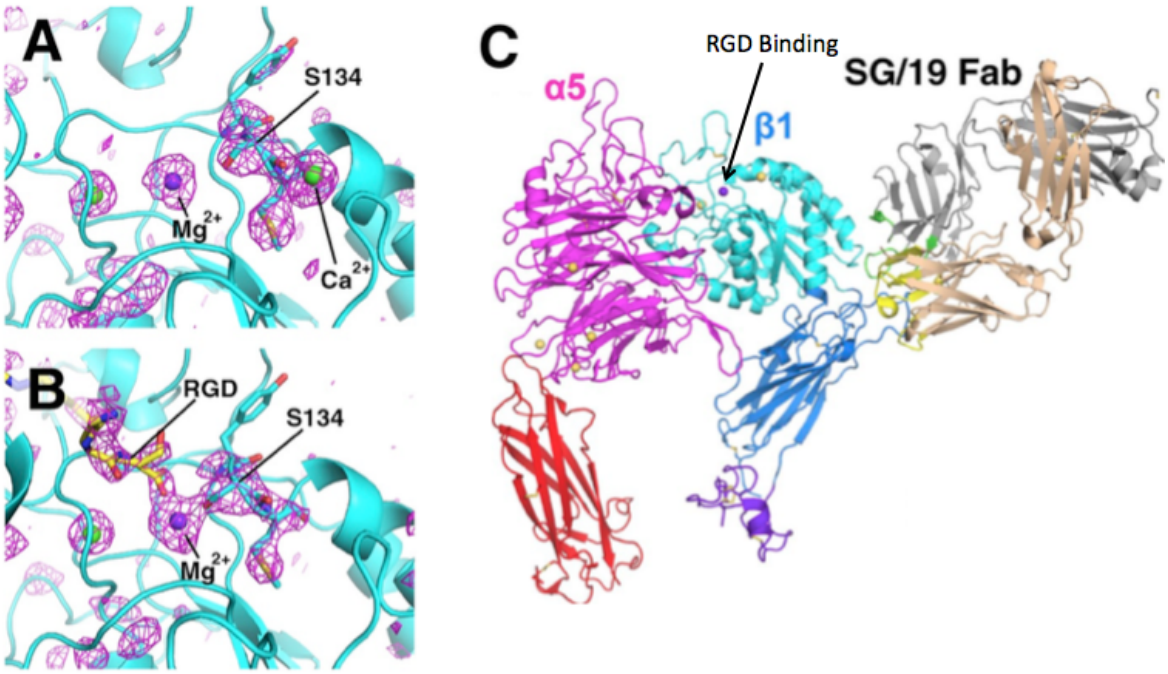

Fig. 1.14 Magnified model structure of the MIDAS in the β_1 subunit both without (**A**) and with (**B**) RDG binding. Magenta wire-frames correspond to Fo-Fc electron density maps. The model structure of $\alpha_5\beta_1$ is shown displaying its horse-shoe like morphology (**C**). Integrin activation resulting in a high affinity conformational shape is induced in the model structure by inclusion of the Ig SG/19 Fab. Adapted with permission from the Journal of Cell Biology, 197/1, Nagae et al., Crystal structure of $\alpha_5\beta_1$ integrin ectodomain: atomic details of the fibronectin receptor, 131-140, Copyright (2012) Rockefeller University Press.

1.3 Biological Application of the Atomic Force Microscope

The study of the very small has always proven to be of significant interest in physics, chemistry and biology alike and has required significant technological development to allow for us to see beyond what we, as human beings, are naturally capable of. The conventional optical microscope is a versatile tool in the observation of the microscopic and has resulted in a vast number of scientific successes and discoveries throughout history however, upon approaching the molecular level its effectiveness is drastically reduced by the diffraction limit - a limitation inherent in the reliance on light in conventional microscopy methods (de Lange et al., 2001; Thorn, 2016). In order to see beyond this boundary scientists have, throughout the years, developed a variety of microscopy techniques which do not rely primarily on light to reveal the surface properties and phenomena of the environment at the nanoscale (Kherlopian et al., 2008). The AFM was invented by Binnig et al. (1986) as a development of the scanning tunnelling microscope. As a member of the scanning probe microscope family, it relies upon the use of a physical probe to scan over the sample and, in the case of the AFM, builds an image based upon the measurement of interactive forces between the tip and surface (Binnig et al., 1986). It is now possible to generate images with near atomic resolution when using state of the art AFMs and specially designed probes (Dufrêne, 2002; Seo and Jhe, 2008). The operational mechanisms, functions and applications of the AFM are fully described in *Section 2.4*.

A huge benefit of AFM when compared to other high resolution imaging techniques, such as electron microscopy, is the ability to perform measurements in a liquid environment (Chang et al., 2012; Putman et al., 1994). This is particularly useful when applied to biological systems, allowing for the *in vitro* studies of both cell structure and behaviour and also the investigation of adhesive and elastic surface properties of living samples (Parot et al., 2007). It also allows for the choice of aqueous substance in order to replicate tissues in their natural environments or for the acquisition of data using specific growth medium to

ensure compatibility with measurements taken via other means (Bolshakova et al., 2004; Weder et al., 2010). Similarly, the AFM does not usually require any of the significant sample preparation, which may impair the biology of the system, that many alternative high-resolution microscopy techniques rely on (Dufrêne, 2008). Furthermore, the ability to obtain topographical information simultaneously with force measurements (using the force-mapping functionality of the AFM) whilst also allowing for desired tip modifications to mimic biological phenomena truly makes the AFM one of the most versatile devices currently available in the realm of biophysics (Alessandrini and Facci, 2005). Here a select few experiments are highlighted which have a significant relevance to this thesis.

1.3.1 Adhesion Studies

The binding affinities of a number of biomolecules have been studied using force spectroscopy (FS; see *Section 2.4.4*). Possibly one of the more widely known dynamic single molecule FS (DSMFS; see *Section 2.4.5*) experiments entails the quantification of DNA unbinding by Struntz et al. (1999). By immobilising oligonucleotides on both the tip and surface they investigated the unbinding of DNA duplexes with 10, 20 and 30 base pairs and probed a single energy barrier for each with dissociation rates proportional to the number of base pairs. Rupture forces varied from 20 pN to 50 pN with an increase in loading rate from 16 pN·s^{-1} to 4,000 pN·s^{-1}. The dissociation rate was found to decrease exponentially with an increase in base pairs (therefore increasing the activation energy), and was found to follow the form $10^{3-0.5n}$ s^{-1} (where n is the number of base pairs). As indicated throughout this *Section 2.4*, the rupture force between tip and sample has been shown to vary with significantly with loading rate (and also with other variables including applied trigger force) and as such any comparison between data groups in two different studies must be made with care (Lee et al., 2008). To illustrate, Lo et al. (2001) observed the unbinding between streptavidin and biotin,

a common linking tether in surface modification protocols, to vary significantly from 167 pN to 442 pN as the loading rate was increased from 40 μm·s^{-1}. to 6,000 μm·s^{-1}.

In more recent adhesion studies with particular relevance to interactions between GAGs and ECM proteins, Mitchell et al. (2007) successfully measured the binding between Hep and FN. A single energy barrier was uncovered using DSMFS with retraction velocities between 0.075 μm·s^{-1} and 6 μm·s^{-1}. By functionalising a glass slide with porcine Hep and a soft triangular cantilever with human plasma FN a dissociation rate of 0.2 ± 0.1 s^{-1} was extracted which inferred a stronger affinity bond than previous reports using other techniques, but is more in agreement with other protein-carbohydrate and cellular-ECM kinetics that have been reported (Benecky et al., 1988; Bentley et al., 1985; Dettmann et al., 2000; Mitchell et al., 2007; Yamada et al., 1980). The study also characterised the bond as somewhat compliant, fairly elastic but possessing the ability to withstand significant deformation, from the extraction of a 3.1 ± 0.2 Å barrier width. Additionally, AFM has been incorporated to map FN molecules and Hep bound FN. In this study Lin et al. (2000) found that it was possible to resolve both HepI and HepII binding domains of FN immobilised on mica by observing HEP-bound gold particles binding to FN at the two distinct regions (see *Figure 1.15*). Conversely, they seemed to observe a greater prevalence of Hep binding to the HepI binding site despite it being considered the lower affinity domain. These findings aside, HepII is still considered the higher affinity binding site which has been supported by many studies (Wang et al., 2005; Woods et al., 2000a).

In fact many ligand-receptor pairs have now been probed using FS including studies of RNA-protein interactions, the binding of integrins with ECM components and antibody-antigen association (Boye et al., 2013; Casalini et al., 2015; Franz et al., 2007; Fuhrmann et al., 2009; Li et al., 2003; Taubenberger et al., 2007). In addition, FS measurements have been extended to cells. This includes both the mapping of specific regions of adhesion on the cell surface and the attachment of live cells to the probe in order to investigate cell-

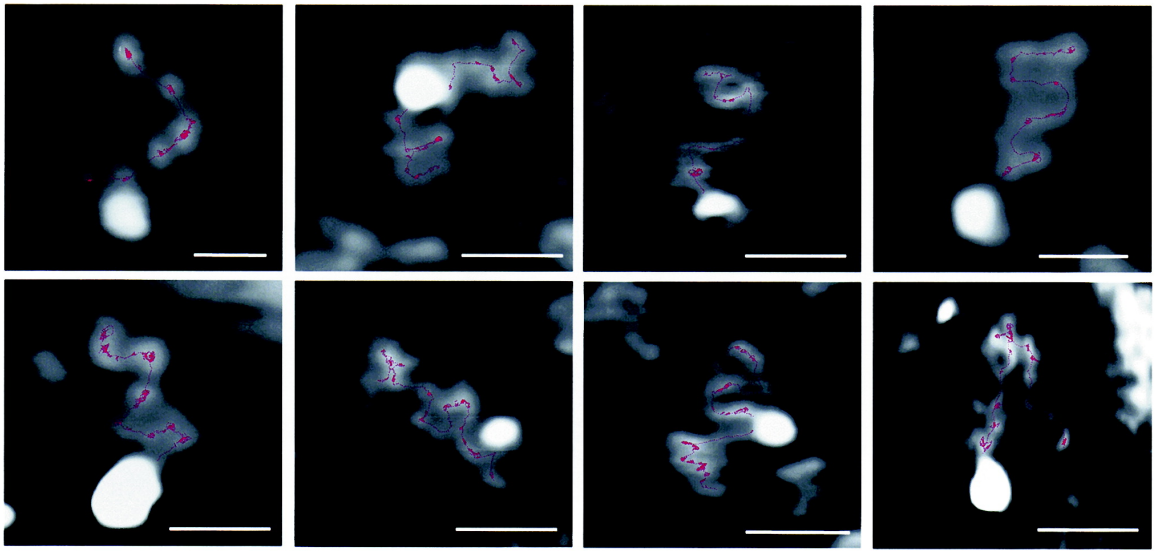

Fig. 1.15 Height profiles taken with tapping mode AFM in air depicting Hep-functionalised gold particles bound to immobilised FN dimers. The positions of the particles can be clearly resolved and correspond to the HepI and HepII binding domains. The estimated FN peptide backbone is highlighted with purple dotted lines. Scale bars: 50 nm. Reprinted with permission from Biochemistry, 39/12, Lin et al., Imaging and mapping heparin-binding sites on single fibronectin molecules with atomic force microscopy, 3192-3196, Copyright (2000) American Chemical Society.

cell interactions Helenius et al. (2008). Adhesive forces between breast cancer cells were investigated by Omidvar et al. (2014) and Zhao et al. (2013) showed that the binding between carbohydrates and lectins (proteins exhibiting a specific binding functionality for sugars) was significantly less stable on the surface of cancer cells than on healthy cells. FS measurements have now been taken on a variety of cell types including eukaryotic, bacterial and even those originating from plants (Beaussart et al., 2013; Weder et al., 2009).

1.3.2 Indentation of Cancerous Tissue

The use of AFM systems in the measurement of the mechanical properties of living cells (see *Section 2.4.6*) is becoming increasingly popular in recent years with a large focus on cancerous eukaryotic tissues. A significant variation in elastic modulus has been reported across different studies, a prime example in the reported elasticity of HeLa cells as 0.2, 0.9, 2.48 and 35 kPa (Charras et al., 2009; Hayashi and Iwata, 2015; Moeendarbary et al., 2014; Tomankova et al., 2012). As such, it is evident that the hardware, experimental parameters and analytical models used in a particular study have a significant effect on the reported mechanical properties of biological material however, this is complicated further when cellular properties are considered. The heterogeneity across a cell surface is likely to result in significant variation between studies, the authors of which may define different regions of the cell to be of more interest in order to reveal properties relevant to their hypotheses, due to differences in the composition of organelles, cytoskeletal components and nuclear material. Furthermore, significant biological differences between cells of the same line, that have been cultured and treated by different groups and with different protocols is likely to contribute to this variation. Again caution must be taken when comparing results from different studies. In fact Chiou et al. (2013) reported that the depth of indentation has a significant effect on the apparent elasticity by revealing a much larger modulus at higher trigger forces (the force applied to the sample by the AFM). They also stated that, in light of

these findings, the indentation force should not exceed 1 nN in order avoid false measurement and membrane damage. This follows from the J-shaped stress-strain curves inherent in soft biological cell membranes which result in a smaller Young moduli at a shallower indentation depths (Hayashi and Iwata, 2015).

The elastic moduli of a wide variety of cancerous tissues have been reported and generally seem to span from a few hundred Pa to the $<$ 10 kPa range. Cross et al. (2007) measured the elasticity of tumour cells in pleural effusions as 0.53 kPa and breast cancer cells have been reported as 0.39 and 0.54 kPa by Li et al. (2008) and also as 0.50 kPa by Nikkhah et al. (2011). Cancerous prostate and bladder cells have been identified with elasticities of 1.95 and 3.0 kPa respectively and Pogoda et al. (2012) has reported melanoma cells with a modulus of up to 5.10 kPa (Lekka et al., 2012; Ramos et al., 2014). These are just a few examples of mechanical measurements reported using the AFM which serve to illustrate both the variation in membrane elasticity between cancerous cells of different tissue types and the power of this technique when extracting them. It has also been used to compare the mechanical properties of cancerous cells with healthy or benign cells and these studies have revealed a dramatic decrease in the elastic modulus of cancerous tissue of around one order of magnitude (Lekka, 2016; Plodinec et al., 2012). A study conducted by Zhao et al. (2015) illustrates this by reporting the elasticity of healthy cervical cells and their cancerous counterparts as 1.20 $\backsim$ 1.32 and 0.35 $\backsim$ 0.47 kPa respectively.

1.4 Aims of the Present Study

The present study aims to investigate the physical properties of HSPG interactions with ECM component FN and to investigate the mechanical properties of both cell elasticity and their attachment to the ECM due to HSPG TILRR amplified activation of IL-1RI. In *Chapter 3* the binding interaction between HSPG SDC4 and FN is characterised using DSMFS which reveals constituent energy barriers contributing to the bound state and provides insights into both the strength of binding and the compliance of the formed bond under external stress (see *Section 2.4.5* and *Section 2.6.1*). These characteristics are important in understanding the nature and relevance of such cell-ECM interactions in a biological context and thus, DSMFS using the AFM is an excellent choice of technique when probing molecular bonds. SDC4 was studied as representative HSPG due to its co-receptor functionality with FGFR, its ubiquitous expression, its prevalence in focal adhesions and its versatile effects (Elfenbein and Simons, 2013; Fears and Woods, 2006; Kimata et al., 2007; Woods and Couchman, 2001). For comparison, the binding of CSPG DCN and cell adhesion receptor $\alpha_5\beta_1$ with FN were characterised using DSMFS.

In *Chapter 5* the effect of TILRR amplified activation of IL-1RI on the binding of HeLa cells with FN is investigated using FS. This model forms a representation of cell-ECM attachment under these conditions (Qwarnstrom et al., 1991). The possibility of chemically modifying the probe with functional FN and of both resolving and quantifying individual rupture forces makes the AFM ideal for these measurements (see *Section 2.6.1*). The focus of *Chapter 6* is in identifying how the previously reported changes in cell shape and cytoskeletal structure under TILRR amplified activation of IL-1RI affect the elasticity of HeLa cells using indentation FS (see *Section 2.4.6*; Zhang et al., 2010). The ability of the AFM in accurately resolving the indentation depth for a given applied force and the possibility of controlling probe geometry (and thus the contact profile between the tip and sample) makes indentation FS an excellent choice of technique (see *Section 2.6.2*). Both FS and indentation

FS employed in *Chapter 5* and *Chapter 6* respectively are also ideal experimental techniques for these applications as they both allow for the investigation of living cells which are able to respond to inflammatory stimulus. The biological system used throughout this thesis employs HeLa cells exclusively where IL-1RI is activated using IL-1β and TILRR expression is up-regulated in cells by transfection of complimentary DNA (cDNA) containing plasmids (see *Section 2.2.5*). This system was selected due to its success in previously reported studies investigating IL-1RI activation and the effects of TILRR on the cell system under these conditions (Smith et al., 2017; Zhang et al., 2012, 2010). These aims are summarised in *Figure 1.16*.

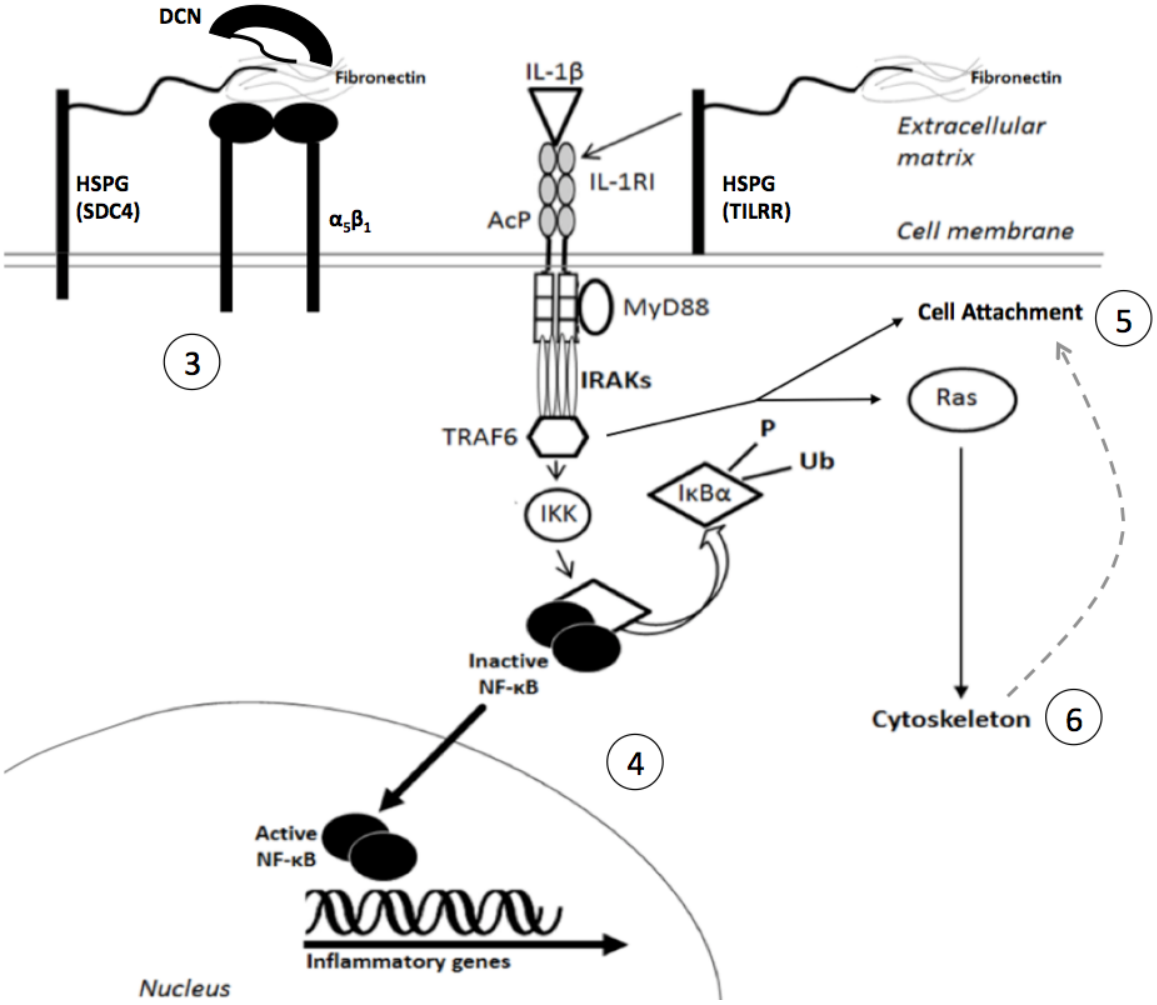

Fig. 1.16 Breakdown of the aims of each chapter in this thesis where chapters are represented by circled numbers. *Chapter 3* aims to measure the unbinding properties between HSPG SDC4 (alongside both DCN and $\alpha_5\beta_1$ for comparison) and FN using DSMFS. *Chapter 4* aims to optimise the necessary biological techniques used within this thesis (for force measurements on living cells) by measurement of NF-κB activity. *Chapter 5* aims to investigate how TILRR amplified activation IL-1RI affects cell attachment to FN (which is likely due to the previously observed changes in cell shape and cytoskeleton [indicated with the dotted grey arrow]). *Chapter 6* aims to investigate how changes in cytoskeletal organisation resulting from TILRR amplified activation of IL-1RI affect cell elasticity. Adapted from PLoS One, 10/6, Rhodes et al. (2015), Computational modelling of NF-κB activation by IL-1RI and Its co-Receptor TILRR, predicts a role for cytoskeletal sequestration of IκBα in inflammatory signalling, e0129888.

Chapter 2

Experimental Methods

2.1 Reagents and Consumables

2.1.1 Biological

Cells: HeLa cells were taken from stocks in cryostorage owned by the Qwarnstrom Group (*Department of Infection, Immunity & Cardiovascular Disease, University of Sheffield, Sheffield, UK*).

Cell reagents: Dulbecco's Modified Eagle Medium (DMEM) and trypsin-ethylenediaminetetraacetic acid (trypsin-EDTA) were purchased from ThermoFisher Scientific Inc. (*Massachusetts, USA*). Foetal calf serum (FCS) and penicillin-streptomycin solution (PS) were obtained from communal stocks (*Department of Infection, Immunity & Cardiovascular Disease, University of Sheffield, Sheffield, UK*). Phosphate-buffered saline (PBS) was purchased from ThermoFisher Scientific Inc. (*Massachusetts, USA*). PolyFect transfection reagent was purchased from QIAGEN® (*Hilden, Germany*). Sodium pyruvate was purchased from Sigma-Aldrich Company Ltd. (*Missouri, USA*).

Kits: Dual-Glo® Luciferase Assay System kits were purchased from Promega (*Southampton, UK*). EndoFree® Plasmid Maxi kits were purchased from QIAGEN® (*Hilden, Germany*).

Plasmids, vectors and cDNAs: IL-8 luciferase, pEGFP-N2, pMono, TILRR-pMono and TK-RL were harvested using frozen glycerol stocks owned by the Qwarnstrom Group (*Department of Infection, Immunity & Cardiovascular Disease, University of Sheffield, Sheffield, UK*).

Proteins and protein components: Heparan sulfate (HS) was purchased from Iduron Ltd. (*Manchester, UK*). Recombinant human decorin (DCN), recombinant human integrin $\alpha_5\beta_1$ ($\alpha_5\beta_1$), recombinant human interleukin-1β (IL-1β), and recombinant human syndecan-4 (SDC4) were purchased from R&D Systems Inc. (*Minnesota, USA*). Bovine plasma fibronectin (FN) was purchased from ThermoFisher Scientific Inc. (*Massachusetts, USA*).

2.1.2 Chemical

Solvents: Ethanol, isopropanol (IPA) and toluene were purchased from Sigma-Aldrich Company Ltd. (*Missouri, USA*).

Surface chemistry: (3-aminopropyl)triethoxysilane (APTES), hydrogen peroxide, (*N*-hydroxysuccinimide)-(polyethylene glycol)-(maleimide) (NHS-PEG-Mal) and sulphuric acid were purchased from Sigma-Aldrich Company Ltd. (*Missouri, USA*).

2.1.3 Physical

Cantilevers and probes: Microlever cantilevers (MLCTs) and Olympus Biolevers (OBLs) were purchased from Bruker AFM Probes (*California, U.S.A.*). Polystyrene beads (10 μm and 25 μm in diameter) were purchased from Sigma-Aldrich Company Ltd. (*Missouri, USA*).

Substrates: Gold-coated AFM disks were purchased from Ted Pella Inc. (*California, USA*).

2.2 Biological Methods

2.2.1 Cell Lines

HeLa cells were used exclusively throughout this PhD project. They take their name from Henrietta Lacks, an African American woman who died from cervical cancer in 1951. These cells are derived directly from her cancer and were the first immortal cell line (Lucey et al., 2009). HeLa cells are routinely used in biological laboratory experiments due to their relative ease to culture and rapid growth rate. As an adherent cell line they require a surface onto which they can attach, build up ECM components and proliferate. Ideally, HeLa cells spread themselves thinly over the surface onto which they are adhered and typically have an approximate diameter between 20 μm and 40 μm. The implementation of this cell line into modern science has aided many medical breakthroughs with significant involvement in, for example, the development of polio vaccines and influenza medication, alongside *in vitro* fertilisation techniques. The success of its survival is likely to be related to the highly aggressive nature of the tumours which grew and replicated with astonishing intensity and has allowed scientists to conduct experiments on living human tissue that otherwise would be impossible (Williams, 2010).

2.2.2 Cell Culture - Maintenance

HeLa cells were split and cultured approximately twice a week in a class II Microflow cabinet (*Bioquell, Andover, UK*) throughout, in order to prevent any contamination and resultant infection from the external environment. In addition, any objects entering the cabinet were sprayed liberally with 70% ethanol for sterilisation and the exterior of disposable neoprene gloves were sprayed periodically throughout protocols to ensure cleanliness. Cells were cultured in Dulbecco's modified Eagle's medium with added D-glucose and L-glutamine (DMEM++). Additionally, 1% sodium pyruvate, 10% foetal calf serum (FCS) and 1%

Table 2.1 Constituent reagents for complete media.

Reagent	Quantity (ml)
DMEM++	500
FCS	50
Sodium Pyruvate	5
PS	5

penicillin-streptomycin solution (PS; containing 10,000 units·ml^{-1} penicillin and 10,000 μg·ml^{-1} streptomycin) was introduced to the DMEM++. This will herby be referred to as complete media throughout this thesis. DMEM++ absent the addition of sodium pyruvate, FCS and PS will now be called serum-free media. Cells were maintained as a monolayer in T75 culture flasks which were incubated in a CO_2 incubator (*SANYO, Osaka, Japan*) in a humidified environment of 95% O_2 and 5% CO_2 at 37 °C. Cells were monitored using a CX2 optical microscope (*Olympus, Tokyo, Japan*) and upon reaching a surface coating of approximately 80% (80% confluence) cells were split into a new T75 flask at a 1:10 ratio of cells to fresh complete media. The number of times a culture of cells has been split is represented by its passage number and each time cells are passaged this number goes up by one. Throughout this work all cells used for experimentation were below a passage number of 20 as it has been shown that cells above this number start to lose or modify their biological function (Frattini et al., 2015). A prime example of this is the ceasing of biological response due to stimulants as a culture gets old. When a culture approaches or reaches passage 20 it is disposed of and a fresh culture is obtained from cryostorage (*Section 2.2.4*). It should be noted that media and all other cell culture fluids were gradually heated to 37 °C in a water bath (*ThermoFisher Scientific, Massachusetts, USA*) before application. Waste cells were sealed in flasks after the liberal addition of Virusolve and left for 24 hours. They were then flushed down specified sinks for biological waste with plenty of water.

2.2.3 Cell Culture - Harvesting and Plating

Upon reaching a monolayer confluence of 70-80%, cultures of HeLa cells were split in order to either produce a new culture of low confluence HeLa cells with an increased passage number for maintenance (*Section 2.2.2*) or to set up a subculture population in a cell-culture dish for further experimentation. Media were removed from the flask by aspiration and the cells were washed twice with 10 ml phosphate-buffered saline (PBS; filtered and sterilised by autoclaving). Cells were then removed from the flask surface by adding 3 ml trypsin-ethylenediaminetetraacetic acid (trypsin-EDTA) and incubating for 3 minutes. Complete detachment was verified using optical microscopy. Trypsin indiscriminately cleaves proteins and is used to remove adherent cell lines from culture flasks by cleaving the structural receptors on the cell surface (Huang et al., 2010). Upon the complete detachment of adherent cells from the surface, 10 ml of complete media were added to the flask resulting in trypsin-EDTA inactivation upon mixture with FCS. 10 ml of this cell suspension was then added to a 50 ml falcon tube and was spun down into a pellet using a Harrier 18/80 centrifuge (*MSE, London, UK*) at 1,500 revolutions per minute (rpm) for 5 minutes. Cell-free supernatant was aspirated from the pellet which was replaced with 10 ml of fresh complete media and cells were resuspended by pipetting. When setting up a new culture for maintenance, 1 ml of this cell suspension was transferred to a flask containing 9 ml of complete media and was incubated and monitored as has been described in *Section 2.2.2*.

When plating cells for experimentation, or for the monitoring of cultures in preparation for cryostorage, it was necessary to perform cell counts in order to obtain an average value of the cell density of the post-centrifuged suspension. This was achieved by use of a hemocytometer (*Hawksley, Lancing, UK*) alongside optical microscopy. The hemocytometer is a glass slide which contains a stage in a chamber on one side. Upon this stage is a 9×9 grid of large squares each of which is split into a smaller grid containing 16 squares. By counting the

Table 2.2 Seeding densities of HeLa cells used throughout this thesis.

Vessel	Cells per Well / Dish / Flask
T75 Flask	1,000,000
6 cm Dish	300,000
96-Well Plate	6,000

number of cells in each region it is possible to determine the cell density of the whole suspension from:

$$C = \frac{N}{V} = \frac{n_{\text{cell}}}{p_{\text{chamber}} v_{\text{square}}} m_{\text{dilution}} \tag{2.1}$$

where C is the concentration of cells in media, N is the number of cells in media, V is the volume of media, n_{cell} is the number of cells counted, p_{chamber} is the proportion of the chamber counted, v_{square} is the volume of squares counted and m_{dilution} is the dilution factor and is relevant if the original concentration has been diluted before counting. All cells incorporated into experiments throughout this thesis were counted in exactly the same way. The hemocytometer stage was covered with a glass coverslip and 10 μl of cell suspension was evenly distributed over the stage by slowly pipetting between the two surfaces. The magnification of the optical microscope was adjusted such that one of the large square sections of the grid filled the field of view and all cells within this section (cells that fell within any of the 16 enclosed smaller squares) were counted. From *Equation 2.1* it can be shown that the amount of cells per ml present in the 10 ml suspension corresponds to the number of cells counted within a section multiplied by 10,000. Due to the variation between the number of cells in each grid section, a minimum of 3 large squares were counted and an average value was taken before plating cells for further work. The approximate number of cells seeded in each cell culture vessel is summarised in *Table 2.2*.

2.2.4 Cell Culture - Cryopreservation

Stocks of HeLa cells were kept in liquid nitrogen for long term storage. This allowed for the easy replacement of cultures reaching a passage number of 20 with those of a lower passage, and therefore more reliable biological activity, or for the replacement of cultures which had become infected. When freezing down cells for storage a culture of lowest passage number possible was selected and was maintained until approximately 80% confluence. This ensured that the cells for freezing down were in the log phase of their cell cycle, where they were ready to divide and multiply exponentially. This was chosen to allow for a rapid growth of the colony upon binging the culture up from storage and therefore the minimisation of disruption from an experimental perspective. Upon reaching the desired confluence, cells were removed from the flask by trypsinisation following washing with PBS as has been described in the *Section 2.2.3*. They were then resuspended in 10 ml of complete media and were spun down by centrifugation at 1,000 rpm for 5 minutes following a count of cell density (see *Section 2.2.3*). Supernatant was removed from the pellet and the cells were resuspended in a freezing medium consisting of 90% FCS and 10% dimethyl sulfoxide (DMSO) at a density of $\backsim 200,000$ cells per ml. DMSO acts to reduce both the temperature at which the medium reaches its freezing point and the rate of cooling which mitigates risks of ice formation within the vials as this can result in the death of the culture. Cells were then aliquoted into specially designed cryogenic vials. $\backsim 200,000$ cells or 1 ml of suspension were pipetted into each vial and these were then placed into Mr. Frosty^{TM} (*ThermoFisher Scientific, Massachusetts, USA*), a commercially available plastic freezing container which has compartments to hold 18 cryotubes and surrounds them with isopropanol (IPA). This system allows for the cooling of cells at a rate of $-1\,^{\circ}$C per minute which is optimal for cell preservation. Mr. Frosty^{TM} is then stored at $-80\,^{\circ}$C for 24 hours to allow for the gradual cooling of the cells before the vials are removed and transferred to storage in liquid nitrogen.

New cultures of HeLa cells were brought up from storage by first obtaining a cryogenic vial from the liquid nitrogen stocks and rapidly thawing it in a water bath preheated to 37 °C. Following complete defrosting of the vial its contents were added to a T75 flask containing 10 ml of complete media which was incubated overnight. The following day the culture was monitored using optical microscopy to observe its confluence and to ensure that the cells had adhered to the flask surface. Media along with the freezing solution were then removed from the flask by pipetting and were replaced with 10 ml of fresh complete media. It is worth mentioning that often after bringing up a fresh culture of cells from cryostorage it was necessary to passage them the following day due to rapid replication. This was undertaken exactly as described in *Section 2.2.3*.

2.2.5 Transfection

In order to force HeLa cells to express desirable qualities (such as the expression of specific receptors) for experimentation, DNA was introduced by means of transfection. In short, transfection is the process by which nucleic acid is transported through the cell membrane into the cytoplasm. DNA was introduced to cells in the form of plasmids which are circular, double-stranded DNA molecules prevalent within bacteria. They replicate autonomously within a host making them ideal for lab-based experiments which use vector plasmids that have been engineered to contain relevant cDNAs (see *Section 2.2.6*). Measurements taken on cDNA-plasmid transfected cells were compared with control cells which were transfected with empty vector (EV), the same plasmid but with the functional cDNA absent, as the transfection process itself is harsh and can have deleterious effects on cells.

Plasmids were transfected into HeLa cells using PloyFect reagent (*QIAGEN, Hilden, Germany*) method. This commercial product consists of dendrimer molecules which are thermally activated at room temperature. The molecules themselves are highly spherical in shape with all branches originating at a central core. These branches contain charged

Table 2.3 Quantities of plasmid per vessel for transfection alongside the amount of Polyfect reagent included. *Where GFP was transfected alongside pMono or TILRR-pMono the total quantity of Polyfect per dish was 25 μl (inclusion of both plasmids did not result in inclusion of double the amount of Polyfect). **1 μg PolyFect reagent per well was added to all 96-well plate transfection regardless of cDNAs added (multiple cDNAs did not require an increase in PolyFect quantity).

Plasmid	Quantity (ng)	Vessel	PolyFect (μl)
pEGFP-N2	500 / 1,000 / 1,500	6 cm Dish	25*
IL-8 Luciferase	120	96-Well Plate	1**
pMono	10 / 20 / 30 / 40	96-Well Plate	1**
pMono	1,500	6 cm Dish	25*
TILRR-pMono	10 / 20 / 30 / 40	96-Well Plate	1**
TILRR-pMono	1,500	6 cm Dish	25*
TK-RL	75	96-Well Plate	1**

terminal-amino groups which bind to the plasmids negatively charged phosphate groups and act to assemble the plasmids into condensed and compact structures enabling them to be more effectively transported into the cell. The resultant PolyFect-plasmid complex contains a net positive charge and upon reaching the cell, binds to negatively charged surface receptors which in turn allows for the complex to be internalised. Once internalised the complex binds to the endosome (a membrane-bound vesicle) and subsequently buffers the lysosome (a eukaryotic organelle containing digestive enzymes) which in turn allows for the pH inhibition of nucleases (proteins responsible for the breakdown of nucleic acids) and as such ensures the stability and longevity of the plasmid while ensuring the transport of intact and functional DNA into the nucleus (QUIGEN, 2000).

Unless stated otherwise, throughout this thesis all HeLa cells were transfected in 6 cm cell culture dishes but it is worth mentioning that transfections in 96-well plates were also conducted in luciferase assay protocols (see *Section 2.2.7*) for the purpose of biological optimisation (see *Section 4.2*). Quantities of cDNA containing plasmids with corresponding PolyFect reagent are are highlighted in *Table 2.3*. The method of transfection was based upon both the guidelines provided in the PolyFect protocol handbook (with some alterations)

alongside those utilised in previous laboratory studies and will be briefly summarised here (QUIGEN, 2000; Zhang et al., 2012, 2010). It should be noted that the transfection protocol begins two days prior to further experimentation and one day prior to the transfection process itself. HeLa cells were first harvested from a culture in a T75 flask as described in *Section 2.2.3*. Cell density was counted and a desired quantity were plated onto a sterile dish. It was found that plating 300,000 HeLa cells into a 6 cm dish resulted in approximately 80% confluence after two days which was ideal for further measurements. These cells were incubated for 24 hours to allow them to adhere to the dish surface, to reproduce ECM components and also to ascertain adequate levels of the IL-1 receptor following treatment with trypsin-EDTA. Following incubation, cells were washed twice with PBS and were replaced with 3 ml of complete media. Stock plasmids, stored at $-20\,^{\circ}$C, were kept on ice and were defrosted only when needed before immediately being re-frozen. The desired amount of plasmid for transfection was taken from the stock and made up to a volume of 150 μl in serum-free media in a 2 ml Eppendorf tube for each dish to be transfected. 25 μl of PolyFect reagent was then added to each Eppendorf and was left for 10 minutes to allow thermal activation of the dendrimer molecules and their subsequent binding to, and the reorganisation of, plasmids. 1 ml of complete media was then added to each of the Eppendorf tubes in order to deactivate the PolyFect reagent and this mixture was added to the relevant plate immediately in a drop-wise manner to ensure an even spread of plasmid throughout the dish. After gentle shaking to mix the PolyFect-plasmid complex, the cells were incubated for a further 24 hours to allow for the successful uptake of plasmid and expression of cDNA function. Following this 24 hour incubation transfected cells were ready for further measurement and experimentation.

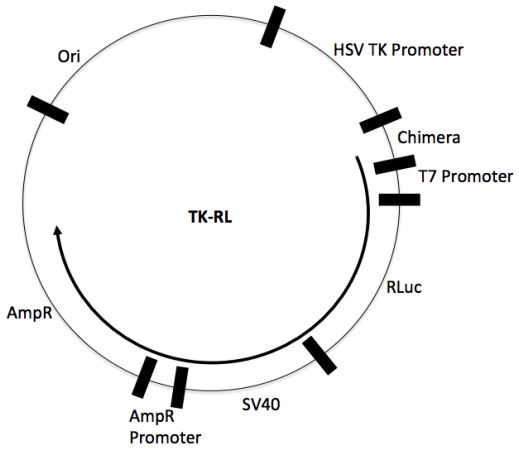

(a) TK-RL map.

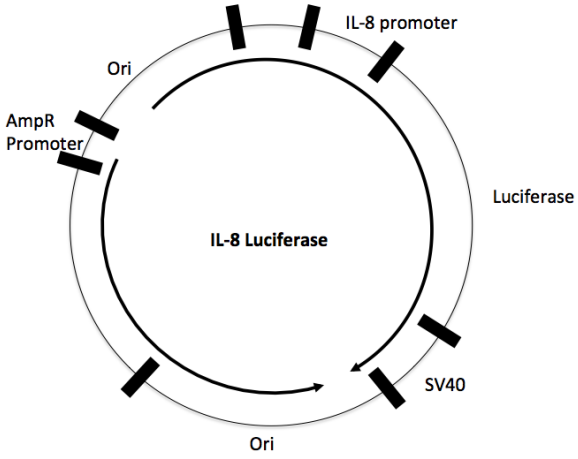

(b) IL-8 luciferase map.

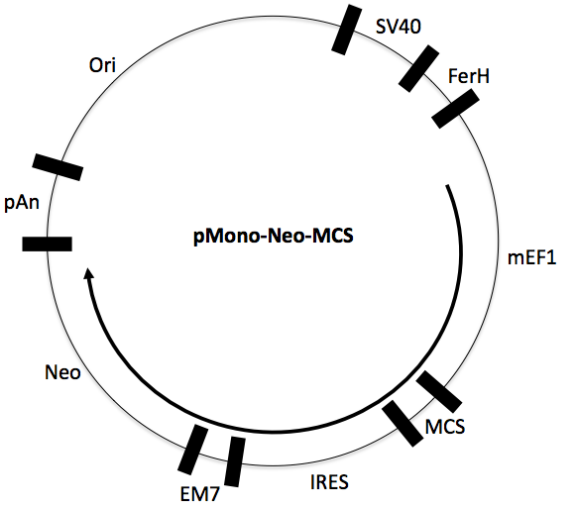

(c) pMono map.

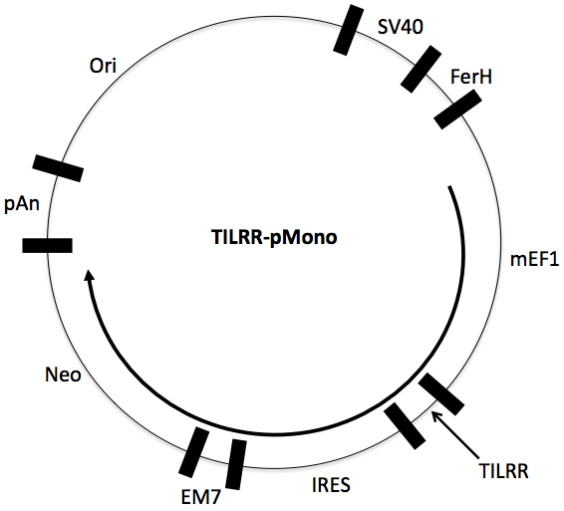

(d) TILRR-pMono map.

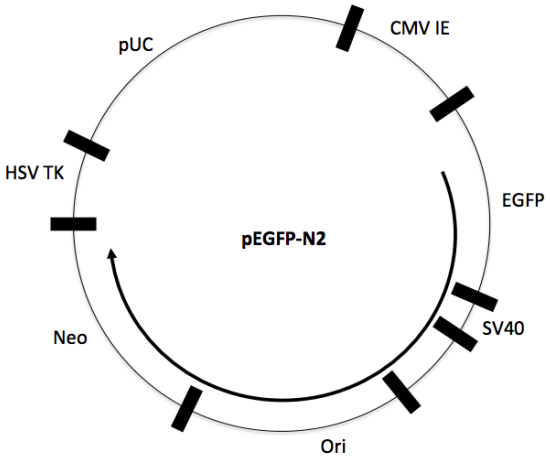

(e) GFP map.

Fig. 2.1 Plasmid maps for TK-RL (a), IL-8 luciferase (b) pMono (c), TILRR-pMono (d) and GFP (e). The locations of restriction sites are indicated alongside the location of inserted TILRR cDNA in TILRR-pMono.

2.2.6 Plasmid Production

Plasmids were extracted from *Escherichia coli* (*E. coli*) bacteria and were purified using the EndoFree® Plasmid Maxi Kit (*QIAGEN®, Manchester, UK*). It was of significant importance to ensure sterility throughout the handling of *E. coli* and all relevant techniques were undertaken in the presence of a lit bunsen burner which improves environmental cleanliness through the creation of an up-draft. Furthermore all consumables and container openings were flamed to destroy biological impurities. 50 μl of *E. coli* from stocks was placed on ice. $\backsim$ 100 ng of DNA was added after 10 mins of thawing. The bacteria-DNA mixture was heat-shocked after 30 minutes at 42 °C for 30 seconds before being placed on ice once again for 5 minutes. 950 μl of super optimal broth with catabolite repression was then added to the cells which were incubated whilst on a shaker set at 250 rpm. Following 1 hour of incubation, the bacteria was spread on antibiotic containing Luria broth (LB) agar plates. The antibiotic contained within the agar plates is tailored to the resistance for each plasmid which is either ampicillin (made up to a concentration of 100 μg·ml^{-1}) or kanamycin (made up to a concentration of 50 μg·ml^{-1}) for all plasmids throughout this thesis. Plasmids and their corresponding antibiotic resistances are indicated in *Table 2.4*. Maps for each plasmid used throughout this thesis are displayed in *Figure 2.1*. Plates were incubated overnight and successful colonies were identified the following day. The bacterial colonies can be frozen down for long-term storage and can then be used to extract plasmids when necessary via the Maxiprep procedure. This was achieved by transferring the colonies into 5 ml LB containing the relevant antibiotic and incubating overnight while once again shaking at 250 rpm. 500 μl of the *E. coli* solution was transferred to a cryovial and 500 μl glycerol was added before being frozen at -80 °C.

It should be noted that buffers and reagents referred to throughout this paragraph are provided in the Maxiprep kit. Small quantities of *E. coli* from the frozen glycerol stocks were transferred into 150 ml fresh, autoclaved LB using a sterile cell-scraper alongside

Table 2.4 The corresponding antibiotic for which each plasmid has resistance used throughout this thesis.

Plasmid	Antibiotic
GFP	Kanamycin
IL-8 Luciferase	Ampicillin
pMono	Kanamycin
TILRR-pMono	Kanamycin
TK-RL	Ampicillin

the relevant antibiotic, and the bacterial culture was incubated in a shaker overnight. The following day the solution was split into 50 ml tubes and the bacteria was spun down into pellets by centrifuging at 6,000g_n for 15 minutes. Supernatant was removed and the pellets were resuspended in 10 ml of buffer P1 into which LyseBlue reagent had been added. 10 ml of the P2 buffer was then added for cell lysis and the two were mixed gently by inverting. The addition of P2 to the P1-LyseBlue-bacteria solution resulted in blue colouring and mixing was complete when this colour was homogenous. After leaving the solution for 5 minutes at room temperature the lysate was neutralised by the addition of 10 ml of buffer P3 and was mixed by inversion until the blue colouring had faded. The solution is then transferred into a QIAfilter cartridge and was left to equilibrate for 10 minutes before the cap was removed and the lysate was filtered into a fresh 50 ml tube using the plunger. 2.5 ml of buffer ER was then added to the filtered lysate which was mixed by gently inverting before being left on ice for 30 minutes. 10 ml of buffer QBT was added to a QIAGEN-tip 500 to equilibrate and was allowed to empty by gravity. The filtered lysate was then added to the tip and was collected by gravity flow. The tip was then washed by addition of 30 ml buffer QC twice before the DNA was eluted into a 30 ml endotoxin free tube by addition of 15 ml buffer QN. DNA was precipitated by addition of 10.5 ml IPA to the eluate which was mixed and immediately centrifuged at a minimum of 15,000g_n for 30 minutes. Supernatant was discarded and the pellet was washed with 5 ml endotoxin-free 70% ethanol and was centrifuged at a minimum of 15,000g_n for 10 minutes. Supernatant was once again discarded and the pellet was dried

in air for 10 minutes before being suspended in endotoxin-free purified water at a desired concentration. Plasmid concentration was precisely determined using a NanoDrop® 1000 (*Thermo Fisher Scientific, Massachusetts, USA*). The NanoDrop was calibrated using 1 μl of endotoxin-free purified water and, upon adding 1 μl of the plasmid solution, determined cDNA concentration by measuring opacity (or more specifically the light absorbance of cDNA in the solution). The quality of the resultant cDNA was also verified by achieving a 260/280 value (the absorbance ratio between cDNA and proteins in solution) of above 1.8. Plasmids were stored at $-20\,^{\circ}$C between uses.

2.2.7 Luciferase Assay

Luciferase assays were employed to assess the magnitude of the IL-1 initiated inflammatory response by measurement of IL-8 activity. This was achieved using the Dual-Glo® Luciferase Assay System (*Promega, Southampton, UK*), a commercial dual reporter kit. 6,000 cells were seeded in each well of a 96-well plate and were incubated overnight. Cells in selected wells were then transfected with 750 ng·ml^{-1} TK-RL and 1200 ng·ml^{-1} IL-8 luciferase in serum-free media (see *Section 2.2.5*) alongside TILRR cDNA and EV where relevant. After incubating for 24 hours the cells were stimulated with desired concentrations of IL-1β in complete media and incubated for a further 6 hours. Cells were then washed twice with PBS and were lysed by adding 50 μl of the lysis buffer which was provided in the commercial reporter kit alongside firefly and *Renilla* luciferase reagents. Complete lysis was verified using optical microscopy. Following complete lysis, 20 μl of lysate from each relevant well was extracted and added to the corresponding wells in a white walled 96-well plate to limit the bleeding of emitted light between wells. 25 μl of firefly luciferase enzyme was added to each lysis containing well and the plate was loaded into a Varioskan Lux plate reader (*ThermoFisher Scientific, Massachusetts, USA*) to measure luminescence. 25 μl of Stop & Glo® *Renilla* luciferase reagent was then added to each relevant well and the plate was

once again measured using the plate reader. It should be noted that alongside allowing for *Renilla* luciferase this reagent also acts to quench luminescence from the firefly reagent. The firefly luciferase directly represents the magnitude of IL-8 activity (and therefore the potency of the inflammatory response in the well culture) by measuring the activation of the IL-8 promotor (and hence the transcription of IL-8) where as the *Renilla* luciferase measures the activity of the HSV-thymidine kinase promotor (Werther and Seitz, 2008). This is expressed constitutively and so is assumed to be at near constant levels in all living cells (Schifera and Hardin, 2011). Hence, the measurement of *Renilla* luciferaise gives some indication of the quantity of cells present in each well and a relative comparison of inflammatory potency between cell cultures in different wells (and therefore different conditions) can be extracted by dividing the firefly luciferase activity by the *Renilla* luciferase activity for a particular well culture. It should be noted that all luciferase assays throughout this thesis were conducted in triplicate.

2.2.8 Fluorescence Microscopy

Fluorescence microscopy is a powerful tool in the study of biological phenomena. Its primary strength is in the isolation or identification of cells which exhibit certain biological qualities (such as the expression of transfected cDNA) or in its ability to resolve cellular components of particular relevance to a particular study (localisation of receptors etc.). It also allows for the direct observation of cellular and intracellular processes in living tissue (Combs, 2010). The fluorescence microscope relies upon the expression of fluorophores, such as GFP, in a biological sample which can be introduced by a variety of different methods including transfection (see *Section 2.2.5*). The sample is illuminated by light of specific wavelength which is (or range of wavelengths that are) absorbed by the fluorophore. This results in the excitation of electrons within the fluorescent dye to energy levels above the ground state as each quantum of light is absorbed. These excited electrons fall down through the energy

levels and eventually return to the ground state. Particular transitions between these energy states can result in light emission of longer wavelength than the initial excitation beam (Hawe et al., 2008). Applying a filter over the optics which allows only light of wavelength specific to the emission quanta allows for the isolation of this signal. This in turn allows for the imaging of specific dye-tagged biological components (Thorn, 2016). Aside from those generated using the fluorescence set-up integrated into the AFM (see *Section 2.5.5*), all images were obtained using a custom Diaphot 300 microscope (*Nikon, Tokyo, Japan*) complete with a CO_2 incubation chamber (*Nikon, Tokyo, Japan*) alongside a C4742-95 digital camera (*Hamamatsu Photonics, Hamamatsu, Japan*).

2.2.9 Real-Time Deformability Cytometry

Real-time deformability cytometry (RTDC) is a relatively new technique in the measurement of cell mechanics and has the ability to resolve the elastic properties of a large number of cells at maximum rates of over 100 cells per second. RTDC measures the deformation of spherical cells in response to a characterised increase in pressure. The set-up consists of two reservoirs which are connected via a 20 μm $\times$ 20 μm channel of length 300 μm. Cells are spun down into a pellet at $115 g_{\mathrm{n}}$ for 5 minutes before being resuspended at a concentration of $\backsim 1,000,000$ cells per ml in a PBS solution in which magnesium and calcium ions are absent and containing 0.5% methylcellulose (PBS$-$). A proportion of this solution is drawn into a 1 ml syringe and this is connected to the initial reservoir via polymeric tubing which is pre-flushed with 70% ethanol and sterile water. A mechanical set-up allows for the automatic flow of cells at a desired rate. Before any data are taken the flow is allowed to stabilise for 2 minutes. The flow transfers cells from the syringe to the initial reservoir, through the channel and into the final reservoir before disposal. As a cell enters and moves through the channel at the predetermined flow rate it experiences a significant increase in shear and pressure due to

constriction and as such exhibits deformation which allows for estimation of cell elasticity. Cellular deformation is defined as its departure from circularity and is given by

$$D_{\mathrm{RTDC}} = 1 - C_{\mathrm{RTDC}}, \tag{2.2}$$

where C_{RTDC} is the circularity. As such the RTDC approach must be limited to both spherical cells and those undergoing deformation from a sphere. Circularity is given by

$$C_{\mathrm{RTDC}} = \frac{2\sqrt{\pi A_{\mathrm{RTDC}}}}{P_{\mathrm{RTDC}}}, \tag{2.3}$$

where A_{RTDC} is the projected surface area of the cell and P_{RTDC} its the perimeter. It is clear that for a perfectly circular cell as observed from a two-dimensional observation point the circularity is equal to 1 and the deformation is 0. Images of cell-flow samples are automatically captured in both the initial reservoir and at the rear end of the channel, to ensure steady state of cell shape, using a MC1362 CMOS camera (*Mikrotron, Munich, Germany*) which provides high enough frame-rate and resolution for analysis. Data are imported into ShapeOut image recognition software (*ZELLMECHANIK, Dresden, Germany*) which sifts though the cells extracting the area and perimeter and calculating the circularity and deformation from *Equation 2.2* and *Equation 2.3*. It should be noted that resulting values of deformation are dependent on the size of the cell. Larger cells will undergo a smaller calculated deformation than those of smaller size and identical elasticity when exposed to the same sheer and pressure forces. As such, the ShapeOut software also imposes isoelasticity lines on resulting deformation-area plots which divide regions encompassing multiples of an arbitrary elastic modulus (Herbig et al., 2018; Mietke et al., 2015; Otto et al., 2015a,b).

2.3 Real-Time Deformability Cytometry Measurements

Initial attempts to quantify cell elasticity were conducted though RTDC due to the appeal of its rapid acquisition and analysis potential. All of these measurements were conducted at a RTDC facility within the University of Cambridge (*Cambridge, UK*). HeLa cells were incubated in complete media until approaching 80% confluence on the day of experimentation. They were detached from the T-75 culture flasks by addition of 3 ml EDTA. No trypsin was used for the removal of cells throughout these experiments to preserve surface receptors as they were harvested directly before measurement. Cells were then centrifuged at $1500g_n$ for 5 minutes and media was removed before resuspending in PBS−. 10 μg·ml^{-1} FN was added to the solution in an attempt to provide ECM components that may be necessary for inflammatory cytoskeletal rearrangement as reported for adhered cells by Zhu et al. (1998) and cells were stimulated with 10^{-11} M IL-1β where relevant. All measurements were conducted at a flow rate of 0.012 μm·s^{-1} and a fluid viscosity of 15 mPa·s. A population of cells was first captured in the reservoir before being captured in the channel immediately after. Data extracted from ShapeOut is presented in *Figure 2.2* where the colour in *Figure 2.2c*, *Figure 2.2d*, *Figure 2.2a* and *Figure 2.2b* represents a cold-to-hot density scale. It should be noted that in order to ensure only spherical and spherical-deformed cells are included, the area-ratio range filter (which divides the absolute captured cell perimeter as determined by ShapeOut image recognition by a fitted smoothed perimeter) was set from 1.00 to 1.05. This is significantly important when considering the shape heterogeneity of HeLa cells.

At a glance, there is an apparent difference between the RTDC data-sets. By comparing *Figure 2.2a* with *Figure 2.2b* and *Figure 2.2c* with *Figure 2.2d*, it is clear that there is a significant increase in deformation when imaged in the channel relative to the population imaged in the reservoir. Comparison of *Figure 2.2a* with *Figure 2.2c* indicates a fairly consistent modal cell size ($\backsim$250 μm^2) and projected deformation ($<$0.025) for cells fitting the circular criteria required for the technique. Comparison of *Figure 2.2b* with *Figure*

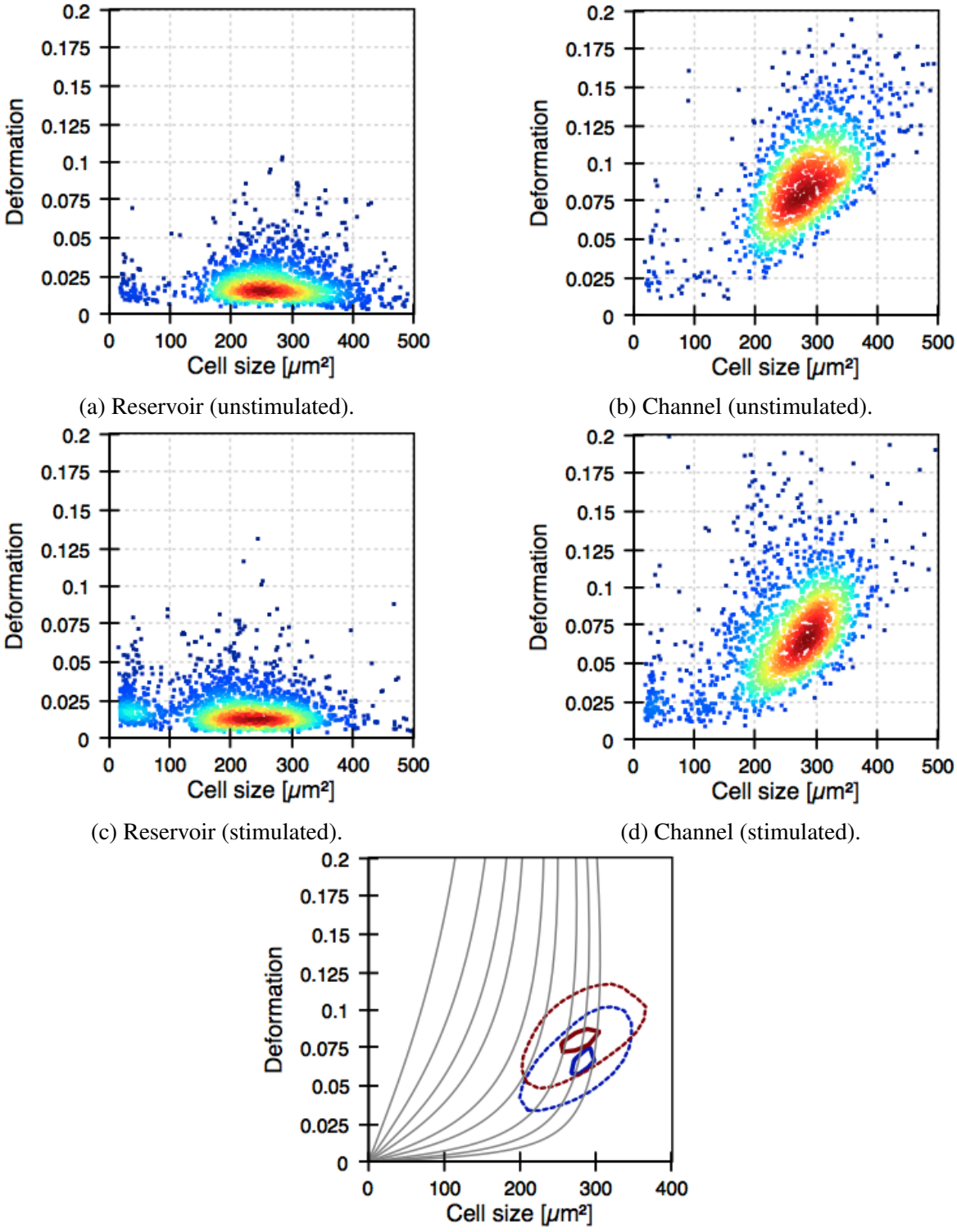

(a) Reservoir (unstimulated).

(b) Channel (unstimulated).

(c) Reservoir (stimulated).

(d) Channel (stimulated).

(e) Unstimulated (red) and stimulated (blue).

Fig. 2.2 RTDC measurements on unstimulated HeLa cells (a, b) and cells stimulated with 10^{-11} M IL-1β (c, d) in the reservoir (a, c) and the channel (b, d). A contour plot representing an arbitrary significant density of data (dotted) and the high data-density range (solid) for RTDC data extracted from HeLa cells in the channel with (blue) and without (red) IL-1β stimulation. Isoelastcity lines are included.

2.2d indicates a slightly reduced deformation for the culture stimulated with IL-1β than for unstimulated cells under compression due to flow. *Figure 2.2e* depicts contour plots describing RTDC data obtained for HeLa cells stimulated with IL-1β (blue) and unstimulated cells (red). Dotted lines represent the data range which describe an arbitrary significant number of measurements and and high data-density regions are enclosed by solid lines. The most probable deformation is contained within these regions and was extracted as $\backsim$ 0.07 for cells stimulated with IL-1β and $\backsim$ 0.08 for unstimulated cells.

Isoelasticity lines are imposed on *Figure 2.2e* which split the plot into areas of similar elasticity, each representing a multiple of an arbitrary elastic modulus, E_{RTDC}, that is dictated by the experimental perimeters and settings. The lines in *Figure 2.2e* represent E_{RTDC}, $1.5E_{\mathrm{RTDC}}$, $2E_{\mathrm{RTDC}}$, $2.5E_{\mathrm{RTDC}}$, $3E_{\mathrm{RTDC}}$, $4E_{\mathrm{RTDC}}$, $5E_{\mathrm{RTDC}}$, $6E_{\mathrm{RTDC}}$ and $8E_{\mathrm{RTDC}}$ from left to right. E_{RTDC} in this experimental set-up corresponds to $\backsim$ 270 Pa (Mietke et al., 2015). The high density region for unstimulated cells seems to encompass areas of the plot corresponding to elastic moduli between $\backsim$ 1.4 kPa and $\backsim$ 1.6 kPa alongside areas corresponding to $\backsim$ 1.6 kPa and $\backsim$ 2.2 kPa. In contrast, the high density region for cells stimulated with IL-1β seems to be mainly confined to the region between the lines describing elastic moduli of $\backsim$ 1.6 kPa and $\backsim$ 2.2 kPa. This may indicate an increased elastic modulus for the population of cells stimulated with IL-1β and could possibly be attributed to structural effects following activation of IL-1RI. It should however be noted that the shape constrains necessary for this technique resulted in the omission most measured HeLa cells from the analysis as it is more optimised for cells such as neutrophils. The apparent reduction in cell deformation cannot therefore be attributed to activation of the IL-1 pathway with confidence as omitted, predominantly non-spherical cells may exhibit different characteristics. Furthermore, this observation may be a result of more trivial differences between cultures such as cell cycle stage or phenotype (Mokbel et al., 2017; Otto et al., 2015b). Further measurements on cells in suspension using the RTDC method were therefore not conducted. Measurements revealing

the effect of IL-1RI on the elasticity of surface (ECM) adhered HeLa cells were conducted using the AFM and this is the focus of *Chapter 6*.

2.4 Force Microscopy and Spectroscopy

2.4.1 Overview of Imaging

Modern AFM systems are now able to produce high quality, near-atomic resolution images and are frequently used in a variety of scientific applications. Generally, the AFM system relies on a probe which consists of a very sharp pyramidal tip, usually in the order of tens of nanometres in diameter at the tip apex, which is affixed onto the end of a flexible cantilever. It should be noted that the available resolution of any generated image is highly dependent on the size of the tip, with a smaller tip yielding a higher resolution (Martínez et al., 2011). The tip end of the cantilever is left free whist the other end, which is often affixed to a silicon chip, is clamped into some form of holder. This is then brought into contact with a sample of interest and an image is built up by raster scanning the tip over the surface in the $x-y$ plane and measuring any subsequent changes in the deflection (or depending on the desired imaging mode, the oscillation; see *Section 2.4.2*) of the cantilever during its lateral motion. A laser, positioned such that the beam is incident on the rear of the cantilever and directly behind the tip, allows for the precise assessment of the cantilever deflection by measurement of the incidence of the laser reflection on a position sensitive quadrant-photodiode detector. The detector position is usually adjusted such that the reflected spot of a cantilever at equilibrium position, where there is no deflection or bend in the cantilever, at its centre. As the cantilever deflects due to interactions between the tip and sample (caused by changes in height, topography or other surface phenomena) the reflection spot moves across the diode and thus, the potential difference across it varies as a function of position. This allows for the cantilever deflection to be extracted with a high degree of certainty (Jalili and Laxminarayana, 2004; Voigtländer, 2015).

The scanner of the AFM system is responsible for both the $x-y$ motion during a measurement and the engagement to, or retraction from the substrate. It is constructed from a

piezoelectric ceramic and hence responds to an applied potential difference with mechanical deformation including the modification of its size in single and multiple dimensions (Kuiper and Schitter, 2008; Quan et al., 2013). This deformation is proportional to the applied potential difference and as such it is possible for the system to have a high level of control over tip motion and position. When scanning, a feedback loop is used to correct the tip height via the z-position of the piezo element in order to return a desired quality of the cantilever back to a predetermined value or set-point. The response of the feedback loop is controlled by two gains, proportional (G_p) and integral (G_i). The gain settings are important as if they are too low the motion of the cantilever is impaired but if they are too high the cantilever will ring in feedback oscillation. The change in height due to feedback (Δz) is given by

$$\Delta z = G_\mathrm{p}\varphi + G_\mathrm{i}\int \varphi dt, \tag{2.4}$$

where φ is the error on the signal and is the difference between the signal output and the set-point (Hall, 2015; Jalili and Laxminarayana, 2004; Voigtländer, 2015).

2.4.2 Imaging Modes

Over recent years there has been significant advancement in both the technological hardware of AFMs (alongside corresponding software platforms for data acquisition and analysis) and the methodologies employed in the measurement of relevant surface phenomena, or for the reduction of error and noise when conducting experiments. However most imaging methods still fall into one of three main categories which are characterised by both the position of the tip as it scans over a surface and the property of the cantilever that is measured in order to build a topographical image. These are broadly termed contact mode, intermittent-contact mode and non-contact mode (Bayakara and Schwarz, 2016; Dufrêne et al., 2017). Generally the maximum image resolution of that can be achieved is governed by both the sharpness of the tip (or the contact area between probe and sample) and by the spring constant of the

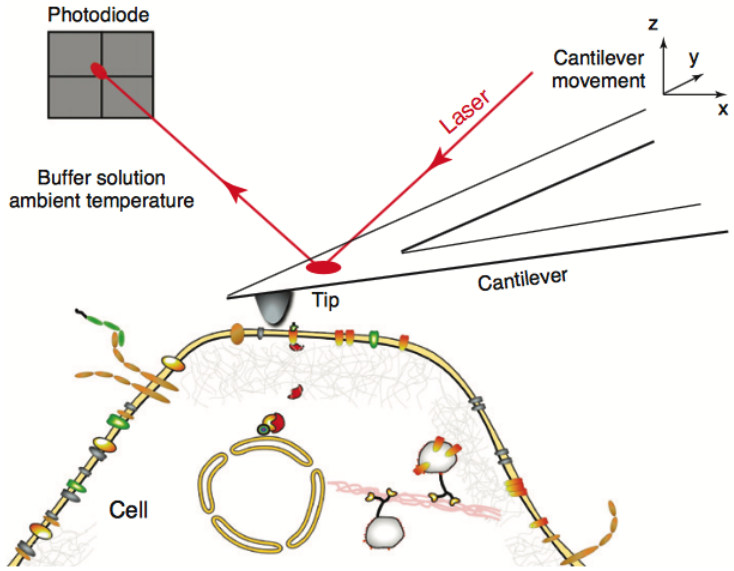

Fig. 2.3 A schematic diagram of the AFM cantilever and laser set-up whilst scanning across the cell surface in contact mode. Reprinted from Trends in Cell Biology, 21/8, Müller and Dufrêne, Atomic force microscopy: a nanoscopic window on the cell surface, 461-469, Copyright (2011) with permission from Elsevier.

cantilever (although this choice is dependent on the properties of the sample surface under investigation).

Contact mode microscopy aims to keep the probe tip in constant contact with the sample as it is laterally raster scanned across it. The probe is initially lowered into contact with the sample or substrate until a user-defined deflection is achieved. This is formally referred to as the trigger point. If the precise spring constant of the cantilever is known it is possible achieve a desired user defined trigger force (see *Section 2.4.4*) and as such, control over the the force exerted on the sample by the tip can be controlled in order to ensure the reproducibility of measurements and to minimise the damage imparted on the sample by the tip. As the probe is scanned across a desired surface, the deflection or force is monitored continuously. Upon encountering a region of higher or lower topographical height, the deflection of the cantilever changes, increasing or decreasing respectively, and the feedback loop triggers a change in

height of the tip via the piezo element that returns the cantilever deflection to the trigger value (Dufrêne, 2008). In this way, the feedback loop acts to keep the magnitude of the force applied to the sample surface constant throughout the scan and the image is built up from the z-position of the piezo. The main drawback of contact mode AFM is in the pressure and lateral forces that are exerted on the sample which can lead to deformation in subsequent images and even damage to the sample over time (Casuso et al., 2009; Dokou et al., 2002).

Intermittent contact, or tapping, mode microscopy involves the driven oscillation of the cantilever near its resonant frequency. The tip is extended toward the sample such that it makes contact with the surface at some point below maximum amplitude which can be controlled by the user through adjusting the gain function (Gaboriaud and Y. F. Dufrêne, 2007). The amplitude of this oscillation is constantly monitored by the scanner and the feedback loop here aims to to keep this value constant. Upon a change in height of the sample surface throughout the scan, the amplitude of cantilever oscillation as measured by the scanner will increase (with a shallower sample surface) or decrease (with a steeper sample surface). With similarity to the the aforementioned contact mode, the feedback loop triggers a change in height of the piezo to correct for this (Putman et al., 1994). Once again, the image from scans in this mode is built up from the z-position of the piezo. Intermittent contact AFM greatly reduces tip-sample adhesion which can distort images and also eliminates lateral forces as all contact with the surface is in the z direction (Dokou et al., 2002). It also limits sample deformation as, due to the high frequency of oscillations, viscoelastic properties of the surface can result in an apparent stiffer behaviour of soft biological materials (Putman et al., 1994).

The non-contact method of AFM, as is suggested by name, does not involve contact between tip and sample surface. With similarity to intermittent contact mode the cantilever is initially driven near its resonant frequency and is subsequently brought into position, which here means that it is hovering above the sample surface such that a user defined amplitude of

oscillation does not allow for the tip to touch the surface. As the oscillating tip is scanned laterally above the sample, van der Waals forces between sample and tip vary with separation and are stronger at closer proximity (at a steeper region of sample) and weaker at larger separation (at a shallower region of the sample). An increase or decrease in this force gradient with separation leads to a shift in the resonant frequency of the cantilever, decreasing with an increase in force gradient (or with a decrease in separation). This results in a reduction of the cantilever oscillation amplitude and, as this shift is near resonance, the change in amplitude is significant and can be detected. The feedback loop here aims to adjust height via the z-piezo to maintain a constant amplitude of oscillation (Bayakara and Schwarz, 2016). The scan image is produced in this mode by either the position of the z-piezo or from the detection of this pronounced change in amplitude. This mode offers the greatest protection to the sample but the lowest resolution and, due to the thickness of fluid contaminants, is sometimes unable to resolve van der Waals forces (Dokou et al., 2002).

2.4.3 Tip-Surface Interactions

The application of the AFM to probe surface properties of various materials is reliant on the detection of interactions between the tip and sample, the character of which are intrinsically linked to their separation (Lower et al., 2000). Therefore it seems relevant to briefly summarise the different types of interfacial phenomena that are possible between two surfaces at close proximity. At maximum separation between tip and surface, the first interactions that are likely to be experienced are electrostatic. These forces can occur at separations of up to $\backsim$ 100 nm and can be either attractive or repulsive depending upon the type and density of the charge exhibited by both surfaces (Dorobantu and Gray, 2010). The strength of these forces are also highly dependent on the surrounding environment as ions in aqueous solution can form layers on the charged surfaces, essentially screening the interaction, and in this way greater ionic strength has a greater reducing effect on electrostatic

forces (Israelachvili, 2011; Xu et al., 2005). This screening effect is dependent on both the ionic content and pH of the environment and on the charge present on each surface (Haugstad, 2012). The magnitude of experienced electrostatic forces are governed by the electrostatic field, and therefore decrease exponentially with separation. They are significant up to $\backsim$ 10 nm of tip-sample separation (Israelachvili, 2011).

As the tip-sample separation is reduced further attractive van der Walls forces can dominate. In aqueous conditions these can have a range of $\backsim$ 15 nm and result from induced dipoles (resulting from weighting of electron density) between neighbouring molecules (Dorobantu and Gray, 2010; Xu et al., 2005). The strength of this binding is reflected by the polarisability of the molecules in question which is generally governed by the number of electrons they possess (Hunt et al., 1981). By reducing the separation even further (in aqueous environments), hydrophobic interactions may be experienced. Broadly these forces originate from the entropic association of nonpolar molecules in preference to water molecules and can occur from $\backsim$ 5 to $\backsim$ 0.2 nm of separation (Haugstad, 2012). This results in the reordering of the water molecules to surround aggregates of hydrophobic molecules which subsequently experience a binding effect. It should be noted that this phenomenon can also result from the repulsion between two hydrophilic molecules due to their preference for neighbouring water molecules as opposed to each other (Berne et al., 2014). At separations below 1 nm, ionic bonding (between oppositely charged ions), hydrogen bonding (between hydrogen containing electronegative atoms) and specific ligand-binding may occur between molecules on the tip and sample surface (Dorobantu and Gray, 2010; Lower et al., 2000).

Ligand-receptor binding events are of significant biological importance and are responsible for much of the function in eukaryotic tissue (see *Section 1.2* throughout). Interactions between these molecules can be studied using the AFM (see *Sections 2.4.4 & 2.4.5*) and require chemical modification of both the probe and substrate surface to exhibit the desired molecules at a chemical terminus. This can be achieved a variety of different ways and

common approaches include the grafting of thoil groups onto gold, through the introduction of reactive amine groups or through the incorporation of high affinity biomolecules as in biotin-avidin chemistry (Barattin & Voyer, 2006). Chemical modification is covered in more detail in *Section 2.5.3*). When chemically modified tips are used it is possible to observe adhesive interactions such as specific unbinding, polymer stretching and polymer unfolding (Carvalho and Santos, 2012; Hughes and Dugan, 2016). In addition steric effects may become noticeable (Haugstad, 2012; Na et al., 2010). These effects can include repulsive forces stemming from the overlap of electron clouds of neighbouring molecules and from the osmotic pressure generated from the unfavourable compression, entropic confinement and entanglement of polymer chains. This effect is highly dependent on the size, spacing and number of polymer chains in a given surface area and also on the surrounding aqueous environment. As such, these effects may be observed from tip-sample separations of $\backsim$ 1 nm to $\backsim$ 100 nm depending upon the interfacial system and polymeric molecules investigated (Abu-Lail and Camesano, 2003; Gao et al., 2011).

2.4.4 Force Spectroscopy

The application of AFM extends beyond imaging a sample surface, it also provides the ability to directly measure the forces exerted back on a probe by the surface (equivalent to forces exerted by the tip on the sample by Newton's third law of motion) and as such can allow for the quantification of adhesion between tip and sample. This feature of modern AFM systems can be exploited and employed in a wide array of physical and scientific disciplines and can be used to measure interaction forces between charged molecules, proteins, polymer systems or networks, cells and consumer products to list just a few examples. More specifically, in recent years force spectroscopy (FS) has cemented itself as a significant and well accepted technique for the measurement of both molecular interactions and energetics and has become an integral component in the field of soft matter sciences.

In short, FS is the process by which the measurement of forces between a probe and sample can be detected by means of physically bringing the probe tip into contact with the desired surface and subsequently detaching them in only the z-direction. As such, the measurement is split up into a two-stage process termed approach phase and retract phase. Raw data are most commonly represented in the form of force curves, an example of which is illustrated in *Figure 2.4*. A FS run starts with the approach phase in which, the probe and surface are sufficiently separated as to ensure no interaction between tip and sample and the piezo-elastic scanner is situated in a withdrawn position (or in a position by which it has sufficient ability to extend and bring the tip into contact with the sample). Upon initiating the run a potential difference is applied across the piezo-element and the tip is brought towards the sample. When the tip and sample separation is sufficiently reduced, to the region of tens of nm, attractive intermolecular forces between the tip and sample can take effect and a snap-in effect can be observed which physically represents a negative deflection of the cantilever as the interaction drags the tip into contact with the surface. As the piezo scanner is extended further, the deflection of the cantilever returns to its neutral position and begins to positively deflect until a user-defined trigger deflection is achieved. This point marks the end of the approach phase and the start of the retract cycle.

Upon reaching the trigger point, the extension due to potential difference across the piezo scanner is halted and reversed. As the scanner retracts the deflection of the cantilever reduces until it returns to its neutral position. In the case of negligible adhesion between probe and sample, the tip will then separate from the surface and the piezo-element will retract back to the starting position. In this case no further cantilever deflection will be observed until such a point when the next approach cycle snaps-in or makes contact with the surface. If there is some adhesive interaction between tip and sample surface any further retraction of the piezo past the cantilevers neutral position results in negative deflection as the tip and sample remain in contact. This further retraction results in an increase in the force exerted on the bound

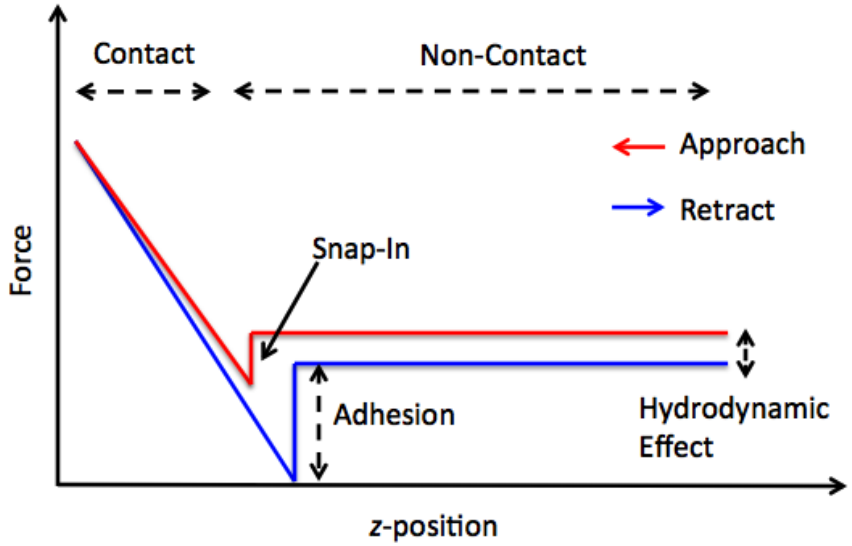

Fig. 2.4 A representation of a force curve taken on an adhesive surface at moderate velocity. The approach and retraction phases are depicted in red and blue respectively. The contact and non-contact regimes are clearly indicated alongside the point of adhesive rupture and the snap-in due to attractive surface forces. The hydrodynamic effect is also indicated which is caused by measurement in a liquid medium and is a product of viscosity.

system by both the piezo element pulling the tip away from the surface and equally by surface pulling on the tip to remain bound. Increasing retraction consequently results in further negative deflection of the cantilever. When the force imparted on the bond between tip and sample becomes great enough it will rupture, releasing the tip and allowing the cantilever to return to equilibrium position at zero deflection. This force physically represents the strength of the binding between the tip and surface regardless of the chemical or physical mechanism by which this binding occurs. Cantilever motion in a FS run is summarised in *Figure 2.5*.

By precise measurement of the cantilever deflection at the point of adhesive failure, the rupture force can be quantified. In fact, as has been mentioned in *Section 2.4.2*, measurement of the cantilever deflection allows for the extraction of forces between the tip and sample throughout both the approach and retraction phase of the FS cycle and as such can also be used to define how much force is exerted on the sample at the trigger deflection. This can then be manually adjusted by the user for optimisation in a given set-up. In order to extract

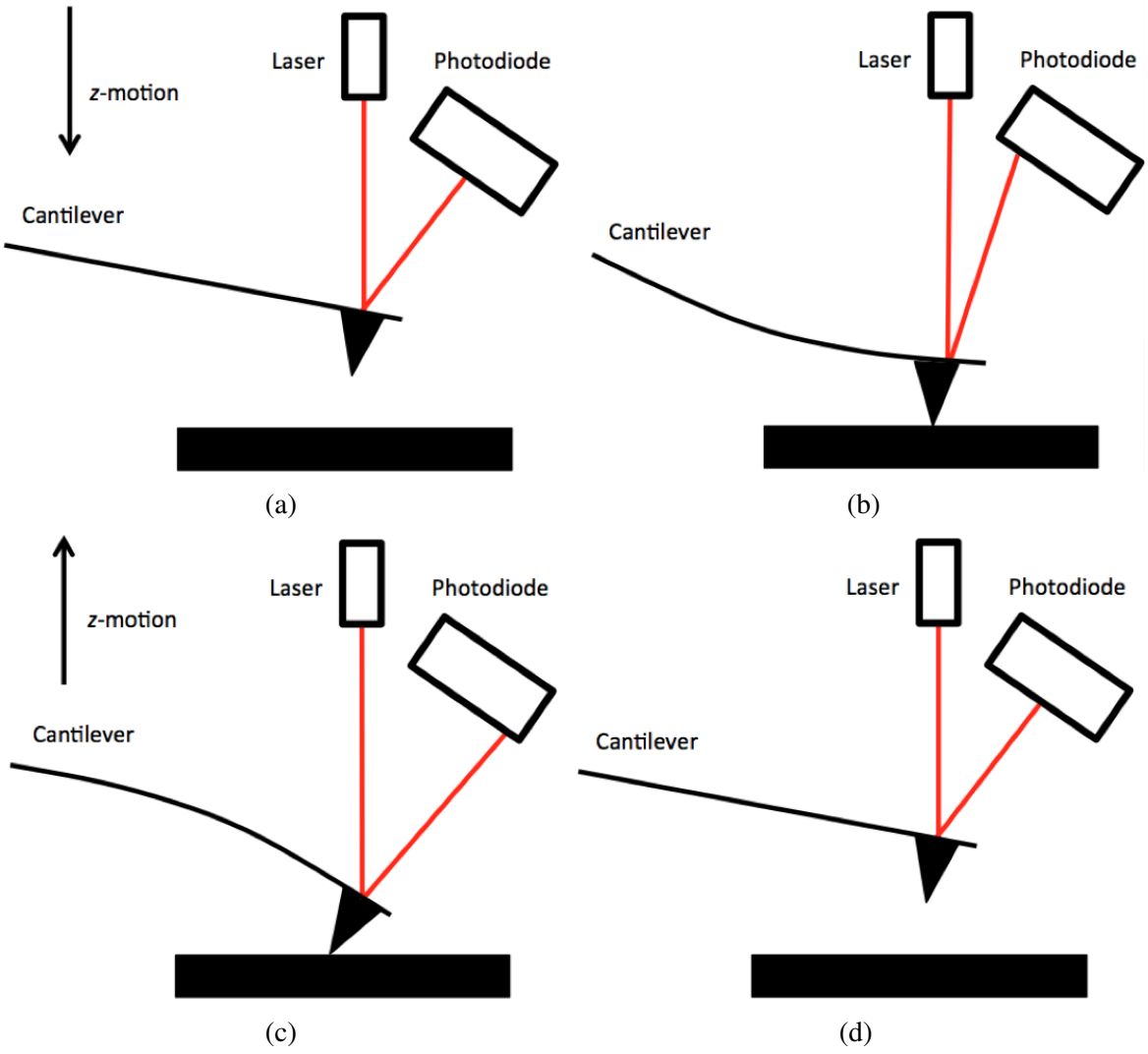

Fig. 2.5 A schematic diagram depicting the deflection of an AFM cantilever due to interfacial interactions with the sample surface throughout a FS loop. Initially the tip and sample are sufficiently separated and the cantilever is in its equilibrium position (a). The cantilever is then brought into contact with the surface and positively deflects as the piezo is lowered further in the z-direction (b). Upon retraction of the cantilever in the z-direction, adhesive interactions can cause the cantilever to deflect negatively (c). Finally, the cantilever is sufficiently separated from the sample and returns to its equilibrium position (d). Respective positions of the laser reflection on the photodiode are indicated in each position.

force values from the cantilever deflection it must be treated as a Hookean spring (see *Figure 2.6*) which assumes a perfectly elastic deflection with no resultant deformation of the probe (Gavara, 2017). This is governed by Hooke's law which is given by

$$F = -kx, \tag{2.5}$$

where x represents the deflection of the cantilever, k represents the spring constant (a constant value representing the stiffness of the cantilever or spring and is defined by both the constituent materials and geometry of the system) and F represents the restoring force - the force contained within the stretched spring or deflected cantilever which acts to return the system to equilibrium. This force is equivalent in magnitude to adhesive forces between the probe and sample and thus, any tip-surface forces exhibited within the FS cycle are simply directly proportional to the cantilever deflection. There are many methods that have been developed to deduce the spring constant of the AFM cantilever but the most widely used is the thermal tune method (Butt and Jaschke, 1995; Hutter and Bechhoefer, 1993). This will be detailed in *Section 2.5.1*.

Rupture forces between tip and sample for a particular system can vary significantly and as such many repeated measurements are necessary to discern an average. There are many methods of analysis to extract useful information from adhesive events such as polymer unfolding, stretching and unbinding. Methods relevant to this thesis will be covered in more detail in *Section 2.5.1*. In general however, force-distance curves are converted into force-separation curves prior to analysis by

$$z_{\text{sep}} = z + x, \tag{2.6}$$

where z_{sep} is the tip separation from the sample surface and z is the position of the piezo in the z-axis (taken to be zero at the non-snap-in contact point at zero deflection; Albon, 2015).

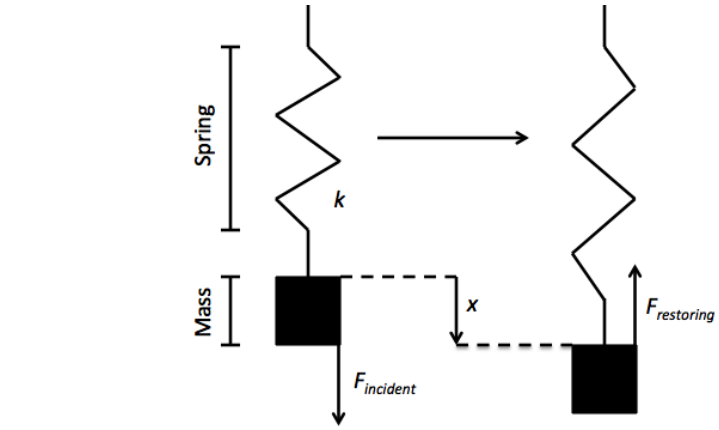

(a)

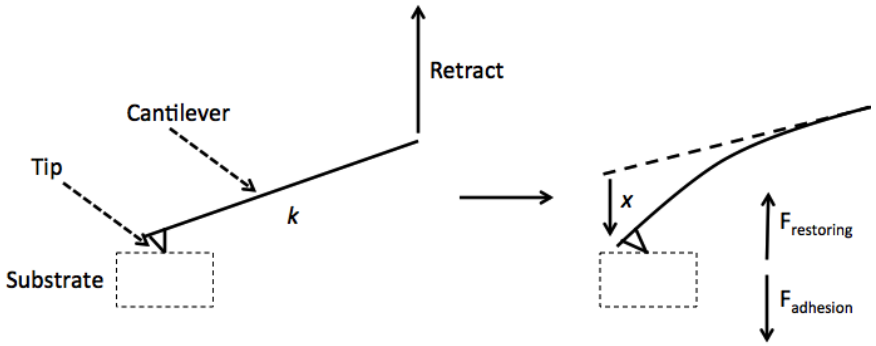

(b)

Fig. 2.6 A schematic diagram of a Hookean spring under an incident load where the incident and restoring forces are equivalent (a). A schematic diagram the Hookean spring model as applied to an AFM cantilever undergoing a deflection due to an adhesive event on the substrate surface (b).

As above, the deflection here is positive when the cantilever is bent such that the tip-side is convex (contact regime) and negative when the tip-side is concave (adhesive phenomena). Multiple parameters have been found to effect the measured rupture force between tip and surface, such as the trigger point, and hence it is important to ensure consistency in experimental settings in all FS studies conducted (Franz et al., 2007).

2.4.5 Dynamic Single Molecule Force Spectroscopy

Dynamic single molecule force spectroscopy (DSMFS) is a technique which has successfully measured the properties of energy barriers associated with unbinding events and is often employed in the characterisation of adhesive interactions between ligands and receptors. It relies upon two basic principles. Firstly, the ability to chemically modify both the tip and the surface as to introduce them in FS loops and discern single unbinding peaks corresponding to the rupture of individual adhered molecules. Secondly, the ability to both control and modify the speed at which the tip retracts from the surface via the piezo-element. The technique was developed from dissociation models reported by Bell (1978) and was proposed by Evans and Ritchie (1997) describing an exponential reduction of the bond lifetime under external forces which takes the form

$$k_{\text{off}}(F) = k_{\text{off}}^{0} \mathrm{e}^{\frac{F\chi_{\text{B}}}{k_{\text{B}}T}}, \tag{2.7}$$

where $k_{\text{off}}(F)$ is the force-induced dissociation rate, k_{off}^{0} is the equilibrium dissociation rate (the dissociate rate under no external loading), F is the force, χ_{B} is the barrier width, k_{B} is the Boltzmann constant and T is the temperature (Mitchell et al., 2007). This is caused by a reduction in the height of the energy barrier, induced by the external force imparted on the bond which is assumed to increase linearly with the time under stress (Kulik et al., 2015). The observed rupture force has then been shown to vary with the loading rate which is dependent on the velocity of retraction of the tip from the sample. The quantification of

the loading rate will be discussed in *Section 2.6.1*. This method has the ability to probe both single and multiple barriers and can describe energetics of interactions including the barrier width, the equilibrium dissociation rate and the energy of adhesion. It is governed by the Bell-Evans model given by

$$F_{\text{rupture}} = \frac{k_{\text{B}}T}{\chi_{\text{B}}} \ln(r) + \frac{k_{\text{B}}T}{\chi_{\text{B}}} \ln\left(\frac{\chi_{\text{B}}}{k^0_{\text{off}} k_{\text{B}} T}\right), \tag{2.8}$$

where F_{rupture} is the rupture force and r is the loading rate. This model represents the rupture event as a kinetic escape from a potential due to external force (Burgos et al., 2009).

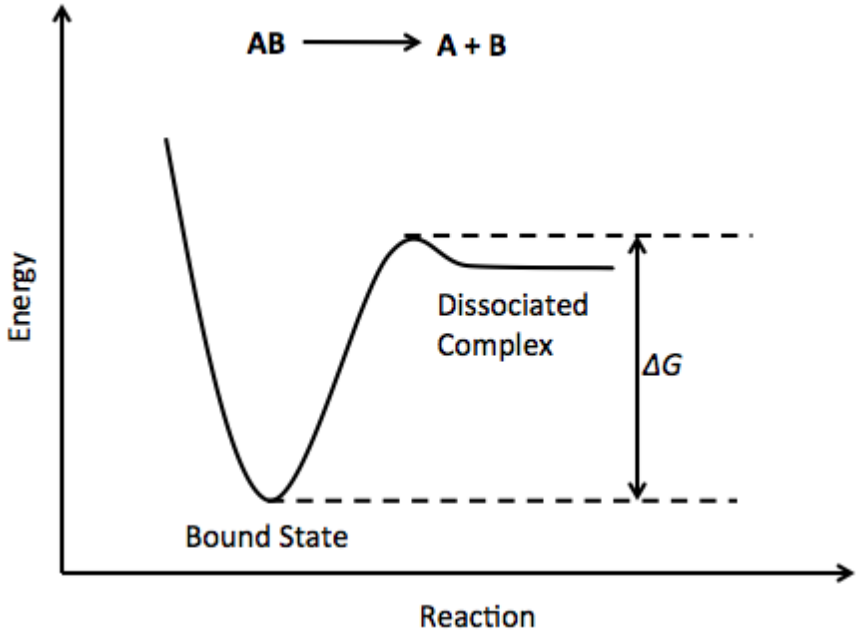

Fig. 2.7 A representation of a ligand unbinding event which is governed by a single energetic barrier. The bound and unbound states are clearly marked and the thermodynamic energy of adhesion (or activation energy for unbinding) is indicated as ΔG.

2.4.6 Indentation Force Spectroscopy

The ability to accurately quantify forces throughout the approach and retract phases of a FS loop also allow for the extraction of elastic properties at the surface of a deformable sample (Costa, 2003). This follows from the general principle that, for a given cantilever stiffness and incident force at which the FS loop triggers, the tip will indent into the surface with a depth that is variable with the elastic properties of the sample. A softer sample will be indented to a greater depth than a comparatively harder one. For significantly stiff and incompressible surfaces the deflection of the cantilever throughout the contact regime of the FS loop is equal to the change in z-position of the piezo element however, for a deformable sample this does not remain true. Instead the deflection is reduced by indentation into the sample and thus the tip-sample separation is now

$$z_{\text{sep}} = z + (x - \delta), \tag{2.9}$$

where δ is the indentation depth. It follows that the force exerted by (and with equivalent magnitude, on) the cantilever from *Equation 2.5* becomes

$$F = -k(x - \delta). \tag{2.10}$$

This can be used to transform force curves into force-indentation curves (see *Section 2.6.2*) to which a variety of mechanical models can be applied to deduce the mechanics of contact between probe and sample.

The Hertz model is a common approach in extracting the mechanical properties (in the form of the Young modulus) of elastic samples and relies upon weak adhesive interfacial forces between tip and sample. It also requires that the magnitude of indentation is small such that $\delta < x$ which, for biological samples, results in the requirement for soft cantilevers. In fact, ideally one would match the spring constant between the lever and sample surface but

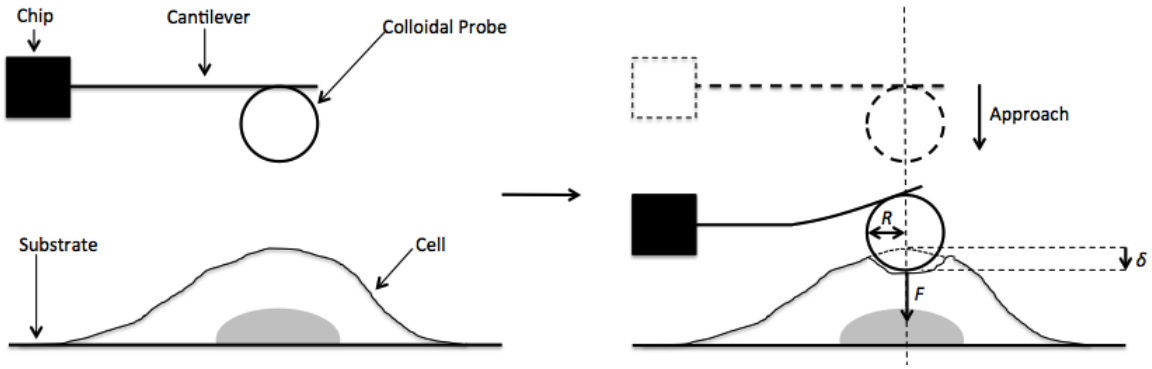

Fig. 2.8 A schematic diagram of a colloidal probe indenting the the cell surface. Variables relevant to the Hertz model for a spherical probe and an elastic half-space are indicated.

this is significantly difficult to achieve practically. The model is highly dependent on both the shape of the probe and sample with a variety of mathematical formulae describing a variety of idealistic contact regimes. The model can therefore be applied to a wide variety of systems. The Hertz model for indenters of two different probe geometries will be outlined here due to their relevance in *Chapter 6* of this thesis. In both cases the sample is approximated to be a homogenous elastic half-space and contact between tip and surface is assumed to be symmetric and frictionless. For a rigid conical indenter the model (Hertz-Sneddon) is given by

$$F = \frac{2E}{\pi(1-\nu^2)}\delta^2 \tan\theta, \tag{2.11}$$

where F is the applied force, E is the Young modulus, ν is the Poisson ratio and θ is the half-angle (the angle that the slope of the tip apex makes with the vertical axis). The relevant model (Hertz) involving a perfectly spherical probe follows the form

$$F = \frac{4}{3}E_r R^{\frac{1}{2}}\delta^{\frac{3}{2}}, \tag{2.12}$$

where E_r is the reduced elastic modulus and R is the radius of the spherical indenter. The elastic modulus of the cell and tip are then related to the reduced modulus by

$$\frac{1}{E_{\mathrm{r}}} = \frac{1-\nu_{\mathrm{tip}}^2}{E_{\mathrm{tip}}} + \frac{1-\nu_{\mathrm{sample}}^2}{E_{\mathrm{sample}}}, \tag{2.13}$$

where ν_{tip} is the Poisson ratio of the tip, ν_{sample} is the Poisson ratio of the sample, E_{tip} is the Young modulus of the tip and E_{sample} is the Young modulus of the sample (Li, 2017). The Poisson ratio is defined as the proportional change in thickness of a material in the lateral direction as it is stretched or compressed in the other (Greaves, 2013).

2.5 Force Measurements

2.5.1 AFM Setup

Unless expressly stated otherwise all force data obtained throughout this thesis were taken using a MFP-3D-BIO^{TM} AFM (*Asylum Research, an Oxford Instruments company, California, U.S.A.*). A ForceRobot® 300 (*JPK, Berlin, Germany*) was employed for a small quantity of measurements in *Chapter 3* due to a period of work which was conducted outside of The University of Sheffield and at Nanjing University (*Nanjing, China*). In short, the molecular force probe (MFP) consists of a head mounted on a stage via three adjustable legs. Contained within the head is the laser, photodetector and piezo-scanner. It also houses a top-down camera with adjustable position and focus which is optimised to observe mounted cantilevers and allows for the precise positioning of the laser on their rear surface. The underside of the head contains a clip-in region for the tip-holder in which the cantilever chip is manually mounted with tweezers via a screw-in clamp which secures it in place (see *Figure 2.9*). This region connects relevant electronics between the two pieces of hardware and also allows the laser to shine into an optical window in the tip-holder and subsequently directly onto the cantilever of choice. Prior to mounting a cantilever chip and conducting experiments with the MFP, the tip-holder was removed and was washed thoroughly in an effort to limit contamination by first immersing in deionised water and sonicating for five minutes using a U300 sonicator (*Ultrawave, Cardiff, UK*). It was then immersed in IPA and sonicated for a further five minutes. Upon completion of experiments on a particular substrate or dish of cells, the tip holder was washed again in water and IPA by repeating the process highlighted above.

The legs of the MFP head slot into grooves on the stage which can be manually moved in the $x-y$ plane using two spring-loaded dials allowing for the positioning of the tip over desired regions of samples. The length of each leg is manually controlled using

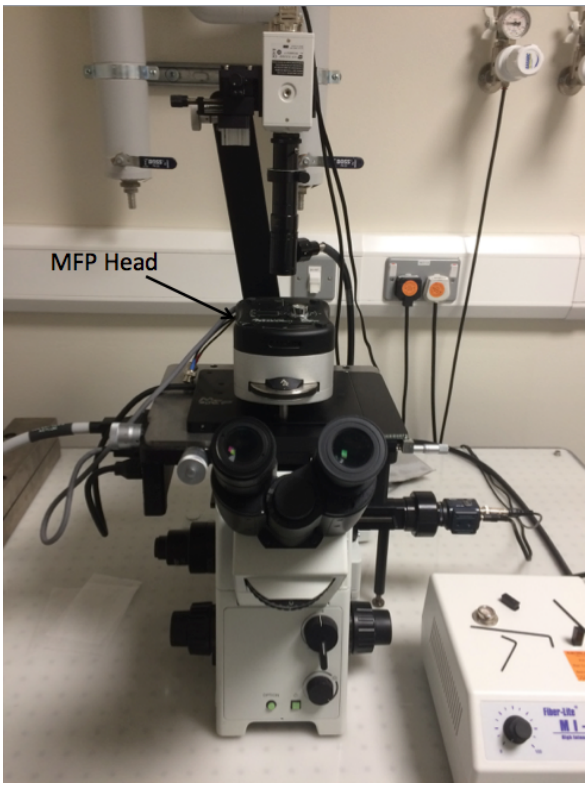

(a) The MFP-3D-BIO AFM system.

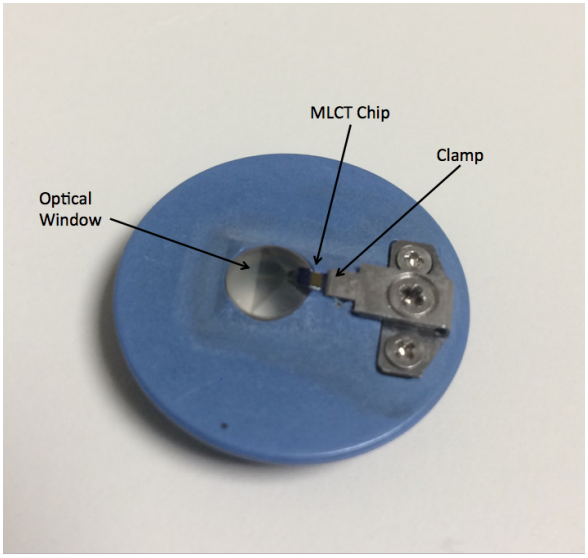

(b) The MFP-3D-BIO tip holder with a mounted microlever cantilever (MLCT) chip.

Fig. 2.9 The MFP-3D-BIO set-up (a) and tip-holder (b). The MFP head, the optical window for propagation of the laser (and top-down optics) and the position of the clamped cantilever chip are clearly indicated.

three wheels which are used as a corse approach method of the tip before a fine approach and engagement is initiated electronically via the piezo-element. The MFP is integrated with an IX71 inverted optical microscope (*Olympus, Toyko, Japan*) which allows for high magnification of translucent biological samples and as such the precise positioning of the tip over the sample when imaging or conducting force measurements. It also allows for the selection of particular biological materials of interest and the elimination of those that are not. The probe and sample were illuminated using a Fiber-Lite MI-LED light source (*Dolan-Jenner Industries, Massachusetts, USA*) which is fed into the MFP optics.

2.5.2 Cantilever Calibration

In order for the Force to be extracted from the precise measurement of the cantilever deflection by *Equation 2.5* it is necessary to calibrate the spring constant of the cantilever with a high degree of accuracy. This must be done prior to taking any force measurements and involves a two stage process. Firstly, the optical lever sensitivity (OLS) of the setup must be calculated. The OLS is essentially the response of the potential difference output of the quadrant-photodetector due to a change in position of the incident laser spot and represents the proportional relationship between the z-position of the piezo-element, or by extension the deflection of the cantilever (see *Section 2.4.6*), and the output voltage. This value is dependent on both the position of the mounted cantilever in the holder and on the position of the optics within the setup, particularly the position of the incident laser spot on the rear of the cantilever tip. As most commercial cantilever products are constructed as one or more probes attached to the end of a rectangular chip which must be mounted into the tip-holder manually, significant variation in the position of mounting is inevitable from one experiment to the next due the handling of their small size. This position is significant as it directly affects the movement between the cantilever tip during deflection and the incident laser spot on the photo-diode. The positioning of the laser spot on the rear of the cantilever is also

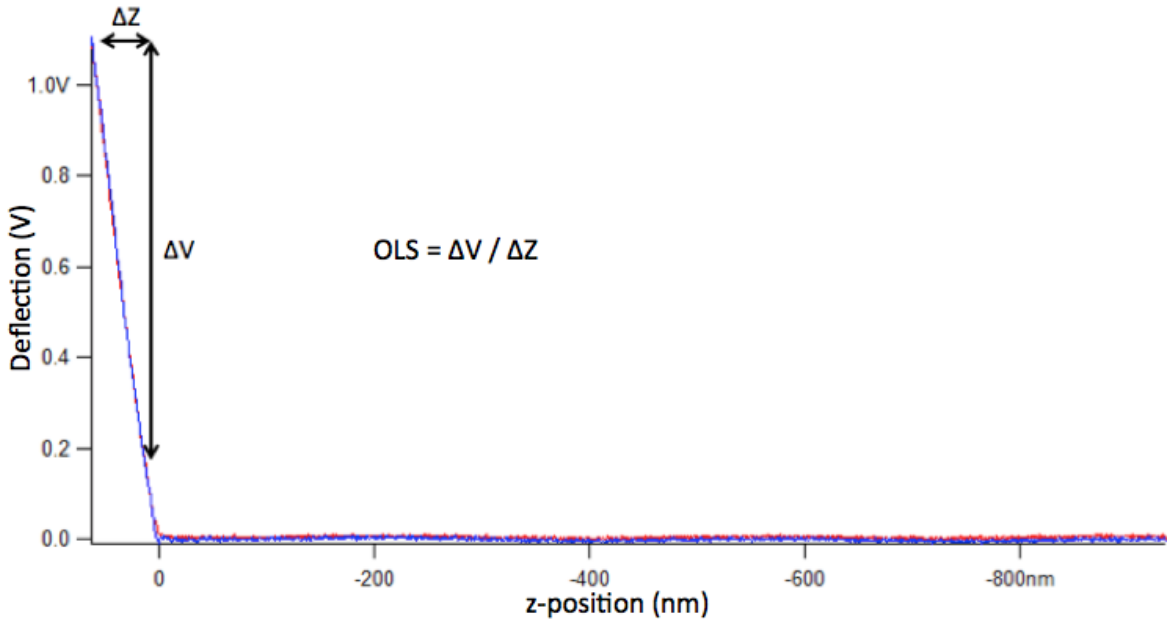

Fig. 2.10 A calibration force-curve taken on a hard and incompressible surface for OLS calculation where ΔV is the change in the deflection voltage in the linear contact regime, ΔZ is the change in z-position in the linear contact regime and the OLS is equal to the ratio of ΔV and ΔZ.

important as the magnitude of cantilever deflection is not uniform along its length. The calculation of the OLS allows for the mitigation of both of these significant causes of error. It is calculated by obtaining a force-curve on an incompressible surface such as glass or mica as to ensure a linear contact regime and then by extracting the gradient of this line. This value is usually outputted by the AFM software as the inverse OLS (InvOLS) with units $\mathrm{nm{\cdot}V^{-1}}$ and is used as a constant of proportionality throughout the whole experiment (until re-calibrated). It should be noted that it is important that the laser spot is centred directly behind the tip when aligning the AFM optics to ensure the reproducibility of data and good output signal levels.

Once the OLS has been determined, the spring constant can be extracted with high accuracy. It should be noted that it is imperative that the OLS is deduced before the spring constant. The most popular approach in measuring the spring constant of the cantilever is by the thermal tune method as it allows for calibration in both air and liquid environments

and does not damage the probe (Butt and Jaschke, 1995; Hutter and Bechhoefer, 1993). The spring constants of all AFM cantilevers used throughout this work have been extracted using this method. The thermal noise method describes the cantilever as a harmonic oscillator which is governed by energy

$$E_{\mathrm{HM}} = \frac{p_{\mathrm{HM}}^2}{2m} + \frac{1}{2}m\omega_0^2 x^2, \tag{2.14}$$

where m is the oscillating mass, p_{HM} is the momentum of the mass, ω_0 is the resonant angular frequency of the system and x is the displacement of the oscillator. The equipartition theorem states that the average value of each quadratic term is given by $\frac{1}{2}k_{\mathrm{B}}T$, therefore

$$\left\langle \frac{1}{2}m\omega_0^2 x^2 \right\rangle = \frac{1}{2}k_{\mathrm{B}}T. \tag{2.15}$$

However $k = \frac{\omega_0^2}{m}$ and by substitution into *Equation 2.15* the spring constant can be extracted by measurement of the mean-square oscillator displacement,

$$k = \frac{k_{\mathrm{B}}T}{\langle x^2 \rangle}. \tag{2.16}$$

The thermal fluctuations are of the order of angstroms and are sufficiently small as to approximate the cantilever as a simple harmonic oscillator with one degree of freedom. In order to isolate the thermal oscillator displacement from other sources the data is examined in the frequency domain. The fluctuation exhibits a Lorentzian shaped power spectrum when damping is small and allows for removal of background noise away from resonance. Integrating the power spectrum is equal to the mean square of the oscillator fluctuations and *Equation 2.16* becomes

$$k = \frac{k_{\mathrm{B}}T}{P}, \tag{2.17}$$

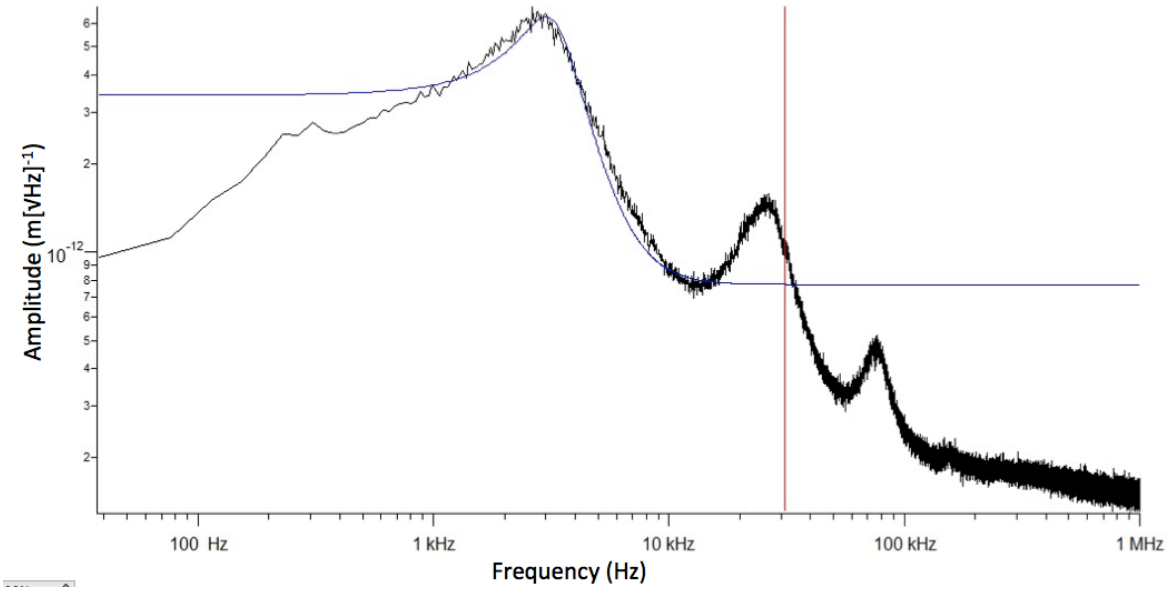

Fig. 2.11 Thermal tune of MLCT tip-D in liquid in the frequency domain. The Lorentzian fit is indicated by the blue line from which a spring constant of 38.51 pN·nm^{-1} was extracted.

where P is the area under the Lorentzian curve.

2.5.3 Surface Chemistry

In order to measure adhesive interactions between ligands and receptors it is necessary to chemically modify the surface of both the substrate and probe to exhibit the desired molecular pair. There are many methods available for the attachment of various functional groups to a variety of surfaces. One of the most popular, and one exploited throughout this thesis, is in the utilisation of the spontaneous adsorption of thiols with gold due to the relatively simple chemistry involved and the speed at which the binding occurs (Barattin and Voyer, 2008). The strength by which these sulphur containing reactive groups associate with gold surfaces has been shown to be comparable to ionic bonding and can comfortably withstand ligand-receptor interactions. Molecules containing thiols and cysteine residues are able to form self-assembled monolayers (SAMs) on gold substates, completely coating the surface with uniform density, which makes them ideal for use in FS applications (Xue et al., 2014).

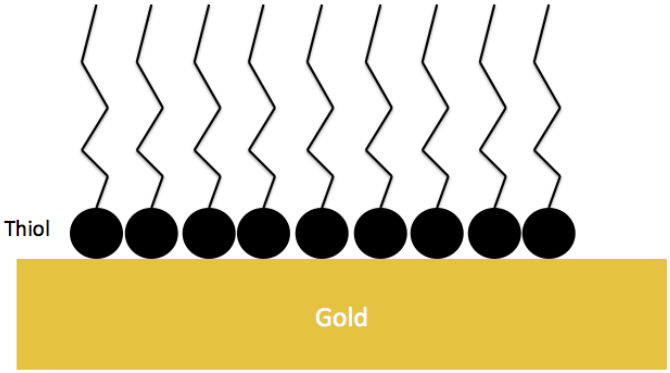

Fig. 2.12 A SAM formed on a gold substrate from direct interaction with sulphur in a reactive thiol group.

Tips and substrates can either be purchased with a gold coating or one can be achieved using vapour deposition, usually on a silicon substrate, via the thermal evaporation of gold under vacuum. Before the deposition of gold it is necessary to first deposit an adhesive layer of chromium to ensure substrate stability (Moazzez et al., 2013).

It is often necessary to chemically modify probes via more complicated protocols in order to ensure low densities on the tip and to introduce linking tethers for better analysis of binding events (see *Section 2.6.1*). The choice of chemistry depends completely on the probe surface and on the desired functional terminal. However, when investigating ligand-receptor interactions, or other biological molecular binding, it is common to once again tether the proteins via cysteine resides. This was achieved throughout this work via the method illustrated in *Figure 2.13* (Barattin and Voyer, 2008). Silicon nitride microlever cantilever (MLCT) AFM probes were immersed in either chromic acid or piranha solution (70% sulphuric acid and 30% hydrogen peroxide) to hydroxylate the surface. A reactive amine group was then introduced using (3-aminopropyl)triethoxysaline (APTES) in toluene which was subsequently oven heated at 50 °C to stabilise the structure (Das et al., 2017). A polyethylene glycol (PEG) linking region was introduced using *N*-hydroxysuccinimede-PEG-maleimide (NHS-PEG-Mal) in water. The NHS terminus of the NHS-PEG-Mal binds

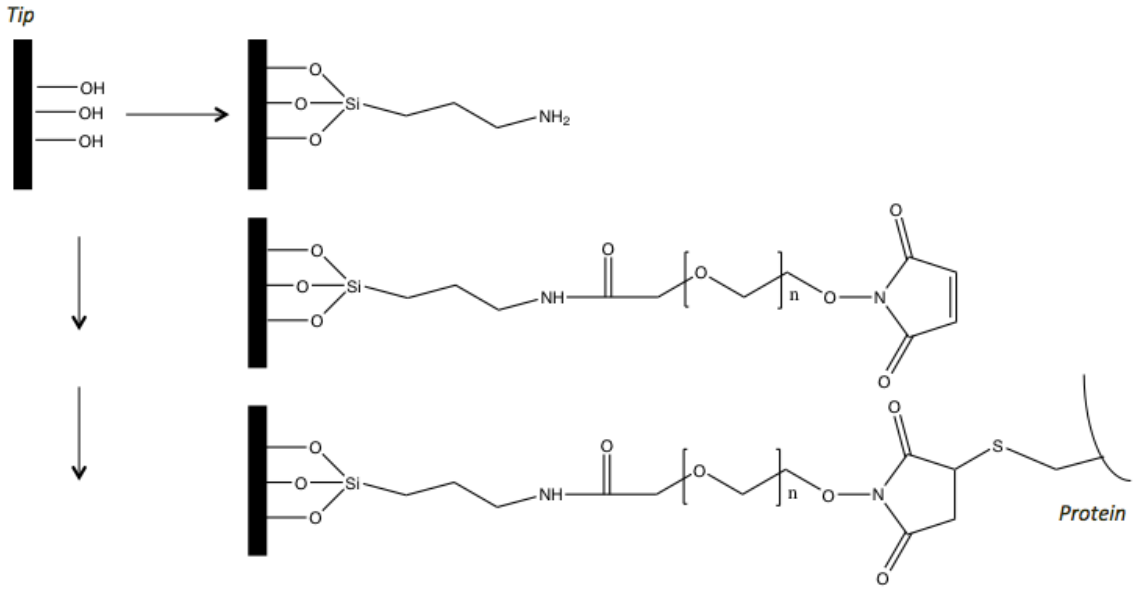

Fig. 2.13 Chemical modification process covalently grafting proteins at cysteine residues to silicon nitride MLCT tips via a PEG linking region.

with the exposed amine group on the tip resulting in a PEG-linked terminal maleimide (Mal; Banerjee et al., 2012). This Mal was bound directly to cysteines in the proteins of interest in PBS solution (Northrop et al., 2015). Between each step of the modification process, tips were dried using absorbent tissue and washed thoroughly with the solvent required for the next step before being tissue dried again. It should be noted that before substrates or probes were functionalised using either method outlined above they were cleaned thoroughly using IPA followed by plasma for 5 minutes and finally with deionised water.

2.5.4 Colloidal Probe Construction

Attaching colloids to a desired probe was achieved using the AFM system itself due to the necessity of physically manipulating the microscopic components involved in the process and also due to the requirement of both the conventionally mounted and inverted optical microscopes. The chip containing the required cantilever was loaded into the tip-holder of

the MFP as normal and the laser was focussed on the the rear the preferential tip using the conventional microscope. Polystyrene beads were significantly diluted from stock solution in deionised water until they could be isolated when pipetted onto a surface. A glass microscope slide was cleaned in IPA and distilled water before 0.5 ml of the colloid solution was pipetted onto the centre of its surface and was spread over the slide by gentle tilting. Failure to clean the slide prior to the addition of the colloid solution resulted in the beads becoming adhered to the surface due to the natural coating of the slide from contaminants from the air. It was necessary to spread the solution over the slide in order to ensure that the beads did not clump together which results in an inability to isolate one for removal and adherence to the probe. The majority of water was removed from the slide by gently dabbing the surface with Kimtech highly absorbent and lint-free tissues. It was important not to use standard tissue paper in order to avoid depositing tissue fibres and other debris on the slide. It was found that a significant proportion of colloids remained on the slide by gently dabbing the surface. Following this, the colloid covered slide was baked at 100 °C in order to remove all water from the surface. It was found through trial and error that this heating stage was significantly important in ensuring that that colloids could be successfully removed from the glass surface of the slide and transferred to the tip of the cantilever by dramatically reducing capillary forces between the beads and the slide.

On a second microscope slide a small amount of Norland Optical Adhesive 81 (*Norland, New Jersey, USA*) was applied to the surface by dipping a 200 μl pipette tip into the bottle and smearing it towards one side of the slide. Using a razor blade an adequate proportion of the adhesive was dragged to the centre of the slide and was fashioned into a sharp vertical line. This slide was placed upon the AFM stage and using the inverted microscope it was possible to locate the sharp divide between the region of the slide coated in adhesive and the uncoated glass surface. The tip was brought into contact with the glass on the clean side of the adhesive strip (on the opposite side of the slide from which the glue was dragged with

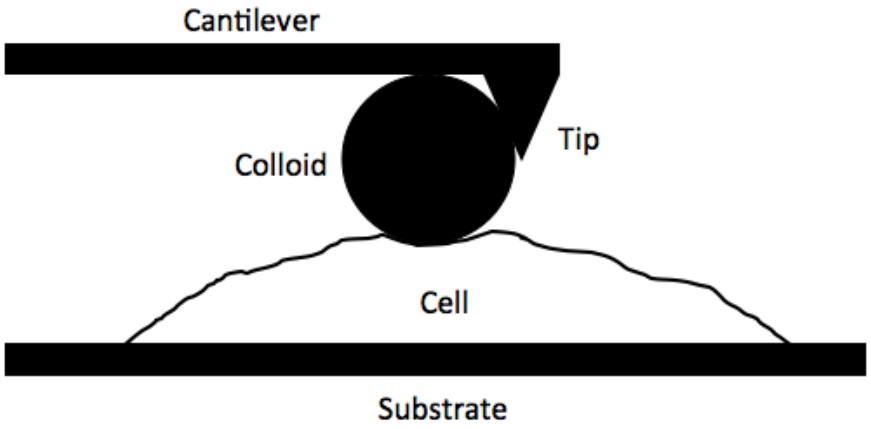

Fig. 2.14 Schematic diagram of a constructed colloidal probe indicating the required position of the adhered polystyrene bead to ensure no sample contact of the pyramidal MLCT tip.

the blade) such that both the cantilever and the adhesive were in the field of view of the microscope. The AFM head was then manually rolled back using the front leg until the tip was just out of contact with the surface and the stage was moved such that the tip hovered over the dividing line between glass and adhesive. The stage is then slowly moved in such a direction that brings the tip into the adhesive containing region until the tip is captured by the glue. The probe is held in constant position for approximately one to two seconds to allow for the adhesive to fully coat the tip region before being manually retracted out of the glue by again adjusting the front leg of the AFM head. The slides were then switched so that the colloid coated slide was on the stage and the beads were brought into focus using the inverted microscope. The probe was brought into contact with a colloid which was sufficiently isolated at the tip region. It was important that the tip and colloid made contact directly behind the protruding tip of the cantilever (*Figure 2.14*) to ensure that the point of contact was indeed the bead surface and that the cantilever would deflect as expected in subsequent measurements taken with these probes. Upon significant contact with the colloid of choice, significant pressure was exerted to ensure binding by further shortening the front AFM leg.

It should be noted that the 10 μm and 25 μm colloids used throughout this thesis protrude much further from the probe than the factory designed pyramidal tip and as such, data collected would not be affected by the two features of the probe. Also, in many cases the first bead which was brought into contact with the adhesive probe would not sustain adhesion with the tip but would remain on the slide surface. It was apparent from the view afforded from the microscope that in many of these occasions much of the glue was pulled from the tip onto the bead and as such these colloids were not subsequently brought back into contact with the tip. This is due to the likelihood of excess glue coating the bead on the underside therefore changing the shape of the contact region which would result in the invalidity of fitting a model which assumes a spherical tip. In many cases there was enough adhesive remaining on the probe to adhere to a previously undisturbed colloid and successfully remove it from the glass surface. Following successful adhesion of a polystyrene bead to the desired region of the probe the tip was manually removed from the surface by slowly and steadily increasing the front leg length of the AFM head. Upon reaching sufficient separation from the surface the head was removed and was placed upside-down with the tip holder facing up. The holder was left clipped into the head and the glue was cured by shining ultraviolet light from a UVL-23R lamp (*UVP, California, USA*) directly upon the tip holder and probe for between one and two minutes. Following this exposure the colloid functionilised probe was sufficiently cured and provided enough rigidity and stability for further experimentation.

2.5.5 Combined Florescence Microscopy and AFM

The MFP allows for the simultaneous use of fluorescence microscopy and AFM via the inverted IX71 microscope. A X-Cite® 120Q fluorescence setup (*Excelitas, Massachusetts, USA*) is integrated into the optics of the MFP which illuminates the sample with blue to ultraviolet light. A U-MWIBA3 filter (*Olympus, Toyko, Japan*) is positioned between the inverted microscope and the stage which allows propagation of green light with wavelength

$\backsim$ 500 nm to $\backsim$ 550 nm. A shutter is positioned alongside the filter to avoid perpetual illumination of the sample between observation of cells which can result in the bleaching of fluorophores and inhibition of florescence. The integration of the fluorescence system into the AFM setup allows for identification of biologically relevant cells by transfection of a GFP plasmid (*Section 2.2.5*).

2.6 Analytical Methods

2.6.1 Quantification of Adhesion

Prior to analysis, obtained force curves were transformed into force-separation curves (see *Section 2.4.4*). Initial analysis of force-separation curves was conducted using the Asylum Research program within Igor Pro (*WaveMetrics, Oregon, U.S.A*). This was essentially a filtration process which differed in implementation between different types of experiments. For data relevant to DSMFS of protein-protein interactions (see *Chapter 3*), curves were manually selected if they exhibited a specific protein-protein binding interaction and were discarded if they did not. Single-molecule features were apparent due to the incorporation of the PEG linking chain (see *Section 2.5.3*) as illustrated in *Figure 2.15*. The PEG-linker acts to separate the specific interaction from the non-specific interaction and allows for both the identification of single-molecule events and the extraction of the loading rate (explained further below). Event identification arises from the tip-surface non-specific interaction occurring at substantially smaller separation between probe and sample than the specific rupture event which will only occur when the PEG chain is fully extended. If the length of the linking chain is known, a range of tip-sample separation (or contour length range) in which the specific unbinding event may occur can be estimated permitting further specificity verification. This attempts to ensure that events caused by other phenomena are not included in the batch for further analysis. The filtration of force-map data was slightly different. Force maps allow for the AFM to simultaneously build up a topographical image in the $x-y$ plane alongside corresponding position specific force phenomena such as adhesion. This is achieved by the AFM conducting FS measurements in an $x-y$ grid of predefined size and resolution. The z-position of the piezo-element upon contact with the surface builds up the height profile while the surface phenomena is constructed from normal feature characterisation of the force-curves (the magnitude of the largest rupture peaks for adhesion).

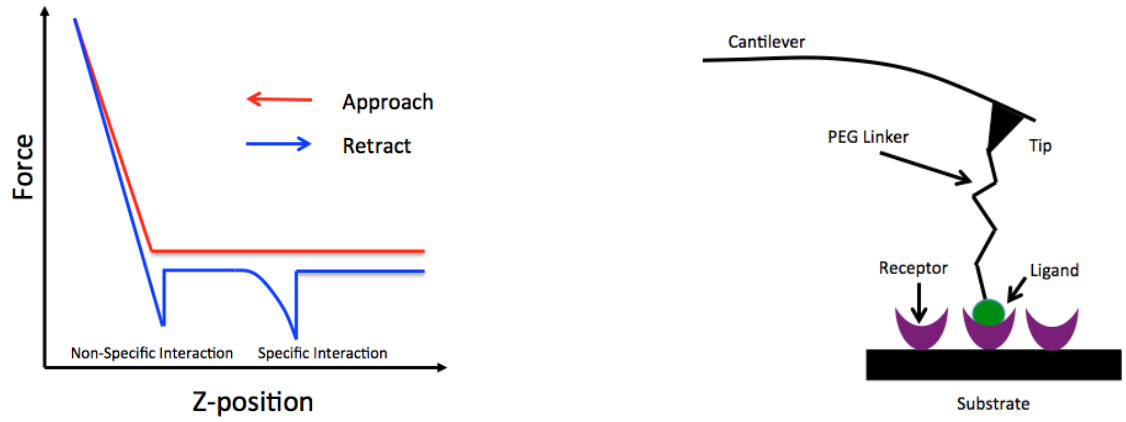

(a) (b)

Fig. 2.15 A representation of a force-curve exhibiting single-molecule protein-protein unbinding via a PEG-linker (a). Spacing between the specific and non-specific events, which are clearly labelled, is depicted. A schematic diagram of a protein-protein unbinding event between a substrate exhibiting a SAM of protein receptors and an AFM probe functionalised with the corresponding ligand via a PEG-linker (b).

The Asylum Research software allows for the extraction of raw force curves from force-maps and it is therefore possible to select for curves that correspond to regions of interest such as the whole cell, specific regions of the cell or specific regions of heightened adhesion and discard those which do not.

Once extracted, the filtered force-separation curves were analysed by one of two methods. Which method was employed for each data-set will be indicated clearly throughout this thesis. Both methods allow for the extraction of the rupture force and the loading rate and therefore provide the necessary information to satisfy the Bell-Evans model (*Equation 2.8*) for DSMFS. The first involves the extraction of force-curves from Igor as .csv files and the subsequent import into a MATLAB® (*MathWorks, Cambridge, United Kingdom*) macro. The script for this macro is a slight variation on one written and used by Mr. Jamie Blakeman (*Department of Physics and Astronomy, University of Sheffield*) and is provided in *Appendix A*. The curves are reproduced by the MATLAB® script in a graphical user interface (GUI) to any user defined magnification. By clicking a crosshair target in the GUI first over the

rupture-point of the peak followed by another along the slope, both the magnitude and the linear gradient of the peak are returned. These values were imported into GraphPad Prism (*GraphPad Software Inc., California, U.S.A*) for analysis.

The second method involves the direct import of force-separation curves in .ibw (Igor binary wave) format into Protein Unfolding and Nano-Indentation Analysis Software (PUNIAS; *PUNIAS, Paris France*). This software has the ability to fit the worm-like chain (WLC) model to user defined regions of the curves and as such can extract both the magnitude and slope of rupture peaks to a high degree of accuracy. The WLC model is used to approximate the behaviour of polymers by treating them as a continuous, semi-flexible chain with persistence length

$$L_{\mathrm{p}} = \frac{\kappa}{k_{\mathrm{B}}T}, \tag{2.18}$$

where κ is the bending stiffness of the polymer. The WLC model is approximated by the interpolated WLC

$$F_{\mathrm{chain}} = \frac{k_{\mathrm{B}}T}{L_{\mathrm{p}}}\left[\frac{1}{4}\left(1-\frac{x_{\mathrm{sep}}}{L_{\mathrm{c}}}\right)^{-2} - \frac{1}{4} + \frac{x_{\mathrm{sep}}}{L_{\mathrm{c}}}\right], \tag{2.19}$$

where F_{chain} is the elastic restoring force of the polymer chain, x_{sep} is the end-to-end separation distance and L_{c} is the contour length (the length of the polymer chain; Bustamante et al. 1994). After fitting the WLC model to each curve of the imported batch, the PUNIAS software returns the fitting results as a Microsoft Excel (*Microsoft, Washington, U.S.A.*) spreadsheet. These were imported into GraphPad Prism for further analysis.

In either of the two analytical methods described above the force-separation curves are able to be characterised such that the parameters necessary for calculation of the size of the energy barrier or the thermodynamic energy of adhesion can be extracted. As has been indicated in *Section 2.4.4*, the measured magnitude of the rupture peak directly yields the

unbinding force. The loading rate is measured in force per unit time and has been estimated in some studies simply as

$$r = kv, \tag{2.20}$$

where v is the retraction velocity. However this approach does not take into consideration the variation in unbinding forces due to polymer stretching, the elasticity of the bond-linker-cantilever syetem and assumes a perfectly steady speed of retraction which in reality is improbable. Instead, it is better to calculate the individual loading rate for each curve at the point of unbinding (the top-third of the peak before rupture). This is

$$r = k_{\text{eff}}v, \tag{2.21}$$

where k_{eff} is the effective spring constant which is given by the gradient of the specific rupture peak at the point of unbinding (Mitchell et al., 2007).

By extracting both the rupture force and loading rate for each curve at a given retraction speed, the respective probability distributions can be represented by histograms. From these, average values of each parameter can be extracted. When the frequency distribution for rupture forces between proteins is constructed, the shape can, instead of a uniform normal distribution, exhibit a tail towards higher forces due to non-linear polymeric tethers which are not accounted for in the Bell-Evans model even when the effective spring constant is deduced. This tether effect has been shown to induce significant systematic errors on the extracted value for the dissociation rate and in an effort to minimise this and to obtain the most probable unbinding forces, average values were determined by fitting Gaussian curves to the probability distributions (Li et al., 2003; Ray et al., 2007). Values extracted from these probability distributions can then be plotted as average force against the natural logarithm of the average loading rate and, for a linear fit, *Equation 2.8* becomes

$$F_{\text{rupture}} = m_{\text{fit}} \ln(r) + c, \tag{2.22}$$

where m_{fit} is the gradient of the line and c is the y-intercept.

It follows from *Equation 2.22* that the width of the energy barrier can be extracted directly from the gradient of the Bell-Evans fit as

$$\chi_{\text{B}} = \frac{k_{\text{B}}T}{m_{\text{fit}}}. \tag{2.23}$$

The equilibrium dissociation rate can then be extracted from the y-intercept as

$$k^0_{\text{off}} = \frac{\chi_{\text{B}}}{k_{\text{B}}T}\left(\text{e}^{\frac{c\chi_{\text{B}}}{k_{\text{B}}T}}\right)^{-1}. \tag{2.24}$$

In *Equation (2.8)* the thermodynamic energy of adhesion is contained within this dissociation rate (Evans, 2001; Evans and Ritchie, 1997). These values can be related by using the Arrhenius equation which treats the unbinding event as a thermally dependent chemical reaction with a defined activation energy (Björnham and Andersson, 2017). This follows the form

$$k^0_{\text{off}} = f_{\text{m}}\text{e}^{-\frac{\Delta G}{k_{\text{B}}T}}, \tag{2.25}$$

where ΔG is the thermodynamic energy of adhesion and f_{m} is the molecular vibration frequency which is dependent on the polymers contained within the binding event and has a range of values between 10^7 and 10^{10} Hz. The higher limit is applicable to small, simple polymers whereas the lower limit represents large complex proteins (Burgos et al., 2009; Ray et al., 2007; Yang and Gruebele, 2003). By substituting *Equation 2.25* into *Equation 2.8* and then equating with the linear fit in *Equation 2.22* it can be shown that

$$\frac{\Delta G}{k_{\mathrm{B}}T} = \ln(f_{\mathrm{m}} m_{\mathrm{fit}}) + \frac{c}{m_{\mathrm{fit}}}. \tag{2.26}$$

2.6.2 Quantification of Elasticity

All cell elasticity measurements calculated throughout this thesis were analysed using the Asylum Research program within Igor Pro. The program has an in-built elastic properties analysis macro which can extract the elastic modulus using a variety of approaches. This software allows for the selection of probe geometry, including both conical with a selectable half-angle and spherical with a selectable radius. The software also allows for the input of all parameters necessary to fit the Hertz model which include the Poisson ratios of both the cell and indenter and also the Young modulus of the probe as discussed in *Section 2.4.6*. It is common in previous indentation studies on biological material such as cells to treat the organisms as incompressible when fitting elastic models and hence and cellular Poisson ratio of 0.5 (for incompressibility; Szymanski et al. 2017) was used throughout all indentation analysis in this work (Li et al., 2008). After the input of parameters and the selection of a relevant fitting model the software automatically converts the force curve to a force-indentation curve (*Equation 2.9*) and performs a line-subtraction procedure on the first ten points of the approach curve (in the non-contact regime) in order to ensure that the curves being processed are flat in the horizontal plane and as such are valid for fitting. Any slant in the baseline of the curve can have a serious impact on the ability of the program to determine the point of contact between probe and sample and can negate the reliability of the modulus extracted. If the initial flattening does not completely rectify any slope in the non-contact region of the curve a manual line-subtraction can be performed in order to make the data sufficient for fitting. The program then scans across the approach curve left to right (non-contact regime to contact regime) until a sufficient change in the gradient of the curve is observed (from flat to inclined). This point is defined as the point of contact and is

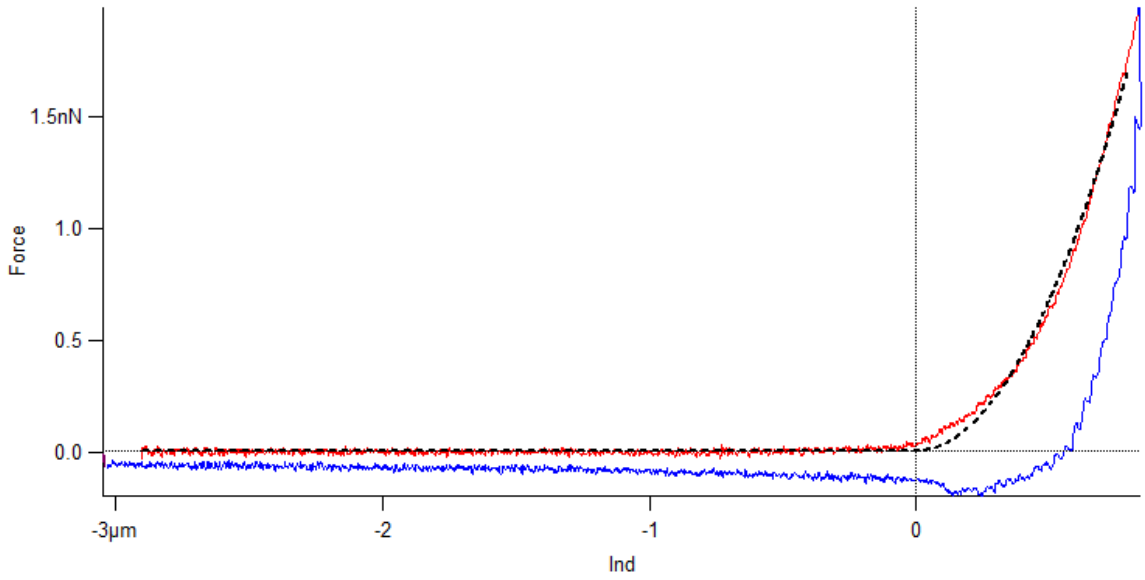

Fig. 2.16 A typical force-indentation curve taken on a HeLa cell. The Hertz model fit is depicted by the dotted line.

offset to zero (Albon, 2015). A typical force-indentation curve taken on a HeLa cell with a spherical indenter is displayed in *Figure 2.16*. Once the fit is complete, a modulus is returned as the main result. For a conical indenter this represents the Young modulus of the cell and for a spherical indenter the returned value is the reduced modulus. In the latter case, the elastic modulus of the cell is computed by the software by substitution into *Equation 2.13*. These values are then extracted into GraphPad Prism for further analysis. Throughout this thesis, the Hertz model was used exclusively for elasticity measurement due to a relatively low adhesive strength between probe and sample surface.

Chapter 3

Characterisation of Fibronectin Binding with Proteoglycans and Proteins

3.1 Introduction and Rationale

Interactions between cellular receptors and components of the ECM have significant effects on biological and intracellular processes, from would repair and healing to the stimulation of proliferation and differentiation (Rosso et al., 2004). As such, the study of binding and dissociation energetics between ligand-receptor complexes has become a popular area of biophysical research and many techniques have been developed in efforts to probe the interaction between such molecules including DSMFS (Carvalho and Santos, 2012). This technique has previously been successful in the characterisation of ligand-receptor binding and has been used to probe protein-carbohydrate interactions, including those between ECM proteins and GAGs (Li et al., 2003; Mitchell et al., 2007; Zhang et al., 2004b). Advantages of DSMFS studies of ligand-receptor unbinding when compared to other techniques, such as surface plasmon resonance, are in its ability to identify and characterise individual energy barriers contributing to dissociation events where the unbinding process may be governed by overcoming multiple barriers (Evans and Ritchie, 1997). Furthermore, single-molecule

studies provide some indication of the behaviour and deformability of the interaction under mechanical forces which, in systems such as cell attachment to ECM components, may give insights into cellular dynamics *in vivo* (Li et al., 2003; Mitchell et al., 2007; Zhang et al., 2004b).

The main focus of this chapter is in characterising the binding between FN and PGs which act as central regulators of a number of receptor systems. This study includes SDC4, a cell surface HSPG, and DCN, a CSPG prevalent in the ECM alongside transmembrane protein $\alpha_5\beta_1$ for comparison. SDC4 was chosen specifically due to its significantly high homology in both structure and function with TILRR and (with current unavailability of a recombinant molecular TILRR variant due to synthesis complexity and high cost) may therefore provide a reasonable estimation of the properties of the TILRR-FN bond. Furthermore, while the measurements in *Chapter 5* and *Chapter 6* were conducted on HeLa cells which utilise TILRR effects through transfection, the large number of receptors on the HeLa cell surface, the relatively low concentration of TILRR on the membrane and the large number of biomolecules that readily bind FN with high affinity likely negate the possibility of extracting TILRR-FN binding energetics using this approach (Pankov and Yamada, 2002). Structurally, both SDC4 and TILRR are cell surface HSPGs and are thought to bind with their ligands exclusively through their exposed HS GAG chains (Vallés et al., 1999). The only significant difference between the two HSPGs is the small intracellular component in SDC4 which interacts with the actin cytoskeleton and is completely unrelated to the ligand binding functionality of the protein (Elfenbein and Simons, 2013). This intracellular region is absent in TILRR (Zhang et al., 2010). Functionally these cell surface HSPGs both act as co-receptors, SDC4 to FGFR and TILRR to IL-1RI, and have similar regulatory effects on signalling (Smith et al., 2017; Zhang et al., 2012, 2010). Additionally both SDC4 and TILRR are prevalent at focal adhesions where they bind FN in the ECM (Couchman and Woods, 1999; Jang et al., 2012).

DMSFS measurements were conducted on DCN-FN unbinding (using the same experimental set-up as for SDC4; see *Section 3.2*) in order to compare HSPG and CSPG binding with FN (for the comparison of binding energetics between different GAG containing PGs and FN) and also on $\alpha_5\beta_1$-FN unbinding to compare PG-FN interactions with protein-FN interactions. DCN is a FN (and collagen) binding CSPG prevalent in the ECM which regulates matrix organisation and, like TGF-βR3, modulates the activity of TGF-β in a similar context as TILRR and SDC4 regulate IL-1RI and FGFR respectively (Ferdous et al., 2007; Jahanyar et al., 2007; Kolb et al., 2001; Li et al., 2006; Schönherr et al., 1995). $\alpha_5\beta_1$, a transmembrane protein dimer, binds with FN at focal adhesions and directly mediates cell adhesion (Zhang et al., 1995a). It is regarded as the primary FN receptor and therefore provides an excellent comparison to GAG mediated PG-FN binding with a direct protein-protein interaction involved in cell anchorage (Schwartz, 1997). Schematic diagrams of the interaction of FN with each protein, with relevant binding sites indicated, in the context of single-molecule measurements conducted throughout this chapter can be found in *Figure 3.1*.

By observing single-molecule unbinding events using the AFM, the average rupture force of the ligand-receptor complex can be quantified at the average loading rate of the bond-cantilever system (Evans and Ritchie, 1997). The loading rate is determined by the combined stiffness of the cantilever, polymeric linking tethers, the bound complex itself and the substrate alongside the probe retraction velocity. By varying the retraction speed, average forces at different loading rates can be obtained. It has been shown that, for each energy barrier involved in unbinding, the average rupture force between ligand-receptor unbinding increases linearly with the natural-logarithm of the loading rate (Evans and Ritchie, 1997). By linear fitting of the Bell-Evans model in *Equation 2.8*, the width of the energy barrier can be extracted from the gradient and the equilibrium dissociation rate (under no loading) can then be extracted from the y-intercept. The barrier width is indicative of the compliance of the ligand-receptor bond and its resilience to external stress (Liphardt et al., 2001; Mitchell

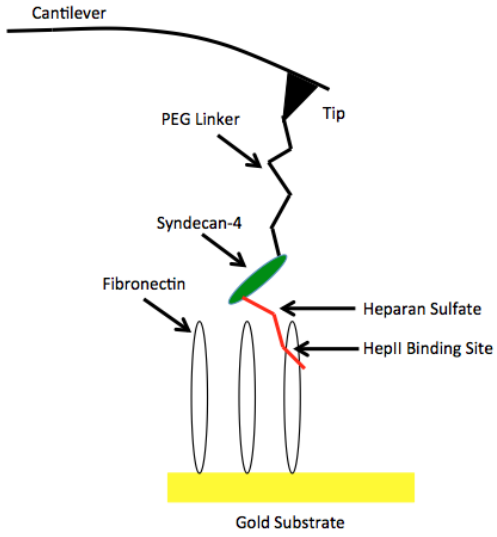

(a) SDC4-FN

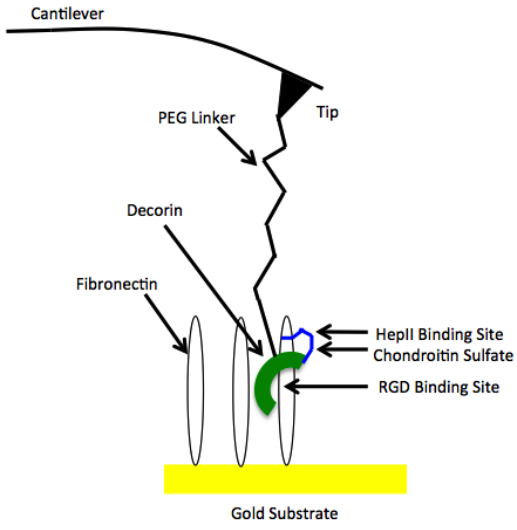

(b) DCN-FN

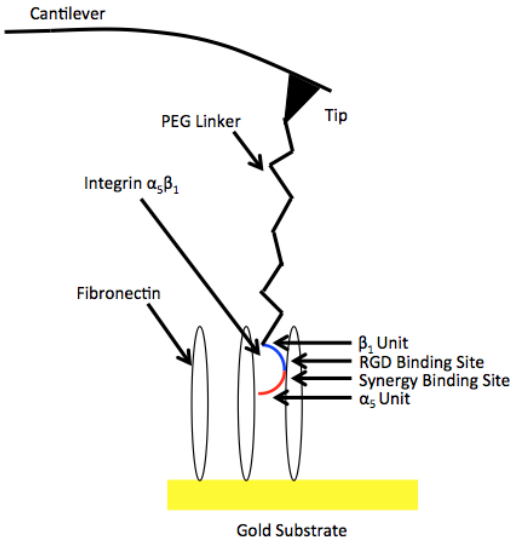

(c) $\alpha_5\beta_1$-FN

Fig. 3.1 Schematic diagrams of the binding interactions of SDC4 (a), DCN (b) and $\alpha_5\beta_1$ (c) with FN. Important units and binding sites are indicated. SDC4 is binds FN at the HepII binding site through its HS GAG chain. Decorin may interact with FN through its core protein at the RGD site or its CS GAG at the HepII site and both possibilities have been indicated. $\alpha_5\beta_1$ interacts with FN at the RGD site via its β_1 subunit and at the synergy site via its α_5 subunit.

et al., 2007). Higher barrier widths characterise bonds which are elastically deformable while reduced ones indicate brittle bonds which can withstand mechanical forces (Bustanji et al., 2002). The equilibrium dissociation rate inversely represents the bond lifetime and is suggestive of the strength of binding (Kühner et al., 2004; Ray et al., 2007). Typically biological receptors and ligands are described by dissociation rates between 0.01 s^{-1} and 10 s^{-1} (Thoumine et al., 2000). Additionally, the thermodynamic energy of adhesion is contained within the equilibrium dissociation rate. It can be extracted from the Arrhenius relation, *Equation 2.25*, or directly from the Bell-Evans fit, *Equation 2.26*, and is dependent on a pre-factor representing the molecular vibration frequency (Ray et al., 2007; Yang and Gruebele, 2003).

3.2 Surface Modification

In order to conduct DSMFS measurements between ligand-receptor pairs it is necessary to chemically modify both the probe and the substrate to exhibit each biomolecule. In these experiments purified SDC4, DCN and $\alpha_5\beta_1$ were covalently linked to AFM probes while FN was immobilised on the substrate. This geometry was selected as studies have have suggested that isolated FN molecules may be conformationally denatured and less stable, with more heterogeneity in adhesive interactions, than their aggregated counterparts and also that repeated mechanical measurements may act to irreversibly deform and destabilise the protein (Meadows et al., 2003; Meadows and Walker, 2005). This set-up allows for the measurement of unbinding events between different FN molecules and the probe-bound proteins at different locations on the substrate, therefore increasing the probability of observing ligand-receptor rupture.

3.2.1 Chemical Functionalisation of Probes

Probes were functionalisied using the chemical modification process outlined in *Section 2.5.3* which has been specifically designed to exhibit low densities of protein on MLCT probes to yield individual unbinding events in measurements. Furthermore, each step of the protocol utilises fairly standard and accepted chemical modification processes and as such the validity of the method is robust. It relies upon the use of small concentrations of reagent throughout to introduce low quantities of saline groups with APTES, small quantities of PEG linking regions using NHS-PEG-Mal and small quantities of protein. It was necessary to determine sufficient quantities of reagent to observe single molecule events. High concentrations yield a large number of events and dramatically reduce the probability of obtaining force-curves which exhibit single specific rupture peaks, or even from which specific peaks can be identified. A concentration too low results in the absence of functional proteins on the tip and no specific events in resulting force curves.

The dependence of rupture event frequency on reagent concentration was tested by functionalising MLCT cantilevers with SDC4 in concentrations of 2 μg·ml^{-1} and 10 μg·ml^{-1} SDC4 in PBS at room temperature for 2 hours. 1,000 force-curves were taken on a FN-functionalised surface for each and the number of both single and double specific rupture events in each curve were counted. No dwell-time on the surface was applied in these measurements and all curves were taken at retraction speeds of 1 μm·s^{-1} and at 10 different locations on the FN surface. It was found that cantilevers modified with 10 μg·ml^{-1} SDC4 solution exhibited $\backsim$ 400 single events and $\backsim$ 100 double events while those functionalised in a 2 μg·ml^{-1} SDC4 solution exhibited $\backsim$ 200 single events and $\backsim$ 40 double events. This implied a larger number of SDC4 molecules grafted onto the tip region of the probe. It has previously been stated that in order to be $\backsim$90% certain that discrete rupture events correspond to the specific unbinding of a single ligand-receptor complex, less than 30% of force-curves should yield events (Franz et al., 2007). Collectively, this implied that a concentration of 2 μg·ml^{-1} SDC4 in PBS was sufficient for DSMFS measurements and this concentration was selected for all further probe modification processes throughout this chapter. Furthermore, tips modified with 10 μg·ml^{-1} SDC4 exhibited a significant number of double events. This is not ideal when trying to characterise single unbinding events as the association of multiple complexes can impact the extracted rupture force and effective spring constant values (Getfert and Reimann, 2012). Furthermore, the presence of multiple peaks can complicate event identification as they can appear similar to unfolding processes (Schonfelder et al., 2016). Probes modified with 2 μg·ml^{-1} SDC4 exhibited significantly less of these double peaks. The concentrations of all reagents used for tip functionalisation are provided in *Table 3.1*.

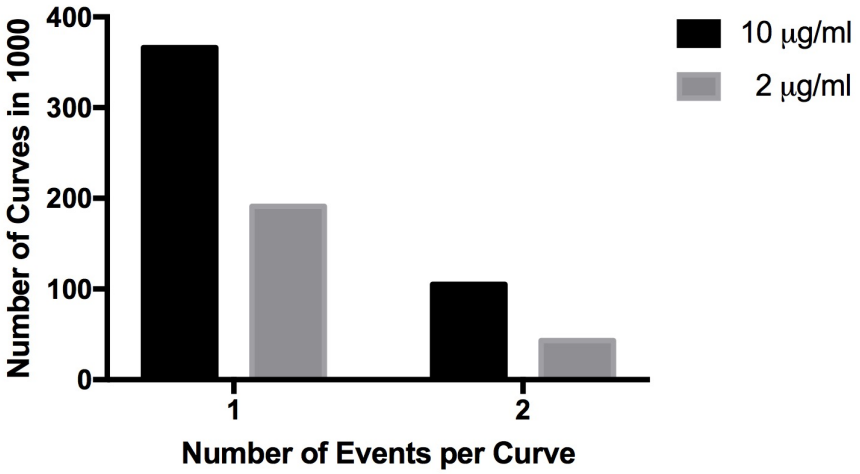

Fig. 3.2 The number of measured events in 1,000 curves taken between a FN surface and a MLCT tip-C probe functionalised with SDC4 in 10 μg·ml^{-1} and a 2 μg·ml^{-1} solutions for 2 hours. The higher concentration yields a significant increase in both single and double specific rupture events observed.

Table 3.1 Quantities of each reagent used for the covalent grafting of protein receptors to MLCT AFM probes. *Piranha solution was made by addition of hydrogen peroxide to concentrated sulphuric acid at a ratio of 3:7.

Reagent	Solvent	Concentration	Time
Piranha*	-	-	30 minutes
APTES	Toluene	3 μl·ml^{-1}	2 hours
NHS-PEG-Mal	Water	0.5 mg·ml^{-1}	2 hours
Protein	PBS	2 μg·ml^{-1}	2 hours

3.2.2 Surface Immobilisation of FN

A biologically functional FN surface (such that it interacts with other biomolecules) was achieved by means of SAM adsorption on a gold-coated AFM disk (see *Section 2.5.3*). As previously mentioned, the surface density of FN has been shown to affect its conformation which has been linked to an ability to bind receptors (Hull et al., 2007). At low surface densities, isolated FN molecules are denatured and binding sites may be conformationally impeded (Meadows et al., 2003). It has also been suggested that irregularity in conformations may result from multiple irreversible bonds between the FN and the substrate (Meadows and Walker, 2005). It seems that the presence of neighbouring molecules in aggregates stabilises FN structure and permits binding, possibly through protective shielding of interactive domains from adhesion with the substrate (Grinnell and Feld, 1981). This was indicated by Meadows and Walker (2005) in the promoted deposition of cells on aggregated FN surfaces when compared with partially covered substrates. To ensure successful unbinding measurements between SDC4, DCN and $\alpha_5\beta_1$ with FN, a solution concentration of 20 μg·ml^{-1} FN in PBS was selected and was applied to the gold surface overnight at 4 °C to ensure a complete coating. A uniform substrate coverage of FN is preferable for single-molecule force measurements as it is not possible to optically target proteins. This concentration is consistent with other studies in which binding sites in FN, such as the RGD peptide, have been shown to be functional (Ballestrem and Müller, 2015; Li et al., 2003; Meadows et al., 2003; Meadows and Walker, 2005). A complete surface coating was verified using tapping mode AFM in a liquid PBS environment with an unmodified probe. Phase images of uncoated gold substrates alongside SAMs of adsorbed FN are depicted in *Figure 3.3*. There is a clear difference in surface morphology between uncoated and FN immobilised surfaces. Furthermore, it is deduced that the surfaces exhibiting FN aggregation display a complete and somewhat uniformly distributed coverage of protein. Additionally, recombinant FN molecules appear in a regular, globular morphology of expected size ($\backsim$ 20 nm radius;

Hull et al., 2007). This corresponds well with previously imaged FN coated surfaces by Kulik et al. (2015) and verifies successful protein immobilisation for force measurements. Tests conducted between SDC4-FN, DCN-FN and $\alpha_5\beta_1$-FN revealed characteristic sawtooth ligand-receptor unbinding events (see *Figure 3.4*) indicating the availability of both HepII and RGD binding domains.

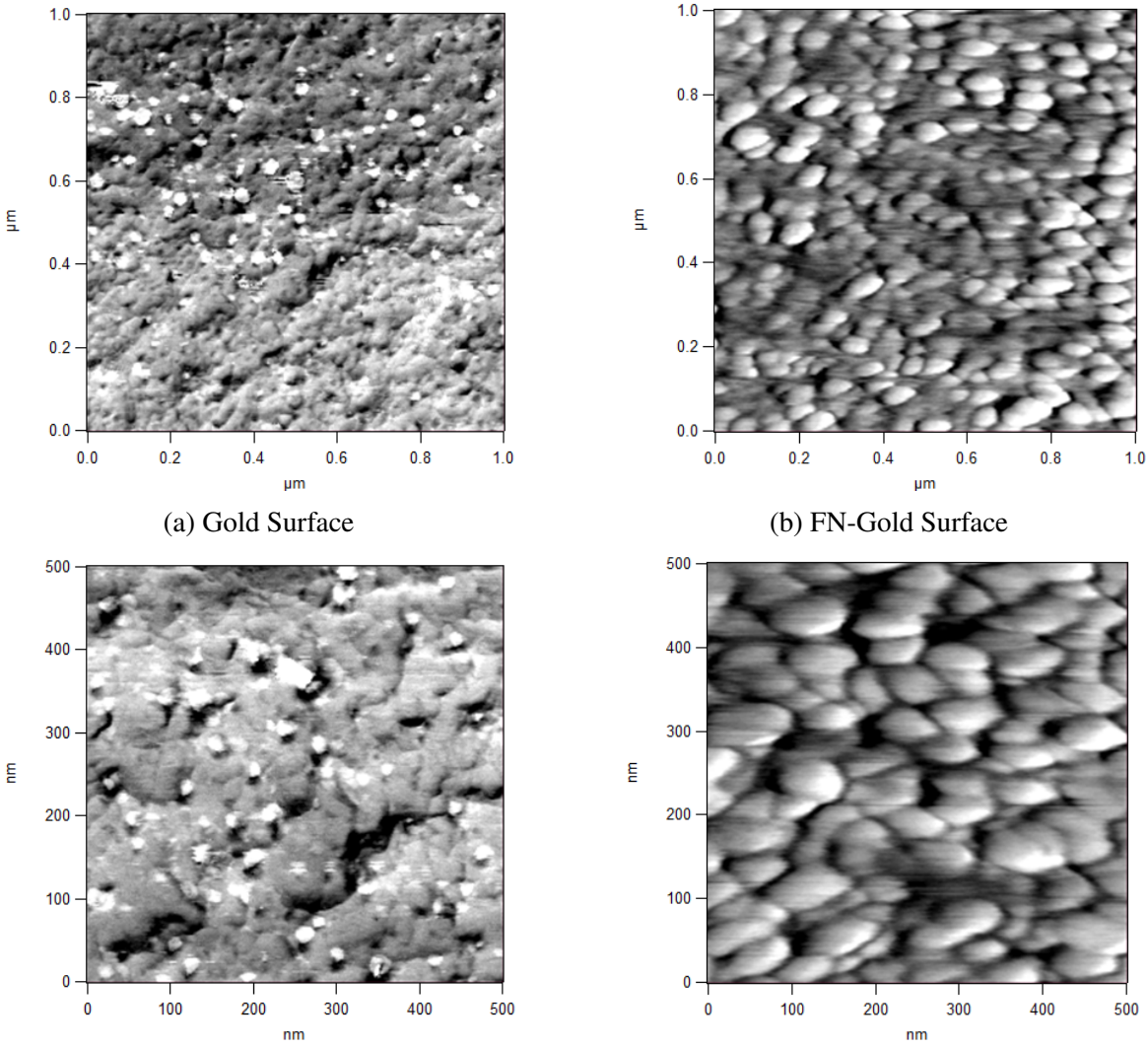

(a) Gold Surface

(b) FN-Gold Surface

(c) Gold Surface

(d) FN-Gold Surface

Fig. 3.3 Phase images of a gold substrate prior to (a, c) and following (b, c) immobilisation of FN taken with tapping-mode AFM in PBS. A clear difference in surface topography can be observed between the untreated gold and FN-coated surfaces. SAMs of FN was observed to be adsorbed onto gold uniformly, completely coating the surface with a relatively even distribution. Furthermore, recombinant FN was observed to be characteristically globular with an expected radius of $\backsim$20 nm.

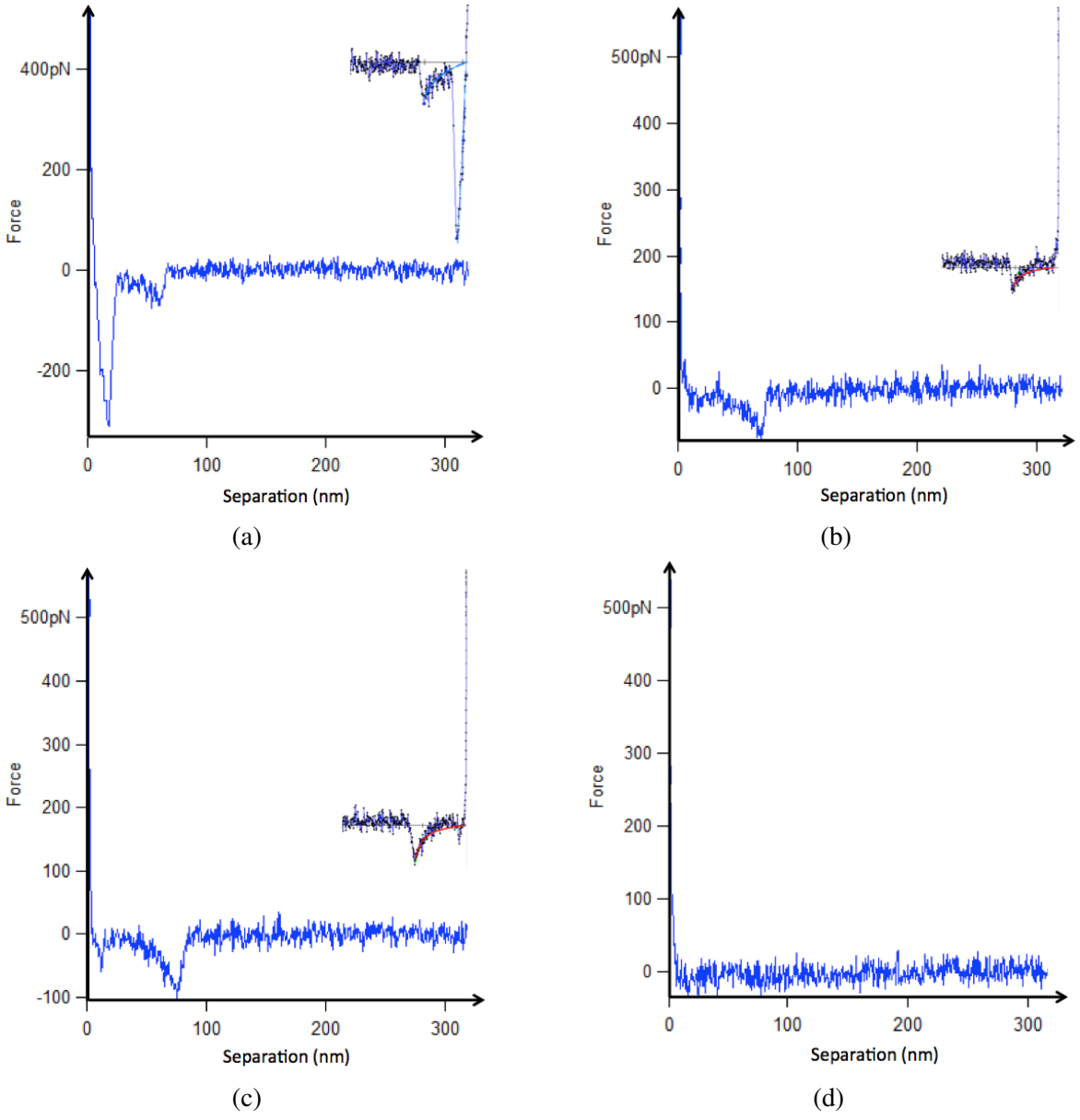

Fig. 3.4 Representative retraction force-curves exhibiting single-molecule unbinding events between a SDC4 functionalised probe and a FN immobilised surface (a, b, c) with corresponding WLC fits (top-right corner of each). These curves demonstrate variation in rupture-forces observed for the unbinding event. The smallest of the 3 rupture events also exhibits a strong non-specific interaction between the MLCT tip and the surface demonstrating the necessity for polymeric spacing regions (a). A typical curve exhibiting no single-molecule interactions is also shown for comparison (d).

3.3 Initial Unbinding Measurements

3.3.1 Control Tests

Control tests were carried out to verify both interaction specificity and that the chemically modified probes successfully exhibited proteins at cysteine residues via PEG chains. The first test simply involved recording the number of events in 1,000 curves on a FN coated substrate and a SDC4 exhibiting probe in a liquid environment of PBS. This surface was then replaced with an unmodified gold substrate (onto which no FN was adsorbed) which was immersed in new PBS and a further 1,000 curves were taken. Single-molecule events characterised in the measurements between the SDC4 probe and the FN surface were not observed on an uncoated gold substrate indicating that the rupture events are a product of the functionalised probe and FN. A second set of control tests were conducted to verify the HS-HepII binding interaction. 1,000 curves were taken with a SDC4 exhibiting probe and a FN-gold surface in PBS as normal. Following acquisition, the substrate was removed from the AFM and the surface was coated with a HS solution in PBS at a saturated concentration of 1 $mg{\cdot}ml^{-1}$ for 30 minutes. This results in the effective removal of Hep binding sites on the immobilised FN surface due to their interaction with free HS chains. Excess HS was then gently washed off the substrate with PBS and a further 1,000 curves were taken, again in a PBS environment. It should be noted that the same probe was used for both sets of curves which was stored in PBS during the 30 minute incubation of the FN-gold substrate in HS solution to ensure its stability and longevity. This test was conducted 3 times to determine significance and is depicted in *Figure 3.5*. The addition of free HS chains results in a reduction of $\backsim 90\%$ ($p = 0.008$) in the number of observed single unbinding curves. This strongly suggests that the measured interaction between SDC4 and FN is the expected interaction between the HS chain and the HepII binding site. This also verifies that the chosen modification set-up of the probe and surface is successful in exhibiting binding between the proteins. All

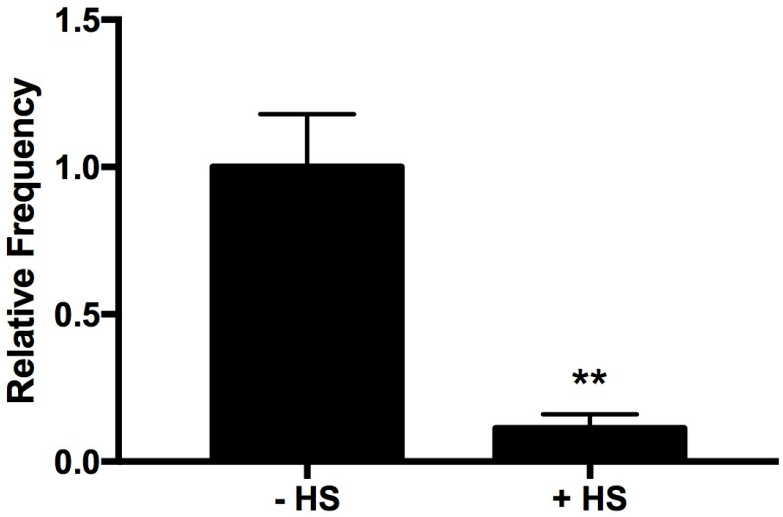

Fig. 3.5 The number of curves exhibiting single specific unbinding events observed in 1,000 for a SDC4 exhibiting probe and a FN functionalised surface followed by same surface after immersion in a 1 mg·ml^{-1} HS solution for 30 minutes. Inhibition of the HepII binding sites on FN due to binding of free HS results in a dramatic reduction of unbinding events verifying the specificity of the interaction. Significance determined using paired t-tests (**$0.001 < p < 0.01$) for $n = 3$.

control tests were conducted at a retraction speed of 1 μm·s^{-1} with a trigger of 500 pN and exhibited a dwell-time of 200 ms on the surface to enhance the probability of ligand-receptor binding. Longer dwell-times were not selected as FN molecules have been shown to exhibit significant binding to SI_3N_4 cantilevers at dwells of 1 s and over (Sumarokova et al., 2018). At shorter dwells and low trigger forces this phenomenon is infrequent and does not need to be considered further. All control tests were also conducted at 10 different regions on the FN coated substrate (the position changed every 100 curves up to 1,000 curves) to ensure that measurements were not taken on unfunctionalised or adversely affected regions.

3.3.2 Preliminary Force Measurements

Preliminary force measurements between probes covalently grafted with SDC4 and FN immobilised on gold were conducted using ForceRobot® 300 AFM systems at Nanjing University. MLCT probes were functionalised using the protocol outlined in *Table 3.1* and

all measurements were conducted in PBS at room temperature. Frequency distributions describing the force of unbinding between specific SDC4-FN bonds are depicted in *Figure 3.6*. These preliminary distributions are predominantly negatively skewed log-normal in shape. The tail spanning over higher unbinding forces may result from non-linear stretching of polymeric tethers (Ray et al., 2007). The distributions exhibit a clear widening as the retraction velocity, and by extension the loading rate, is increased which is characteristic of ligand-receptor unbinding by DSMFS (Evans and Ritchie, 1997). This results in an increasing modal average which can be determined by fitting Gaussian or log-Gaussian curves to the distributions. *Figure 3.6d* depicts the measured rupture force against the contour length, extracted through WLC model fitting, of a SDC4-FN unbinding experiment conducted in preliminary measurements at Nanjing University (*Nanjing, China*). The contour length is the total length from tip-surface contact to unbinding including the length of the rupture slope and describes the length of the polymeric linking region (Tong et al., 2017). The single-molecule unbinding events showed a clear dominance of contour length at $\backsim$ 30 nm to $\backsim$ 40 nm across all forces which corresponds well with the PEG linking lengths used throughout these preliminary measurements, between $\backsim$ 30 nm and $\backsim$ 50 nm. Any slight reductions in the trend from the expected value may be caused by reductions in PEG length by water induced structure changes (Kreuzer et al., 1999; Tong et al., 2017). This coherence provides further confidence in the set-up of these force-pulling measurements as it implies that the binding between tip-and surface is located at the terminus of the PEG linking region (where the SDC4 protein is grafted). It should be noted that rupture forces determined in preliminary measurements using the ForceRobot® 300 were not included in the dynamic force spectra for extraction of interaction energetics in order to limit errors induced through the use of two AFM systems, each with their own mechanisms of operation. Additionally, data taken with each AFM is outputted in differing formats and requires analysis using different software platforms which may induce further errors.

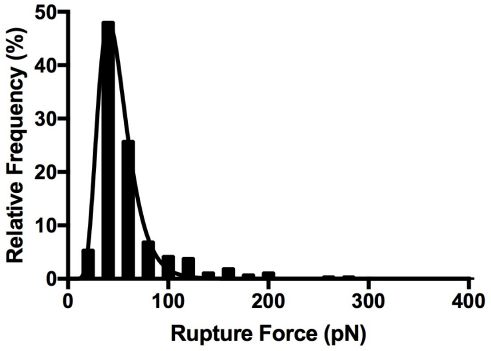

(a) SDC4-FN unbinding with an average rupture force of 41 $\pm$ 1 pN.

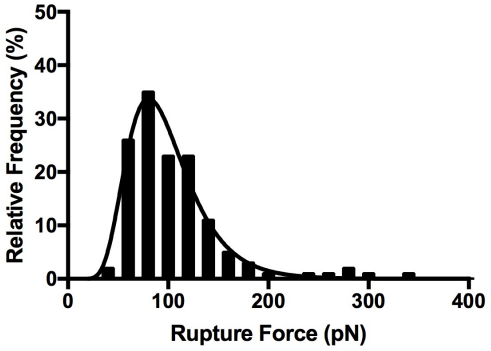

(b) SDC4-FN unbinding with an average rupture force of 81 $\pm$ 2 pN.

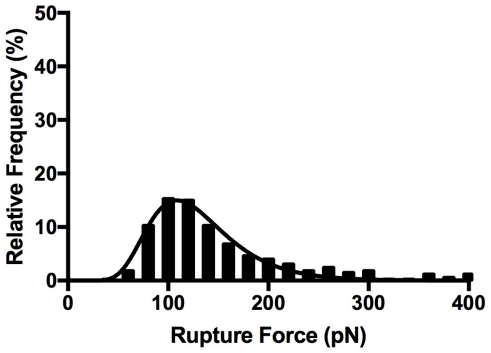

(c) SDC4-FN unbinding with an average rupture force of 109 $\pm$ 3 pN.

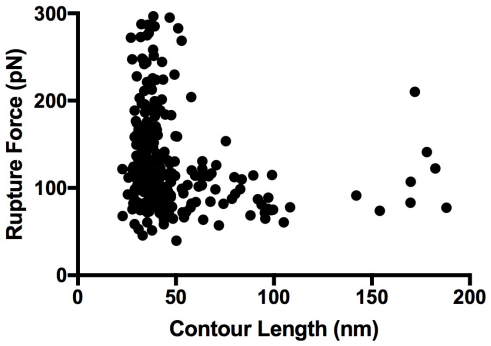

(d) Extracted rupture force against corresponding contour length for SDC4-FN unbinding.

Fig. 3.6 Frequency distributions describing the measured rupture force between SDC4 and FN at increasing retraction velocities of 0.4 μm·s^{-1} (a), 1.0 μm·s^{-1} (b) and 5.0 μm·s^{-1} (c). The distribution broadens with increasing retraction speed and averages determined from displayed log-Gaussian fits are indicated alongside the SE of the fit. The observed rupture force against extracted contour length from WLC fits for an experimental run at 5.0 μm·s^{-1} suggests a reproducibility of unbinding length-scales and is in agreement with the PEG linking length used in preliminary measurements (d).

3.4 Curve Analysis

3.4.1 Extraction of Rupture Force and Loading Rate

Curves exhibiting desired single-molecule events were first analysed using the MATLAB® code provided in *Appendix A* and described in *Section 2.6.1*. Analysis of a selected force-curve is illustrated in *Figure 3.7a*. Following several unsuccessful analysis attempts using this method it became clear that, while adequate when extracting the magnitude of rupture forces, this process was not accurate enough to estimate the effective spring constant of the bound complex, polymeric linker and cantilever system which resulted in poorly defined loading rates and the inability to reveal dynamic force spectra. This problem arises from the difficulty in approximating the slope of the rupture peak by eye using two cursors and the significant change in the extracted gradient that any off-centred cursor clicks caused. This was compounded further when applied to non-linear peaks and when considering the peak-to-peak noise of extracted AFM data (the fluctuation thickness of the curve) which somewhat varied with retraction speed up to $\backsim$ 20 pN. It has been reported that the effective spring constant should be defined as the the linear slope as applied to the final third of the non-linear peak but even this is difficult to approximate by eye (Franz et al., 2007). It was clear from these issues that a more effective method of loading rate characterisation was necessary reveal any meaningful energetics of the interaction. PUNIAS was utilised to provide the necessary accuracy in extracting the effective spring constant by means of fitting the WLC model (see *Section 2.6.1*). The WLC fit applied to the same selected force-curve is displayed in *Figure 3.7b*. From these fits it was possible to extract average values of the effective spring constant with confidence which can then be converted into the loading rate by multiplication with the retraction velocity *Equation 2.21*. It should be noted that when generating histograms of extracted rupture fore for each retraction velocity, the bin-width should not fall below the peak-to-peak noise as to ensure a true average can be revealed (particularly at high pulling

velocities) but should also remain as small as possible for accuracy. For these reasons a bin-width of 20 pN was selected.

3.4.2 Correction for Hydrodynamic Drag

When conducting DSMFS to quantify the binding interaction between ligands and receptors in a liquid environment it is crucial to correct for the effect of hydrodynamic drag on the cantilever as the extracted average of the rupture force can vary in ranges as small as several pN between loading rates. The hydrodynamic effect originates from the viscosity of the liquid medium in which the force measurements are taken. As the probe is moved through this environment, forces opposing the direction of the motion are imparted on the cantilever. The magnitude of these forces are governed by the size, shape and velocity of the cantilever alongside the viscosity of the fluid. Physically, this results in a constant slight deflection of the cantilever in the non-contact region of the force-curve and in the direction of the hydrodynamic force. When analysing unbinding curves, the effect of this force causes an underestimation of the rupture force due to the cantilever failing to return to zero deflection following dissociation and is more pronounced at higher retraction velocities (Franz et al., 2007). The hydrodynamic effect is illustrated in *Figure 3.8a* and *Figure 3.8b*. It is necessary to correct for these drag forces at all pulling velocities at 1 μm·s^{-1} and over to uncover a true dynamic force spectra (Li et al., 2003).

The hydrodynamic effect manifests itself in force curves as a vertical separation between the approach and retraction curves in the non-contact region. This is caused by a positive shift in the deflection on approach and an equivalent negative shift in deflection on retraction caused by the equal but opposing hydrodynamic force in each regime. The total separation between the approach and retract curve in pN is then

$$\Delta F_{\text{baseline}} = 2F_{\text{hydro}}, \tag{3.1}$$

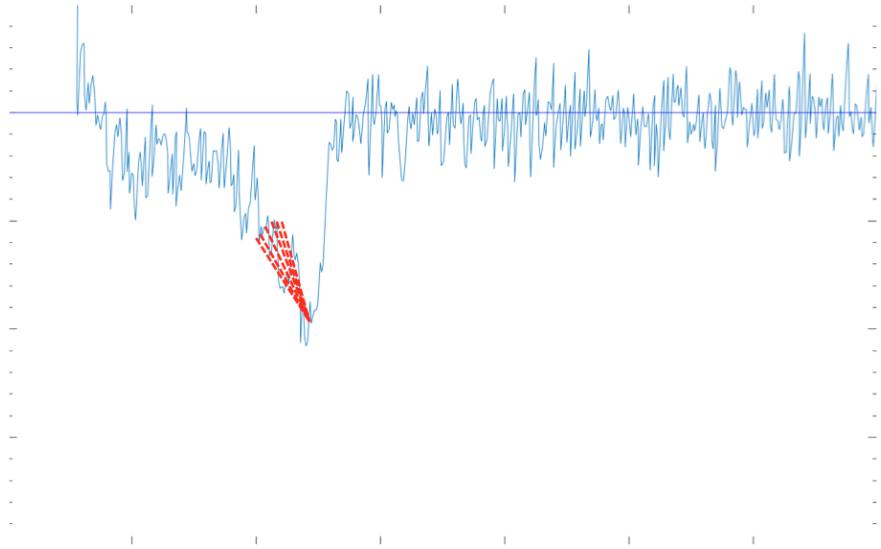

(a) MATLAB®

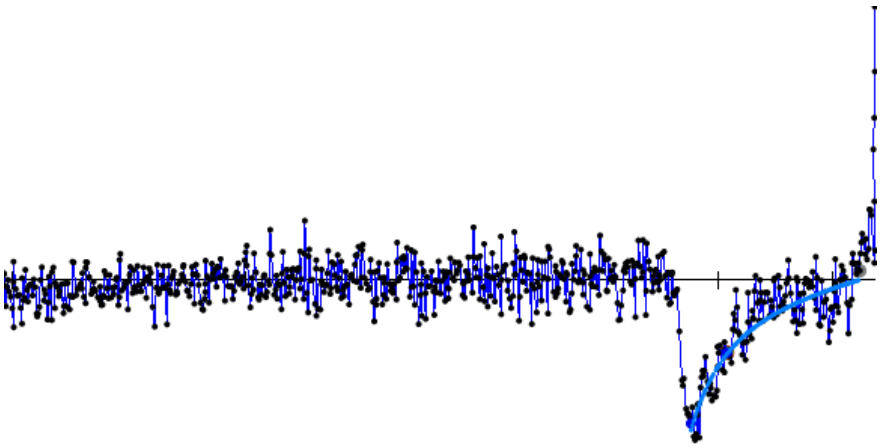

(b) PUNIAS

Fig. 3.7 Analysis of unbinding events for the extraction of rupture forces and loading rates (a, b). The MATLAB® analysis is displayed alongside red dotted-lines which illustrate difficulties in manual extraction of the effective spring constant (a). The PUNIAS analysis is depicted alongside a blue curve which represents the WLC fit (b).

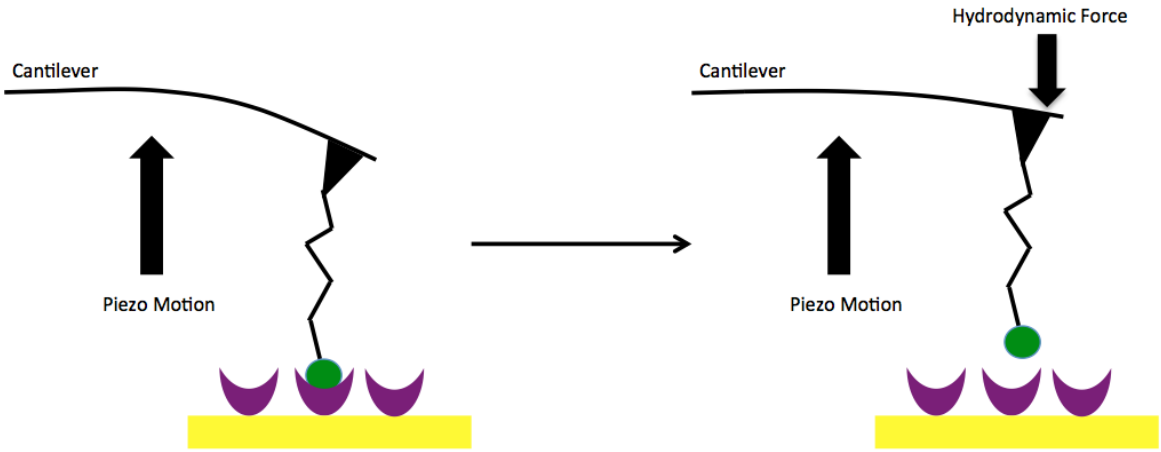

(a)

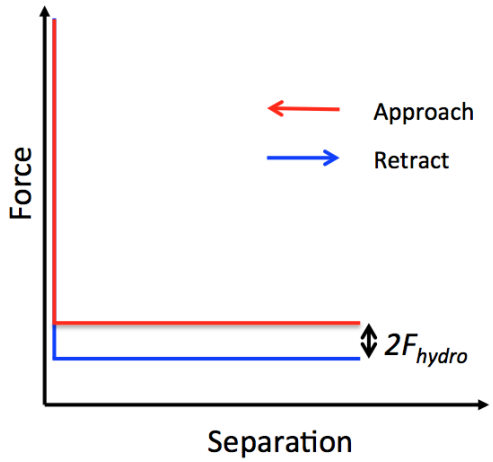

(b)

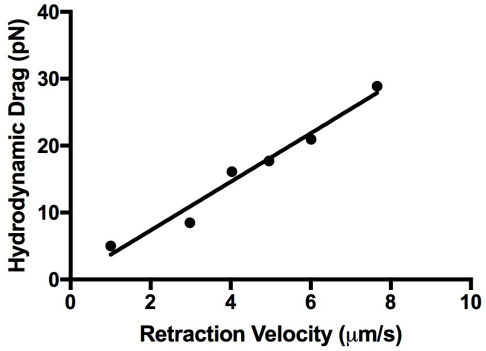

(c)

Fig. 3.8 Schematic diagrams depicting the measured underestimation of the true rupture force by force-spectroscopy in liquid environments caused by hydrodynamic drag (a). The effect of hydrodynamic drag is revealed in force-separation curves as a spacing in the deflection or force axis between the extend and retraction curves (b). Acquisition of force curves in a range of retraction speeds for a cantilever in a liquid environment reveals the resulting drag forces at each (c). The gradient of this linear fit reveals the coefficient of hydrodynamic drag which can be applied as a correction factor to extracted forces. The fit for this cantilever reveals a drag coefficient of 3.6 pN·s·μm^{-1} with a correlation factor of $R^2 = 0.9693$.

where F_{hydro} is the magnitude of the hydrodynamic force at a given pulling velocity. By acquisition of force-curves at a variety of retraction speeds and measurement of the hydrodynamic force at each of these speeds, the hydrodynamic coefficient can be deduced for each cantilever as the gradient of the linear fit for observed hydrodynamic force against retraction velocity. This is depicted in *Figure 3.8c*. The hydrodynamic correction can then be applied to each observed rupture force by multiplying the hydrodynamic coefficient by the retraction speed and adding this constant onto the force. Forces extracted from DSMFS measurements typically report using a hydrodynamic correction coefficient of $\backsim 2$ pN·s·μm^{-1} for the 310 μm $\times$ 20 μm MLCT tip-C cantilevers (with a measured spring constant of $k = 18 \pm 2$ pN·nm^{-1} here) in water and water-based buffer environments (Li et al., 2003; Mitchell et al., 2007; Wojcikiewicz et al., 2006).

3.5 Dynamic Force Spectra

3.5.1 Dynamic Unbinding of Syndecan-4 and Fibronectin

Force pulling between a SDC4 exhibiting probe and a FN SAM surface were conducted over a range of loading rates between $\backsim$ 900 pN·s^{-1} and $\backsim$ 65,000 pN·s^{-1}. The dynamic force spectrum describing the unbinding is illustrated in *Figure 3.9*. The energetic landscape in this range is governed by single energy barrier and, when fitted with the Bell-Evans model in *Equation 2.8*, is described by a linear regression of

$$F = (12.2 \pm 0.6)\ln(r) - (42 \pm 6), \tag{3.2}$$

with a correlation factor of $R^2 = 0.9844$.

3.5.2 Dynamic Unbinding of Decorin and Fibronectin

Force pulling at retraction speeds between a DCN exhibiting probe and a FN SAM surface were conducted over a range of loading rates between $\backsim$ 3,000 pN·s^{-1} and $\backsim$ 45,000 pN·s^{-1}. The dynamic force spectrum describing the unbinding is illustrated in *Figure 3.10*. The energetic landscape in this range is governed by single energy barrier and, when fitted with the Bell-Evans model in *Equation 2.8*, is described by a linear regression of

$$F = (30.4 \pm 1.6)\ln(r) - (215 \pm 15), \tag{3.3}$$

with a correlation factor of $R^2 = 0.9841$.

3.5.3 Dynamic Unbinding of Integrin $\alpha_5\beta_1$ and Fibronectin

Force pulling at retraction speeds between an $\alpha_5\beta_1$ exhibiting probe and a FN SAM surface were conducted over a range of loading rates between $\backsim$500 pN·s^{-1} and $\backsim$90,000 pN·s^{-1}.

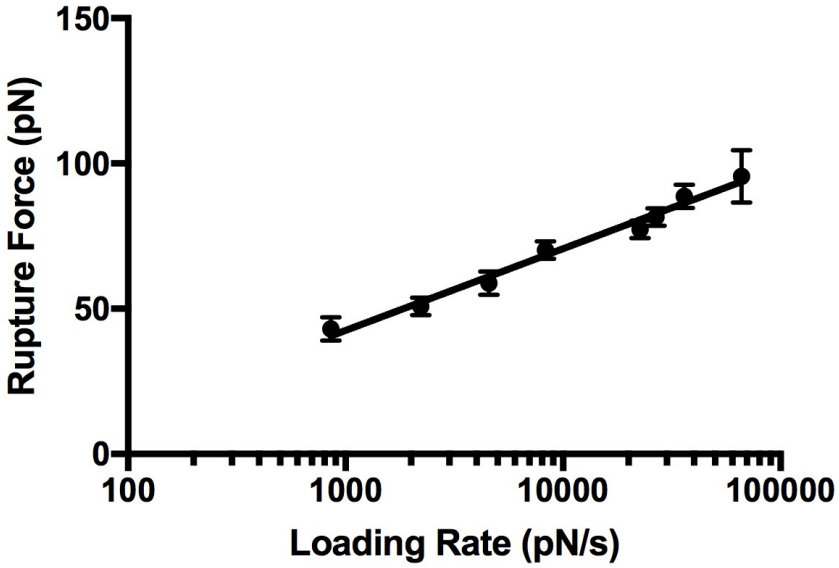

Fig. 3.9 The dynamic force spectrum describing the unbinding between SDC4 and FN. The linear increase between average rupture force and the natural logarithm of the average loading rate for each pulling velocity, fitted using the Bell-Evans relation (*Equation 2.8*), is shown. Included errors correspond to the width of the 95% confidence interval of Gaussian fits from which average rupture forces were extracted.

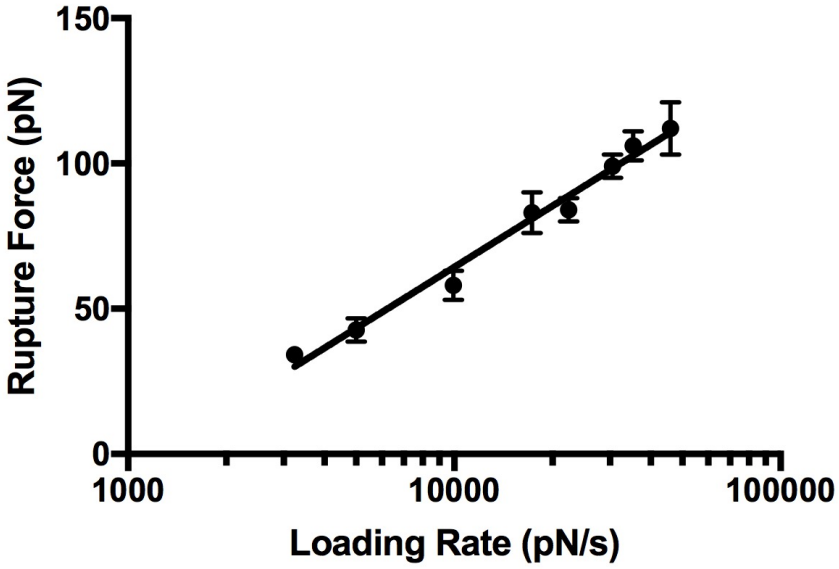

Fig. 3.10 The dynamic force spectrum describing the unbinding between DCN and FN. The linear increase between average rupture force and the natural logarithm of the average loading rate for each pulling velocity, fitted using the Bell-Evans relation (*Equation 2.8*), is shown. Included errors correspond to the width of the 95% confidence interval of Gaussian fits from which average rupture forces were extracted.

The dynamic force spectrum describing the unbinding is illustrated in *Figure 3.11*. The energetic landscape in this range is governed by two energy barriers. When fitted with the Bell-Evans model in *Equation 2.8*, the inner barrier is described by a linear regression of

$$F = (60 \pm 3)\ln(r) - (500 \pm 30), \tag{3.4}$$

with a correlation factor of $R^2 = 0.9935$. The outer barrier is described by a linear regression of

$$F = (6.2 \pm 0.6)\ln(r) - (1 \pm 4), \tag{3.5}$$

with a correlation factor of $R^2 = 0.9712$.

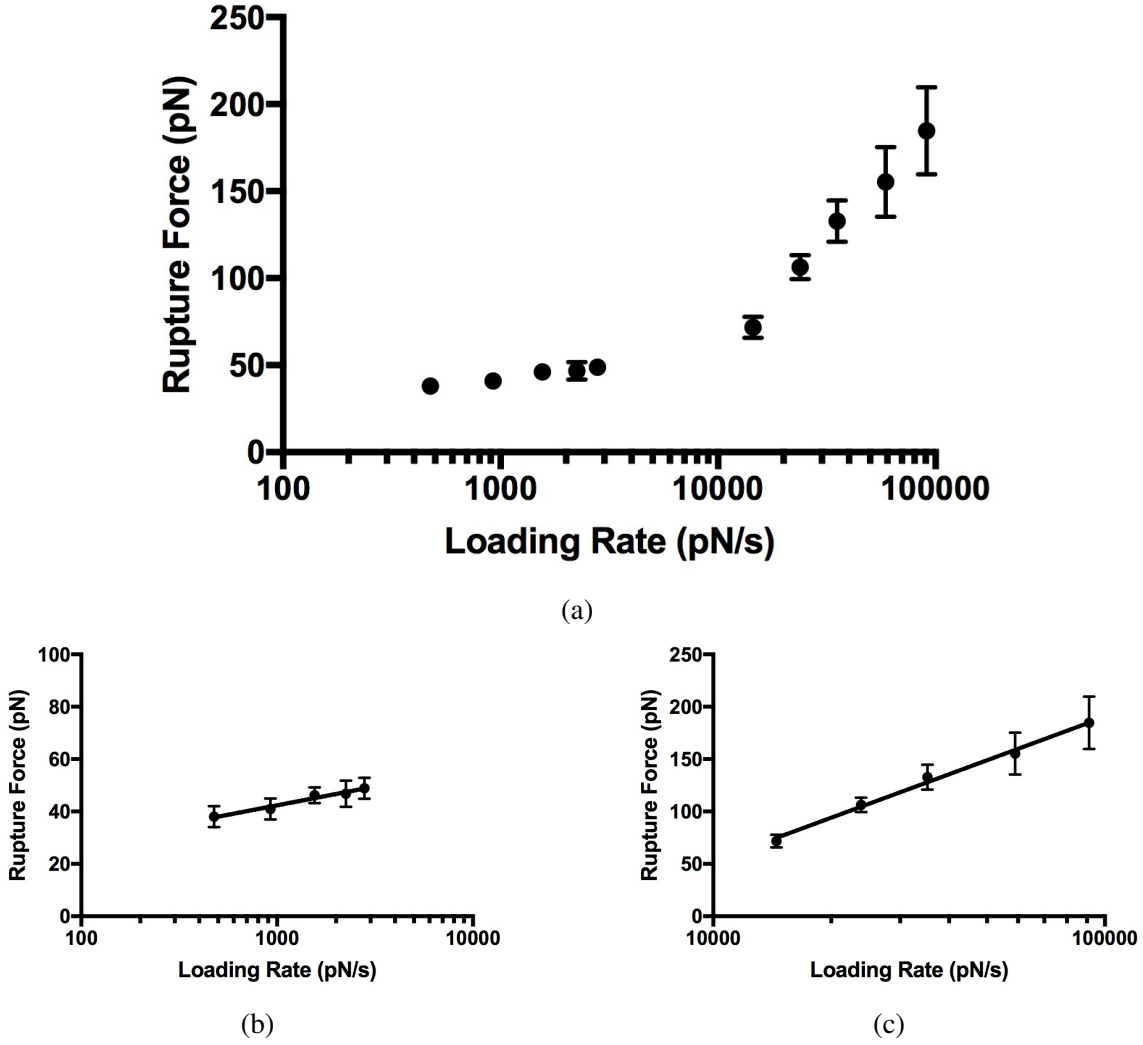

Fig. 3.11 The dynamic force spectrum describing the unbinding between $\alpha_5\beta_1$ and FN which reveals two distinct energy barriers (a). The linear increase between average rupture force and the natural logarithm of average loading rate for each for each pulling velocity, fitting using the Bell-Evans relation (*Equation 2.8*), is shown for the outer (a) and inner (b) barriers. Included errors correspond to the width of the 95% confidence interval of Gaussian fits from which average rupture forces were extracted.

Table 3.2 Extracted energetics for each energy barrier revealed in the dynamic spectra for SDC4-FN, DCN-FN and $\alpha_5\beta_1$-FN unbinding.

Interaction	χ_B (Å)	k_{off}^0 (s^{-1})	$\Delta G(k_BT)^{-1}$
SDC4-FN	3.4 ± 0.2	2.4 ± 0.4	15.2 ± 0.2
DCN-FN	1.4 ± 0.1	40 ± 4	12.4 ± 0.1
$\alpha_5\beta_1$-FN (inner)	0.69 ± 0.03	70 ± 40	11.9 ± 0.6
$\alpha_5\beta_1$-FN (outer)	6.6 ± 0.7	0.18 ± 0.13	17.8 ± 0.7

3.6 Extraction of Binding Energetics from Dynamic Force Spectra

From the linear Bell-Evans fits for each energy barrier revealed in the dynamic force spectra depicted in *Figure 3.9*, *Figure 3.10* and *Figure 3.11*, energetic properties characterising the binding interactions can be extracted. The width of each energy barrier can be extracted directly from the gradient of the linear fit using *Equation 2.23*. The equilibrium dissociation rate describing each barrier can be extracted from the y-intercept of the linear fit from *Equation 2.24*. By incorporation of the Arrhenius relation (*Equation 2.25*), an estimate of the thermodynamic energy of adhesion can be extracted from the equilibrium dissociation rate directly or from the Bell-Evans fit by substitution (*Equation 2.26*). This is dependent on a frequency factor that describes the molecular vibration. It has been reported that, for large or complex proteins, this factor can be approximated as $f_m \approx 10^{-7}$ s^{-1} (Lapidus et al., 2000; Ray et al., 2007; Yang and Gruebele, 2003). This value is likely to describe the resultant complex formed in FN-receptor binding due to both its size and domain structures. $f_m \approx 10^{-7}$ s^{-1} was consequently used for the binding energy estimates for all barriers observed in this study. The energetics characterising each barrier for SDC4-FN, DCN-FN and $\alpha_5\beta_1$-Fn unbinding are summarised in *Table 3.2*.

3.7 Discussion

The binding energetics of SDC4, DCN and $\alpha_5\beta_1$ with FN were successfully probed using DSMFS. Comparison between control tests utilising a SDC4 exhibiting probe and a FN-coated surface followed by a FN surface immersed in free HS for 30 minutes showed a clear reduction by $\backsim 90\%$ in event frequency due to the masking of heparin binding sites in FN molecules by HS ($p = 0.008$). This specificity test verified that the unbinding events observed in force-curves resulted from HS chains in SDC4 and the heparin binding sites in FN. Despite FN containing three heparin binding sites, it has been reported that the high-affinity HepII domain is the primary site (Barkalow and Schwarzbauer, 1991; Benecky et al., 1988). Single-molecule studies between Hep and FN have previously indicated the dominance of the HepII binding domain and this is supported here with no apparent rupture peaks corresponding to secondary binding sites being observed (Mitchell et al., 2007). As such, the dynamic force spectra extracted from unbinding measurements between SDC4 and FN revealed only a single energy barrier. This is consistent with previous studies investigating the binding between Hep and FN conducted by Mitchell et al. (2007). Furthermore the width of the energy barrier probed in this chapter is only $\backsim 10\%$ larger (and falls within the range of associated errors) than the width of 3.1 ± 0.1 Å reported in the aforementioned Hep study. This suggests a similar bond compliance in both HS-FN binding and Hep-FN binding indicating the bond formed between HSPGs and extracellular FN is somewhat resilient to mechanical stress and deformation. Combined, these results verify numerous studies that have indicated that HSPGs bind FN exclusively through the GAG chain and that the core protein has no role in binding (Vallés et al., 1999). Furthermore, these studies may indicate that the binding interaction of HS with the HepII binding domain of FN, and perhaps with other similar ligands, may be described by similar barrier widths (and by extension a similar compliance of the bound complex) for all HSPGs and are comparable to that of the Hep-FN interaction.

Comparison of the equilibrium dissociation rate extracted for the SDC4-FN interaction in this study reveals a $\backsim$ 12-fold increase when compared with that reported for the Hep-FN complex by Mitchell et al. (2007) suggesting a somewhat weaker interaction between SDC4 and FN than for Hep with FN. This is logical as HS chains contain significantly fewer sulphated domains than that of Hep, the biomolecule containing the highest negative charge density currently characterised (Weiss et al., 2017). This contradicts the statement by Mitchell et al. (2007) that the binding affinity for all HSPGs can described by the Hep-FN interaction. Instead, each HSPG may bind to the HepII domain of FN with varying affinity, which is likely to be related to the location and density of the GAG sulphated domains on each particular HSPG. This may suggest that the binding between HSPGs and ligands may be specifically modulated by deliberate patterning of the GAG chains (Garg et al., 2003; Nagamine et al., 2012). Using the SDC-FN interaction to characterise the TILRR-FN interaction may therefore provide a useful estimation (due to the significant similarity between SDC4 and TILRR which underpinned the rational in the experimental design). It is likely that the width of the energy barrier is similar to that revealed for both the SDC4-FN and Hep-FN interaction. The dissociation rate, and by extension the thermodynamic energy of adhesion, is however less easy to approximate. It is likely to be larger than the 0.2 ± 0.1 s^{-1} estimated for the Hep-FN interaction and may be more comparable to 2.4 ± 0.4 s^{-1} as determined for SDC4 (Mitchell et al., 2007). It should be noted that both the width of the barrier and the dissociation rate extracted from the dynamic force spectra for the SDC-FN interaction are comparable to values reported for other protein-carbohydrate interactions which further supports the validity of these results (Dettmann et al., 2000; Evans et al., 2001).

The single energy barrier revealed in the dynamic force spectrum for the DCN-FN interaction implies a much smaller barrier width and a much larger dissociation rate than those extracted from the SDC4-FN interaction. These suggest that the observed bond formed between DCN and FN in this study is much more brittle, with less deformability, than

that measured for HSPG SDC4 with FN. These values also indicate a significantly smaller strength of binding between this CSPG and FN than that resulting from the association of HS chains to the HepII binding site. It has previously been suggested that, while binding between CS and HepII occurs, it is not as strong as as the Hep-HepII interaction (Barkalow and Schwarzbauer, 1994). However, it has also been suggested that HS and CS GAGs are likely to compete for binding which implies that, even if CS-HepII binds with slightly lower affinity, the properties of HS-FN and CS-FN interactions may be comparable (Clark, 2013; Minguell et al., 1992; Schwarzbauer and DeSimone, 2011; Wasylnka and Moore, 2000). Instead, the interaction measured here may correspond to the binding of the DCN core protein to the RGD site in FN. This interaction has been suggested in many publications and has been supported by many experimental studies (Bidanset et al., 1992; Ferdous et al., 2010; Schmidt et al., 1991; Trowbridge and Gallo, 2002). In fact, the energetics extracted for this interaction may be more characteristic of binding events between proteins (particularly that of an ionic internal energy barrier) than protein-GAG dissociation when compared with vales extracted for HS-FN unbinding here and previous DSMFS studies in the literature (Hanley et al., 2003; Li et al., 2003; Mitchell et al., 2007; Panorchan et al., 2005; Zhang et al., 2004b). Furthermore, previous studies of DCN-FN binding and DCN-collagen binding (which likely occurs via similar mechanisms) using more conventional techniques have reported nM dissociation constants which are significantly stronger than that inferred by the equilibrium dissociation rate extracted from the single barrier uncovered in this study (Schmidt et al., 1991; Schönherr et al., 1995). Addiationally, these studies have also indicated that binding occurs via the DCN core protein and that the CS chains may form bonds with adjacent matrix components to aid in ECM structure. Consideration of these reports may infer the presence an outer energy barrier at relatively low loading rates ($< 3,000$ pNs^{-1}) and low external forces (< 30 pN) which is easily suppressed, allowing the bond to exhibit a brittle nature (as revealed in this study). When considering the structural role of DCN in the

ECM, it seems logical that the bond formed with other matrix components has the capacity to remain resilient to substantial external forces. Similarly, it is also possible that additional energy barriers are present outside the range of loading rates probed in this study which better characterise GAG-protein unbinding. The role of DCN-FN as a PG comparison with the SDC4-FN interaction in this work indicates that PGs have the capacity to form bonds of a variable character and via various different mechanisms with relevant biomolecules. Comparison of the significant differences between these two barriers also supports the validity of the set-up as the only major difference between each was the covalent protein-grafting step of the tip-modification process.

Two energy barriers characterising the unbinding of $\alpha_5\beta_1$ and FN have been identified in this study. This is consistent with previous studies of $\alpha_5\beta_1$-FN unbinding by Li et al. (2003) which utilised cellular expression of the integrin as opposed to isolated PEG-linked molecules in this work, and also with other studies of integrins wth ECM components (Boye et al., 2013; Zhang et al., 2004b). Increasing loading rates result in a suppression of the outer barrier and reveal the internal binding regime. This is characterised by a steep barrier of small, sub-angstrom width suggesting a brittle bond which is highly resistant to external forces. It is not uncommon to report subatomic internal barrier widths for ligand-receptor dissociation (Boye et al., 2013; Bustanji et al., 2002; Li et al., 2003; Tees et al., 2001; Wojcikiewicz et al., 2006). Previous studies on the binding of of the integrin β_1 subunit with ECM proteins by Zhang et al. (2004b) have suggested that this barrier is representative of the ionic interaction between the RGD domain in cell-binding matrix components and the chelated Mg^{2+} ion in the β_1 MIDAS (see *Figure 1.14*). The outer barrier governs the unbinding at lower loading rates (and lower forces) and is characterised by a wide width which implies that the bond in this regime can withstand significant deformation. It has previously been suggested that, for molecules with adhesive functionality, the dependence of the energy landscape on two

barriers may be a common property as modulation of their magnitudes may allow for varied response to differing external mechanical force (Bizzarri and Cannistraro, 2012).

The extracted dissociation rate for the outer barrier suggests a relatively high affinity bond between $\alpha_5\beta_1$ and FN which is consistent with the cell attachment function of integrin-ECM binding and also with previous studies which investigated native $\alpha_5\beta_1$ (Li et al., 2003). In these studies, wild-type $\alpha_5\beta_1$ was compared with $\alpha_5\beta_1$ activated with antibody TS2/16. Activation results in the change in conformation of the β_1 subunit and permits higher affinity binding with ligands (Calderwood, 2004). Further DSMFS studies investigating the binding characteristics of other integrins with their respective ligands ($\alpha_4\beta_1$ with vascular adhesion molecule 1 in this case), reported that recombinant integrin variants exhibit the binding characteristics of the high affinity state and it was suggested that the receptors were exhibiting a shape resembling the activated conformer (Zhang et al., 2004b). Additionally, these results may infer that recombinant integrin complexes are free to assume a variety of different conformations when unhindered by the cell membrane and can interact with ligands with maximal efficiency. In contrast to these reports, the binding kinetics reported in this study for the recombinant, PEG-linked $\alpha_5\beta_1$ variant (particularly the equilibrium dissociation rate of the outer barrier), when compared with those reported for wild-type $\alpha_5\beta_1$-FN unbinding by (Li et al., 2003), indicate that the lower affinity interaction has been observed here. This may infer that $\alpha_5\beta_1$ requires interaction with cellular components (likely with the cytoskeleton) to induce structural stability in the receptor complex and allow it to bind with extracellular FN most efficiently. It should be noted that both the dissociation rates and the width of each barrier extracted in this work are comparable to other integrin-ECM studies (Li et al., 2003; Masson-Gadias et al., 1999; Zhang et al., 2004b). The energy landscape for both wild-type and activated, native $\alpha_5\beta_1$-FN unbinding is indicated in *Figure 3.12*. The estimated thermodynamic energy of adhesion for the outer barrier is in agreement with the value of $\backsim 17.3\ k_{\mathrm{B}}T$ which was extracted from equilibrium affinity

constants acquired in surface plasmon resonance measurements for inactivated $\alpha_5\beta_1$ by Takagi et al. (2001). This correlation further supports the notion that these measurements obtained with recombinant $\alpha_5\beta_1$ are representative of its lower affinity binding with FN and also adds a significant degree of confidence to the validity of the extracted dynamic spectrum. In actuality the external binding regime is likely to consist of a combination of both barriers, where the external barrier is elevated via an intermediate state between the inner and outer transitions (see *Figure 3.12*). Comparison of the thermodynamic energy of adhesion as measured for both the inner and outer barriers suggests a $\backsim 6\ k_{\mathrm{B}}T$ step following the escape from the internal barrier and represents the actual height of the external regime from the intermediate state.

The characterisation of the energy barriers involved in recombinant $\alpha_5\beta_1$-FN dissociation offers excellent comparison and positive control for the unbinding energetics between PGs SDC4 and DCN with FN which have been measured throughout this study. The characterisation of two separate barriers for the $\alpha_5\beta_1$-FN interaction, as supported by literature, compared with the single barriers revealed for the PG-FN interactions at a similar range of loading rates suggests significant difference in the binding properties between protein-FN and PG-FN unbinding and additionally supports the validity of the experimental set-up (Li et al., 2003). Furthermore the significant strength of binding between the cell adhesion-mediating $\alpha_5\beta_1$ with FN offers excellent context to the energetics extracted from PG-FN unbinding, particularly when considering the identical experimental design. The bond formed between HS chains in SDC4 with FN and DCN with FN are of significantly lower affinity than those formed by the $\alpha_5\beta_1$ complex with FN. Furthermore, by inclusion of multiple energy barriers in the dissociation mechanism and modulation of the outer regime, bound $\alpha_5\beta_1$-FN can sustain both much greater deformation and is resilient to much greater external forces.

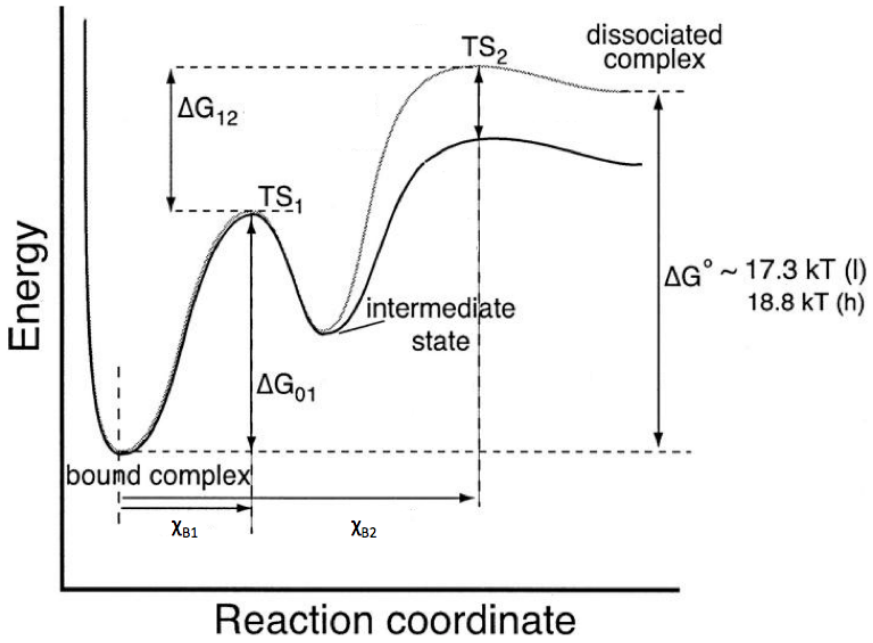

Fig. 3.12 The energetic landscape of $\alpha_5\beta_1$ unbinding with FN for low (l) and high (h) affinity complexes. Two clear barriers are depicted in order to reach transition states (TSs) TS_1 and TS_2 and the location of the widths from equilibrium and energetic height for each are indicated. Equilibrium free energies (G^0), estimated from, Takagi et al. (2001), are indicated for each affinity complex. Adapted with permission from the Biophysical Journal, 84/2, Li et al., Force measurements of the $\alpha_5\beta_1$ integrin-fibronectin interaction, 1252-1262, Copyright (2003) Elsevier.

3.8 Summary and Conclusion

To conclude, the dynamic force spectra for the unbinding of FN (immobilised on gold substrates) with SDC4, DCN and $\alpha_5\beta_1$ (recombinant and chemically grafted onto AFM probes via PEG-linkers) have been identified. Single energy barriers were uncovered for both SDC4-FN and DCN-FN unbinding while two were found to participate in the dissociation of $\alpha_5\beta_1$ with FN. These are consistent with previous dynamic force studies on Hep-FN unbinding and cellular $\alpha_5\beta_1$-FN unbinding (Li et al., 2003; Mitchell et al., 2007). Using the Bell-Evans model, descriptive energetics of dissociation were extracted directly from the dynamic force spectrum characterising each energy barrier.

SDC4 dissociation with FN was characterised by a barrier width of 3.4 ± 0.2 Å and a dissociation rate of 2.4 ± 0.4 s^{-1} which yields an estimated thermodynamic energy of adhesion of 15.2 ± 0.2 k_BT. These values suggest binding between the HS GAG chain in SDC4 and the HepII binding site in FN results in a bond of moderate strength which exhibits both a capacity to exhibit deformation and a resilience to external mechanical stress. These properties are comparable to other measured ligand-carbohydrate bonds, including those between cellular and ECM components (Dettmann et al., 2000; Evans et al., 2001; Mitchell et al., 2007). The barrier width is also very similar to that of the measured Hep-FN interaction while the affinity seems somewhat lower. This may indicate that all HSPG-FN interactions are comparable in terms of bond compliance but vary in binding energy, most likely with the density of sulphation along the chain. These parameters may then be used to approximate the barrier width and, with limitation, the off-rate of other HSPGs such as TILRR.

The DCN-FN interaction was found to be characterised by 1.4 ± 0.1 Å and 40 ± 4 s^{-1} which permits the estimation of the thermodynamic energy of adhesion as 12.4 ± 0.1 k_BT. Based on these properties the binding interaction was deemed to be of relatively low affinity, distinctly lower than those observed between cell-surface receptors or HSPGs with ECM

components, and was deemed to be brittle with little capacity for deformation. These values also imply a much weaker strength of binding between DCN and FN than has been reported for DCN and ECM components in previous studies (Schmidt et al., 1991; Schönherr et al., 1995). Considering these points, it is reasonable to suggest that the interaction described by this barrier was between the DCN core protein and not the CS GAG chain and that the equilibrium dissociation rate (and therefore binding affinity) is governed by an external barrier present at lower loading rates than those investigated in this study.

The interaction between $\alpha_5\beta_1$ and FN is characterised by an internal and external energy barrier, the latter of which is suppressed at higher loading rates. The internal barrier can be described by a barrier width of 0.69 ± 0.03 Å and a dissociation rate of 70 ± 40 s^{-1} which allows for an estimated thermodynamic energy of adhesion of $11.9 \pm 0.6\ k_B T$. This corresponds to internal energy barriers observed for other integrin interactions with ECM proteins which reportedly result from the ionic binding between the Mg^{2+} ion in the β_1 subunit MIDAS and the RGD peptide (Zhang et al., 2004b). The external energy barrier is characterised by a barrier width of 6.6 ± 0.7 Å and a dissociation rate of 0.18 ± 0.13 s^{-1} which allows for the estimation of the thermodynamic energy of adhesion as $17.8 \pm 0.7\ k_B T$. These correspond well with estimates of the binding affinity extracted from surface plasmon resonance (Li et al., 2003; Takagi et al., 2001). Together, these two energy barriers allow the binding between $\alpha_5\beta_1$ and FN to sustain both significant deformation and large external forces depending on the loading regime of the external stress. This likely results in the ability of $\alpha_5\beta_1$ to initiate and sustain significant adhesion of the cell to the ECM, even under testing conditions such as high flow rates.

It should be noted that both the SDC4 and $\alpha_5\beta_1$ (under low loading) bonds formed with FN exhibit a relatively elastic character. These molecules primarily function by interacting with extracellular FN at focal adhesion sites and it is possible that the bonds capacity for withstanding deformation may be a necessary characteristic, perhaps by allowing bonds to

remain long enough to induce or potentiate signalling while under motion. In contrast, the brittle nature of the DCN-FN interaction (under relatively low loading) alongside the high loading regime of the $\alpha_5\beta_1$-FN bond may be be a necessary characteristic of structural and attachment molecules, allowing the organisation of the biological system or tissue to remain resilient to external stresses.

Chapter 4

Optimisation of Biological Techniques for Force Measurements on HeLa Cells

4.1 Introduction

This chapter focuses on the use of biological methods to optimise cell treatment for force measurements using the AFM in *Chapter 5* and *Chapter 6*. In these chapters stimulation with IL-1β and transfection with TILRR cDNA are utilised to exhibit inflammatory responses and cytoskeletal effects in HeLa cells. Optimal doses of IL-1β and TILRR cDNA were determined using luciferase assays (with the IL-8 promoter as a read-out) which measure the inflammatory activity of NF-κB. Furthermore, GFP plasmid concentration for sufficient transfection efficiency was determined using fluorescence microscopy. This allowed for the identification of cells successfully transfected with TILRR cDNA or EV for AFM-based force measurements.

4.2 Luciferase Assays

4.2.1 Dependence of Inflammatory Potency on Agonist IL-1

The dose dependence on potency of the inflammatory response due to IL-1β stimulation was deduced using luciferase assays. These gave an indication of NF-κB activity by measurement of the IL-8 promoter (through the magnitude of luminescence). This was highly effective due to NF-κB's function in controlling the up-regulation of IL-8 (Elliott et al., 2001). Luciferase assays were conducted using the method described in *Section 2.2.7*. *Figure 4.1* depicts the measured inflammatory response in HeLa cells resulting from stimulation concentrations of 10^{-15} M, 10^{-13} M, 10^{-11} M and 10^{-9} M IL-1β alongside unstimulated cells. Low concentrations of IL-1β were achieved using serial dilutions due to the requirement of small volumes of reagent.

It is clear from *Figure 4.1* that a stimulation concentrations of 10^{-15} M had little effect on inflammatory potency when compared with unstimulated cells. 10^{-13} M IL-1β seemed to illicit a relatively small increased response in comparison to control cultures. Cells in the presence of 10^{-11} M IL-1β displayed a clear $\backsim$ 7 fold increase in inflammatory activity when compared with control cultures. Furthermore cells stimulated with 10^{-9} M IL-1β exhibited a dramatic $\backsim$ 17 fold increase in IL-8 activity with respect to control cells and a $\backsim$ 2 fold increase when compared to those stimulated with 10^{-11} IL-1β. Many previous studies have reported that this represents a saturation point (further increase of IL-1β concentration does not result in an increase in inflammatory activity due to receptor availability and regulatory mechanisms; Fasano et al., 1991; Nichols, 2017; Smith et al., 2017; Vallés et al., 1999; Zhang et al., 2012, 2010). Therefore, for the work described in *Chapter 6* a concentration of 10^{-9} M IL-1β was selected to yield the largest possible response in cell cultures.

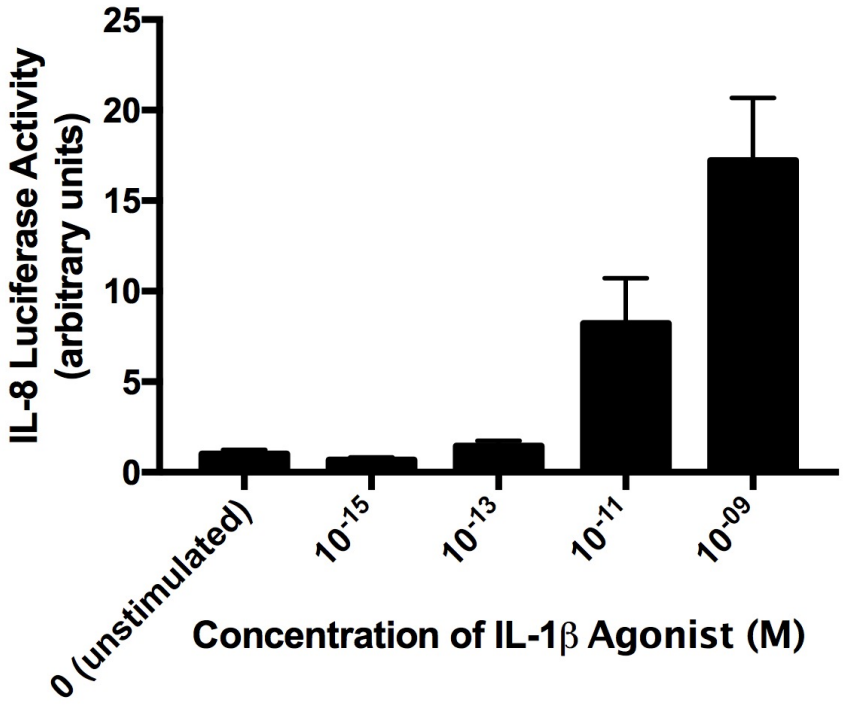

Fig. 4.1 A luciferase assay which depicts the dose dependence of IL-1β (in the range of 10^{-15} M to 10^{-9} M) on NF-κB activity alongside unstimulated HeLa cells. Only very small concentrations of IL-1β are required to observe a large inflammatory response due to the exponential nature of its signalling cascade. It is clear to see that a concentration of 10^{-15} M IL-1β is not sufficient to induce any increase in activity. 10^{-13} M IL-1β seems to induce a small increased response, 10^{-11} M IL-1β induces a relatively strong response and a large response is observed under 10^{-9} M IL-1β. Bars represent the triplicate mean $\pm$ SEM for a single experimental run and are presented relative to unstimulated control cultures.

4.2.2 Dependence of Inflammatory Potency on TILRR Expression

The transfection quantity of TILRR cDNA for use in further experiments (in order to induce maximal expression in cells) was also determined by means of luciferase (using the IL-8 promoter as a readout). It was decided that the best concentration of TILRR cDNA would be that which induced the largest inflammatory response in a measured culture of cells. This may both be because of any TILRR mediated biological effects being more apparent in measurements on single cells at these concentrations and also due to the uptake of cDNA by a maximum amount of cells, thereby allowing a higher proportion of individual cells targeted by the AFM to be expressing elevated levels of TILRR. IL-1β stimulation at a concentration of 10^{-11} M was selected alongside TILRR transfection as it has been shown from *Figure 4.1* and from previous studies that these levels induce a moderately strong response but leave scope for the potentiating effects of TILRR on NF-κB activity when compared with measurements at saturation (Nichols, 2017).

Figure 4.2 displays the strength of NF-κB activation in response to IL-1, amplified by varying levels of TILRR expression. TILRR concentrations of 10 ng, 20 ng, 30 ng and 40 ng per well were investigated. All cultures, were made up to the same quantity of plasmid (40 ng of combined EV and TILRR cDNA [depending on the desired concentration] alongside the 75 ng of TKRL and 120 ng of IL-8 luciferase per well; see *Section 2.2.7*). It is clear that all cultures transfected with TILRR cDNA exhibit an increase in NF-κB activity measured through the IL-8 promoter. The magnitude of this activity increases with TILRR cDNA dosage up to a maximum, $\backsim$ 1.7 fold increase from control. This dose is in agreement with previously reported data by Nichols (2017) and Zhang et al. (2010). Further increase in TILRR cDNA dosage did not seem in illicit further increases in NF-κB activity. Therefore a transfection concentration of 30 ng TILRR cDNA per well was selected as an optimal dose for further experiments and is equivalent to a concentration of 5 μg per million plated cells. When scaled up to transfection in a 6 cm dish at similar confluence (with a plating density of

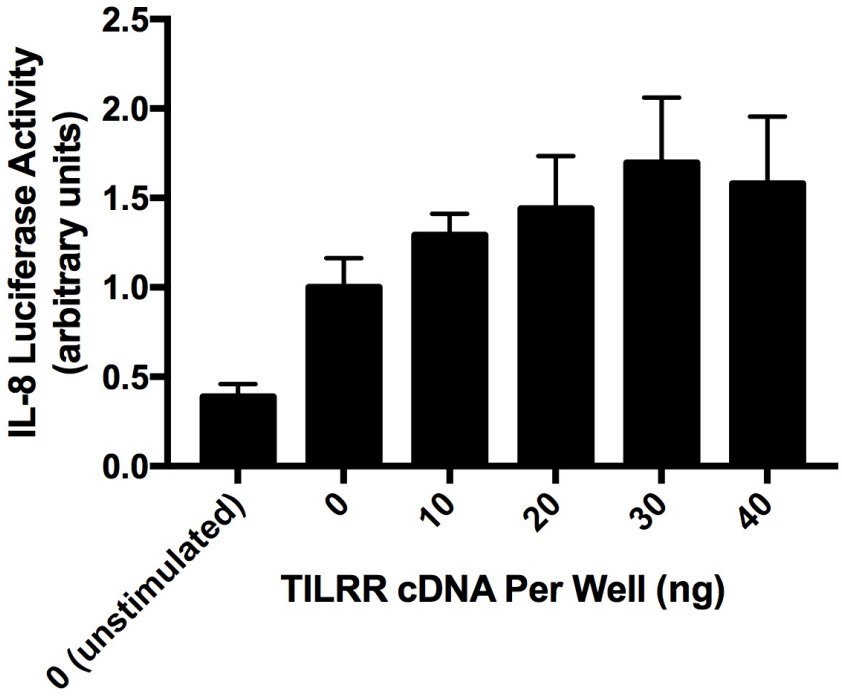

Fig. 4.2 A luciferase assay which depicts the dose dependence of TILRR cDNA (in the range of 10 ng to 40 ng alongside stimulation of 10^{-11} M IL-1β) on NF-κB activity alongside unstimulated and stimulated control cells (where both cultures were transfected with EV). All cells transfected with TILRR cDNA exhibit an increase in activity when compared with control cells. Increased dosage seems to increase activity up to a concentration of 30 ng TILRR cDNA per well. Above this no further increase is observed. Bars represent the triplicate mean $\pm$ SEM for a single experimental run and are displayed relative to cells transfected with EV.

300,000 HeLa cells per dish) for AFM measurements, this corresponds to a concentration of 1.5 μg per dish which is used throughout *Chapter 5* and *Chapter 6*. It should be noted that the same concentration of EV was used throughout *Chapter 5* and *Chapter 6* as a transfection control.

4.3 GFP Transfection Efficiency

Following initial adhesion measurements (with FN functionalised probes; see *Section 5.3*) on cells transfected with TILRR cDNA it became apparent that a method by which successfully transfected cells could be identified was necessary. This was achieved by co-transfecting EV (for transfection control) and TILRR cDNA alongside GFP containing plasmid, pEGFP-N2. Because of the way the transfection process works, it is highly likely that plasmids are delivered equivalently into the same cells (Xie et al., 2011). The inclusion of GFP allows for the identification of successfully transfected cells whilst simultaneously conducting force measurements using the fluorescence system built into the MFP. Before conducting physical measurements on cells however, it was first necessary to determine how much GFP was required to be transfected alongside TILRR cDNA and EV. This was achieved using the florescence set-up described in *Section 2.2.8*.

Figure 4.3 depicts both bright-field and corresponding fluorescence images taken of HeLa cells transfected with varying quantities of GFP (0.5 μg, 1.0 μg and 1.5 μg per dish). 25 μg of PolyFect per 6 cm dish was used in order to remain consistent with EV and TILRR cDNA transfections. It should be noted that cells were plated at a density of 300,000 cells per dish (as in *Chapter 5* and *Chapter 6*) to achieve adequate confluence on the day of transfection and $\backsim$ 80% confluence the following day for further work. Approximate GFP transfection efficiency was deduced from wide-field observations while on the florescence microscope simply as the ratio between the number of transfected cells to the total number of cells in each field. A low efficiency of $\backsim$ 10% was deduced for cells transfected with 0.5 μg GFP per dish. Furthermore, *Figure 4.3a* alongside *Figure 4.3b* suggests that the proportion of healthy cells (those exhibiting normal morphology) which have taken up GFP is negligible. HeLa cells transfected with 1.0 μg GFP per dish exhibited a much better transfection efficiency of $\backsim$ 50%. Observation of *Figure 4.3c* and *Figure 4.3d* shows that a significant number of healthy cells with typical morphology were successfully transfected. *Figure 4.3e* and *Figure*

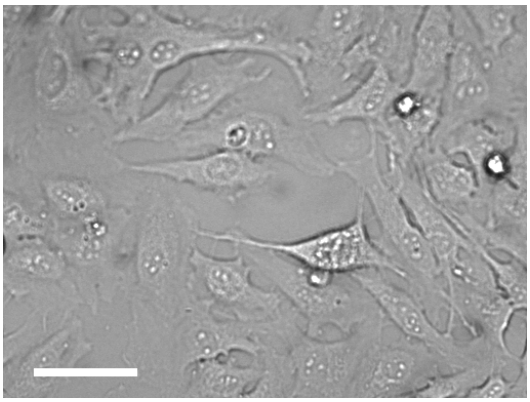

(a) 0.5 μg GFP

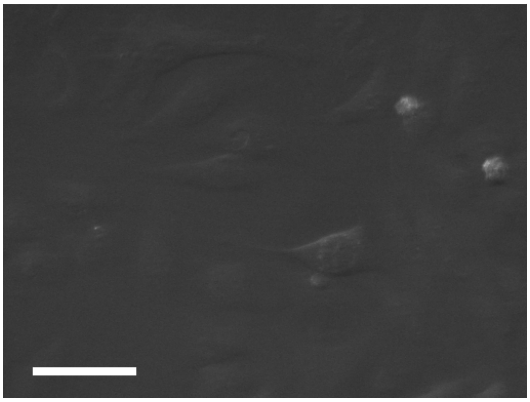

(b) 0.5 μg GFP

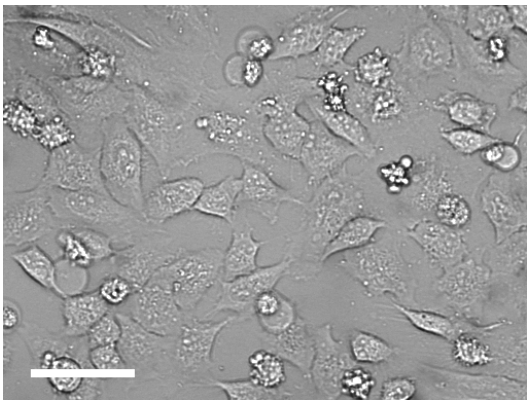

(c) 1.0 μg GFP

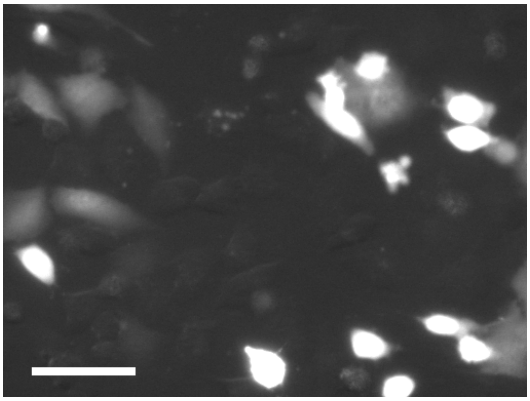

(d) 1.0 μg GFP

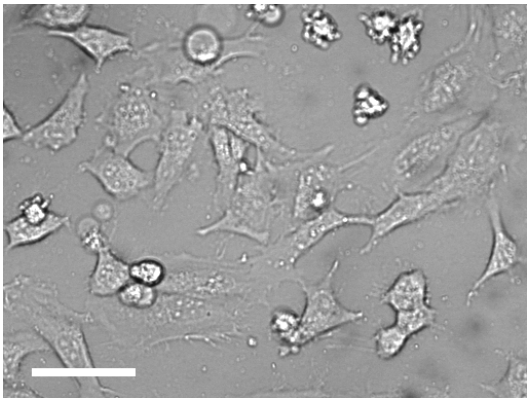

(e) 1.5 μg GFP

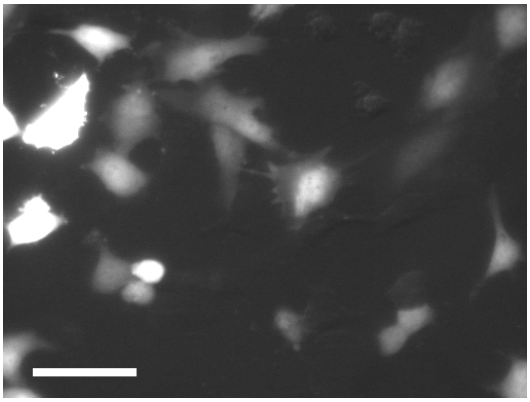

(f) 1.5 μg GFP

Fig. 4.3 Bright-field images (a, c and e) alongside fluorescence images (b, d and f) of GFP transfection levels in HeLa cells using quantities 0.5 μg (a and b), 1.0 μg (b and c) and 1.5 μg (e and f) of plasmid per 6 cm dish. Transfection occurred 24 hours after plating cells at a density of 300,000 per dish and images were taken 24 hours after transfection. Scale bars: 50 μm.

4.3f depict cells transfected with 1.5 μg GFP per dish and it is clear that the majority of healthy cells are expressing GFP. Counts from wide-field viewpoints suggested an efficiency of $\backsim$ 80%. Despite the culture transfected with 1.5 μg GFP per dish exhibiting the highest transfection efficiency, a quantity of 1.0 μg per dish was selected for further experiments. The rationale for this choice is two-fold. Firstly, when conducting laboratory work on cells using the AFM, individual cells are selected and so a very high efficiency is not required. Limiting this helps reduce unnecessary, transfection induced toxicity to cells. Secondly, as the transfection concentration of TILRR cDNA has been optimised to provide the highest inflammatory response (scaled up from 96-well plate cultures) which implies expression in a high percentage of cells, by reducing the quantity of GFP one can be more confident that each fluorescent cell will have also taken up sufficient quantities of EV or TILRR cDNA.

4.4 Summary and Conclusion

To summarise, the concentrations of IL-1β and TILRR cDNA for use in future AFM-based experiments were optimised using luciferase assays. An assay varying the dose of IL-1β from 10^{-15} M to 10^{-9} M indicated that a small increase in activity was observed under 10^{-13} M IL-1β and a moderately large response was observed under 10^{-11} M IL-1β. The largest response was observed at 10^{-9} M IL-1β which was deemed to be a saturation point from previous various previous studies. This concentration was selected for use in future experiments in *Chapter 6* and 10^{-13} M IL-1β was used in *Chapter 5*. The concentration dependence of TILRR cDNA on NF-κB activity was tested using concentrations between 10 ng and 40 ng per well alongside stimulation with 10^{-11} M IL-1β and was measured alongside cells transfected with EV for comparison. Cells showed an increase in response with increasing TILRR transfection concentration up a maximum of of 30 ng per well. Further increase of TILRR cDNA did not seem to amplify NF-κB activity beyond this concentration. Therefore a transfection concentration of 30 ng per well (5 μg per million cells) was selected which, when scaled up into 6 cm dishes, equates to 1.5 μg per dish. For identification of transfected cells in AFM experiments the transfection efficiency of GFP was determined using florescence microscopy. By testing transfection quantities of 0.5 μg, 1.0 μg and 1.5 μg per dish it was deduced that 1.0 μg was appropriate for expression in a sufficient number of healthy HeLa cells whilst limiting toxicity.

Chapter 5

Effect of Inflammatory Amplifiers on HeLa Cell Attachment to Fibronectin

5.1 Introduction and Rationale

Force studies using the AFM provide the ability to characterise the strength of adhesion on living biological material *in vitro* and can allow for measurements in environments analogous to physiological conditions (Schön, 2017). By specific experimental design, it is therefore possible to obtain quantitative information from desired biological processes by artificially recreating conditions in lab cultures. The role of PGs as mediators of cellular processes has been characterised in numerous studies (Borland et al., 2017; Schaefer et al., 2016; Templeton, 1992; Zhang et al., 2012, 2010). The function of IL-1RI is induced by ligand (IL-1) binding and is amplified by association of HSPG co-receptor, TILRR. TILRR-induced signal amplification of IL-1RI requires both IL-1/IL-1RI binding and the association of TILRR with extracellular FN via its HS GAG chain at sites of cell-matrix interaction (focal adhesions; Vallés et al. 1999). Studies by (Zhang et al., 2010), using a TILRR varient incorporating a GFP-tag demonstrated its localisation at the cell surface and near the cell

edge (see *Figure 1.7a*). The positions of focal adhesions in HeLa cells are depicted in *Figure 5.1*.

Zhang et al. (2010) showed that TILRR amplification of IL-RI is required for IL-1 induced activation of the Ras GTPase which results in pronounced changes to both the cytoskeletal structure and the cell shape and also in a reduction of extended processes. The effective blocking of TILRR was shown to inhibit these structural changes under IL-1 saturation. This study also demonstrated that increased TILRR expression (achieved through transfection of cDNA) was sufficient to induce these mechanical effects in the presence of endogenous levels of IL-1. These findings were consistent with earlier studies which demonstrated that FN attachment affects IL-1/IL-1RI binding at focal adhesions and that IL-1 stimulation under these conditions affects both cell attachment and cell shape (Qwarnstrom et al., 1991, 1988; Vallés et al., 1999; Zhu et al., 1998). In particular, Qwarnstrom et al. (1991) demonstrated a partial loss of contact between extended processes and the dish (ECM) under IL-1 stimulation (and in the presence of FN) using scanning electron microscopy (see *Figure 1.11*) which corresponded to the phosphorylation and redistribution of talin at focal adhesions. Collectively, these reports may indicate a reduction in binding strength between the ECM and the cell due to TILRR amplification of the IL-1RI receptor complex and subsequent activation of the Ras GTPase. This is investigated throughout this chapter using both the force mapping application of the AFM and the simulation of the ECM by modification of the probe.

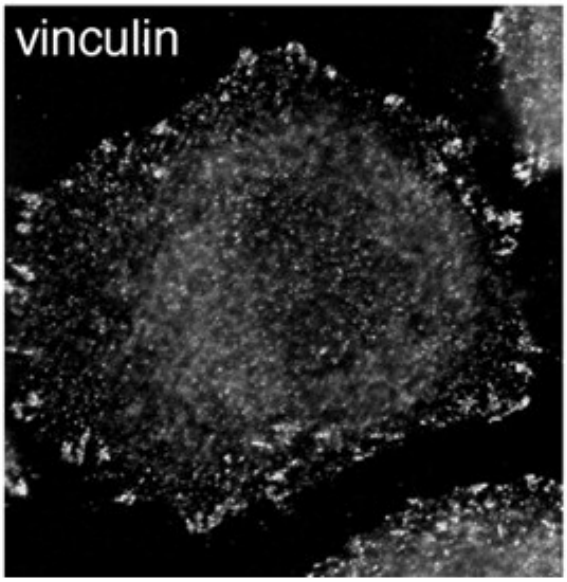

Fig. 5.1 Localisation of vinculin in a HeLa cell as a marker for focal adhesion positions. It is clear from this image that focal adhesions are prevalent at the cell edge. Reproduced from the Journal of Cell Biology, 186/1, Teckchandani et al., Quantitative proteomics identifies a Dab2/integrin module regulating cell migration, 99-111, Copyright (2009) with permission of Rockefeller University Press.

5.2 Development of Methodology

5.2.1 Preliminary Cell Measurements

It was decided that force measurements were to be taken on the surface of HeLa cells at regions where cell-ECM interactions can occur. Deflection images of HeLa cells taken with contact mode AFM are depicted in *Figure 5.2*. Numerous features of the cell can be seen with clarity in these images including cytoskeletal components and adhesive contact positions both between individual cells and between cells and the dish surface, (inferring the positions of cell-ECM contact). Initial force-maps were conducted on HeLa cells to determine both the capability of the AFM in targeting specific areas of the cell surface and the relevant experimental parameters for measurement of single-molecule rupture forces. The height profile of a 30 μm $\times$ 30 μm force-map over a HeLa cell is depicted in *Figure 5.3a*. The break between cell and substrate is clearly apparent but the locations of individual extended

processes and focal adhesions cannot be resolved with sufficient clarity using the force-mapping application of the AFM. It may be possible to achieve a high enough resolution by increasing the number of pixels (force-curves) in the scan but this results in increasing the time taken for a single map beyond reasonable limits. Moreover the optics afforded by the MFP inverted microscope, the need to approximate the tip location on the reverse side of the cantilever from the viewpoint and the size of the tip itself further complicate this. It was therefore decided that smaller, 5 μm $\times$ 5 μm force-maps were to be conducted at various positions along the cell edges and force-curves containing unbinding events which correspond to the edge would be considered for rupture analysis. This allows for the targeting of force measurements at regions of the cell where interactions with ECM components such as FN are more likely to occur, as demonstrated by the surface localisation of TILRR by Zhang et al. (2010). The cell edge was defined somewhat arbitrarily by first few lines of pixels following the cell-dish break as observed from the force-map height profiles and was verified by non-linearity in the contact regime of the corresponding force-curves (implying measurements on the soft cell surface as opposed to the harder dish). *Figure 5.3b* depicts the height profile of a 5 μm $\times$ 5 μm force map in which the cell edge can be resolved. It should be noted that other AFM based adhesion studies between ECM components and ECM binding cell receptors, such as integrins, have reported success over the general cell surface and so the validity of this approach seems reasonable (Hong et al., 2012; Hyonchol et al., 2002; Lehenkari and Horton, 1999; Li et al., 2003; Zhang et al., 2004b). Furthermore, while most prevalent at focal adhesions and the cell edge (see *Figure 5.4a*), ECM-binding cell receptors have been shown be present throughout the entirety of the cell (see *Figure 5.4b*).

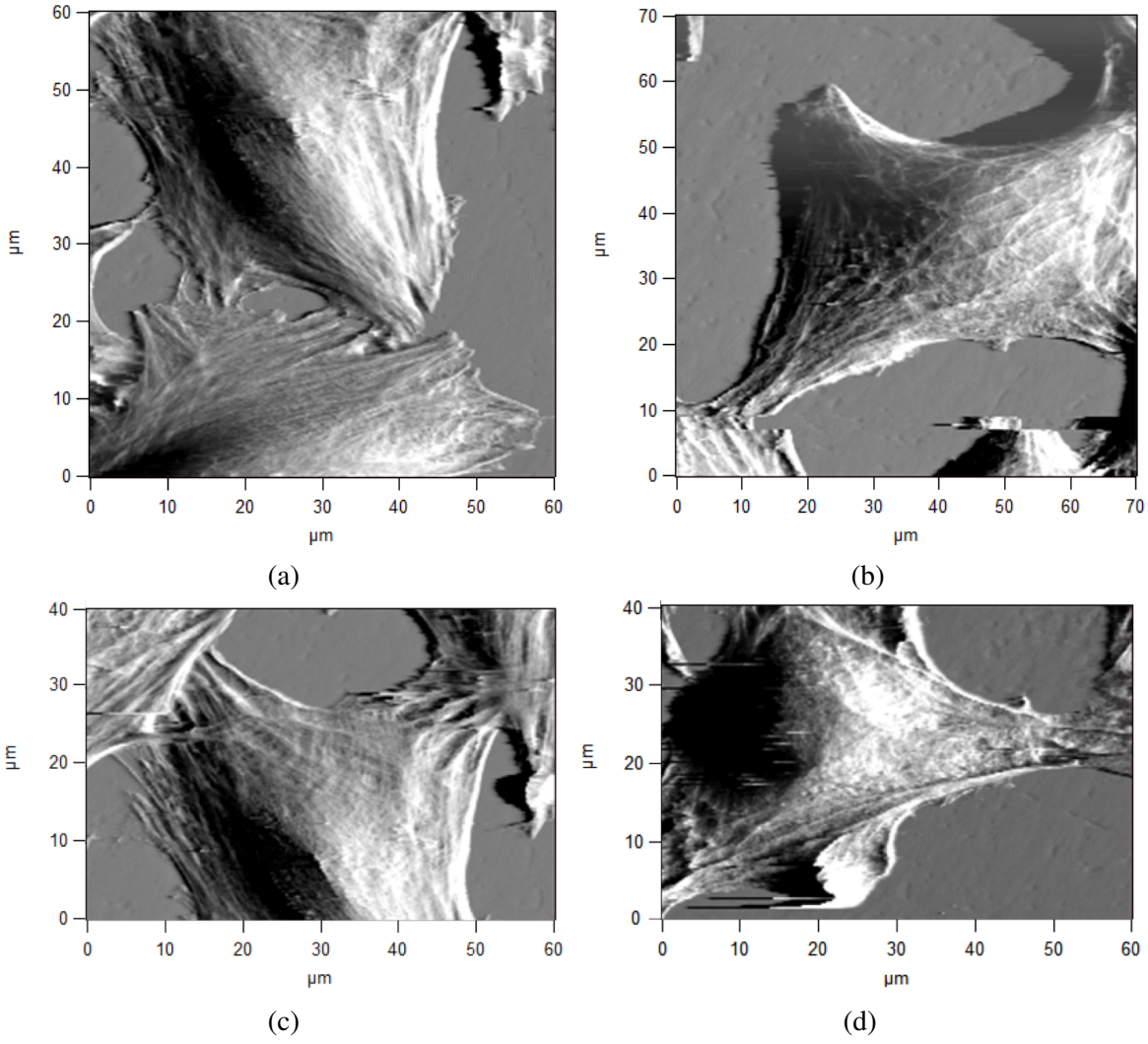

Fig. 5.2 Deflection images of HeLa cells taken with contact-mode AFM using the MFP. Contact points between cells and between the dish (ECM) and cells alongside cytoskeletal components can be seen with clarity.

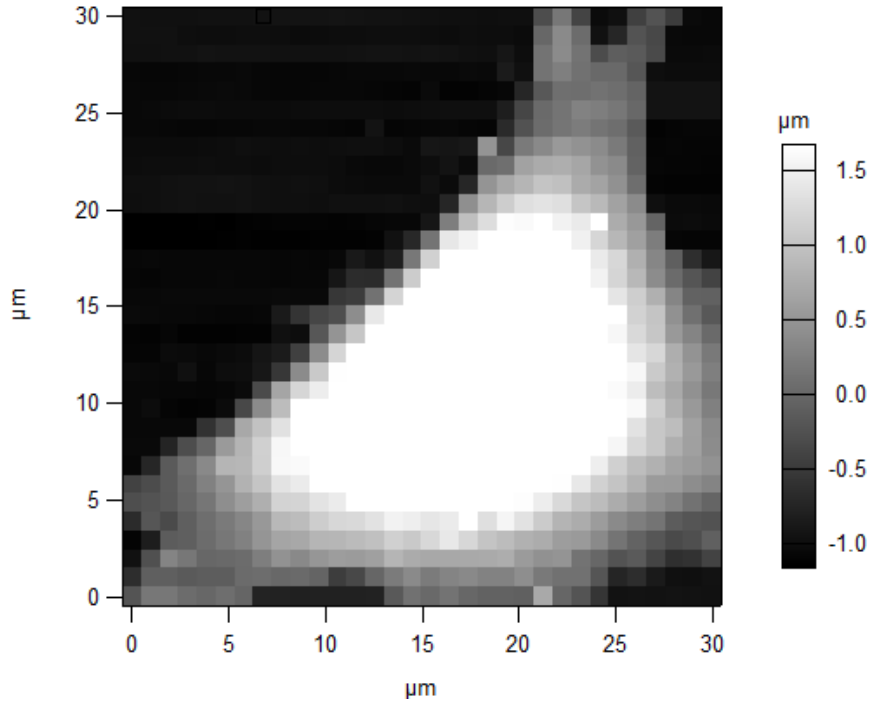

(a)

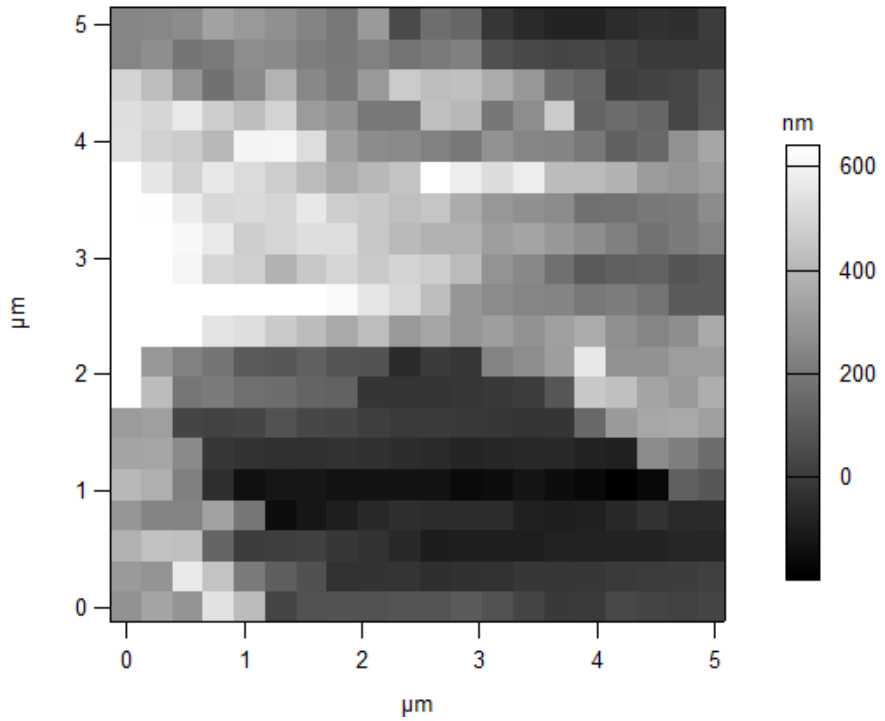

(b)

Fig. 5.3 Height profiles of 30 μm $\times$ 30 μm (a) and 5 μm $\times$ 5 μm (b) AFM force-maps on HeLa cells. The cell edge can be resolved with clarity in both images. The 5 μm $\times$ 5 μm maps were used for adhesion measurements alongside FN functionalised probes and allow for force-curves corresponding to the cell edge to be identified.

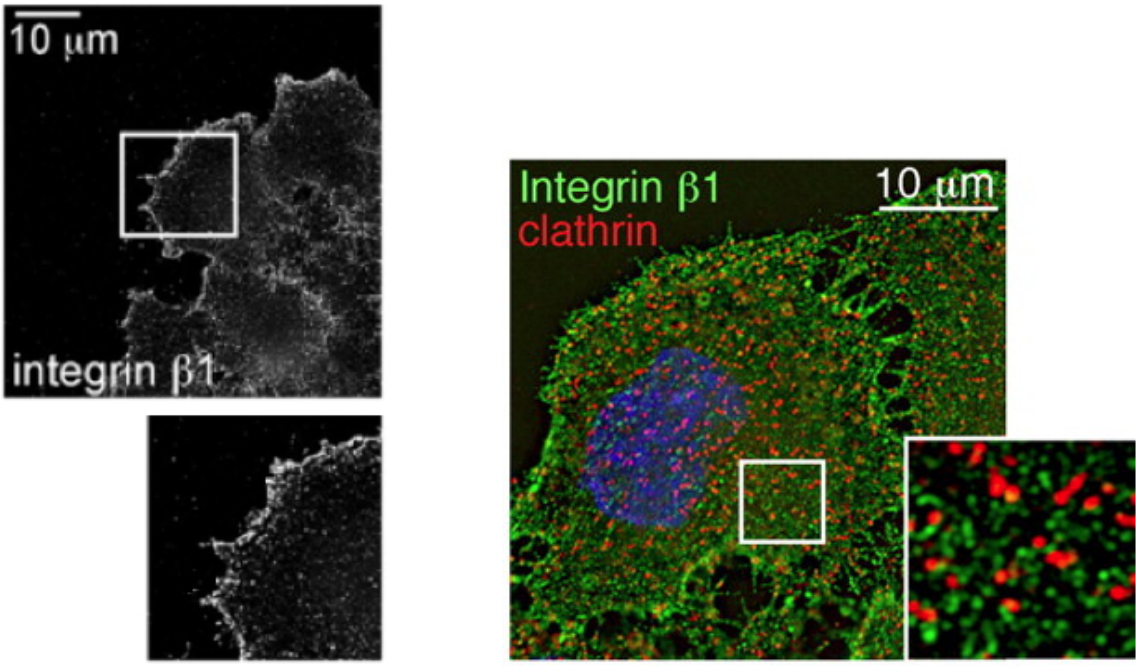

(a) (b)

Fig. 5.4 Localisation of the β_1 integrin in HeLa cells by treatment of the anti-integrin β_1 antibody. Most of the β_1 is located at the cell edge (a) but is also prevalent throughout the cell (b). Note: the cell has also been stained with anticlathrin antibody depicted in red (clathrin is an intracellular protein involved in the formation of vesicles; b). Reproduced from the Journal of Cell Biology, 186/1, Teckchandani et al., Quantitative proteomics identifies a Dab2/integrin module regulating cell migration, 99-111, Copyright (2009) with permission of Rockefeller University Press.

The experimental parameters decided upon for all further measurements throughout this chapter were trigger forces of 250 pN to limit indentation into the cell surface, damage to the cell and the appearance of non-specific interactions alongside a relatively low approach and retract velocity of 1 μm·s^{-1} to ensure sufficient contact time between the probe and cell surface for the formation of bonds, to limit both noise and the hydrodynamic effect and also to eliminate the possibility of multiple energy barriers (for particular ligand-receptor bonds) which may complicate comparative measurements. Representative force-curves between FN-functionalised probes (see *Section 5.2.2*) and cells transfected with TILRR cDNA (alongside GFP, see *Section 5.3* and *Section 5.4*) exhibiting different quantities of events are displayed in *Figure 5.5*. To ensure the quantification of rupture events corresponding to single-molecule interactions only the magnitude of the final peak (before the deflection returns to zero) in each event-exhibiting retraction curve was considered for analysis. It is clear from *Figure 5.5* that these peaks can clearly be identified. Rupture forces were quantified using the MATLAB® analysis method outlined in *Section 2.6.1*. All cells in subsequent experiments were stimulated with 10^{-13} M IL-1β in order to induce low levels of NF-κB activity (see *Section 4.2.1*; Nichols, 2017). Higher concentrations of IL-1β were not used to limit responses in control cultures and as TILRR potentiation of inflammatory stimulus may not be observable under saturated stimulant levels. Furthermore, Zhang et al. (2010) observed structural changes in cells transfected with TILRR cDNA with endogenous levels of IL-1β so this approach seemed justified.

5.2.2 Functionalisation of AFM Probes

In order to simulate cell-ECM interactions with FN using the AFM, it was necessary to functionalise probes to exhibit ECM component proteins on their surface. This was achieved through immobilisation of FN on gold-coated cantilevers due to the well-characterised strength of thiol-gold binding, the relative simplicity when compared with other tip modifi-

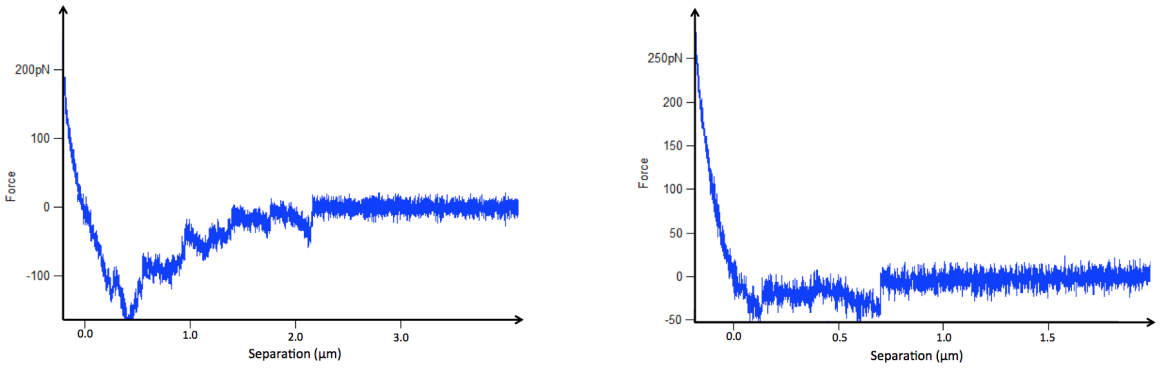

(a) (b)

Fig. 5.5 Force-curves taken between FN-functionalised probes and HeLa cells co-transfected with TILRR cDNA and GFP exhibiting different numbers of events. The rupture force for each event exhibiting curve was taken as the magnitude of the final peak in the retraction regime directly before returning to the baseline at zero deflection. Both curves were taken at an approach and retraction speed of 1 μm·s^{-1}.

cation methods and the success of biologically active FN-gold substrates in *Section 3.2.2*. Olympus BioLever (OBL) cantilevers were used for the experiments described in *Section 5.3* but the main results for this chapter, described in *Section 5.4*, were achieved using gold-coated MLCT probes (achieved by in-house evaporation) because of limited OBL availability and their temperamental nature when used alongside the MFP. Gold-coating was achieved through thermal evaporation of a $\backsim$ 40 nm gold layer following a $\backsim$ 5 nm chromium adhesive layer (Barattin and Voyer, 2008). As discussed fully in *Section 3.2.2*, the surface density of FN seems to impact its biological binding functionality and so concentrations of FN for tip immobilisation were therefore used which have been successful in previous force spectroscopy studies (Schön et al., 2013; Verbelen and Dufréne, 2009). Therefore gold-coated probes were immersed in a 10 μg·ml^{-1} solution of FN in PBS at overnight before use.

5.3 Initial Force Measurements Between FN and HeLa Cells Transfected with TILRR

Initial force measurements utilising a FN functionalised probe were conducted on cell cultures transfected with an optimal TILRR cDNA concentration of 5 μg per million plated cells (or 1.5 μg per dish) as determined in *Section 4.2.2* and by Zhang et al. (2010). Force maps were conduced at regions near the cell edge as depicted in *Figure 5.3b* and adhesive measurements taken at the edge as described by the height profile and the contact regime of the force-curve (see *Section 5.2.1*) were extracted. The resulting frequency distribution, taken over numerous maps of the cell edge for 20 cells, is depicted in *Figure 5.6*. While observation of the distribution indicates a distinct skewing towards lower forces, it also seems to consist of two normal distributions. Fitting the data with a double-Gaussian reveals two frequency maxima at rupture forces of 30 ± 8 pN and 80 ± 35 pN where the errors are taken from the width of the 95% confidence interval on each Gaussian fit. While optimised concentrations of TILRR cDNA are used for transfection throughout this study, a significant quantity of cells in the culture will not have taken up plasmid. Studies of single cells using the AFM may be significantly affected by this phenomenon when compared with experiments which measure large quantities of cells such as luciferase assays. The apparent double distribution may correspond to force measurements on both HeLa cells significantly affected by TILRR controlled responses and those which have not undergone transfection. This however cannot be verified by these results. It became clear that for meaningful measurements between FN and transfected HeLa cells it was necessary to incorporate a system by which successfully transfected cells can be identified and unaffected ones could be ruled out. This was achieved by co-transfection of a GFP containing construct alongside TILRR cDNA (see *Section 4.3*) and allows for identification using the fluorescence set-up built into the MFP.

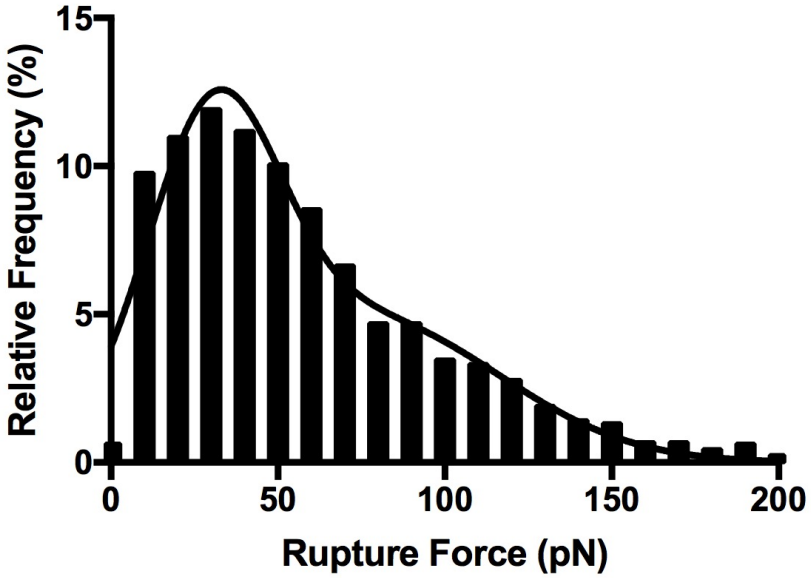

Fig. 5.6 A frequency distribution depicting the rupture force between FN-functionalised probes and HeLa cells transfected with TILRR at a concentration of 5 μg per million cells. Two normal distributions may be contained within corresponding to modal averages of 30 $\pm$ 8 pN and 80 $\pm$ 35 pN deduced through a double-Gaussian fit as displayed. This may be due to the measurement of both transfected and non-transfected cells.

5.4 Measurement of Adhesive Changes Between FN and HeLa Cells due to TILRR Transfection

Following the tests on the concentration dependence of GFP expression in HeLa cells described in *Section 4.3*, force measurements between FN functionalised probes and cells transfected with 1.5 μg per dish TILRR cDNA alongside 1 μg per dish pEGFP-N2 were conducted. Cells transfected with 1.5 μg EV per dish alongside 1 μg per dish pEGFP-N2 were measured as a control for both the comparison of cells with and without TILRR cDNA, to reveal its effect on cellular adhesion with the ECM, and to verify that any observed adhesion change was not a result of the transfection process itself. Bright-field and fluorescence images of a cell expressing TILRR and GFP, taken using the MFP inverted microscope system, can be seen in *Figure 5.7*.

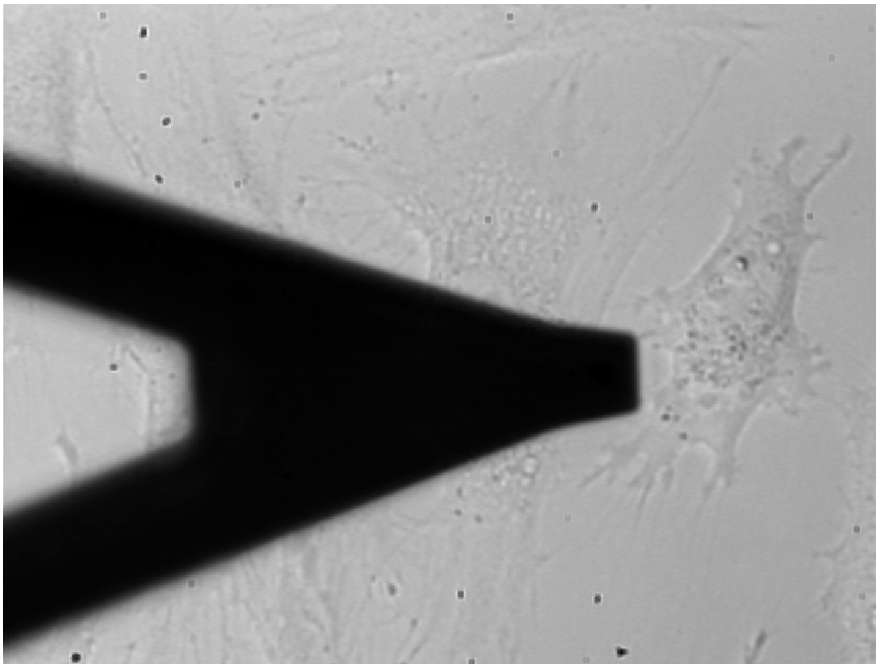

(a)

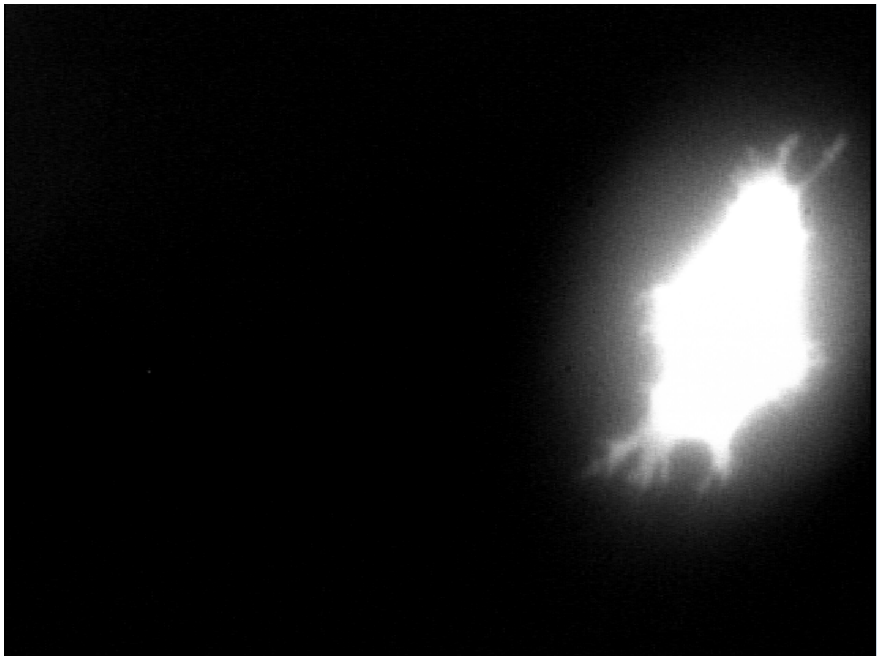

(b)

Fig. 5.7 Bright-field (a) and fluorescence (b) images of a HeLa cell co-transfected with GFP and TILRR cDNA using the inverted microscope in the MFP set-up.

Table 5.1 Modal rupture forces between FN-functionalised probes and HeLa cells transfected with EV and GFP and with TILRR cDNA and GFP extracted from the Guassian fits in *Figure 5.8a* and *Figure 5.8b*. Errors are determined from the width of the 95% confidence interval for each fit.

Transfection Condition	Modal Rupture Force (pN)
EV + GFP	59 ± 2
TILRR cDNA + GFP	35 ± 1

1,000 curves corresponding to FN-cell binding events near the cell edge for each condition were obtained using the experimental parameters outlined in *Section 5.2.1*. A minimum of 15 cells for each condition were mapped at different positions around the cell edge and rupture forces corresponding to positions near the circumference were quantified. Relative frequency distributions for extracted rupture forces between the FN tip and cells transfected with EV, and the FN tip and cells transfected with TILRR cDNA are displayed in *Figure 5.8a* and *Figure 5.8b* respectively. These figures suggest that, for control cells, the adhesive forces between the cell and FN are described by a normal distribution. Transfection of TILRR cDNA results in a shift in the distribution resulting in a positively-skewed log-normal shape and an inferred reduction of the most probable rupture force. Modal averages, extracted from Gaussian fits of the frequency distributions for each condition, are displayed in *Table 5.1* and the modal reduction is displayed graphically in *Figure 5.8*. Errors of the most probable rupture force for each condition are taken as the width of the 95% confidence interval of the Gaussian fits.

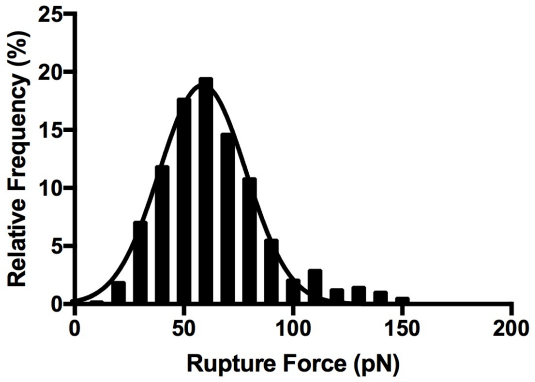

(a) − TILRR

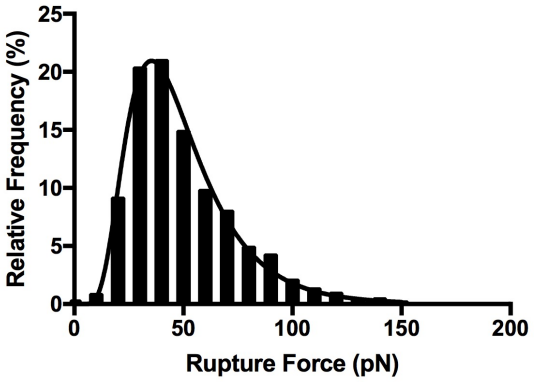

(b) + TILRR

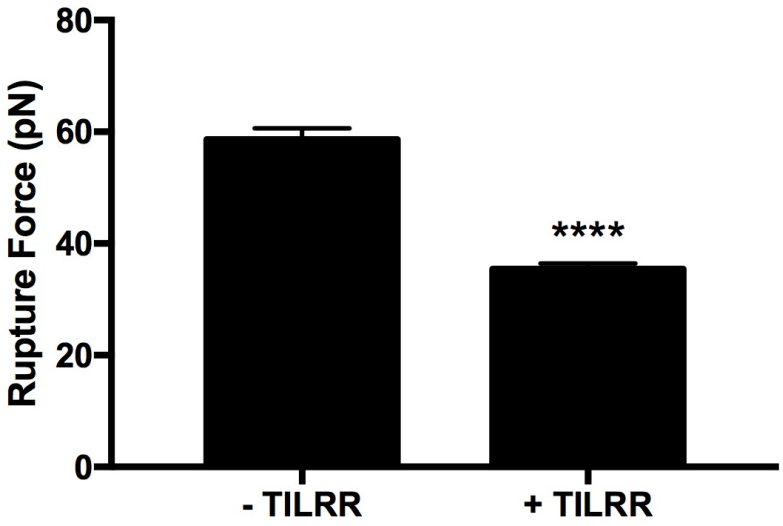

(c)

Fig. 5.8 Frequency distributions of extracted rupture forces between FN-functionalised probes and HeLa cells transfected with EV and GFP (a) and with TILRR cDNA and GFP (b). It is clear that the transfection of TILRR cDNA seems to result in a clear skewing of the distribution towards lower forces resulting in a reduced modal rupture force. Gaussian fits for extraction of average rupture forces are included in both distributions. The reduction in modal rupture force (extracted from each Guassian fit) is depicted graphically (c) where errors were determined as $\pm$ half of the 95% confidence interval for the fit. Significance was determined using Mann-Whitney non-parametric tests ($****p < 0.0001$).

5.5 Discussion

Measurement of the adhesive interaction between FN-functionalised probes and the surface of the cell, near the edge, revealed a reduction of the most probable rupture force for those transfected with TILRR cDNA when compared with cells transfected with EV. The magnitude of this reduction is $\backsim 40\%$ and was deduced to be extremely statistically significant ($p < 0.0001$) by use of the Mann-Whitney non-parametric test. This test was applied due to the difference in observed distribution shape describing the extracted rupture forces for each condition. This supports previous studies which have identified a partial loss of contact with the cell dish following activation of the IL-1RI receptor complex (Qwarnstrom et al., 1991). The edge of the cell was specifically targeted using force-maps in an attempt to record interactions between the ECM and cell at regions corresponding to focal adhesions or, at a minimum, with receptors responsible for cell-ECM interactions which localise at the edge (Teckchandani et al., 2009). It is not clear if a similar adhesive reduction would be observed over different areas of the cell surface (although this is likely as in tissues cells reside in a 3D ECM and can form attachments on all sides). This result demonstrates a general reduction in the strength of binding between the cell and ECM at possible focal adhesion sites due to the activation of the IL-1RI/TILRR complex and may infer a potentiating effect on cellular migration (perhaps aiding in both the disassembly of focal adhesions at the rear of of the cell and the extension of the leading edge; Cumberbatch et al. 1997; Filippi et al. 2015; Huttenlocher and Horwitz 2011; Lin et al. 2009; Qwarnstrom et al. 1991). This may have a significant impact in diseases such as atherosclerosis (Smith et al., 2017). It should be noted that modal rupture forces of initial cell-FN unbinding taken on un-targetted cells transfected with TILRR cDNA (extracted by fitting a double-Gaussian; see *Section 5.3*) correlate well with the main results in *Table 5.1*.

Changes in the magnitude of unbinding events, contained within the retraction regime of force-curves, may reflect a change in adhesive strength between several receptor systems at the cell surface with the probe-immobilised FN. Specifically, FN binding with the $\alpha_5\beta_1$ integrin is expected to contribute significantly to the change in cell-ECM interaction observed in these results as it is the main adhesion receptor which permits binding between the cell and extracellular FN and is highly prevalent at the cell edge (Teckchandani et al., 2009). The reduced cell-FN adhesion observed here may be induced following a reduction in the binding strength between between integrins and FN, which is likely to be due a change in integrin conformation (Askari et al., 2009; Luo and Springer, 2006; Takagi et al., 2001). Cellular adhesion to the ECM via integrins is intrinsically related to the cytoskeletal structure of the cell through the link of the β-component cytoplasmic tail in the receptor complex to actin filaments (Calderwood et al., 2000). In this way, cells can detect interactions with the ECM and mechanical perturbations of the cytoskeleton caused by external stimuli (Bershadsky et al., 2003). Should the binding between $\alpha_5\beta_1$ and FN be responsible for this reduced cell adhesion, consideration of the properties of the bond may be relevant. *Chapter 3*, alongside previous DSMFS studies, demonstrated two distinct energy barriers characterising the $\alpha_5\beta_1$-FN unbinding interaction (Li et al., 2003). The relatively low retraction velocity of 1 μm·s^{-1} selected throughout this chapter indicates that the unbinding is characterised by the low-loading regime and therefore by a compliant bond. This reduction in adhesive force between the cell and ECM in the more elastic $\alpha_5\beta_1$-FN unbinding regime and under slow motion (such as extension of the leading edge) may further support an increased capacity for cell migration. It is unclear if high-loading cell-ECM unbinding, perhaps characterised by the more brittle $\alpha_5\beta_1$-FN barrier, is affected by activation of the IL1-RI/TILRR complex and so the cell may or may not remain resilient to significant external stresses.

The observed changes in cell attachment are likely a consequence of the IL-1RI/TILRR activation of the Ras GTPase and the resultant effects on both the cytoskeleton and cell shape (Rhodes et al., 2015; Zhang et al., 2010; Zhu et al., 1998). This ultimately likely results in a change in FN-integrin binding and function (Askari et al., 2009). A strong interdependence of cell attachment and cell shape is consistent with the close link between integrin-mediated adhesion and the structure of actin filaments in the cytoskeleton (Puech et al., 2006). It is likely that the effect of the IL-1RI signalling system on rupture forces observed in this study is also facilitated by the IL-1 induced phosphorylation of talin, which together with vinculin provides an intrinsic link between the ECM, integrins and the actin cytoskeleton (Calderwood et al., 2000; Qwarnstrom et al., 1991). Changes in the interaction with the ECM and perturbations of the cytoskeleton, such as those induced by activation of the IL-1RI/TILRR complex, allow cells to detect alterations caused by external stimuli (Bershadsky et al., 2003). This signalling crosstalk between soluble mediators such as IL-1 and structural events, regulated through cell adhesion and the extracellular matrix, provide a mechanism whereby cells can recognise multiple inputs and modify signal amplification according to their environment.

5.6 Summary and Conclusion

Using the AFM, transfection of TILRR cDNA into HeLa cells was shown to result in a statistically significant $\backsim 40\%$ reduction of the most probable adhesive force between the cell surface, near the edge, and ECM component FN. This is consistent with previous studies which have reported a reduction in the size of extended processes and a partial loss of their contact with the cell surface, inferring a reduction in adhesion between the cell and ECM at focal adhesions, alongside a significant change in cell shape induced by the TILRR controlled IL-1RI response (Zhang et al., 2010; Zhu et al., 1998). The results presented here both verify and quantify this inferred TILRR regulated reduction in binding strength between the ECM and the cell. This reduction in cell-ECM affinity may by induced by conformational changes in transmembrane adhesion receptors, such as $\alpha_5\beta_1$, via direct phosphorylation, phosphorylation of talin and the previously observed redistribution of the actin cytoskeleton (Qwarnstrom et al., 1991). When considered in the context of TILRR controlled IL-1RI activation, this altered adhesion with the ECM may allow for the migration of cells at the site of injury and inflammation. Furthermore, the chronic activation of pro-inflammatory signalling with abnormally high PG expression is a characteristic feature of many diseases including atherosclerosis and cancer. It is somewhat possible that this PG regulated reduction in cell-ECM adhesion may contribute to the destabilisation of atherosclerotic plaques or tumour metastasis and malignancy (Beauvais and Rapraeger, 2004; Nikolova et al., 2009; Smith et al., 2017). In addition, this study demonstrates that the AFM has the capacity to observe structural changes in cells by measurement of adhesive interactions with ECM components.

Chapter 6

Effect of Inflammatory Amplifiers on the Elasticity of HeLa Cells

6.1 Introduction and Rationale

The focus of this chapter is to determine if the TILRR controlled activation IL-1RI affects the surface elasticity of HeLa cells using indentation-force spectroscopy. Multiple previous studies have reported that (with sufficient ECM) activation of IL-1RI has a dramatic effect on cytoskeletal structure, resulting in a clear disorganisation of the actin filaments (Qwarnstrom et al., 1991; Zhu et al., 1998). This has been shown to significantly affect the cell shape and impacts attachment with the ECM at focal adhesions (see *Chapter 5*). Furthermore, Zhang et al. (2010) showed that this cytoskeletal rearrangement requires TILRR association with the receptor complex and that increased TILRR expression (achieved through transfection of TILRR cDNA) alongside endogenous levels of IL-1 is sufficient to induce these changes. These mechanical effects, induced through activation of IL-1RI/TILRR, are mediated by activation of the Ras GTPase which has been shown to modulate the positions of polymerised actin filaments in the cell (and the general organisation of the cytoskeleton; Choi and Helfman 2014; Prendergast and Gibbs 1993). This chapter therefore describes attempts to measure

if these cytoskeletal effects result in observable changes in the elastic modulus of the cell. Elasticity measurements on cells under IL-1 saturation and cells with increased TILRR expression were conducted using the AFM and the ability of both standard pyramidal and colloidal probes, alongside different regions of the cell surface, in reproducible modulus extraction was investigated. Preliminary measurements using the RTDC method to estimate the elasticity of cells in suspension can be found in *Section 2.3*.

6.2 Initial Indentation Measurements

6.2.1 Pyramidal Probes

Prior to investigating the effects of IL-1RI activation on cell elasticity using indentation-force spectroscopy, initial measurements were performed to determine the variation in extracted Young moduli across the cell surface. This was necessary as a significant natural heterogeneity in elastic modulus over different regions of the cell surface could result in a wide range of measured values from which no meaningful average can be discerned. This would therefore make it impossible to deduce any differences between cells measured under different biological conditions and could potentially negate any useful conclusions from this study. A 23×23, 30 μm^2 force map over a HeLa cell using MLCT tip-C is displayed in *Figure 6.1* alongside three force-indentation curves corresponding to different regions of the surface. The map was taken at an approach and retract velocity of 10 μm$\cdot$s^{-1} at a trigger force of 1 nN and was operated with closed-loop feedback control. It is clear from *Figure 6.1b* that the measured tip indentation depth throughout the map varies significantly across the cell. In fact, significant variation can be seen in the magnitude of indentation between adjacent points due to the small area probed by the pyramidal MLCT tip. A significantly uniform and harder region of the cell is highlighted by the red circle and is likely to correspond to the subsurface presence of organelles such as the nucleus. This map clearly demonstrates that the position of the probe on the cell surface greatly affects the depth to which it is indented at a given force and as such directly effects the measurement of elasticity. The three different force-indentation curves displayed in *Figure 6.1c* clearly illustrate the significant variation in indentation across the cell and correspond to a depth of $\backsim$200 nm, $\backsim$1 μm and $\backsim$1.5 μm for the blue, red and black curves respectively. By approximating the tip as conical with a half-angle of 36° the respective Young moduli can be extracted using the Hertz-Sneddon model, *Equation 2.11*, as $\backsim$40 kPa, 1kPa and $\backsim$400 Pa.

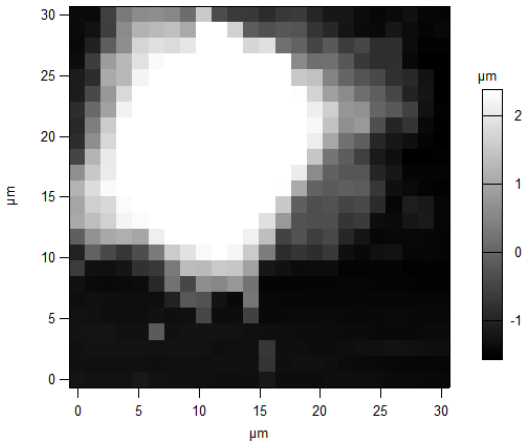

(a) Height profile of force map taken over a HeLa cell.

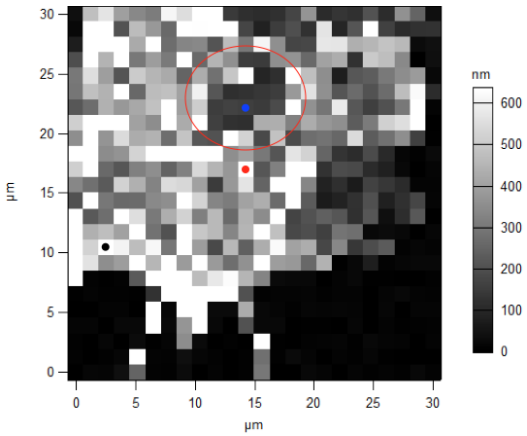

(b) Indentation profile of force map taken over a HeLa cell.

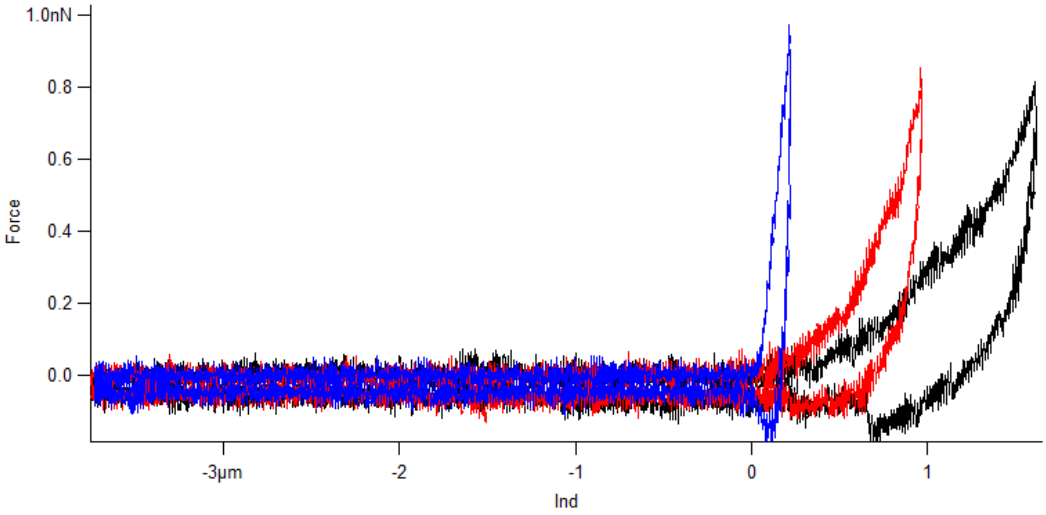

(c) Force-indentation curves taken on different regions of the HeLa cell surface.

Fig. 6.1 Height (a) and indentation (b) profiles of a HeLa cell from force mapping. Significant variation in indentation depth can be observed across the cell surface. A significantly stiffer area is indicated with a red circle. Three curves force-indentation curves corresponding to regions of varying stiffness on the cell are displayed (c). The locations of these measurements are indicted by coloured dots (b).

6.2.2 Colloidal Probes

It is clear from figure *Figure 6.1* that the experimental methodology must be significantly improved for any cellular elasticities to be extracted and compared with those of other biological conditions with any significance. It seems that much of the elastic heterogeneity over the cell surface is caused by indenting very small areas which may be mechanically affected by the presence of individual actin filaments and the presence of other small-scale structures. In order to limit this large variation in measured elastic moduli, colloidal probes were used which result in an indentation over much larger areas and allow for the extraction of cellular mechanical properties at the macroscale. Colloidal probes were constructed as outlined in *Section 2.5.4*. *Figure 6.2* depicts two force-maps taken using MLCT tip-C probes functionalised with polystyrene beads of diameter 10 μm. Data were taken at an approach and retraction velocity of 10 $\mu\text{m}\cdot\text{s}^{-1}$ with a trigger force of 2 nN. As always, the AFM system was operated with closed-loop control. Contact mechanics were characterised with the Hertz model for a spherical indenter using parameters 3 GPa and 0.33 for the Young modulus and Poisson ratio of the polystyrene bead respectively. The value of the Poisson ratio approximated for the cells remained as 0.5. It is clear from this figure that the indentation depth is much more uniform across the cell when employing colloidal probes in comparison to pyramidal tips. It is also apparent that any changes over the surface are much more gradual due to the more macroscopic measurements. The cell displayed in *Figure 6.2a* shows a very uniform depth of indentation throughout the central region and a general depth reduction as the tip moves closer to the top-most edge. This is likely to represent a reduced indentation due to a thinner region of the cell where substrate effects are imparted on the probe. *Figure 6.2b* displays a cell in which regions of generally higher and lower depths of indentation are observed and changes seem relatively gradual. These regions may correlate to the presence of organelles or high actin densities alongside effects caused by cell thickness. *Figure 6.2c* and *Figure 6.2d* display three force-indentation curves taken at different regions of the cell

which are clearly indicated in *Figure 6.2a* and *Figure 6.2b*. These curves show that for both cells the depth of indentation varies from $\backsim$ 0.5 μm to $\backsim$1.5 μm. By applying the Hertz model (*Equation 2.12* and *Equation 2.13*), Young moduli of $\backsim$1.5 kPa, $\backsim$390 Pa and $\backsim$360 Pa were extracted from the black, red and blue curves in *Figure 6.2c* and $\backsim$1.0 kPa, $\backsim$410 Pa and $\backsim$270 Pa from the red, black and blue curves in *Figure 6.2d*. This shows a general heterogeneity in elasticity across the cells, particularly in the central regions and therefore, by using colloidal probes, macroscale measurements can identify moduli from which an accurate average can be extracted. This method therefore allows for the elastic comparison of cells under different biological conditions.

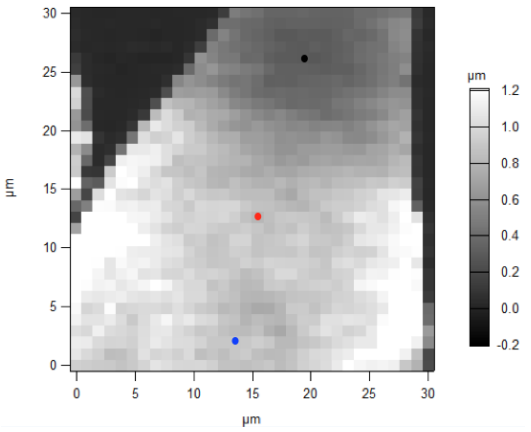

(a) Indentation profile of force map taken over a HeLa cell with colloidal probe.

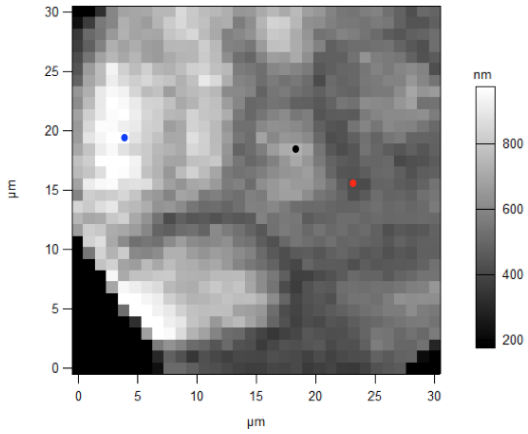

(b) Indentation profile of force map taken over a HeLa cell with colloidal probe.

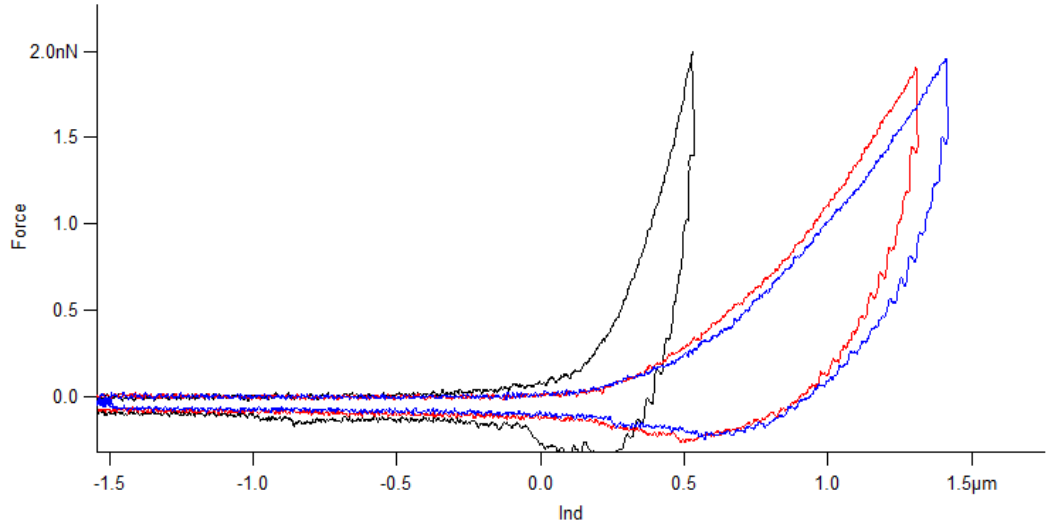

(c) Force-indentation curves taken on different regions of the HeLa cell surface (a).

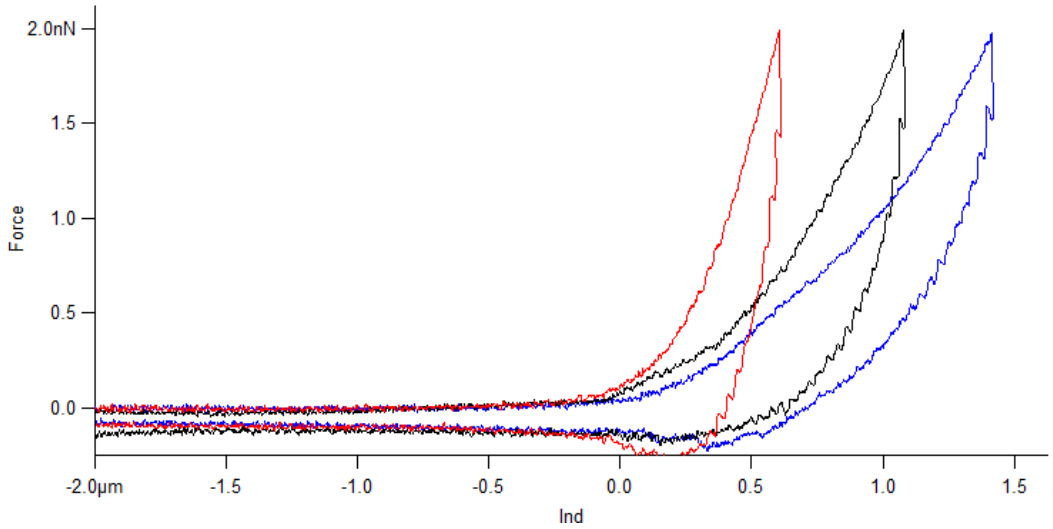

(d) Force-indentation curves taken on different regions of the HeLa cell surface (b).

Fig. 6.2 Indentation profiles of a HeLa cells from force mapping with 10 μm colloidal probes (a, b). Three force-indentation curves taken on different surface regions for each cell are indicated (c, d). The locations of these measurements are indicted by coloured dots (a, b).

6.3 Methodology for Quantifying the Effects of IL-1RI Activation on Cell Elasticity

6.3.1 Optimised Indentation Using Colloidal Probes

Due to the observed homogeneity in measured elasticity using colloidal probes at central regions of HeLa cells (see *Section 6.2.2*), the methods outlined throughout this section were used to determine the pro-inflammatory effects (resulting from IL-1RI activation) on the elastic modulus as a result of both IL-1β stimulation and transfection of TILRR cDNA. *Figure 6.3* depicts 5 μm by 5 μm indentation maps (triggered at 1 nN) on two separate HeLa cells and describes relative homogeneity across the map region (ranges of $\backsim$200 nm) and also across both cells suggesting that reliable and reproducible elasticity data can be achieved through mapping these regions of the cell. 5 μm by 5 μm maps ensure that the elasticity is not measured over either the nuclear region or close to the cell edge. Incorporation of 25 μm diameter colloidal probes ensures macroscale measurements throughout the maps. *Figure 6.4* displays three force-indentation curves taken at the same point in three consecutive maps and shows very high reproducibility across measurements. It also indicates that indentation curves taken at a speed of 3 μm$\cdot$s^{-1} have enough time to return to physiological conditions (a return in surface morphology to that prior to indentation) between measurements and as such biologically relevant data can be extracted.

6.3.2 Biological Conditions

The subsequent experiments described in this chapter were conducted using the method outlined throughout this section and the only difference in the way individual cell dishes were treated was in the inclusion or omission of IL-1 stimulation and/or transfection with either EV or TILRR cDNA to satisfy desired biological conditions. Six conditions were measured in total: control HeLa cells; HeLa cells stimulated with IL-1β; HeLa cells transfected with EV;

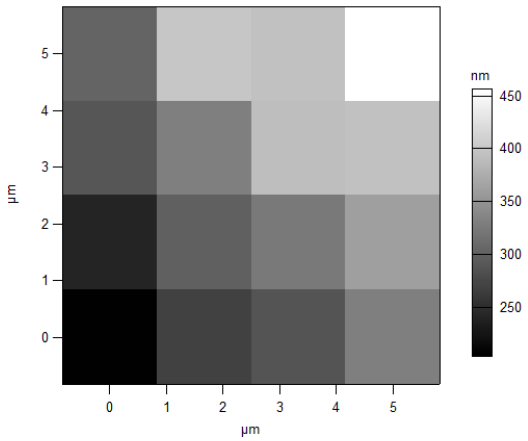

(a) 5 μm by 5 μm map of indentation depth on a HeLa cell.

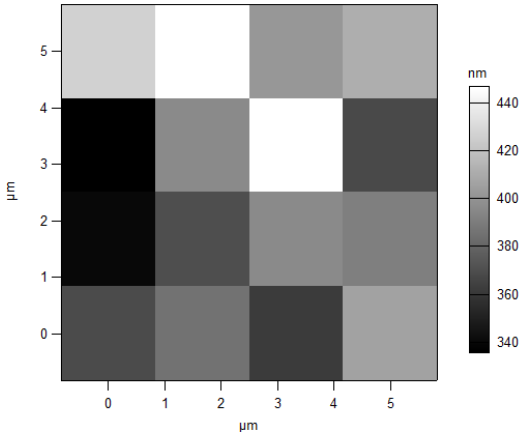

(b) 5 μm by 5 μm map of indentation depth on a HeLa cell.

Fig. 6.3 5 μm by 5 μm maps of indentation depth on two different HeLa cells displaying small variations in indentation depth on each map and between different cells. Taken with 25 μm colloidal probes at at 3 μm·s^{-1} with a trigger force of 1 nN.

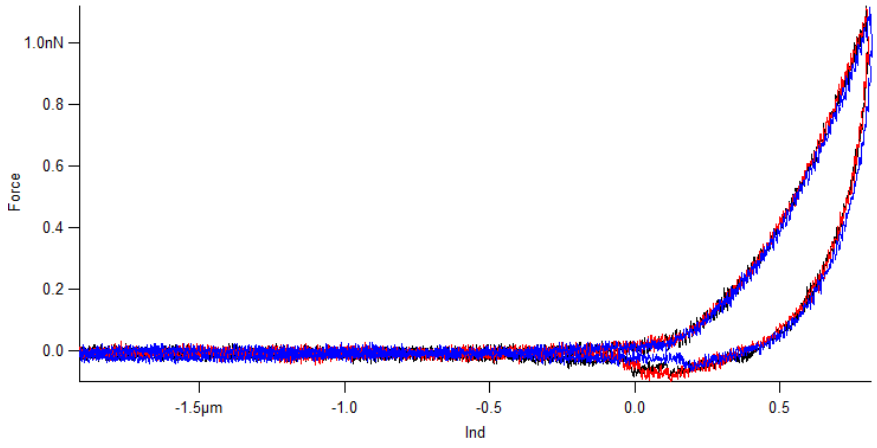

Fig. 6.4 Three force-indentation curves depicting the homogeneity in measured elasticity at the same point on subsequent force-maps. Taken with a 25 μm colloidal probe at 3 μm·s^{-1}.

HeLa cells transfected with TILRR cDNA; HeLa cells transfected with EV alongside IL-1β stimulation and HeLa cells transfected with TILRR cDNA alongside IL-1β stimulation. These conditions are indicated throughout. HeLa cells were cultured as described in *Section 2.2.2* and *Section 2.2.3*. 300,000 cells were seeded on FN coated 6 cm dishes (incubated with 10 μg·ml^{-1} FN in PBS for 30 minutes prior to addition of cells) two days prior to force-indentation measurements at a confluence of approximately 50% - 60%. Control HeLa cells were incubated for the duration of the two days (media was replaced after 24 hours) before being washed twice with PBS and immersed in 4 ml of fresh complete media immediately before experimentation. In order to investigate the short-term effect of IL-1 on cell surface elasticity, IL-1β agonist was added to relevant dishes to a resulting concentration of 10^{-9} M, after the replacement of 4 ml media and as close to the start of data collection as was possible (following cantilever calibration). From *Figure 4.1* and previous studies, this represents a saturation point yielding a large inflammatory response and provides the best condition to observe changes in cell shape (Qwarnstrom et al., 1991; Zhang et al., 2010; Zhu et al., 1998). Measurement of the effect of increased TILRR on cellular elasticity was achieved through transfection of TILRR cDNA as described in *Section 2.2.5* alongside cultures transfected with EV to reveal the effect of the transfection process. Quantities of 1.5 μg of both EV and TILRR cDNA per dish were used throughout in order to ensure sufficient transfection efficiency and expression in cells (see *Section 4.2.2*). All conditions incorporating EV or TILRR cDNA were co-transfected with 1 μg of the GFP containing construct pEGFP-N2 per dish for identification of successfully transfected cells (see *Section 2.2.5*). A minimum of two cultures for each condition were measured to ensure that results were a product of biology and did not result from compromised cells.

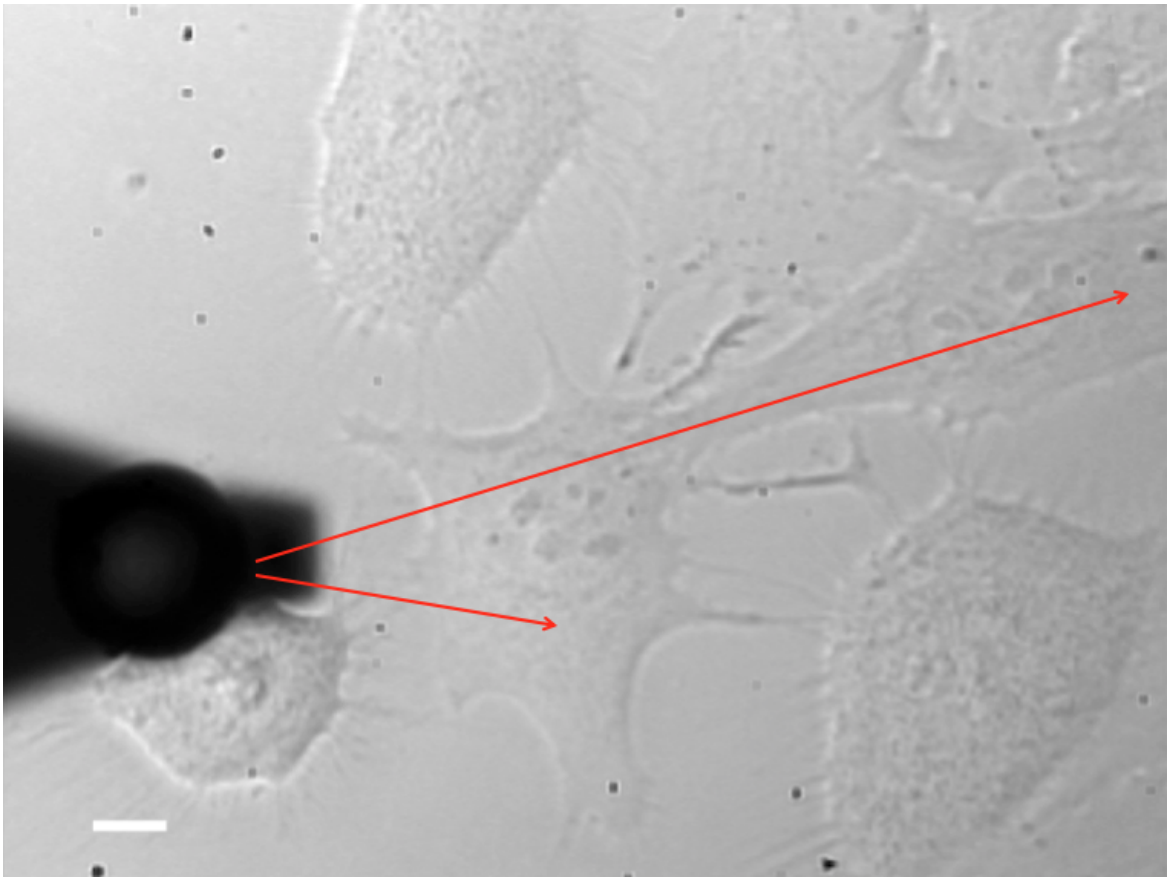

Fig. 6.5 An image of HeLa cells taken with the inverted MFP microscope. A probe functionalised with a 25 μm polystyrene colloid can clearly be seen out of contact with the surface. Representative regions of interest in terms of indentation measurement are indicated with arrows. Scale bar: 10 μm.

6.3.3 Indentation Measurements

The entirety of the data reported in this chapter were collected using the MFP, into which a pre-made and verified (*Section 2.5.4*) 25 μm diameter colloidal probe was loaded. A colloid diameter of 25 μm was selected in an attempt to ensure homogeneity in measurements across the surface due to its relatively large contact area when compared with conventional probes. MLCT tip-C was selected exclusively throughout these measurements due to it being the softest probe readily available. As has previously been stated, it is important when conducting indentation measurements to try to match the spring constant of the probe to the stiffness of the sample in attempt to indent the surface and deflect the cantilever symmetrically. This probe offered the best approximation to the soft eukaryotic cells. Force maps were conducted over the central region of the cell, but away from the nucleus, over an area of 25 μm^2 in a 4×4 grid. Each cell was mapped 10 times and 20 cells were mapped for each biological condition. A trigger set-point of 1 nN was selected throughout in order to avoid the extraction of a falsely high stiffness due to the non-linear stress-strain regime and to ensure reproducibility of successive measurements (Hayashi and Iwata, 2015). A 3 $\mu m \cdot s^{-1}$ approach and retract speed was selected which was held constant by operating the system with closed-loop feedback control. This speed was chosen to compromise between the apparent hardening of soft biological material when indenting at high speeds and the creeping of the surface away from the probe. The latter possibility can occur due to both repeated measurements and also from the initiation of biological responses when incident at low speeds (Guz et al., 2014). This speed also allowed for the acquisition of data in a reasonable amount of time with respect to the lifetime of the exposed cell culture. It should be noted that the inverted fluorescence system was incorporated when measuring cells transfected with GFP alongside either EV or TILRR cDNA in order to identify those that were transfected successfully. Values of 3 GPa, 0.33 and 0.5 were used for the Young

modulus of the polystyrene bead, the Poisson ratio of the polystyrene bead and the Poisson ratio of the cell respectively.

6.3.4 Analysis

Following data acquisition, the Hertz model was fitted to each curve individually from *Equation 2.12* using the Asylum Research software in Igor Pro and the Young modulus was extracted using *Equation 2.13*. Microsoft Excel and GraphPad Prism were used for statistical analysis and the production of plots respectively. After data processing and the successful extraction of Young moduli from each curve (in each force map) obtained under a particular biological condition, averages were deduced. Broad averages were taken over all 20 cells measured for each condition. The shape of resulting frequency distributions describing extracted Young moduli (using the Hertz model) for all conditions throughout this study can be described as positively-skewed log-normal distributions. Therefore median averages $\pm$ median absolute deviation (MAD) were extracted for each as these have previously been shown to adequately describe elasticity data of this form (Albon, 2015). Furthermore, the average elasticity of each individual cell measured for each condition was quantified from their respective frequency distributions of extracted elastic moduli. These are depicted in *Appendix C* in their entirety and a selection of representative distributions describing control HeLa cells can be observed in *Figure 6.6*. Individual cell elasticities were extracted in order to deduce the variation between cells which may result from their morphology, stage of their cell cycle, or from differences in the region of the surface mapped for each cell. These measurements also allow for the identification of the general trend of elasticity for each condition and for the identification and removal of anomalous cells from analysis which may skew the data. Outliers were defined as cells described by an average elastic modulus equal to or greater than two standard deviations (SDs) away from the mean value over all 20 cells. The shape associated with the distributions describing the extracted elastic moduli for each

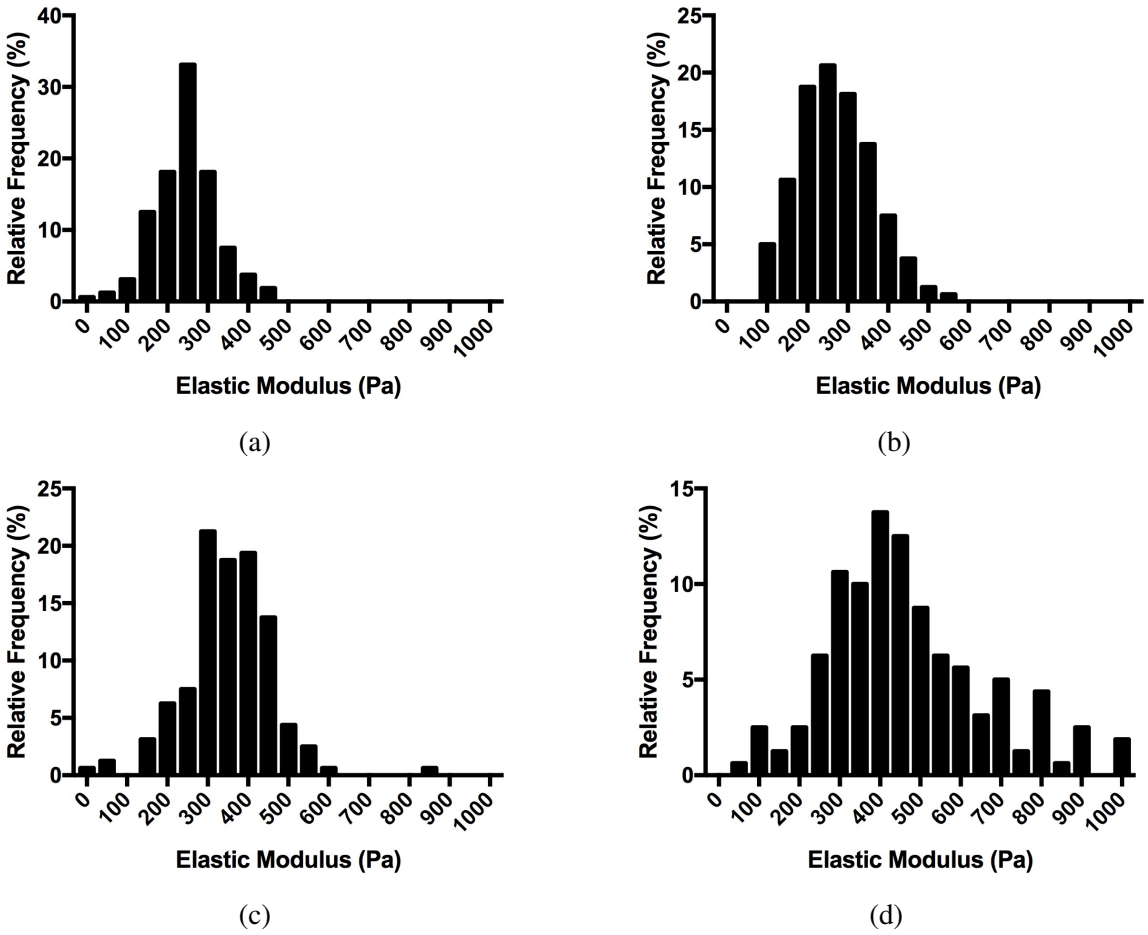

Fig. 6.6 Representative frequency distributions describing extracted elastic moduli from individual HeLa cells. Each distribution is the product of 10 repeated force-maps over the cell surface and each corresponds to a different HeLa cell (all unstimulated and absent transfection). These exhibit a shape best described by the normal distribution and suggest that mean values can be extracted from each with significant confidence.

individual cell (which in general are best described by normal distributions) infer that mean averages are appropriate for profiling each cell. It should be noted that associated SEMs for each cell (where n = number of force measurements) displayed in *Figure 6.7b*, *Figure 6.8b*, *Figure 6.9b*, *Figure 6.10b*, *Figure 6.11b* and *Figure 6.12b* are not biologically relevant and simply represent the confidence of the mean extracted from the AFM data. Mean values calculated over all cells for each condition are more biologically relevant (where n = number of cells).

6.4 Measurement of Elasticity Changes in HeLa Cells Resulting from TILRR Controlled Activation of IL-1RI

6.4.1 Elasticity of HeLa Cells

The elasticity of unstimulated HeLa cells (without any transfection) were measured as a control for the extraction of Young moduli for all other conditions using the experimental parameters described in *Section 6.3*. A frequency distribution displaying all Young moduli values extracted from the 20 control HeLa cells measured (up to 1 kPa) is displayed in *Figure 6.7a*. These data are described by a median average of 360 ± 140 Pa. *Figure 6.7b* displays the mean moduli extracted from each individual HeLa cell. A clear outlier is observed (cell 14, highlighted in grey) and is omitted from further analysis (average cell elasticity lies outside the range of $2 \times$ SD of the inferred mean over all 20 cells). This may be explained by the inclusion of substrate effects due to measurement over thin regions of cell, or by mapping over areas of the cell containing the nucleus or other organelles. Both of these factors result in the reporting of comparably stiffer modulus values. In fact, it is known that most causes of experimental error in force-indentation data will tend to increase the extracted Young modulus.

6.4.2 Elasticity of HeLa Cells Stimulated with IL-1

The elasticity of HeLa cells stimulated with IL-1β were measured to determine if the previously reported short-term effects on cell cytoskeletal structure resulting from IL-1RI activation result in a quantifiable change in surface elasticity. A frequency distribution displaying all Young moduli values extracted from the 20 HeLa cells stimulated with IL-1β is displayed in *Figure 6.8a*. These data are described by a median average of 160 ± 60 Pa. *Figure 6.8b* displays the mean moduli extracted from each individual HeLa cell stimulated with IL-1β. A clear outlier is observed (cell 3, highlighted in grey) and is omitted from

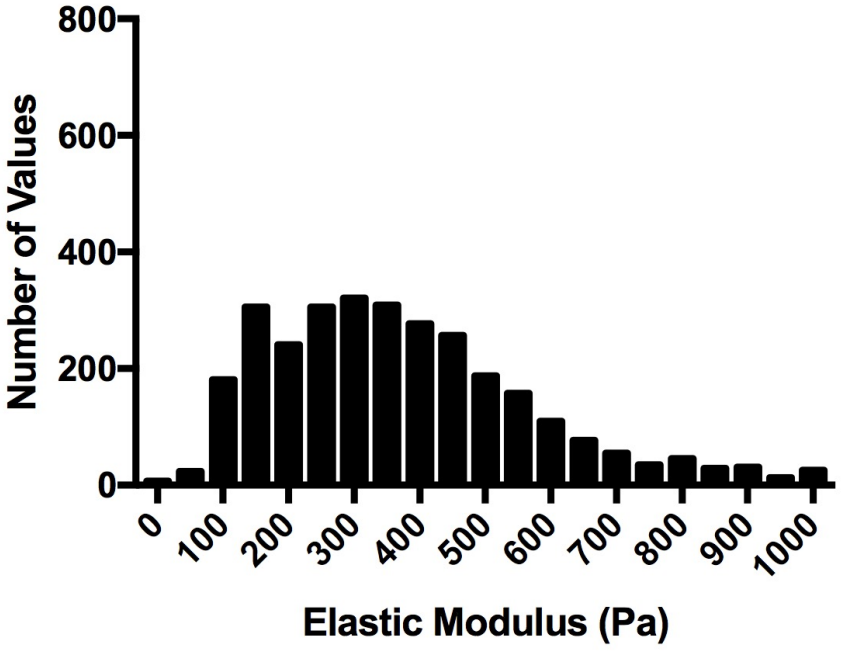

(a)

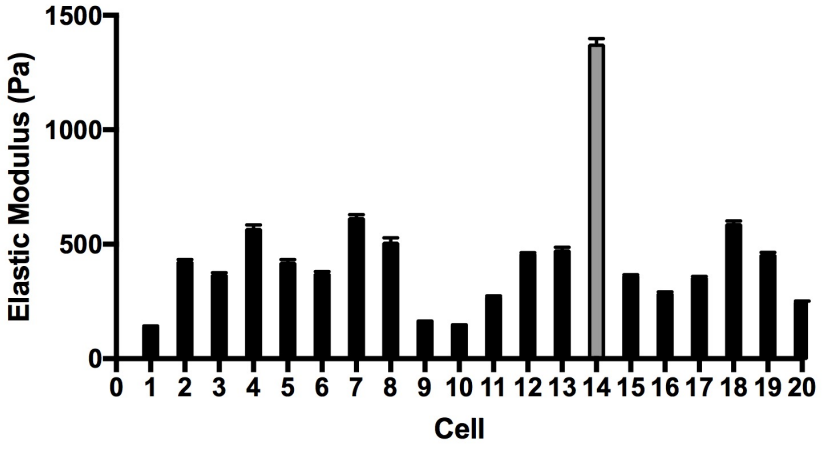

(b)

Fig. 6.7 Frequency distribution of all elastic moduli extracted from control HeLa cells (a). Described by a SD of 311 Pa. Mean elastic moduli extracted from each cell (b). Outliers are highlighted in grey.

further analysis (average cell elasticity lies outside the range of $2 \times$ SD of the inferred mean over all 20 cells).

6.4.3 Elasticity of HeLa Cells Transfected with EV

The elasticity of HeLa cells transfected with EV were measured as a control comparison for all other transfection conditions. It is known that transfection is abrasive and harmful to cells and as such it is possible that the stiffness of the cell surface is significantly altered. Furthermore it has been suggested that the harshness of the transfection procedure can illicit low levels of inflammatory mechanisms in cells and so this control is necessary for ay meaningful comparison of other transfected conditions (Jacobsen et al., 2009; Kim and Eberwine, 2010). A frequency distribution displaying all Young moduli values extracted from the 20 HeLa cells transfected with EV is displayed in *Figure 6.9a*. These data are described by a median average of 220 ± 80 Pa. *Figure 6.9b* displays the mean moduli extracted from each individual HeLa cell transfected with EV. A clear outlier is observed (cell 9, highlighted in grey) and is omitted from further analysis (average cell elasticity lies outside the range of $2 \times$ SD of the inferred mean over all 20 cells).

6.4.4 Elasticity of HeLa Cells Transfected with TILRR

The Young moduli of HeLa cells transfected with TILRR cDNA were measured to determine the effect on cell elasticity of TILRR amplified activation of IL-1RI with residual levels of IL-1. It has previously been shown that this condition is sufficient for activation of Ras GTPase with resulting cytoskeletal rearrangement similar to that observed under saturation of IL-1β (Zhang et al., 2010). A frequency distribution displaying all Young moduli values extracted from the 20 HeLa cells transfected with TILRR cDNA is displayed in *Figure 6.10a*. These data are described by a median average of 180 ± 90 Pa. *Figure 6.10b* displays the mean moduli extracted from each individual HeLa cell transfected with TILRR cDNA. Three

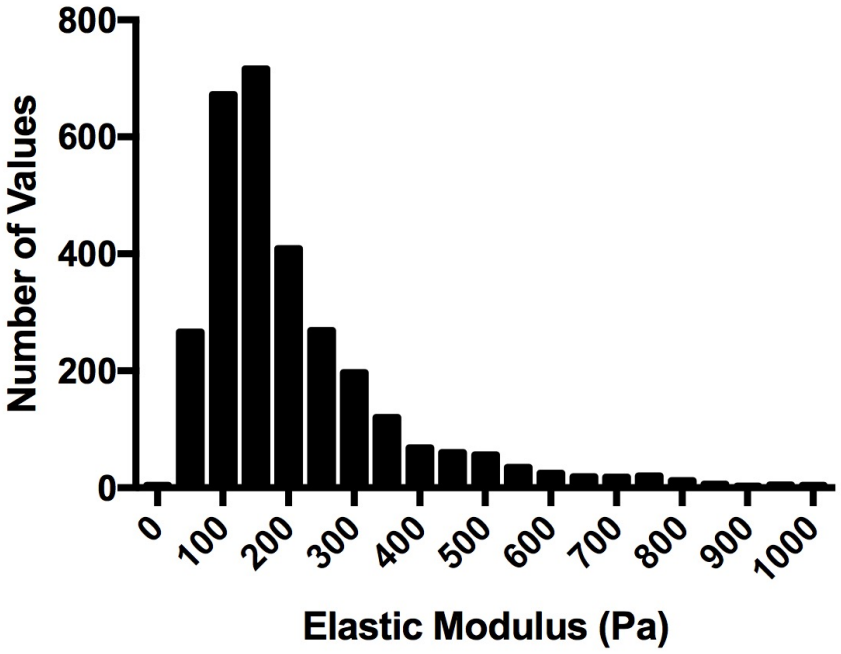

(a)

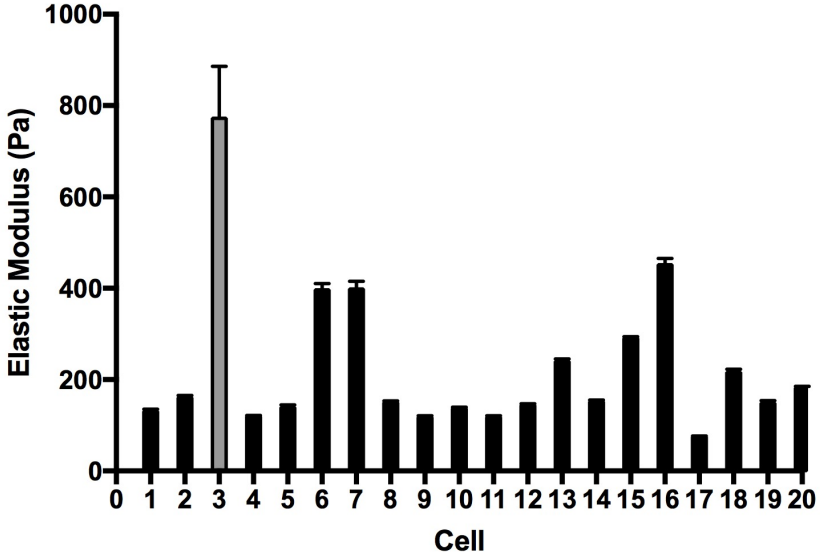

(b)

Fig. 6.8 Frequency distribution of all elastic moduli extracted from HeLa cells stimulated with 10^{-9} M IL-1β (a). Described by a SD of 245 Pa. Mean elastic moduli extracted from each cell (b). Outliers are highlighted in grey.

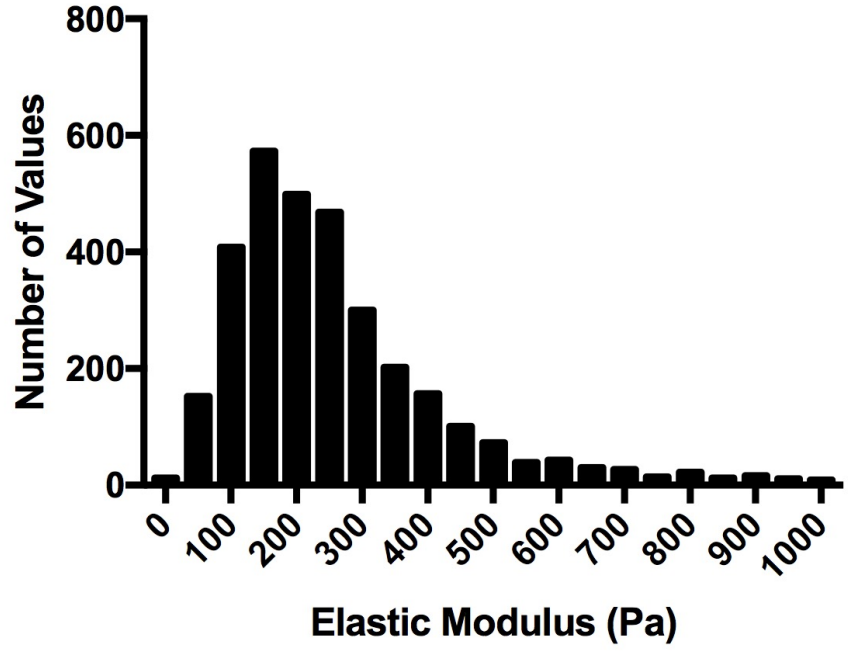

(a)

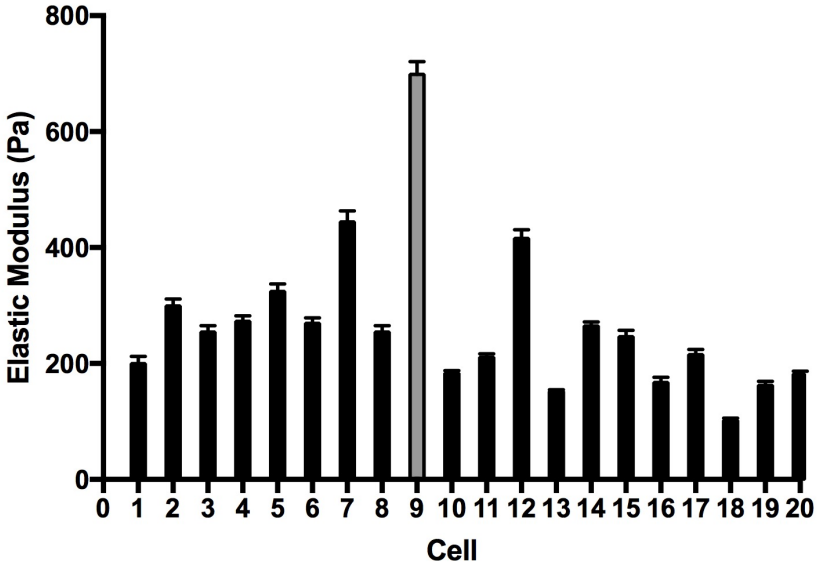

(b)

Fig. 6.9 Frequency distribution of all elastic moduli extracted from HeLa cells transfected with 1.5 μg EV (alongside 1 μg GFP) per dish (a). Described by a SD of 190 Pa. Mean elastic moduli extracted from each cell (b). Outliers are highlighted in grey.

clear outliers are observed (cell 2, cell 14 and cell 17, highlighted in grey) and are omitted from further analysis (average cell elasticity lies outside the range of $2 \times$ SD of the inferred mean over all 20 cells).

6.4.5 Elasticity of HeLa Cells Transfected with EV and Stimulated with IL-1

The elastic moduli of HeLa cells transfected with EV and stimulated with IL-1β were measured to deduce their elasticity resulting from IL1-RI activation with endogenous levels of TILRR. This has previously been reported to show similar changes in cell shape as cells transfected with TILRR cDNA and as such provides a good comparison with those investigated in this study (Qwarnstrom et al., 1991; Zhang et al., 2010; Zhu et al., 1998). Furthermore, the observed elastic moduli of these cells can be compared with those extracted from cells stimulated with IL-1β absent transfection in order to provide an insight into the magnitude Ras GTPase mediated change in surface stiffness for cells which have undergone different biological treatment. A frequency distribution displaying all Young moduli values extracted from the 20 HeLa cells transfected with EV and stimulated with IL-1β is displayed in *Figure 6.11a*. These data are described by a median average of 160 ± 70 Pa. *Figure 6.11b* displays the mean moduli extracted from each individual HeLa cell transfected with EV and stimulated with IL-1β. Two clear outliers are observed (cell 4 and cell 17, highlighted in grey) and are omitted from further analysis (average cell elasticity lies outside the range of $2 \times$ SD of the inferred mean over all 20 cells).

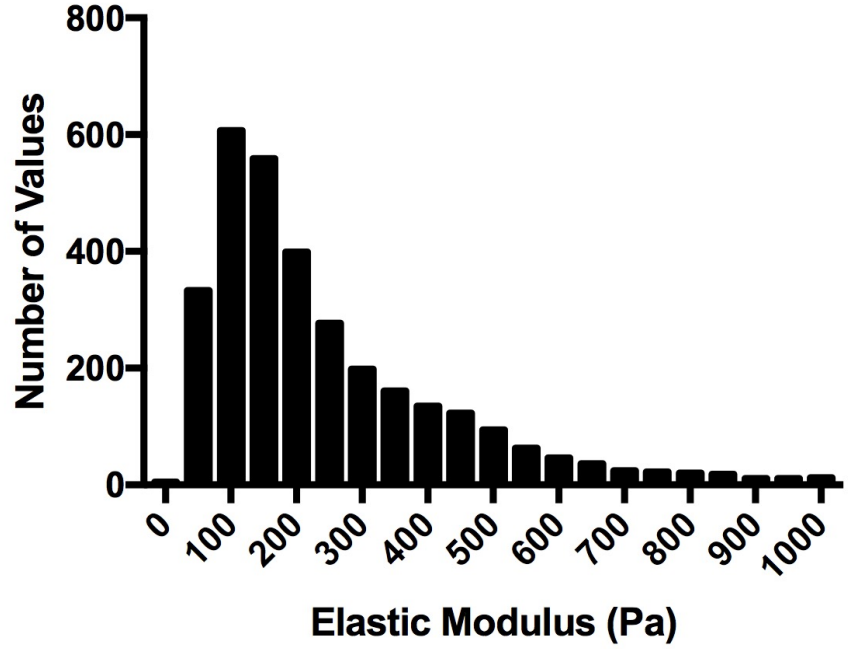

(a)

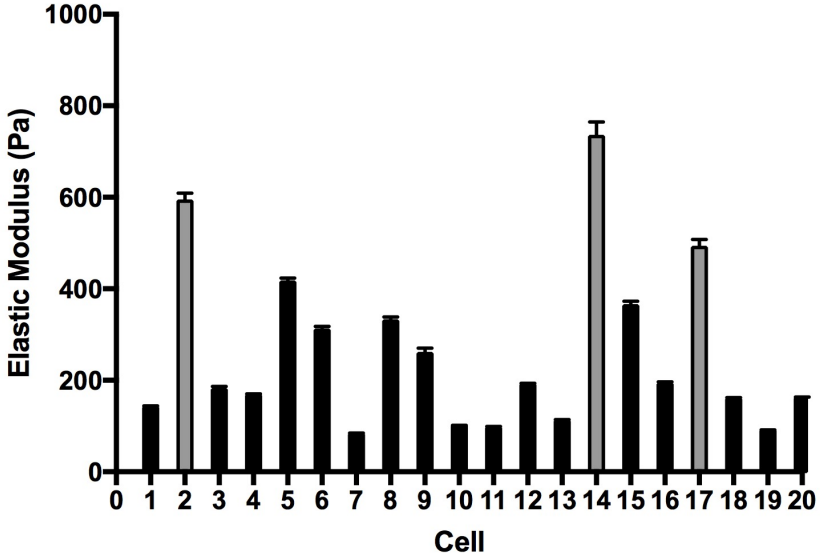

(b)

Fig. 6.10 Frequency distribution of all elastic moduli extracted from HeLa cells transfected with 1.5 μg TILRR cDNA (alongside 1 μg GFP) per dish (a). Described by a SD of 221 Pa. Mean elastic moduli extracted from each cell (b). Outliers are highlighted in grey.

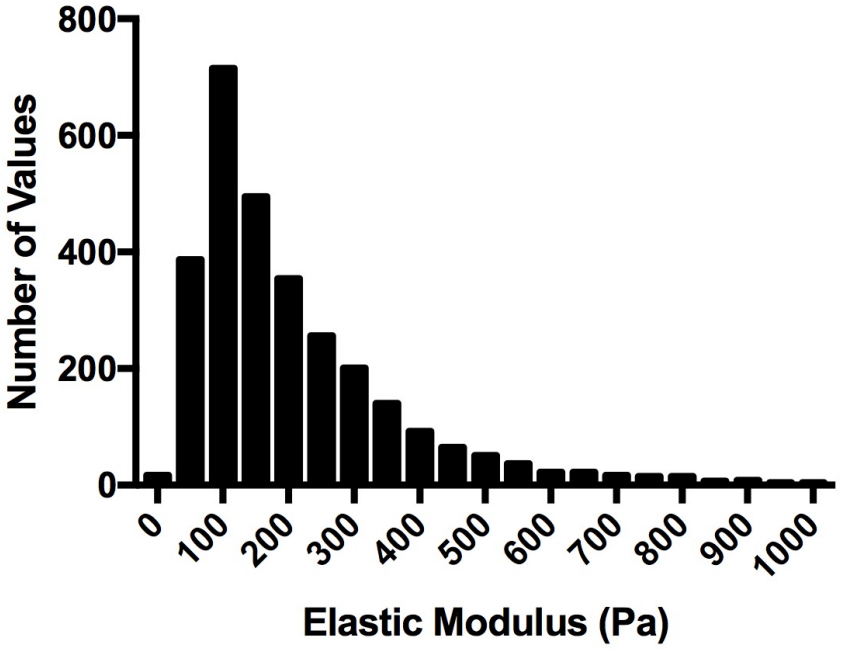

(a)

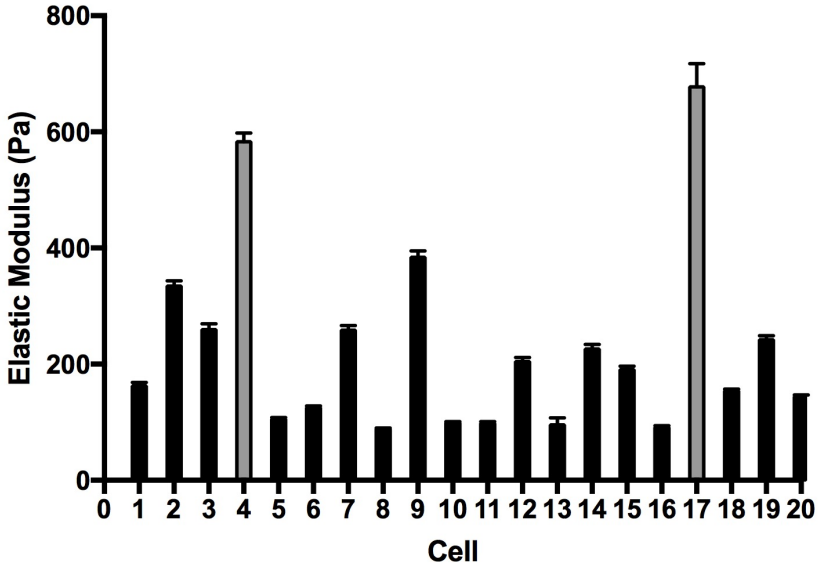

(b)

Fig. 6.11 Frequency distribution of all elastic moduli extracted from HeLa cells transfected with 1.5 μg EV (alongside 1 μg GFP) per dish and stimulated with 10^{-9} M IL-1β(a). Described by a SD of 216 Pa. Mean elastic moduli extracted from each cell (b). Outliers are highlighted in grey.

6.4.6 Elasticity of HeLa Cells Transfected with TILRR and Stimulated with IL-1

The elastic moduli of HeLa cells transfected with TILRR cDNA and stimulated with IL-1β were measured to examine the result on cell elasticity due to IL-1RI activation in cells over-expressing TILRR at saturated levels of IL-1 (and maximal inflammatory activation). This can be compared with measured cells independently transfected with TILRR cDNA or stimulated with IL-1β in order to ascertain how sensitive any changes in surface elasticity are to increased stimuli or if the shape changes observed in previous studies are maximally induced by both TILRR transfection with residual levels of IL-1 and IL-1β stimulation with endogenous levels of TILRR (Qwarnstrom et al., 1991; Zhang et al., 2010; Zhu et al., 1998). A frequency distribution displaying all Young moduli values extracted from the 20 HeLa cells transfected with TILRR cDNA and stimulated with IL-1β is displayed in *Figure 6.12a*. These data are described by a median average of 150 $\pm$ 60 Pa. *Figure 6.12b* displays the mean moduli extracted from each individual HeLa cell transfected with TILRR cDNA and stimulated with IL-1β.

6.4.7 Presentation of Results

Median average values extracted from frequency distributions containing all elastic moduli extracted for each biological condition (see *Figure 6.7a*, *Figure 6.8a*, *Figure 6.9a*, *Figure 6.10a*, *Figure 6.11a* and *Figure 6.12a*) are summarised in *Table 6.1*. Mean modulus values which have been extracted from the calculation of individual mean values for all measured cells (see *Appendix C*) are summarised in *Table 6.2*. *Figure 6.13* describes the weighting of extracted mean averages from individual cells for each biological condition. The range and interquartile range describing these data are summarised in *Table 6.3*.

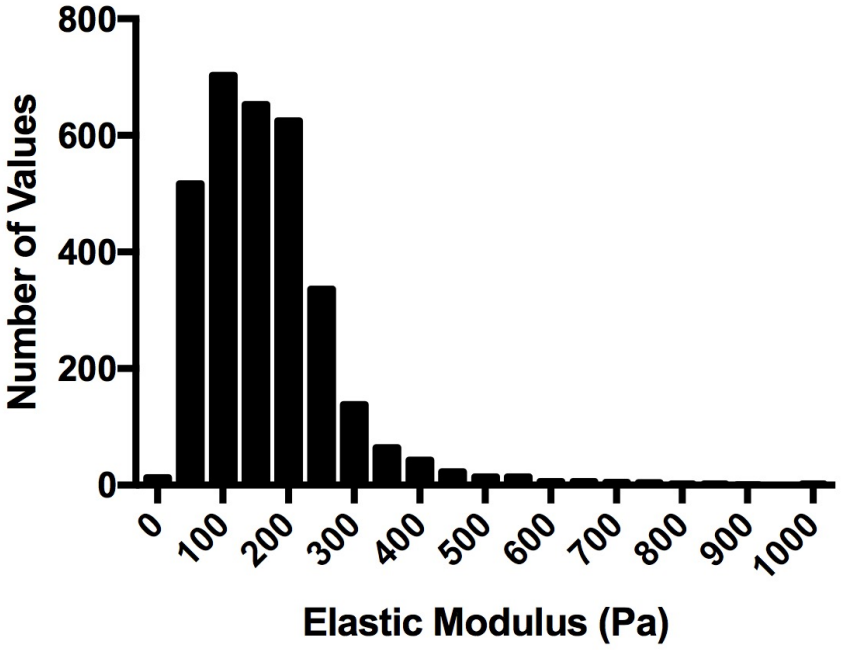

(a)

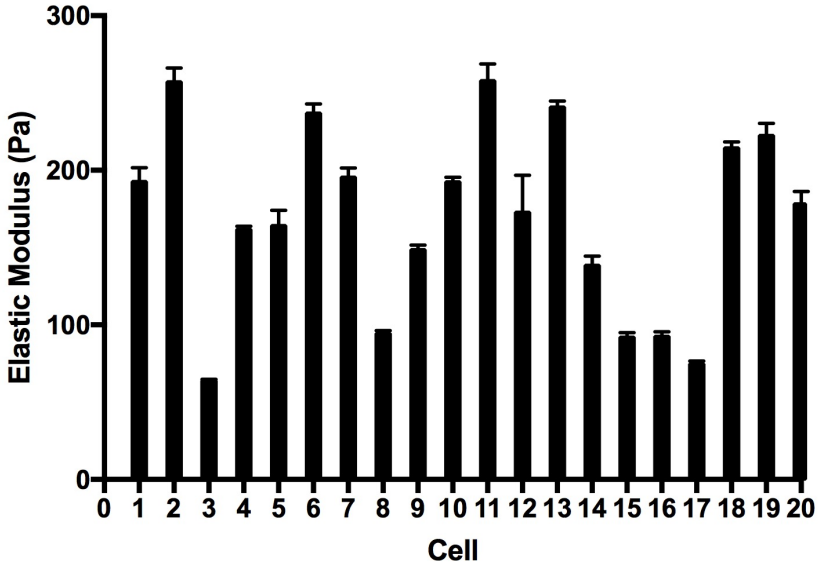

(b)

Fig. 6.12 Frequency distribution of all elastic moduli extracted from HeLa cells transfected with 1.5 μg TILRR cDNA (alongside 1 μg GFP) per dish and stimulated with 10^{-9} M IL-1β (a). Described by a SD of 193 Pa. Mean elastic moduli extracted from each cell (b).

Table 6.1 Median elasticity values across all extracted elastic moduli for each cell condition where $+$ represents stimulation with 10^{-9} IL-1β and $-$ represents unstimulated cells.

HeLa Cell Condition	Median Elastic Modulus $\pm$ MAD (kPa)
HeLa (-)	0.36 ± 0.14
HeLa (+)	0.16 ± 0.06
EV Transfection (-)	0.22 ± 0.08
TILRR cDNA Transfection (-)	0.18 ± 0.09
EV Transfection (+)	0.16 ± 0.07
TILRR cDNA Transfection (+)	0.15 ± 0.06

Table 6.2 Mean elasticity values across all extracted elastic moduli for each cell condition where $+$ represents stimulation with 10^{-9} IL-1β and $-$ represents unstimulated cells. Averages were derived from means calculated for each cell measured.

HeLa Cell Condition	Mean Elastic Modulus $\pm$ SEM (Pa)
HeLa (-)	380 ± 35
HeLa (+)	200 ± 25
EV Transfection (-)	240 ± 20
TILRR cDNA Transfection (-)	195 ± 25
EV Transfection (+)	180 ± 20
TILRR cDNA Transfection (+)	170 ± 15

Table 6.3 The range and interquartile range of the average elastic modulus values extracted from each cell for a given condition where $+$ represents stimulation with 10^{-9} IL-1β and $-$ represents unstimulated cells.

HeLa Cell Condition	Range (kPa)	Interquartile Range (kPa)
HeLa (-)	0.14 - 0.61	0.27 - 0.47
HeLa (+)	0.07 - 0.45	0.13 - 0.24
EV Transfection (-)	0.10 - 0.44	0.18 - 0.27
TILRR Transfection (-)	0.08 - 0.41	0.11 - 0.28
EV Transfection (+)	0.09 - 0.38	0.10 - 0.25
TILRR cDNA Transfection (+)	0.06 - 0.26	0.11 - 0.22

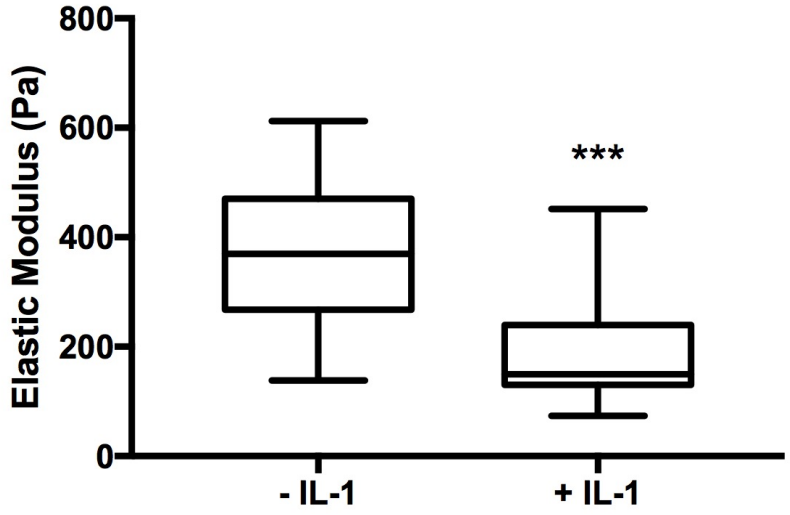

(a)

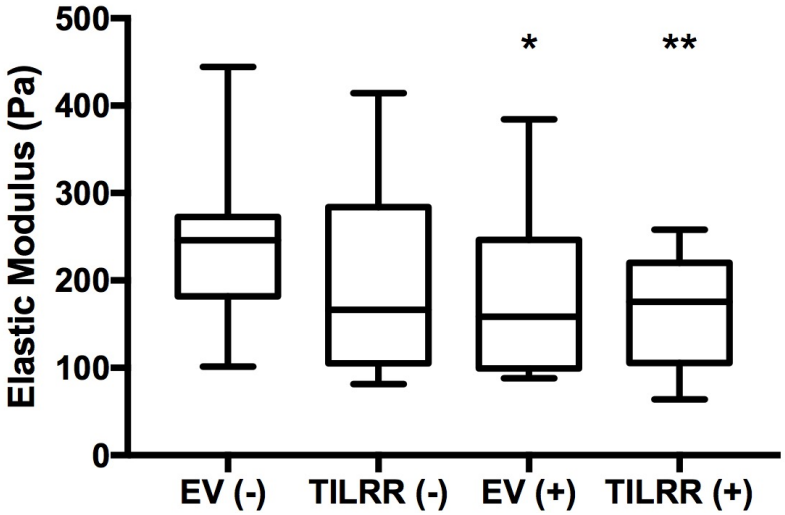

(b)

Fig. 6.13 The spread and weighting of mean elastic moduli (extracted from individual cells) for control HeLa cells (−IL-1) alongside HeLa cells stimulated with 10^{-9} M IL-1β (+IL-1; a) and for cells transfected with 1.5 μg EV or TILRR cDNA (alongside 1 μg GFP) per dish where + represents stimulation with 10^{-9} IL-1β and − represents unstimulated cells (b). Significance in relation to controls, −IL-1 and EV(−), was determined using both unpaired t-tests and Mann-Whitney non-parametric tests (*$0.01 < p < 0.05$, **$0.001 < p < 0.01$, ***$0.0001 < p < 0.001$).

6.5 Discussion

The frequency distributions representing all extracted Young moduli for each condition take the form of positively-skewed log-normal distributions. As such the median can provide a reasonable general average for each condition in order to reveal how IL-1RI activation affects HeLa cell elasticity (Albon, 2015). These averages however provide little insight into the IL-1 induced effects on individual cell profiles. Median averages are summarised in *Table 6.1* and the statistical significance between medians of two conditions was deduced using the Mann-Whitney non-parametric test. Control HeLa cells were found to exhibit a median elastic modulus of $\backsim$ 360 Pa using the experimental parameters outlined in *Section 6.3*. This correlates well with reports from other cancerous cell lines, including studies designed to probe the cell cortex in cervical cells, measured using similar methodologies, trigger forces and indentation depths (Hayashi and Iwata, 2015; Zhao et al., 2015). A variety of Young moduli have been reported for HeLa cells (using the force-indentation technique) by different groups and these discrepancies seem to stem from selected experimental perimeters, the location of the cell studied and the shape of the indenter (which relates to the contact area between the cell and the probe; Hayashi and Iwata 2015; Tomankova et al. 2012). As shown in *Section 6.2* the contact area and the region of the surface measured have a significant effect on the magnitude of the extracted modulus and the apparent variation across the surface. In fact, the $\backsim$ 40 kPa modulus extracted from the observed stiffer region of the cell at the centre (likely to be the nucleus) in *Figure 6.1b* corresponds very well with reported values in these previous studies in which the nuclear region was measured. When pyramidal probes were replaced with colloidal probes (resulting in an increase in tip-cell contact area) the observed elasticity of the cell was much more heterogeneous. These probes along with relatively shallow indentation depths (the order of hundreds of nm) seemed to allow for the mechanical profiling of the actin cortex (Fritzsche et al., 2016).

HeLa cells stimulated with IL-1β at saturation show a statistically significant reduction ($p < 0.0001$) in median Young's modulus of $\backsim 55\%$ when compared to control cells. This reduction in stiffness is supported by observations in previous studies which describe a dramatic rearrangement of the actin cytoskeleton in response to activation of IL-1RI resulting in a pronounced rounding of cell shape (Qwarnstrom et al., 1991; Zhang et al., 2010; Zhu et al., 1998). Furthermore, this effect has been reported by many other groups in a variety of different cells and Liu et al. (1994) observed that the change in cell shape was accompanied by a complete dissolution of filamentous actin (Komine et al., 2001; Lee et al., 2004; Qi et al., 2006b). The large observed reduction in median elastic modulus of cells stimulated with IL-1β when compared to control cultures clearly demonstrates that the previously reported changes in cellular shape and structure results in a general softening of the cell which can likely be attributed to the disorganisation of cytoskeletal actin. This then demonstrates that pronounced changes in the cytoskeleton can be observed via external physical measurement of the cell using the AFM which provides further evidence that cell stiffness is generally dictated by cytoskeletal structure (Haase and Pelling, 2015; Kubitschke et al., 2017). Physically, this reduction in elastic modulus is logical as, from previous staining studies by Zhu et al. (1998), the induced rearrangement is a clear disorganisation and without a rigid filamentous scaffold, the cellular structure is less well defined. A similar reduction in elastic modulus was observed for human tenocytes under more long term exposure to IL-1β by micropipette aspiration alongside a disruption of actin filaments (Qi et al., 2006b). Additionally a reduction in cell stiffness, of similar magnitude to the decrease in modulus here, was observed by direct disruption of actin filaments in living cells using cytochalasin D (Wang, 1998). It should be noted that the apparent decrease in cell deformability (and implied increase of elastic modulus for a proportion of the cell population due to IL-1β) as observed in preliminary RTDC measurements (see *Section 2.3*) may suggest different structural effects in suspended

cells (in which the internal structure is likely to be significantly different in the absence of focal adhesions etc.) but this is unclear.

When comparing cells transfected with EV and GFP against control HeLa cells a statistically significant ($p < 0.0001$) reduction in median elastic modulus of $\backsim 40\%$ is observed which indicates that the transfection process itself results in the softening of HeLa cells. This is logical as the transfection of plasmid is somewhat toxic to cells and has been shown to induce a variety of transcription factors, including pro-inflammatory NF-κB, which has been attributed to the observation of false phenomena in a range of studies (Jacobsen et al., 2009; Kim and Eberwine, 2010). HeLa cells transfected with TILRR cDNA exhibited a $\backsim 50\%$ and $\backsim 20\%$ reduction in elastic modulus when compared with control HeLa cells ($p < 0.0001$) and HeLa cells transfected with EV ($p < 0.0001$) respectively. This reduction in comparison with cells transfected with EV infers that an increase in TILRR expression results in detectable alterations in cell stiffness, likely impacting the structure of the cytoskeleton, alongside endogenous levels of IL-1. Previous studies have shown that the changes in cell shape and cytoskeleton depend upon the substrate (requiring sufficient ECM components, particularly FN) and occur under conditions designed potentiate both endogenous TILRR expression and TILRR association with IL-1RI (Caunt et al., 2001; Vallés et al., 1999; Zhu et al., 1998). This is supported by Zhang et al. (2010) who reported pronounced changes in cell shape for unstimulated cells expressing increased TILRR, which were comparable to those observed for cells stimulated with saturated levels of IL-1. The study also demonstrated that inhibition of TILRR using siRNA resulted in no change in cell shape under IL-1 stimulation suggesting that TILRR is vital for these structural changes to occur. The present study reinforces the potency of TILRR (in the presence of FN) on these mechanical effects. It should be noted that the elastic modus for cells transfected with TILRR cDNA does not seem to be as low as the modulus observed for HeLa cells in cultures that were stimulated with IL-1 (despite the relatively large errors associated with these medians; $p < 0.0001$) and

may suggest a smaller structural effect on cells transfected with TILRR cDNA in comparison to those saturated with IL-1 which seems logical.

HeLa cells transfected with EV and stimulated with IL-1β were shown to exhibit a $\backsim 55\%$ reduction in median elastic modulus when compared with control cells ($p < 0.0001$) and a $\backsim 25\%$ reduction when compared with unstimulated cells transfected with EV ($p < 0.0001$). The extracted median average for this biological condition (and the reduction from control HeLa cells) is very similar to the value extracted for cells stimulated with IL-1 absent transfection and suggests a very similar cytoskeletal rearrangement indicating that, while having an effect on the elasticity of the cell, the transfection procedure does not affect the reduced elasticity of cells that are saturated with IL-1. This may infer either very similar cytoskeletal affect (with comparable magnitude) for all cells in response to IL-1RI activation or may describe a lower limit on cell modulus due to IL-1 saturation and associated structural effects. The very similar median average extracted from HeLa cells both transfected with TILRR cDNA and stimulated with IL-1β (exhibiting only a small reduction from other stimulated conditions [$p < 0.0001$] and a $\backsim 30\%$ reduction when compared with unstimulated cells transfected with EV [$p < 0.0001$]) further supports these suggestions. It has been reported that, for some intracellular mechanisms, the TILRR potentiating effects on IL-1RI activation are greatly reduced (and in some cases negligible) alongside saturated levels of IL-1 (Nichols, 2017). Under a lower dose of IL-1 greater differences in elasticity between stimulated cells and those both stimulated and transfected with TILRR cDNA may have been observed. It is possible that a lower limit on the Young modulus due to TILRR controlled IL-1RI activation is observed here due to a complete cytoskeletal disruption under the saturation of IL-1 (particularly when plated on FN). The median averages of elastic moduli reported here support observations in previous studies which demonstrate substantial changes in cell shape induced by TILRR association with IL-1RI (Zhang et al.,

2010). Furthermore, this work has revealed the potent effect on mechanical properties of the cell that these effects have.

The mean elastic moduli (extracted from mean values calculated for each individual cell) for each biological condition are summarised in *Table 6.2*. These values may be a more appropriate representation of the average trend for each condition, particularly with respect to measurement of the cytoskeletal cortex, due to the omission of anomalous cells. It should be noted that all omitted outliers were of significantly higher elastic modulus and may result from the acquisition of force-indentation data over regions of the cell containing organelles or on thinner parts of the surface where substrate effects are experienced by the probe. It has been reported that these effects may be relevant if more than 10% of the cell thickness is indented (Kuznetsova et al., 2007; Marthur et al., 2001). The mean elastic moduli exhibit almost identical reductions in modulus as the median moduli (extracted from all force-indentation measurements) when compared with relevant controls. The range and weighting of the mean elastic moduli for each measured cell are described in *Figure 6.13* (alongside statistical significance from control cultures) and *Table 6.3*. *Figure 6.13a* shows that the entire range of mean moduli extracted from each HeLa cell stimulated with IL-1β exhibits a general shift towards lower magnitude and the size of the interquartile range is reduced when compared with control cells. It is possible that the wider interquartile range in control cultures may result from a variation in cytoskeletal structure between cells (resulting from differences in cell shape, in the locations of cell-ECM adhesive contacts and from other general mechanical variations) which under IL-1 saturation is disrupted to a comparable degree in most cells.

It can be seen from *Figure 6.13b* that the moduli of cells which have undergone transfection are significantly lower than control HeLa cells. This reduction seems to affect the whole range of measured cells (as transfected cells were specifically targeted using GFP) and infers that the transfection of plasmids into eukaryotic cells, at quantities sufficient to induce

significant gene expression, has a large effect on the mechanical structure of the cell. While the toxicity of transfection on cells is widely appreciated, no reports of its affect on cell mechanics were found in a review of literature while composing this thesis. Transfection of TILRR cDNA into cells alongside endogenous levels of IL-1 seemed to result in a weighting of the interquartile range at lower elastic moduli but the distribution obtained here was not deduced to be statistically significant from control transfection cultures. Saturation of IL-1β in cells transfected with EV reduced the weighting of the interquartile range and was deduced to be statistically significant when compared to control cultures. Combined transfection of TILRR cDNA and stimulation of IL-1β similarly resulted in a statistically significant weighting of the interquartile range at lower elastic moduli when compared with control cells. When compared with cells transfected with EV and stimulated with IL-1β the extracted average elastic moduli were very similar. However the upper range of cells seems to be significantly reduced for those transfected with TILRR and saturated with IL-1 and the significance from control cells was noticeably higher. This may indicate a TILRR induced potentiation of the IL-1RI signal in cultures not by increasing the magnitude of the signal exhibited by activated cells (resulting in more pronounced actin disorganisation), but by making the cells more sensitive to activation by IL-1 and subsequently resulting in higher numbers of signalling cells. A study by (Tay et al., 2010) reported a digital character of NF-κB activation (here activated by stimulant tumor necrosis factor alpha [TNFα]) in cells and that the overall response was largely governed by the number of cells activated. Furthermore the study reports that cells were activated heterogeneously (some cells seemed to respond to stimulant while others did not) and the proportion activated was largely related to the concentration of stimulant in media. This reduced upper range of extracted moduli for cells both transfected with TILRR cDNA and stimulated with IL-1β (which may reflect a higher proportion of cells measured with disrupted cytoskeletal structures) could indicate a similar digital mechanism of NF-κB activation induced by IL-1β as observed for TNFα.

Furthermore, studies have shown that amplification of IL-1RI activation due to TILRR result both from an increase in receptor expression and from increased binding of IL-1 upon association with the receptor complex (Zhang et al., 2012, 2010). Consideration of these studies with the results presented here may suggest a TILRR facilitated increased sensitivity to stimulus at the single cell level. It should be noted that no statistical significance was found between HeLa cells stimulated with IL-1β, HeLa cells transfected with TILRR cDNA, HeLa cells transfected with EV and stimulated with IL-1β and HeLa cells transfected with TILRR cDNA and stimulated with IL-1β.

6.6 Summary and Conclusion

To summarise, preliminary measurements conducted with RTDC (see *Section 2.3*) seemed to suggest an increase in the elastic modulus of HeLa cells under inflammatory conditions (IL-1β stimulus). However as RTDC performs best on suspended, spherical cells and, as HeLa cells are generally surface adherent and heterogeneous in shape, it was deduced that these results are not conclusive. Furthermore these results seem to contradict studies on attached cells using the AFM. It should be noted however that, should this change in elasticity result from structural effects following IL-1 stimulation, these results may infer different mechanical mechanisms for cells in suspension when compared with adhered cells. Indentation experiments on cells were tested using both pyramidal and colloidal probes. It was deduced that using pyramidal probes resulted in too great a variation of extracted Young moduli to generate any useful average values in characterising the cell as a whole. This was due to small contact areas which are elastically affected by small changes in cellular composition and would negate any comparison between cells under different biological conditions. By using colloidal probes however, macroscale measurements seemed to yield reproducible results and were conducted over the central region of the cell but away from the nucleus. This region seemed to exhibit the smallest variation in elasticity and was therefore the most feasible in generating defined averages for cells under different biological conditions.

HeLa cells were found to exhibit an average elastic modulus of $\backsim$ 360 Pa (median) to $\backsim$ 380 Pa (mean) which is consistent with measurements of cancerous cervical cells (among numerous other cancerous cell lines) in previous studies (Hayashi and Iwata, 2015; Zhao et al., 2015). Initiation of pro-inflammatory responses by stimulation with IL-1 has been shown to reduce the modulus by $\backsim$ 55%. This is in agreement with more long-term studies of IL-1 treatment on human tenocytes (Qi et al., 2006a,b). Furthermore, these results support work published by Zhu et al. (1998) and Qwarnstrom et al. (1991) which clearly

demonstrate that short term effects of stimulation with IL-1β dramatically disorganises the the actin cytoskeleton and changes the cell shape under conditions designed to amplify TILRR association with IL-1RI. Subsequent studies by Caunt et al. (2001) and Zhang et al. (2010) revealed that this these effects result from IL1-RI activation of the GTPase Ras and that this activation is controlled by TILRR (with an increase in TILRR expression permitting these structural changes at residual levels of IL-1 and an inhibition of TILRR preventing them even under IL-1 saturation). Co-transfection of EV and GFP was shown to have a large effect on the mechanical properties of the cell and may be attributed to cytotoxicity and the activation of various transcription factors (Jacobsen et al., 2009; Kim and Eberwine, 2010). Cells co-transfected with TILRR cDNA and GFP seem to exhibit a reduction in elastic modulus when compared with control (transfected) cells but this was not deduced to be statistically significant. Cells both transfected with EV and stimulated with IL-1 exhibited a similar elastic modulus to those stimulated absent transfection and may therefore infer a similar cytoskeletal effect or a lower limit on the elastic modulus under IL-1 saturation. A reduced interquartile range (and complete range) of the extracted Young moduli for cells both transfected with TILRR cDNA and stimulated with IL-1 when compared with other saturated cultures may suggest that the TILRR induced potentiation of IL-1RI activation occurs by increasing sensitivity to stimulants at the single cell level.

Chapter 7

Conclusions and Further Work

The work presented throughout this thesis has used physical techniques to probe ligand-receptor binding interactions between both proteoglycans (PGs) and cell-surface receptors with extracellular matrix (ECM) component fibronectin (FN) and has also investigated the mechanical and adhesive effects of heparan sulfate proteoglycan (HSPG) Toll-like and interleukin-1 receptor regulator (TILRR; as a co-receptor and signal amplifier of the interleukin-1 receptor, type I [IL-1RI]) on HeLa cells. To achieve these measurements a variety of force-sensitive applications of the atomic force microscope (AFM) were employed including imaging, rupture-force spectroscopy and indentation-force spectroscopy in order to visualise biological material on surfaces, characterise unbinding events between biomolecules and measure cell elasticity. In tandem, a variety of biological and chemical methods were utilised to increase the expression of TILRR in cells and to manipulate the surface properties of both AFM probes and substrates for the affixion of proteins.

The work conducted in *Chapter 3* revealed energy barriers describing the unbinding between substrate immobilised FN and recombinant syndecan-4 (SDC4), decorin (DCN) and integrin $\alpha_5\beta_1$ ($\alpha_5\beta_1$), grafted to the apex of the AFM probe. A single energy barrier was uncovered describing the interaction between SDC4 and FN which was characterised by

$\chi_B = 3.4 \pm 0.2$ Å, $k_{off}^0 = 2.4 \pm 0.4$ s^{-1} and $\Delta G = 15.2 \pm 0.2\, k_B T$. Comparison of these kinetics with those extracted from the unbinding between heparin (Hep) and FN ($\chi_B = 3.1 \pm 0.2$ Å and $k_{off}^0 = 0.2 \pm 0.1$ s^{-1}) by Mitchell et al. (2007) suggests a similar barrier width, and therefore bond deformability, between the HS chain in SDC4 with FN as for the Hep-FN interaction. This may suggest that the compliance of the bond formed between all heparin sulphate (HS) chains (in all HSPGs) with FN are comparable, regardless of the pattern of sulphation. This value seems logical for cell surface HSPGs which, when interacting with the ECM, may have to undergo relatively large deformations while remaining bound to permit signal regulatory functions. The equilibrium dissociation rate extracted from SDC4-FN unbinding was found to be approximately twelve times higher than that extracted from the Hep-FN study by Mitchell et al. (2007), inferring a significantly lower affinity bond. Therefore, despite a similar barrier width, it seems that the degree to which the HS glycosaminoglycan (GAG) chain is sulphated significantly affects its ability to form strong bonds and may suggest that by specific pattering of the PG GAG chain, the binding affinity with ECM components can be modulated deliberately.

A single energy barrier was uncovered for the unbinding between DCN and FN. This was characterised by $\chi_B = 1.4 \pm 0.1$ Å, $k_{off}^0 = 40 \pm 4$ s^{-1} and $\Delta G = 12.4 \pm 0.1\, k_B T$. The extracted energy barrier suggests a brittle bond which is resistant to external forces but can exhibit little deformability. DCN is prevalent within the ECM and binds along fibrils of collagen and FN. As it is not a cell surface receptor this brittle nature may be preferable in sustaining the interaction as it may be exposed to significant shear stress but little deformation. Comparison of the barrier width with SDC4-FN unbinding and with other studies may suggest that this bond results from the interaction of the DCN core protein with the RGD site in FN (as opposed to the chondroitin sulphate [CS] GAG chain with Hep binding sites). In future studies it may be interesting to expose DCN to a chondroitinase and test if binding persists absent CS chains and also if the characteristics of any resulting energy barriers are affected.

The equilibrium dissociation rate extracted from this barrier reveals a low affinity bond which is significantly weaker than binding strengths extracted using other techniques. This may indicate the presence of an outer, more compliant barrier that is only observable under low loading conditions and at very low rupture forces. This barrier may have been suppressed in the loading range probed in this study. Further single-molecule measurements taken at low retraction velocities (and possibly with more sensitive AFM probs such as OBLs) may be able to reveal this barrier should it exist.

The unbinding between $\alpha_5\beta_1$ and FN was shown to be governed by two energy barriers which is consistent with other DSMFS measurements on integrin-ECM interactions. This allows the character of the bond to be modulated in response to external loading stimuli. The internal energy barrier is characterised by $\chi_B = 0.69 \pm 0.03$ Å, $k_{off}^0 = 70 \pm 40$ s^{-1} and $\Delta G = 11.9 \pm 0.6\ k_B T$ and the external energy barrier by $\chi_B = 6.6 \pm 0.7$ Å, $k_{off}^0 = 0.18 \pm 0.13$ s^{-1} and $\Delta G = 17.8 \pm 0.7\ k_B T$. The internal barrier is highly brittle and allows the bond to remain resistant to significant forces under high loading conditions. This is likely to result from an ionic bond formed between the RGD peptide in FN and the Mg^{2+} ion (located in the metal ion-dependent adhesion site) in the β-component of $\alpha_5\beta_1$ and is likely to be crucial to the stability of cell attachment under large external stresses. The outer energy barrier is much more elastic and describes a more deformable character of the bond under low loading conditions. This may be important in permitting cell migration. The estimated binding affinity (extracted from the equilibrium dissociation rate of the outer barrier) is consistent with values obtained in other studies using different techniques.

The results presented in *Chapter 5* and *Chapter 6* characterise the adhesive and mechanical effects of the TILRR potentiated activation of IL-1RI in HeLa cells. IL-1RI activation by the binding of ligand interleukin-1 (IL-1) activates NF-κB which subsequently induces the expression of many pro-inflammatory genes. Amplification of IL-1RI function by HSPG co-receptor TILRR requires the binding of the HS GAG chain with extracellular FN at the

cell edge. It has been shown by Zhang et al. (2010) that IL-1RI amplification by TILRR induces activation of the Ras GTPase which subsequently results in pronounced changes in cell shape, cytoskeletal organisation and contact with the ECM at focal adhesions. The results described in *Chapter 5* demonstrate that TILRR amplification of IL-1RI results in a $\backsim 40\%$ reduction in the strength of binding between HeLa cells and FN at the cell edge. This infers a general reduction in adhesive strength at focal adhesion sites between cells and the ECM. It is likely that this change in cell attachment results from a reduction in binding strength between FN and the $\alpha_5\beta_1$ integrin due to conformational changes in the receptor complex. This in turn is likely to result from the aforementioned changes in the cytoskeleton and possibly from the previously observed phosphorylation and redistribution of talin at focal adhesions (under IL-1 saturation and in the presence of FN) which forms a direct link between the cytoskeleten and integrins. When considered in the context of IL-1RI, it is possible that this reduction in adhesion may increase the capacity for cell migration at the site of injury and inflammation and may have a significant impact in diseases such as atherosclerosis and cancer (perhaps by aiding in tumour malignancy and plaque destabilisation). To further this study, it may be interesting to investigate this reduction in cell-FN adhesion at different concentrations of IL-1 stimulus and transfected TILRR cDNA. This may allow for the quantification of how TILRR regulates cell adhesion under different levels of inflammatory stimulus and how potentiating effects of increasing TILRR expression affect cell-matrix adhesion at the single cell level. Furthermore, in the prescence of IL-1, it may be of interest to scan FN-functionalised probes over the edge of both control cells and cells expressing elevated levels of TILRR using tapping mode AFM (where distortions in the resulting images can infer the binding between probe and sample) in order to map adhesive sites in detail and to characterise changes in adhesive profiles due to TILRR expression.

The results presented in *Chapter 6* demonstrate that the elasticity of HeLa cells can be well quantified using indentation-force spectroscopy with 25 μm colloidal probes and an average Young modulus of $\backsim$ 380 Pa was extracted from the Hertz model. Under conditions designed to potentiate TILRR association with IL-1RI, the stimulation of IL-1 at saturated levels was shown to reduce the elastic modulus of HeLa cells by $\backsim$ 55%. Increasing the expression of TILRR by transfection of cDNA seemed to potentiate this effect, not by further reduction of the modulus but by a reduction in the upper interquartile range of average elastic moduli for the cells measured in this study. The IL-1 induced reduction in the elastic moduli of cells likely results from the disorganisation of actin filaments contributing to the cell cytoskeleton. Increased TILRR expression seemed to result in a greater quantity of cells responding to IL-1 stimulus and exhibiting what may be a maximum IL-1 induced reduction in elasticity. This may indicate a digital nature of NF-κB activation and is supported by previous studies in which this has been suggested (Tay et al., 2010). At the single cell level, higher TILRR expression may increase the sensitivity of cells to IL-1 stimulus and the amplification of NF-κB activity as observed in assays containing a large quantity of cells may therefore result from increased numbers of cells signalling (Zhang et al., 2010). Indentation studies of cells under lower concentrations of IL-1 stimulation (10^{-13} M to 10^{-11} M) may allow for better quantification of the sensitivity of their mechanical properties with respect to the expression of TILRR.

To conclude, this study has shown that the AFM has the capability to measure changes in the mechanical properties of cells induced by external stimulus and regulated by PGs. Both cell adhesion and cell elasticity have been shown to be significantly affected by TILRR amplification of IL-1RI. Furthermore, DSMFS has been used to extract the binding kinetics between SDC4, DCN and integrin $\alpha_5\beta_1$ with FN. This study, among numerous others in recent years, demonstrates the versatility of the AFM in quantitive biophysics.

References

Abu-Lail, N. I. and Camesano, T. A. (2003). Role of ionic strength on the relationship of biopolymer conformation, DLVO contributions, and steric interactions to bioadhesion of *pseudomonas putida* KT2442. *Biomacromolecules*, 4:1000–1012.

Afonina, I. S., Müller, C., Martin, S. J., and Beyaert, R. (2015). Proteolytic processing of interleukin-1 family cytokines: Variations on a common theme. *Immunity*, 42:991–1004.

Alberts, B., Johnson, A., Lewis, J., Raff, M., Roberts, K., and Walter, P. (2002). *Molecular Biology of the Cell*. Garland Science, New York, USA, 4th edition.

Albon, J. (2015). *Developing and Using Atomic Force Microscopy to Investigate Mechanisms of Tumour Metastasis*. PhD thesis, University of Sheffield.

Alessandrini, A. and Facci, F. (2005). AFM: a versatile tool in biophysics. *Meas. Sci. Technol.*, 16:R65–R92.

Alexopoulou, L., Holt, A. C., Medzhitov, R., and Flavell, R. A. (2001). Recognition of double-stranded RNA and activation of NF-κB by Toll-like receptor 3. *Nature*, 413:732–738.

Askari, J. A., Buckley, P. A., Mould, P., and Humphries, M. J. (2009). Linking integrin conformation to function. *J. Cell Sci.*, 122:165–170.

Bai, D., Ueno, L., and Vogt, P. K. (2009). Akt-mediated regulation of NFκB and the essentialness of NFκB for the oncogenicity of PI3K and Akt. *Int. J. Cancer*, 125:2863–2870.

Ballestrem, C. and Müller, T. (2015). Cell adhesion via the $\alpha_5\beta_1$ integrin receptor to fibronectin. *JPK Instruments Application Note*, pages 1–4.

Banerjee, S. S., Aher, N., Patil, R., and Khandare, J. (2012). Poly(ethylene glycol)-prodrug conjugates: Concept, design, and applications. *J. Drug Deliv.*, 2012:103973.

Barattin, R. and Voyer, N. (2008). Chemical modifications of AFM tips for the study of molecular recognition events. *Chem. Commun.*, 48:1513–1532.

Barkalow, F. J. and Schwarzbauer, J. E. (1991). Localization of the major heparin-binding site in fibronectin. *J. Biol. Chem.*, 266:7812–7818.

Barkalow, F. J. and Schwarzbauer, J. E. (1994). Interactions between fibronectin and chondroitin sulfate are modulated by molecular contex. *J. Biol. Chem.*, 269:3957–3962.

Bayakara, M. Z. and Schwarz, U. D. (2016). Noncontact atomic force microscopy iii. *Beilstein J. Nanotechnol.*, 7:946–947.

Beaussart, A., E-Kirat-Chatel, S., Herman, P., Alsteens, D., Mahillon, J., Hols, P., and Dufrêne, Y. F. (2013). Single-cell force spectroscopy of probiotic bacteria. *Biophys. J.*, 104:1886–1892.

Beauvais, D. M. and Rapraeger, A. C. (2004). Syndecans in tumor cell adhesion and signaling. *Reprod. Biol. Endocinol.*, 2:3.

Bell, G. (1978). Models for the specific adhesion of cells to cells. *Science*, 200:618–627.

Benecky, M. J., Kolvenbach, C. G., Amrani, D. L., and Mosesson, M. W. (1988). Evidence that binding to the carboxyl-terminal heparin-binding domain (Hep ii) dominates the interaction between plasma fibronectin and heparin. *Biochemistry*, 27:7565–7671.

Bentley, K. L., Klebe, R. J., Hurst, R. E., and M., H. P. (1985). Heparin binding is necessary, but not sufficient, for fibronectin aggregation. a fluorescence polarization study. *J. Biol. Chem.*, 260:7250–7256.

Berliner, J. A., Navab, M., Fogelman, A. M., Frank, J. S., Demer, L. L., Edwards, P. A., Watson, A. D., and Lusis, A. J. (1995). Atherosclerosis: basic mechanisms. Oxidation, inflammation, and genetics. *Circulation*, 1995:2488–2496.

Berne, B. J., Weeks, J. D., and Zhou, R. (2014). Dewetting and hydrophobic interaction in physical and biological systems. *Annu. Rev. Phys. Chem.*, 60:83–103.

Bershadsky, A. D., Balaban, N. Q., and Geiger, B. (2003). Adhesion-dependent cell mechanosensitivity. *Annu. Rev. Cell Dev. Biol.*, 19:677–695.

Beutler, B. (2004). Innate immunity: an overview. *Mol. Immunol.*, 40:845–859.

Bidanset, D. J., LeBaron, R., Rosenberg, L., Murphy-Ullrich, J. E., and Hook, M. (1992). Regulation of cell substrate adhesion: effects of small galactosaminoglycan-containing proteoglycans. *J. Cell Biol.*, 118:1523–1531.

Bingham, R. J. and Potts, J. R. (2010). Fibronectin structure: a new piece of the puzzle emerges. *Structure*, 18:660–661.

Binnig, G., Quate, C. F., and Gerber, C. (1986). Atomic force microscope. *Phys. Rev. Lett.*, 56:930–933.

Bizzarri, A. R. and Cannistraro, S. (2012). *Dynamic Force Spectroscopy and Biomolecular Recognition*. CRC Press, Inc., Boca Raton, FL, USA, 1st edition.

Björnham, O. and Andersson, M. (2017). Theory for nonlinear dynamic force spectroscopy. *Eur. Biophys. J.*, 46:225–233.

Bloom, L., Ingham, K. C., and Hynes, R. O. (1999). Fibronectin regulates assembly of actin filaments and focal contacts in cultured cells via the heparin-binding site in repeat III_{13}. *Mol. Biol. Cell*, 10:1521–1536.

Boehm, T. (2012). Evolution of vertebrate immunity. *Curr. Biol.*, 22:R722–R732.

Bolshakova, A. V., Kiselyova, O. I., and Yaminsky, I. V. (2004). Microbial surfaces investigated using atomic force microscopy. *Biotechnol. Prog.*, 20:1615–1622.

Borland, S. J., Morris, T. G., Borland, S. C., Morgan, M. R., Francis, S. E., Merry, C. L. R., and Canfield, A. E. (2017). Regulation of vascular smooth muscle cell calcification by syndecan-4/FGF-2/PKCα signaling and cross-talk with TGFβ. *Cardiovasc. Res.*, 113:1639–1652.

Boskey, A. L. and Robey, P. G. (2013). Chapter 11 - The regulatory role of matrix proteins in mineralization of bone. In Marcus, R., Feldman, D., Dempster, D. W., Luckey, M., and Cauley, J. A., editors, *Osteoporosis (Fourth Edition)*, pages 235–255. Academic Press, San Diego.

Boye, K., Ligezowska, A., Eble, J. A., Hoffmann, B., and Klösgen, B. Merkel, R. (2013). Two barriers or not? Dynamic force spectroscopy on the integrin $\alpha_7\beta_1$ invasin complex. *Biophys. J.*, 105:2711–2780.

Burgos, P., Zhang, Z., Golestanian, R., J., L. G., and Geoghegan, M. (2009). Directed single molecule diffusion triggered by surface energy gradients. *ACS Nano*, 3:3235–3243.

Bustamante, C., Marko, J., Siggia, E., and Smith, S. (1994). Entropic elasticity of lambda-phage DNA. *Science*, 265:1599–1600.

Bustanji, Y., Arciola, C. R., Conti, M., Mandello, E., Montanaro, L., and Samorí, B. (2002). Dynamics of the interaction between a fibronectin molecule and a living bacterium under mechanical force. *PNAS*, 100:13292–13297.

Butt, H. J. and Jaschke, M. (1995). Calculation of thermal noise in atomic force microscopy. *Nanotechnology*, 6:1–7.

Calderwood, D. A. (2004). Integrin activation. *J. Cell Sci.*, 117:657–666.

Calderwood, D. A., Shattil, S. J., and Ginsberg, M. H. (2000). Integrins and actin filaments: Reciprocal regulation of cell adhesion and signaling. *J. Biol. Chem.*, 275:22607–22610.

Campbell, I. D. and Humphries, M. J. (2011). Integrin structure, activation, and interactions. *Cold Spring Harb. Perspect. Biol.*, 3:a004994.

Capila, I. and Linhardt, R. J. (2002). Heparin-protein interactions. *Angew. Chem. Int. Ed.*, 41:390–412.

Carsons, S. E. (1989). *Fibronectin in Health and Disease*. CRC Press, Florida, USA, 1st edition.

Carvalho, F. A. and Santos, N. C. (2012). Atomic force microscopy-based force spectroscopy - biological and biomedical applications. *IUBMB Life*, 64:465–472.

Casalini, S., Dumitru, A. C., Leonard, F., Bortolotti, C. A., Herruzo, E. T., Campana, A., de Oliveira, R. F., Cramer, T., Garcia, R., and Biscarini, F. (2015). Multiscale sensing of antibody-antigen interactions by organic transistors and single-molecule force spectroscopy. *ACS Nano*, 9:5051–5056.

Casuso, I., Kodera, N., Grimellec, C. L., Ando, T., and Scheuring, S. (2009). Contact-mode high-resolution high-speed atomic force microscopy movies of the purple membrane. *Biophys J.*, 97:1354–1361.

Caunt, C. J., Kiss-Toth, E., Carlotti, F., Chapman, R., and Qwarnstrom, E. E. (2001). Ras controls tumor necrosis factor receptor-associated factor (TRAF)6-dependent induction of nuclear factor-κb. *J. Biol. Chem.*, 276:6280–6288.

Celsus, A. C. (0025). *De medicina*. *Self Published*.

Chang, K.-C., Chiang, Y.-W., Yang, C.-H., and Liou, J.-W. (2012). Atomic force microscopy in biology and biomedicine. *Tzu Chi Med. J.*, 24:162–169.

Chaplin, D. D. (2010). Overview of the immune response. *J. Allergy Clin. Immunol.*, 125:S3–S23.

Charras, G. T., Mitchinson, T. J., and Mahadevan, L. (2009). Animal cell hydraulics. *J. Cell Sci.*, 122:3233–3241.

Chiou, Y.-W., Lin, H.-K., Tang, M.-J., Lin, H.-H., and Yeh, M. (2013). The influence of physical and physiological cues on atomic force microscopy-based cell stiffness assessment. *PLOS One*, 8:e77384–e77395.

Choi, C. and Helfman, D. M. (2014). The Ras-ERK pathway modulates cytoskeleton organization, cell motility and lung metastasis signature genes in MDA-MB-231 LM2. *Oncogene*, 33:3668–3676.

Chovatiya, R. and Medzhitov, R. (2014). Stress, inflammation, and defense of homeostasis. *Mol. Cell*, 54:281–288.

Clark, R. A. (2013). *The Molecular and Cellular Biology of Wound Repair*. Springer Science & Business Media, Berlin, Germany, 2nd edition.

Combs, C. A. (2010). Fluorescence microscopy: A concise guide to current imaging methods. *Curr. protec. Neurosci.*, Unit2.1:1–19.

Costa, K. D. (2003). Single-cell elastography: Probing for disease with the atomic force microscope. *Dis. Markers*, 19:139–154.

Couchman, J. R. and Woods, A. (1999). Syndecan-4 and integrins: combinatorial signaling in cell adhesion. *J. Cell Sci.*, 112:3415–3420.

Coussens, L. M. and Werb., Z. (2002). Inflammation and cancer. *Nature*, 420:860–867.

Cross, S. E., Jin, Y.-S., Rao, J., and Gimzewski, J. K. (2007). Nanomechanical analysis of cells from cancer patients. *Nat. Nanotechnol.*, 2:780–783.

Crozat, K. and Beutler, B. (2004). TLR7: A new sensor of viral infection. *Proc. Natl. Acad. Sci. USA*, 101:6853–6856.

Cumberbatch, M., Dearman, R. J., and Kimber, I. (1997). Interleukin 1 beta and the stimulation of Langerhans cell migration: comparisons with tumour necrosis factor alpha. *Arch. Dermatol. Res.*, 289:227–284.

Daley, W. P., Peters, S. B., and Larsen, M. (2008). Extracellular matrix dynamics in development and regenerative medicine. *J. Cell Sci.*, 121:255–264.

Das, T., Roy, A., Uyama, H., Roy, P., and Nandi, M. (2017). 2-Hydroxy-naphthyl functionalized mesoporous silica for fluorescence sensing and removal of aluminum ions. *Dalton Trans.*, 46:7317–7326.

de Lange, F., Cambi, A., Huijbens, R., de Bakker, B., Rensen, W. Garcia-Parajo, M., van Hulst, N., and Figdor, C. G. (2001). Cell biology beyond the diffraction limit: near-field scanning optical microscopy. *Cell J. Sci.*, 114:4153–4160.

Dempsey, P. W., Vaidya, S. A., and Cheng, G. (2003). The art of war: Innate and adaptive immune responses. *Cell Mol. Life Sci.*, 60:2604–2621.

Dettmann, W., Grandbois, M., André, S., Benoit, M., Wehle, A., Kaitner, H., Gabius, H. J., and Gaub, H. E. (2000). Differences in zero-force and force-driven kinetics of ligand dissociation from beta-galactoside-specific proteins (plant and animal lectins, immunoglobulin G) monitored by plasmon resonance and dynamic single molecule force microscopy. *Arch. Biochem. Biophys.*, 383:157–170.

Dokou, E., Zhang, L., and Barteau, M. A. (2002). Comparison of atomic force microscopy imaging methods and roughness determinations for a highly polished quartz surface. *J. Vac. Sci. Technol. B*, 20:2183–2186.

Dorobantu, L. S. and Gray, M. R. (2010). Application of atomic force microscopy in bacterial research. *Scanning*, 32:74–96.

Dufrêne, Y. F. (2002). Atomic force microscopy, a powerful tool in microbiology. *Analyst*, 184:297–301.

Dufrêne, Y. F. (2008). AFM for nanoscale microbe analysis. *J. Bacteriol.*, 133:5205–5213.

Dufrêne, Y. F., Ando, T., Garcia, R., Alsteens, D., Martinez-Martin, D., Engel, A., Gerber, C., and Müller, D. J. (2017). Imaging modes of atomic force microscopy for application in molecular and cell biology. *Nat. Nanotechnol.*, 12:295–307.

Dyck, S. M. and Karimi-Abdolrezaee, S. (2015). Chondroitin sulfate proteoglycans: Key modulators in the developing and pathologic central nervous system. *Exp. Neurol.*, 269:169–187.

Elefteriou, F., Exposito, J.-Y., Garrone, R., and Lethias, C. (2001). Binding of tenascin-x to decorin. *FEBS Lett.*, 495:44–47.

Elfenbein, A. and Simons, M. (2010). Auxiliary and autonomous proteoglycan signaling networks. *Methods Enzymol.*, 480:3–33.

Elfenbein, A. and Simons, M. (2013). Syndecan-4 signaling at a glance. *J. Cell Sci.*, 126:3799–3804.

Elliott, C. L., Allport, V. C., Loudon, J. A., Wu, G. D., and Bennett, P. R. (1998). Chemokines IL-8, GROα, MCP-1, IP-10, and Mig are sequentially and differentially expressed during phase-specific infiltration of leukocyte subsets in human wound healing. *Am. J. Pathol.*, 153:1849–1860.

Elliott, C. L., Allport, V. C., Loudon, J. A., Wu, G. D., and Bennett, P. R. (2001). Nuclear factor-kappa B is essential for up-regulation of interleukin-8 expression in human amnion and cervical epithelial cells. *Mol. Hum. Reprod.*, 7:787–790.

Erickson, R. P. and Wynshaw-Boris, A. J. (2016). *Epstein's Inborn Errors of Development: The Molecular Basis of Clinical Disorders of Morphogenesis*. Oxford University Press, Oxford, UK, 3rd edition.

Evans, E. (2001). Probing the relation between force-lifetime-and chemistry in single molecular bonds. *Annu. Rev. Biophys. Biomol. Struct.*, 30:105–128.

Evans, E., Leung, A., Hammer, D., and Simon, S. (2001). Chemically distinct transition states govern rapid dissociation of single L-selectin bonds under force. *PNAS*, 98:3784–3789.

Evans, E. and Ritchie, K. (1997). Dynamic strength of molecular adhesion bonds. *Biophys. J.*, 72:1541–1555.

Fasano, M. B., Cousart, S., Neal, S., and McCall, C. E. (1991). Increased expression of the interleukin 1 receptor on blood neutrophils of humans with the sepsis syndrome. *J. Clin. Invest.*, 88:1452–1459.

Fears, C. Y. and Woods, A. (2006). The role of syndecans in disease and wound healing. *Matrix Biol.*, 25:443–456.

Feidler, L. R. and Eble, J. A. (2009). Decorin regulates endothelial cell-matrix interactions during angiogenesis. *Cell Adh. Migr.*, 3:3–6.

Ferdous, Z., Peterson, S. B., Tseng, H., Anderson, D. K., Iozzo, R. V., and Grande-Allen, K. (2010). A role for decorin in controlling proliferation, adhesion, and migration of murine embryonic fibroblasts. *J. Biomed. Mater. Res. A*, 93:419–428.

Ferdous, Z., Wei, V. M., Iozzo, R., Höök, M., and Grande-Allen, K. J. (2007). Decorin-transforming growth factor-β interaction regulates matrix organization and mechanical characteristics of three-dimensional collagen matrices. *J. Biol. Chem*, 282:35887–35898.

Filippi, I., Carraro, F., and Naldini, A. (2015). Interleukin-1β affects MDAMB231 breast cancer cell migration under hypoxia: Role of HIF-1α and NFκB transcription factors. *Hindawi*, 2015:1–10.

Franz, C. M., Taubenberger, A., Puech, P. H., and Muller, D. J. (2007). Studying integrin-mediated cell adhesion at the single-molecule level using AFM force spectroscopy. *Sci. STKE*, 406:pl5–pl20.

Frattini, A., Fabbri, M., Valli, R., Paoli, E., Montalbano, G., Gilbrado, L., Pasquali, F., and Maserati, E. (2015). High variability of genomic instability and gene expression profiling in different HeLa clones. *Sci. Rep.*, 5:15377–15385.

Fritzsche, M., Erlenkämper, C., Moeendarbary, E., Charras, G., and Kruse, K. (2016). Actin kinetics shapes cortical network structure and mechanics. *Sci. Adv.*, 2:e1501337.

Fuhrmann, A., Scheoning, J. C., Ansekmetti, D., Staiger, D., and Ros, R. (2009). Quantitative analysis of single-molecule rna-protein interaction. *Biophys. J.*, 96:5030–5039.

Gabay, C., Lamacchia, C., and Palmer, G. (2010). Il-1 pathways in inflammation and human diseases. *Nat. Rev. Rheumatol.*, 6:232–241.

Gaboriaud, F. and Y. F. Dufrêne, Y. F. (2007). Atomic force microscopy of microbial cells: application to nanomechanical properties, surface forces and molecular recognition forces. *Colloids Surf. B*, 54:10–19.

Gandhi, N. S. and Mancera, R. L. (2008). The structure of glycosaminoglycans and theirinteractions with proteins. *Chem. Biol. Drug Des.*, 72:455–482.

Gao, G., Yu, K., Kindrachuk, J., Brookes, D. E., Hancock, R. E. W., and Kizhakkedathu, J. N. (2011). Antibacterial surfaces based on polymer brushes: investigation on the influence of brush properties on antimicrobial peptide immobilization and antimicrobial activity. *Biomacromolecules*, 1639:3715–3127.

Garg, H. G., Yu, L., Hales, C. A., Toida, T., Islam, T., and Linhardt, R. J. (2003). Sulfation patterns in heparin and heparan sulfate: effects on the proliferation of bovine pulmonary artery smooth muscle cells. *Biochem. Biophys. Acta.*, 1639:225–231.

Garlanda, C., Dinarello, C. A., and Mantovani, A. (2013). The interleukin-1 family: Back to the future. *Immunity*, 39:1003–1018.

Gavara, N. (2017). A beginner's guide to atomic force microscopy probing for cell mechanics. *Microsc. Res. Tech.*, 80:75–84.

Gay, N. J. and Gangloff, M. (2007). Structure and function of Toll receptors and their ligands. *Annu. Rev. Biochem.*, 76:141–165.

Getfert, S. and Reimann, P. (2012). Hidden multiple bond effects in dynamic force spectroscopy. *Cell Press*, 102:1184–1193.

Getz, G. F. (2005). Bridging the innate and adaptive immune systems. *J. Lipid Res.*, 46:619–622.

Glorieux, F. H. (2008). Osteogenesis imperfecta. *Best Pract. Res. Clin. Rheumatol.*, 22:85–100.

Goodsell, D. S. (1999). The molecular perspective: the ras oncogene. *Oncologist*, 4:263–264.

Greaves, G. N. (2013). Poisson's ratio over two centuries: challenging hypotheses. *Notes Rec. R. Soc. Lond.*, 67:37–58.

Greenfeder, S. A., Nunes, P., Kwee, L., Labow, M., Chizzonite, R. A., and Ju, G. (1995). Molecular cloning and characterization of a second subunit of the interleukin 1 receptor complex. *J. Biol. Chem.*, 270:13757–13765.

Grinnell, F. and Feld, M. K. (1981). Adsorption characteristics of plasma fibronectin in relationship to biological activity. *J. Biomed. Mater. Res.*, 15:363–381.

Gu, J. and Taniguchi, N. (2004). Regulation of integrin functions by *n*-glycans. *Glycoconj. J.*, 21:9–15.

Gulati, K. and Poluri, K. M. (2016). Mechanistic and therapeutic overview of glycosaminoglycans: the unsung heroes of biomolecular signaling. *Glycoconj. J.*, 33:1–17.

Guz, N., Dokukin, M., Kalaparthi, V., and Sokolov, I. (2014). If cell mechanics can be described by elastic modulus: Study of different models and probes used in indentation experiments. *Biophys. J.*, 107:564–575.

Haase, K. and Pelling, A. E. (2015). Investigating cell mechanics with atomic force microscopy. *J. Royal Soc. Interface*, 12:20140970.

Habuchi, H., Habuchi, O., and Kimata, K. (2004). Sulfation pattern in glycosaminoglycan: Does it have a code? *Glycoconj. J.*, 21:47–52.

Hall, A. (2015). *Surface adhesion of the pathogens Leishmania mexicana and Streptococcus pneumoniae*. PhD thesis, University of Sheffield.

Hanley, W., McCarty, O., Jadhav, S., Tseng, Y., Wirtz, D., and Konstantopoulos, K. (2003). Single molecule characterization of P-selectin/ligand binding. *J. Biol. Chem.*, 278:10556–10561.

Hansson, G., Robertson, A. K., and Söderberg-Nauclér, C. (2006). Inflammation and atherosclerosis. *Annu. Rev. Pathol.*, 1:297–329.

Haugstad, G. (2012). *Atomic Force Microscopy: Understanding Basic Modes and Advanced Applications*. Wiley-Blackwell, New Jersey, USA, 1st edition.

Hawe, A., Sutter, M., and Jiskoot, W. (2008). Extrinsic fluorescent dyes as tools for protein characterization. *Pharm. Res.*, 25:1487–1499.

Hayashi, F., Smith, K. D., Ozinsky, A., Hawn, T. R., Yi, E. C., Goodlett, D. R., Eng, J. K., Akira, S., Underhill, D. M., and Aderem, A. (2001). The innate immune response to bacterial flagellin is mediated by Toll-like receptor 5. *Nature*, 410:1099–1103.

Hayashi, K. and Iwata, M. (2015). Stiffness of cancer cells measured with an AFM indentation method. *J. Mech. Behav. Biomed. Mater.*, 49:105–111.

Helenius, J., Heisenberg, C.-P., Gaub, H. E., and Muller, D. J. (2008). Single-cell force spectroscopy. *J. Cell Sci.*, 121:1785–1791.

Herbig, M., Kräter, M., Plak, K., Müller, P., Guck, J., and Otto, O. (2018). Real-time deformability cytometry: Label-free functional characterization of cells. *Methods Mol. Biol.*, 1678:347–369.

Hoesel, B. and Schmid, J. A. (2013). The complexity of NF-κB signaling in inflammation and cancer. *Mol. Cancer*, 12:86–100.

Hoffmann, J. A., Kafatos, F. C., Janeway, C. A., and Ezekowitz, R. A. B. (1999). Phylogenetic perspectives in innate immunity. *Science*, 284:1313–1318.

Hong, Z., Sun, Z., Li, Z., Mesquitta, W.-T., Trzeciakowski, J. P., and Meininger, G. A. (2012). Coordination of fibronectin adhesion with contraction and relaxation in microvascular smooth muscle. *Cardiovasc. Res.*, 96:73–80.

Huang, H.-L., Hsing, H.-W., Lai, T.-C., Chen, Y.-W., Lee, T.-R., Chan, H.-T., Lyu, P.-C., Wu, C.-L., Lu, Y.-C., Lin, S.-T., Lin, C.-W., Lai, C.-H., Chang, H.-T., Chou, H.-C., and Chan, H.-L. (2010). Trypsin-induced proteome alteration during cell subculture in mammalian cells. *J. Biol. Sci.*, 17:36–45.

Hughes, M. L. and Dugan, L. (2016). The physics of pulling polyproteins: a review of single molecule force spectroscopy using the AFM to study protein unfolding. *Rep. Prog. Phys.*, 79:076601.

Hull, J. R., Tamura, G. S., and Caster, D. (2007). Structure and reactivity of adsorbed fibronectin films on mica. *Biophys. J.*, 93:2852–2860.

Humphrey, J. D., Dufresne, E. R., and Schwartz, M. A. (2014). Mechanotransduction and extracellular matrix homeostasis. *Nat. Rev. Mol. Cell Biol.*, 15:802–812.

Hunt, K. L. C., Zilles, B. A., and Bohr, J. E. (1981). Effects of van der Waals interactions on the polarizability of atoms, oscillators, and dipolar rotors at long range. *J. Chem. Phys.*, 75:3079–3086.

Huttenlocher, A. and Horwitz, A. R. (2011). Integrins in cell migration. *Cold Spring Harb. Perspect. Biol.*, 3:a005074.

Hutter, J. L. and Bechhoefer, J. (1993). Calibration of atomic force microscope tips. *Review of Scientific Instruments*, 64:1868–1873.

Hyonchol, K., Arakawa, H., Osada, T., and Ikai, A. (2002). Quantification of fibronectin and cell surface interactions by AFM. *Colloids. Surf. B. Biointerfaces*, 25:33–43.

Israelachvili, J. N. (2011). *Intermolecular and Surface Forces*. Elsevier Academic Press, Massachusetts, USA, 3rd edition.

Jackson, R. L., Busch, S. J., and Cardin, A. D. (1991). Glycosaminoglycans: molecular properties, protein interactions, and role in physiological processes. *Physiol. Rev.*, 71:481–539.

Jacobsen, L., Calvin, S., and Lobenhofer, E. (2009). Transcriptional effects of transfection: the potential for misinterpretation of gene expression data generated from transiently transfected cells. *Biotechniques*, 47:617–624.

Jahanyar, J., Joyce, D. L., Southard, R. E., Loebe, M., Noon, G. P., Koerner, M. M., Torre-Amione, G., and Youker, K. A. (2007). Decorin-mediated transforming growth factor-β inhibition ameliorates adverse cardiac remodeling. *J. Heart Lung Transplant.*, 26:34–40.

Jalili, N. and Laxminarayana, K. (2004). A review of atomic force microscopy imaging systems: application to molecular metrology and biological sciences. *Mechatronics*, 14:907–945.

Jang, E., Albadawi, H., Watkins, M. T., Edelman, E. R., and Baker, A. B. (2012). Syndecan-4 proteoliposomes enhance fibroblast growth factor-2 (FGF-2)-induced proliferation, migration, and neovascularization of ischemic muscle. *PNAS*, 71:1679–1684.

Järveläinen, H., Sainio, A., Koulu, M., Wight, T. N., and Penttinen, R. (2009). Extracellular matrix molecules: potential targets in pharmacotherapy. *Pharmacol. Rev.*, 61:198–223.

Kapila, Y. L., Niu, J., and Johnson, P. W. (1997). The high affinity heparin-binding domain and the V region of fibronectin mediate invasion of human oral squamous cell carcinoma cells *in vitro*. *J. Biol. Chem.*, 272:18932–18938.

Katsuda, S. and Kaji, T. (2003). Atherosclerosis and extracellular matrix. *J. Atheroscler. Thromb.*, 10:267–274.

Kawai, T. and Akira, S. (2010). The role of pattern-recognition receptors in innate immunity: update on Toll-like receptors. *Nat. Immunol.*, 11:373–384.

Kenny, E. F. and O'Neill, L. A. (2008). Signalling adaptors used by Toll-like receptors: an update. *Cytokine*, 43:342–349.

Kherlopian, A, R. W., Song, T., Duan, Q., Neimark, M. A., Po, M., J., Gohagan, J. K., and Laine, A. F. (2008). A review of imaging techniques for systems biology. *BMC Syst. Biol.*, 2:74–91.

Kim, T. K. and Eberwine, J. H. (2010). Mammalian cell transfection: the present and the future. *Anal. Bioanal. Chem.*, 397:3173–3178.

Kimata, K., Habuchi, O., Habuchi, H., and Watanabe, H. (2007). 4.10 - knockout mice and proteoglycans. In Kamerling, H., editor, *Comprehensive Glycoscience*, pages 159–191. Elsevier, Oxford.

Kleemann, R., Zadelaar, S., and Kooistra, T. (2015). Cytokines and atherosclerosis: a comprehensive review of studies in mice. *Cardiovasc. Res.*, 6:360–375.

Klein, S., de Fougerolles, A. R., Blaikie, P., Khan, L., Pepe, A., Green, C. D., Koteliansky, V., , and Giancotti, F. G. (2002). $\alpha 5\beta 1$ integrin activates an NF-κB-dependent program of gene expression important for angiogenesis and inflammation. *Mol. Cell Biol.*, 22:5912–5922.

Kolb, M., Margetts, P. J., Sime, P. J., and Gauldie, J. (2001). Mammalian cell transfection: the present and the future. *Am. J. Physiol. Lung Cell. Mol. Physiol.*, 280:L1327–L1334.

Komine, M., Rao, L. S., Freedberg, I. M., Simon, M., Milisavljevic, V., and Blumenberg, M. (2001). Interleukin-1 induces transcription of keratin K6 in human epidermal keratinocytes. *J. Investig. Dermatol.*, 116:330–338.

Krappmann, D. and Scheidereit, C. (1997). Regulation of NF-κB activity by IκBα and IκBβ stability. *Immunobiology*, 198:3–13.

Kreuzer, H. J., Wang, R. L. C., and Grunze, M. (1999). Effect of stretching on the molecular conformation of oligo (ethylene oxide): a theoretical study. *New J. Phys.*, 1:1–16.

Kubitschke, H., Schnauss, J., Nnetu, K. D., Warmt, E., Stange, R., and Kaes, J. (2017). Actin and microtubule networks contribute differently to cell response for small and large strains. *New J. Phys.*, 19:093003.

Kühner, F., Costa, L. T., Bisch, P. M., Thalhammer, S., Heckl, W. M., and Gaub, H. E. (2004). LexA-DNA bond strength by single molecule force spectroscopy. *Biophys. J.*, 87:2683–2690.

Kuiper, S. and Schitter, G. (2008). Active damping of a piezoelectric tube scanner using self-sensing piezo actuation. *Mechatronics*, 79:656–665.

Kulik, A. J., Lekka, M., Lee, K., Pyka-Fościak, G., and Nowak, W. (2015). Probing fibronectin-antibody interactions using AFM force spectroscopy and lateral force microscopy. *Bielstein J. Nanotechnol.*, 6:1164–1175.

Kuznetsova, T. G., Starodubetseva, M. N., Yegorenkov, N. I., Chizhik, S. A., and Zhdanov, R. I. (2007). Atomic force microscopy probing of cell elasticity. *Micron*, 38:824–833.

Lapidus, L. J., Eaton, W. A., and Hofrichter, J. (2000). Measuring the rate of intramolecular contact formation in polypeptides. *Proc. Natl. Acad. Sci. USA*, 97:7220–7225.

Lee, C. K., Wang, Y. M., Huang, L. S., and Lin, S. (2008). Atomic force microscopy and spectroscopy. *Rep. Prog. Phys.*, 71:16101–16123.

Lee, H. T., Lee, J. G., Na, M., and Kay, E. P. (2004). FGF-2 induced by interleukin-1 through the action of phosphatidylinositol 3-kinase mediates endothelial mesenchymal transformation in corneal endothelial cells. *J. Biol. Chem.*, 279:32325–32332.

Lehenkari, P. P. and Horton, M. A. (1999). Single integrin molecule adhesion forces in intact cells measured by atomic force microscopy. *Biochem. Biophys. Res. Commun.*, 259:645–650.

Lekka, M. (2016). Discrimination between normal and cancerous cells using AFM. *Bionanoscience*, 6:65–80.

Lekka, M., Gil, D., Pogoda, K., Dulińska-Litewka, J., Jack, R., Gostek, J., Klymenko, O., Prauzner-Bechcicki, S., Stachura, Z., Wiltowska-Zuber, J., Okoń, K., and Laidler, P. (2012). Cancer cell detection in tissue sections using AFM. *Arch. Biochem. Biophys.*, 518:151–156.

Li, F., Redick, S. D., Erickson, H. P., and Moy, V. T. (2003). Force measurements of the $\alpha_5\beta_1$ integrin-fibronectin interaction. *Biophys. J.*, 84:1252–1262.

Li, M. (2017). *Investigations of Cellular and Molecular Biophysical Properties by Atomic Force Microscopy Nanorobotics*. Springer Theses, Berlin, Germany, 1st edition.

Li, Q. S., Lee, G. Y., Ong, C. N., and Lim, C. T. (2008). AFM indentation study of breast cancer cells. *Biochem. Biophys. Res. Commun.*, 374:609–6013.

Li, X., McFarland, D. C., and Velleman, S. G. (2006). Effect of transforming growth factor-β on decorin and $\beta 1$ integrin expression during muscle development in chickens. *J. Poult. Sci.*, 85:326–332.

Libby, P., Ridker, P. M., and Hansson, G. K. (2009). Inflammation in atherosclerosis: from pathophysiology to practice. *J. Am. Coll. Cardiol.*, 54:2129–2138.

Lin, C. C., Kuo, C. T., Cheng, C. Y., Wu, C. Y., Lee, C. W., Hsieh, H. L., Lee, I. T., and Yang, C. M. (2009). IL-1 β promotes A549 cell migration via MAPKs/AP-1- and NF-κB-dependent matrix metalloproteinase-9 expression. *Cell Signal.*, 21:1652–1662.

Lin, H., Lal, R., and Clegg, D. O. (2000). Imaging and mapping heparin-binding sites on single fibronectin molecules with atomic force microscopy. *Biochemistry*, 39:3192–3196.

Lin, X. (2004). Functions of heparan sulfate proteoglycans in cell signaling during development. *Development*, 131:6009–6021.

Lindström, T. M. and Bennett, P. R. (2005). The role of nuclear factor kappa B in human labour. *Reproduction*, 130:569–581.

Liphardt, J., Onoa, B., Smith, S. B., Tinoco Jr, I., and Bustamante, C. (2001). Reversible unfolding of single RNA molecules by mechanical force. *Science*, 292:733–737.

Liu, W., Shafit-Zagardo, B., Aquino, D. A., Zhao, M. L., Dickson, D. W., Brosnan, C. F., and Lee, S. C. (1994). Cytoskeletal alterations in human fetal astrocytes induced by interleukin-1 beta. *J. Neurochem.*, 279:1625–1634.

Liu, X., Qu, T., Sachar, A., and Svoboda, K. K. (2015). Chapter 4 - cell-matrix interactions and signal transduction. In Vishwakarma, A., Sharpe, P., Shi, S., and Ramalingam, M., editors, *Stem Cell Biology and Tissue Engineering in Dental Sciences*, pages 47–60. Academic Press, Boston.

Lo, Y.-S., Zhu, Y.-J., and Beebe. T. P., J. (2001). Loading-rate dependence of individual ligand-receptor bond-rupture forces studied by atomic force microscopy. *Langmuir*, 17:3741–3748.

Lower, S. K., Tadanier, C. J., and Hochella, M. F. (2000). Measuring interfacial and adhesion forces between bacteria and mineral surfaces with biological force microscopy. *Geochim. Cosmochim. Acta.*, 64:3133–3139.

Lucey, B. P., Nelson-Rees, W. A., and Hutchins, G. M. (2009). Henrietta lacks, HeLa cells, and cell culture contamination. *Arch. Pathol. Lab. Med.*, 133:1463–1467.

Luo, B.-H. and Springer, T. A. (2006). Integrin structures and conformational signaling. *Curr. Opin. Cell Biol.*, 18:579–586.

Lusis, A. (2000). Atherosclerosis. *Nature*, 407:233–241.

Mahalingam, Y., Gallagher, J. T., and Couchman, J. R. (2007). Cellular adhesion responses to the heparin-binding (Hepii) domain of fibronectin require heparan sulfate with specific properties. *J. Biol. Chem.*, 282:3221–3230.

Mak, T. W. (2005). *The Immune Response: Basic and Clinical Principles*. Elsevier Academic Press, San Diego, California, USA, 1st edition.

Mao, Y. and Schwarzbauer, J. E. (2006). Accessibility to the fibronectin synergy site in a 3D matrix regulates engagement of $\alpha_5\beta_1$ versus $\alpha_v\beta 3$ integrin receptors. *Cell Commun. Adhes.*, 21:267–277.

Marthur, A. B., Collinsworth, A. M., Reichert, W. M., Kraus, W. E., and Truskey, G. A. (2001). Endothelial, cardiac muscle and skeletal muscle exhibit different viscous and elastic properties as determined by atomic force microscopy. *J. Biomech.*, 34:1545–1553.

Martin, M., Böl, G. F., Eriksson, A., Resch, K., and Brigelius-Flohé, R. (1994). Interleukin-1-induced activation of a protein kinase co-precipitating with the type I interleukin-1 receptor in T cells. *Eur. J. Immunol.*, 24:1566–1571.

Martin, M. U. and Wesche, H. (2002). Summary and comparison of the signaling mechanisms of the Toll/interleukin-1 receptor family. *Biochim. Biophysica. Acta.*, 1592:265–280.

Martínez, L., Tello, M., Díaz, M., Román, E., Garcia, R., and Huttel, Y. (2011). Aspect-ratio and lateral-resolution enhancement in force microscopy by attaching nanoclusters generated by an ion cluster source at the end of a silicon tip. *Rev. Sci. Instrum.*, 82:023710.

Masson-Gadias, B., Pierres, A., Benoliel, A.-M., Bongrand, P., and Lissitzsky, J.-C. (1999). Integrin α and β subunit contribution to the kinetic properties of $\alpha_2\beta_1$ collagen receptors on human keratinocytes analyzed under hydrodynamic conditions. *J. Cell Sci.*, 112:2335–2345.

May, M. and Ghosh, S. (1997). Rel/NF-κB and IκB proteins: an overview. *Semin. Cancer Biol.*, 8:63–71.

McMahan, C. J., Slack, J. L., Mosley, B., Cosman, D., Lupton, S. D., Brunton, L. L., Grubin, C. E., Wignall, J. M., Jenkins, N. A., and Brannan, C. I. (1991). A novel IL-1 receptor, cloned from B cells by mammalian expression, is expressed in many cell types. *Trends Cell Biol.*, 10:2821–2832.

Meadows, P. Y., Bemis, J. E., and Gilbert, C. W. (2003). Single-molecule force spectroscopy of isolated and aggregated fibronectin proteins on negatively charged surfaces in aqueous liquids. *Langmuir*, 19:9566–9572.

Meadows, P. Y. and Walker, G. C. (2005). Force microscopy studies of fibronectin adsorption and subsequent cellular adhesion to substrates with well-defined surface chemistries. *Langmuir*, 21:4096–4107.

Medzhitov, R., Preston-Hurlburt, P., and A., J. C. (1997). A human homologue of the *drosophila* toll protein signals activation of adaptive immunity. *Nature*, 388:394–397.

Mietke, A., Otto, O., Girado, S., Rosendahl, P., Golfier, S., Ulbricht, E., Aland, S., Guck, J., and Fischer-Friedrich, E. (2015). Extracting cell stiffness from real-time deformability cytometry: Theory and experiment. *Biophys. J.*, 109:2023–2036.

Minguell, J. J., Hardy, C., and Tavassoli, M. (1992). Membrane-associated chondroitin sulfate proteoglycan and fibronectin mediate the binding of hemopoietic progenitor cells to stromal cells. *Exp. Cell Res.*, 201:200–207.

Mitchell, G., Lamontagne, C.-A., Lebel, R., Grandbois, M., and Malouin, F. (2007). Single-molecule dynamic force spectroscopy of the fibronectin-heparin interaction. *Biochem. Biophys. Res. Commun.*, 364:595–600.

Moazzez, B., O'Brien, S. M., and Merschrod, E. F. (2013). Improved adhesion of gold thin films evaporated on polymer resin: Applications for sensing surfaces and MEMS. *Sensors*, 13:7021–7032.

Moeendarbary, E., Valon, L., Fritzsche, M., Harris, A. R., A., M. D., and Adrian, J. (2014). The cytoplasm of living cells behaves as a poroelastic material. *Nat. Matter.*, 12:251–261.

Mogensen, T. H. (2009). Pathogen recognition and inflammatory signaling in innate immune defenses. *Clin. Microbiol. Rev.*, 22:240–273.

Mokbel, M., Mokbel, D., Mietke, A., Träber, N., Girado, S., Otto, O., Guck, J., and Aland, S. (2017). Numerical simulation of real-time deformability cytometry to extract cell mechanical properties. *ACS Biomater. Sci. Eng.*, 3:2962–2973.

Moresco, E. M., LaVine, D., and Beutler, B. (2011). Toll-like receptors. *Curr. Biol.*, 21:R488–R493.

Mosher, D. F. and Furcht, L. T. (1981). Fibronectin: review of its structure and possible functions. *J. Invest. Dermatol.*, 77:175–180.

Müller, D. J. and Dufrêne, Y. F. (2011). Atomic force microscopy: a nanoscopic window on the cell surface. *Trends Cell Biol.*, 21:461–469.

Mythreye, K. and Blobe, G. C. (2010). Proteoglycan signaling co?receptors: Roles in cell adhesion, migration and invasion. *Cell Signal.*, 21:1548–1558.

Na, C., Mcnamara, C. J., Konkol, N. R., Bearce, K. A., Mitchell, R., and Martin, S. T. (2010). The use of force-volume microscopy to examine bacterial attachment to titanium surfaces. *Ann. Microbiol.*, 60:495–502.

Nagae, M., Re, S., Mihara, E., Nogi, T., Sugita, Y., and Takagi, J. (2012). Crystal structure of $\alpha 5\beta 1$ integrin ectodomain: atomic details of the fibronectin receptor. *J Cell Biol.*, 97:131–140.

Nagamine, S., Tamba, M., Ishimine, H., Araki, K., Shiomi, K., Okada, T., Ohto, T., Kunita, S., Takahashi, S., Wismans, R. G. P., van Kuppevelt, T. H., Masu, M., and Keino-Masu, K. (2012). Organ-specific sulfation patterns of heparan sulfate generated by extracellular sulfatases Sulf1 and Sulf2 in mice. *J. Biol. Chem.*, 287:9579–9590.

Nakashima, Y., Wight, T. N., and Sueishi, K. (2008). Early atherosclerosis in humans: role of diffuse intimal thickening and extracellular matrix proteoglycans. *Cardiovasc. Res.*, 79:14–23.

Nichols, A. (2017). *Regulation of Inflammatory and Anti-Apoptotic Signals through TILRR, a Novel IL-1RI Co-Receptor: The Impact of TILRR Single Nucleotide Polymorphisms*. PhD thesis, University of Sheffield.

Nicholson, L. B. (2016). The immune system. *Essays Biochem.*, 60:275–301.

Nikkhah, M., Strobl, J. S., Schmelz, E. M., and Masoud, A. (2011). Evaluation of the influence of growth medium composition on cell elasticity. *J. Biomech.*, 44:762–766.

Nikolova, V., Koo, C. Y., Ibrahim, S. A., Wang, Z., Spillmann, D., Dreier, R., Kelsch, R., Fischgräbe, J., Smollich, M., Rossi, L. H., Sibrowski, W., Wülfing, P., Keisel, L., Yip, G. W., and M., G. (2009). Differential roles for membrane-bound and soluble syndecan-1 (CD138) in breast cancer progression. *Carcinogensis*, 30:397–407.

Northrop, B. H., Frayne, S. H., and Choudhary, U. (2015). Thiol-maleimide "click" chemistry: evaluating the influence of solvent, initiator, and thiol on the reaction mechanism, kinetics, and selectivity. *Polym. Chem.*, 6:3415–3430.

Nüsslein-Volhard, C., Kluding, H., and Jürgens, G. (1985). Genes affecting the segmental subdivision of the *drosophila* embryo. *Cold Spring Harb. Symp. Quant. Biol.*, 50:145–154.

Nüsslein-Volhard, C. and Wieschaus, E. (1980). Mutations affecting segment number and polarity in *Drosophila*. *Nature*, 287:795–801.

Okamura, Y., Watari, M., Jerud, E. S., Young, D. W., Ishizaka, S. T., Rose, J., Chow, J. C., and Strauss, J. F. r. (2001). The extra domain A of fibronectin activates Toll-like receptor 4. *J. Biol. Chem.*, 276:10229–10233.

Omidvar, R., Tafazzoli-Shadpour, M., Shokrgozar, M. A., and Rostami, M. (2014). Atomic force microscope-based single cell force spectroscopy of breast cancer cell lines: an approach for evaluating cellular invasion. *J. Biomech.*, 47:3373–3379.

O'Neill, L. A. (2008). The interleukin-1 receptor/toll-like receptor superfamily: 10 years of progress. *Immunol. Rev.*, 226:10–18.

Otto, O., Rosendahl, P., Golfier, S., Mietke, A., Herbig, M., Jacobi, A. Topfner, N., Herold, C., Klaue, D., Girardo, S., Winzi, M., Fischer-Freidrich, E., and Guck, J. (2015a). Real-time deformability cytometry as a label-free indicator of cell function. *Conf. Proc. IEEE Eng. Med Biol. Soc.*, 2015:1861–1864.

Otto, O., Rosendahl, P., Mietke, A., Golfier, S., Herold, C., Klaue, D., Girardo, S., Pagliara, S., Ekpenyong, A., Jacobi, A., Wobus, M., Topfner, N., Keyser, U. F., Mansfield, J., Fischer-Freidrich, E., and Guck, J. (2015b). Real-time deformability cytometry: on-the-fly cell mechanical phenotyping. *Nature Methods*, 12:199–202.

Page, C. (2013). Heparin and related drugs: Beyond anticoagulant activity. *ISRN Pharmacol.*, 2013:1–13.

Pankov, R. and Yamada, K. M. (2002). Fibronectin at a glance. *J. Cell Sci.*, 115:3861–3863.

Panorchan, P., Thompson, M. S., Davis, K. J., and Tseng, Y. (2005). Single-molecule analysis of cadherin-mediated cell-cell adhesion. *J. Cell Sci.*, 119:66–74.

Pap, T. and Bertrand, J. (2013). Syndecans in cartilage breakdown and synovial inflammation. *Nat. Rev. Rheumatol.*, 9:43–55.

Parot, P., Dufrêne, Y. F., Hinterdorfer, P., Le Grimellec, C., Navajas, D., Pellequer, J.-L., and Scheuring, S. (2007). Past, present and future of atomic force microscopy in life sciences and medicine. *J. Mol. Recognit.*, 20:418–431.

Peters, V. A., Joesting, J. J., and Freund, G. G. (2013). IL-1 receptor 2 (IL-1R2) and its role in immune regulation. *Brain Behav. Immun.*, 32:1–8.

Plodinec, M., Loparic, M., Monnier, C. A., Obermann, E. C., Zanetti-Dallenbach, R., Oertle, P., Hyotyla, J. T., Aebi, U., Bentires-Alj, M., Lim, R. Y. H., and Schoenenberger, C.-A. (2012). The nanomechanical signature of breast cancer. *Nat. Nanotechnol.*, 7:757–765.

Pogoda, K., Jaczewska, J., Wiltowska-Zuber, J., Klymenko, O., Zuber, K., Fornal, M., and Lekka, M. (2012). Depth-sensing analysis of cytoskeleton organization based on AFM data. *Eur. Biophys. J.*, 41:79–87.

Prakash, A., Janosi, L., and Doxastakis, M. (2011). GxxxG motifs, phenylalanine, and cholesterol guide the self-association of transmembrane domains of ErbB2 receptors. *Biophys. J.*, 101:1949–1958.

Prendergast, G. C. and Gibbs, J. B. (1993). Pathways of Ras function: Connections to the actin cytoskeleton. *Adv. Cancer Res.*, 62:19–64.

Proctor, R. A. (1987). Fibronectin: a brief overview of its structure, function, and physiology. *Rev. Infect. Dis.*, 9:S317–S321.

Puech, P.-H., Poole, K., Knebel, D., and Muller, D. J. (2006). A new technical approach to quantify cell?cell adhesion forces by AFM. *Ultramicroscopy*, 106:637–644.

Putman, C. A. J., van der Werf, K. O., de Grooth, B. G., van Hulst, N. F., and Greve, J. (1994). Tapping mode atomic force microscopy in liquid. *Appl. Phys. Lett.*, 64:2454–2456.

Qi, J., Chi, L., Maloney, M., Yang, X., Bynum, D., and Banes (2006a). IL-1β increases elasticity of human bioartificial tendons. *J. Tissue Eng.*, 12:2913–2925.

Qi, J., Fox, A. M., Alexopaulos, L. G., Chi, L., Bynum, D., Guilak, F., and Banes, A. J. (2006b). IL-1beta decreases the elastic modulus of human tenocytes. *J. Appl. Physiol.*, 101:189–195.

Quan, X., Marvin, C. W., Seebald, L., and Hutchison, G. R. (2013). Single-molecule piezoelectric deformation: Rational design from first-principles calculations. *J. Phys. Chem. C*, 117:16783–16790.

QUIGEN (2000). *PolyFect Transfection Reagent Handbook*. QUIGEN.

Qwarnstrom, E. E., MacFarlane, S. A., Page, R. C., and Dower, S. K. (1991). Interleukin 1β induces rapid phosphorylation and redistribution of talin: A possible mechanism for modulation of fibroblast focal adhesion. *Proc. Natl. Acad. Sci. USA*, 88:1232–1236.

Qwarnstrom, E. E., Page, R. C., Gills, S., and Dower, S. K. (1988). Binding, internalization, and intracellular localization of interleukin-1β in human diploid fibroblasts. *J. Biol. Chem.*, 263:8261–8269.

Ramos, J. R., Pabijan, J., Garcia, R., and Lekka, M. (2014). The softening of human bladder cancer cells happens at an early stage of the malignancy process. *Beilstein J. Nanotechnol.*, 10:447–457.

Ray, C., Brown, J. R., and Akhremitchev, B. B. (2007). Rupture force analysis and the associated systematic errors in force spectroscopy by AFM. *Langmuir*, 23:6076–6083.

Reddy, S. A. G., Huang, J. H., and Liao, W. S.-L. (1997). Phosphatidylinositol 3-kinase in interleukin 1 signaling. *J. Biol. Chem.*, 272:29167–29173.

Rhodes, D. M., Smith, S. A., Holcombe, M., and Qwarnstrom, E. E. (2015). Computational modelling of NF-κB activation by IL-1RI and its co-receptor TILRR, predicts a role for cytoskeletal sequestration of IκBα in inflammatory signalling. *PLoS One*, 10:e0129888.

Robson, R. R., Westwick, J., and Brown, Z. (1995). Interleukin-1-induced IL-8 and IL-6 gene expression and production in human mesangial cells is differentially regulated by cAMP. *Kidney Int.*, 48:1767–1777.

Romero, R., Brody, D. T., Oyarzun, E., Mazor, M., Wu, Y. K., Hobbins, J. C., and Durum, S. K. (1989). Infection and labor. III. interleukin-1: a signal for the onset of parturition. *Am. J. Obstet. Gynecol.*, 160:1117–1123.

Rosso, F., Giordano, A., Barbarisi, M., and Barbarisi, A. (2004). From cell-ECM interactions to tissue engineering. *J. Cell Biol.*, 199:174–180.

Ruoslahti, E. (1996). Brain extracellular matrix. *Glycobiology*, 6:489–492.

Rutz, M., Metzger, J., Gellert, T., Luppa, P., Lipford, G. B., Wagner, H., and Bauer, S. (2004). Toll-like receptor 9 binds single-stranded CpG-DNA in a sequence- and pH-dependent manner. *Eur. J. Immunol.*, 34:2541–2550.

Samokhin, A., Francis, S., and Qwarnstrom, E. (2014). 154 blocking the IL-1RI co-receptor TILRR reduces vascular inflammation - *in vivo* analysis using TILRR knockout mice. *Heart*, 100:A90–A90.

Sarrazin, S., Lamanna, W. C., and Esko, J. D. (2011). Heparan sulfate proteoglycans. *Cold Spring Harb. Perspect. Biol.*, 3:a4952–a4984.

Schaefer, L. and Iozzo, R. V. (2008). Biological functions of the small leucine-rich proteoglycans: From genetics to signal transduction. *J. Biol. Chem.*, 283:21305–21309.

Schaefer, L., Tredup, C., Gubbiotti, M. A., and Iozzo, R. V. (2016). Proteoglycan neofunctions: regulation of inflammation and autophagy in cancer biology. *FEBS J.*, 284:10–26.

Schaffner, F., Ray, A. M., and Dontenwill, M. (2013). Integrin $\alpha5\beta1$, the fibronectin receptor, as a pertinent therapeutic target in solid tumors. *Cancers (Basel)*, 5:27–47.

Schifera, A. S. and Hardin, J. A. (2011). Factors modulating expression of *renilla* luciferase from control plasmids used in luciferase reporter gene assays. *Anal. Biochem.*, 396:167–172.

Schmidt, G., Hausser, H., and Kresse, H. (1991). Interaction of the small proteoglycan decorin with fibronectin. involvement of the sequence NKISK of the core protein. *Biochem. J.*, 280:411–414.

Schön, P. (2017). Atomic force microscopy of RNA: State of the art and recent advancements. *Semin. Cell Dev. Biol.*, 73:209–219.

Schön, P., Kutnyanszky, E., Donkelaar, B., Santonicola, M. G., Tecim, T., Aldred, N., Clare, A. S., and Vancso, G. J. (2013). Probing biofouling resistant polymer brush surfaces by atomic force microscopy based force spectroscopy. *Colloids Surf. B*, 102:923–930.

Schonfelder, J., Sancho, D. D., and Perez-Jimenez, R. (2016). The power of force: Insights into the protein folding process using single-molecule force spectroscopy. *J. Mol. Biol.*, 428:4245–4257.

Schönherr, E., Witsch-Prehm, P., Harrach, B., Robenek, H., Rauterberg, J., and Kresse, H. (1995). Interaction of biglycan with type I collagen. *J. Biol. Chem.*, 270:2776–2783.

Schwartz, M. A. (1997). Integrins, oncogenes, and anchorage independence. *J. Cell Biol.*, 139:575–578.

Schwarzbauer, J. E. and DeSimone, D. W. (2011). Fibronectins, their fibrillogenesis, and in vivo functions. *Cold Spring Harb. Perspect. Biol.*, 3:a005041–a005059.

Schwarzbauer, J. E. and Sechler, J. L. (1999). Fibronectin fibrillogenesis: a paradigm for extracellular matrix assembly. *Curr. Opin. Cell Biol.*, 11:622–627.

Seidler, D. G. (2012). The galactosaminoglycan-containing decorin and its impact on diseases. *Curr. Opin. Struct. Biol.*, 22:578–582.

Seo, Y. and Jhe, W. (2008). Atomic force microscopy and spectroscopy. *Rep. Prog. Phys.*, 71:16101–16123.

Shephard, R. J. (2001). Sepsis and mechanisms of inflammatory response: is exercise a good model? *Br. J. Sports Med.*, 35:223–230.

Shoulders, M. D. and Raines, R. T. (2009). Collagen structure and stability. *Annu. Rev. Biochem.*, 78:929–958.

Silbert, J. E. and Sugumaran, G. (2002). Biosynthesis of chondroitin/dermatan sulfate. *IUBMB Life*, 54:177–186.

Simons, M. and Horowitz, A. (2001). Syndecan-4-mediated signalling. *Cell. Signal.*, 13:855–862.

Sims, J. E., Gayle, M. A., Slack, J. L., Alderson, M. R., Bird, T. A., Giri, J. G., Colotta, F., Re, F., Mantovani, A., Shanebeck, K., Grabstein, K, H., and Dower, S. K. (1993). Interleukin 1 signaling occurs exclusively via the type i receptor. *Proc. Natl. Acad. Sci. USA*, 90:6155–6159.

Sims, J. E. and Smith, D. E. (2010). The il-1 family: regulators of immunity. *Nat. Rev. Immunol.*, 10:89–102.

Sizemore, N., Leung, S., and Stark, G. R. (1999). Activation of phosphatidylinositol 3-kinase in response to interleukin-1 leads to phosphorylation and activation of the NF-κB p65/RelA subunit. *Mol. Cell Biol.*, 19:4798–4805.

Smith, S. A., Samokhin, A. O., Alfaidi, M., Murphy, E. C., Rhodes, D., Holcombe, W. M. L., Kiss-Toth, E., Storey, R. F., Yee, S.-P., Francis, S. E., and Qwarnstrom, E. E. (2017). The IL-1RI co-receptor TILRR (*FREM1* isoform 2) controls aberrant inflammatory responses and development of vascular disease. *JACC Basic Transl. Sci.*, 2:398–414.

Struntz, T., Oroszlan, K., Schäfer, R., and Güntherodt, H.-J. (1999). Dynamic force spectroscopy of single dna molecules. *Proc. Natl. Acad. Sci. USA*, 96:11277–11282.

Sumarokova, M., Iturri, J., and Toca-Herrera, J. L. (2018). Adhesion, unfolding forces, and molecular elasticity of fibronectin coatings: An atomic force microscopy study. *Microsc. Res. Tech.*, 81:4245–4257.

Suzuki, N., Suzuki, S., Duncan, G. S., Millar, D. G., Wada, T., Mirtsos, C., Takada, H., Wakeham, A., Itie, A., Li, S., Penninger, J. M., Wesche, H., Ohashi, P. S., Mak, T. W., and Yeh, W. C. (2012). Severe impairment of interleukin-1 and Toll-like receptor signalling in mice lacking IRAK-4. *Nature*, 416:750–756.

Symons, A. L., Polak, B., Powell, R. N., and Seymour, G. J. (1995). Interleukin-1 (IL-1) bioactivity and inhibition of IL-1 bioactivity in supernatant fluid from cultured microphthalmic (mi) mice teeth of different ages. *J. Oral Pathol. Med.*, 24:365–373.

Szymanski, J. M., Zhang, K., and Feinberg, A. W. (2017). Measuring the Poissons ratio of fibronectin using engineered nanofibers. *Sci. Rep.*, 7:13413.

Takagi, J., Erickson, H. P., and Springer, T. A. (2001). C-terminal opening mimics 'inside-out' activation of integrin $\alpha 5\beta 1$. *Nat. Struct. Biol.*, 8:412–416.

Takagi, J., Strokovich, K., Springer, T. A., and Walz, T. (2003). Structure of integrin $\alpha_5\beta_1$ in complex with fibronectin. *EMBO J.*, 22:4607–4615.

Takeda, K., Kaisho, T., and Akira, S. (2003). Toll-like receptors. *Annu. Rev. Immunol.*, 21:335–376.

Taubenberger, A., Cisneros, D. A., Freidrichs, J., Puech, P.-H., Muller, D. J., and Franz, C. M. (2007). Revealing early steps of $\alpha_2\beta_1$ integrin-mediated adhesion to collagen type i by using single-cell force spectroscopy. *Mol. Biol. Cell*, 18:1634–1644.

Tay, S., Hughey, J. J., Lee, T. K., Lipniacki, T., Quake, S. R., and Covert, M. W. (2010). Single-cell NF-κB dynamics reveal digital activation and analog information processing in cells. *Nature*, 466:267–271.

Teckchandani, A., Toida, N., Goodchild, J., Henderson, C., Watts, J., Wollschied, B., and Cooper, J. A. (2009). Quantitative proteomics identifies a Dab2/integrin module regulating cell migration. *J. Cell Biol.*, 186:99–111.

Tees, D. F. J., Waugh, R. E., and Hammer, D. A. (2001). A microcantilever device to assess the effect of force on the lifetime of selectin-carbohydrate bonds. *Biophys. J.*, 80:668–682.

Templeton, D. M. (1992). Proteoglycans in cell regulation. *Crit. Rev. Clin. Lab. Sci.*, 29:141–184.

Thorn, K. (2016). A quick guide to light microscopy in cell biology. *Mol. Biol. Cell*, 27:219–222.

Thoumine, O., Kocian, P., Kottelat, A., and Meister, J. J. (2000). Short-term binding of fibroblasts to fibronectin: optical tweezers experiments and probabilistic analysis. *Eur. Biophys. J.*, 29:398–408.

Tkachenko, E., Rhodes, J. M., and Simons, M. (2005). Syndecans. *Circ. Res.*, 96:488–500.

Tomankova, K., Kolar, P., Malohlava, J., and Kolarova, H. (2012). Mechanical characterisation of hela cells using atomic force microscopy. *Current Microscopy Contributions to Advances in Science and Technology, Formatex Research Center*, 27:549–554.

Tomasini-Johansson, B. R., Annis, D. S., and Mosher, D. F. (2007). The N-terminal 70-kDa fragment of fibronectin binds to cell surface fibronectin assembly sites in the absence of intact fibronectin. *Matrix Biol.*, 25:282–293.

Tong, Z., Mikheikin, A., Krasnoslobodtsev, A., Lv, Z., and Lyubchenko, Y. L. (2017). Novel polymer linkers for single molecule AFM force spectroscopy. *PMC*, 60:161–168.

Tracey, R. P. (2006). The five cardinal signs of inflammation: *Calor*, *Dolor*, *Rubor*, *Tumor* ... and *Penuria* (apologies to aulus cornelius celsus, *De medicina*, c. a.d. 25). *J. Gerontol. A Biol. Sci. Med. Sci.*, 60:1051–1052.

Trowbridge, J. M. and Gallo, R. L. (2002). Dermatan sulfate: new functions from an old glycosaminoglycan. *Glycobiology*, 12:117R–125R.

Turvey, S. E. and Broide, D. H. (2010). Chapter 2: Innate immunity. *J. Allergy Clin. Immunol.*, 125:S24–S32.

Tuttolomondo, A., Di Raimondo, D., Pecoraro, R., Arnao, V., Pinto, A., and Licata, G. (2012). Atherosclerosis as an inflammatory disease. *Curr. Pharm. Des.*, 18:4266–4288.

Vallés, S., Tsoi, C., Huang, W.-Y., Wyllie, D., Carlotti, F., Askari, J. A., Humphries, M. J., Dower, S. K., and Qwarnstrom, E. E. (1999). Recruitment of a heparan sulfate subunit to the interleukin-1 receptor complex. regulation by fibronectin attachment. *J. Biol. Chem.*, 274:20103–20109.

Verbelen, C. and Dufréne, Y. F. (2009). Direct measurement of *mycobacterium*?fibronectin interactions. *Integr. Biol.*, 1:296–300.

Voigtländer, B. (2015). *Scanning Probe Microscopy: Atomic Force Microscopy and Scanning Tunnelling Microscopy*. Springer-Verlag, Berlin, Germany, 1st edition.

Wang, N. (1998). Mechanical interactions among cytoskeletal filaments. *Hypertension*, 32:162–165.

Wang, R., Clark, R. A., Mosher, D. F., and Ren, X. D. (2005). Fibronectin's central cell-binding domain supports focal adhesion formation and rho signal transduction. *J. Biol. Chem.*, 280:28803–28810.

Wasylnka, J. A. and Moore, M. M. (2000). Adhesion of *Aspergillus* species to extracellular matrix proteins: Evidence for involvement of negatively charged carbohydrates on the conidial surface. *Infect. Immun.*, 68:28803–28810.

Weber, A., Wasiliew, P., and Kracht, M. (2010). Interleukin-1 (IL-1) pathway. *Sci. Signal.*, 3:1–6.

Weber, I. T., Harrison, R. W., and Iozzo, R. V. (2001). Model structure of decorin and implications for collagen fibrillogenesis. *J. Biol. Chem.*, 271:31767–31770.

Weder, G., Blondiaux, N., Giazzon, M., Matthey, N., Klein, M., Pugin, R., Heinzelmann, H., and Liley, M. (2010). Use of force spectroscopy to investigate the adhesion of living adherent cells. *Langmuir*, 26:8180–8186.

Weder, G., Vörös, J., Giazzon, M., Mathey, N., Heinzelmann, H., and Liley, M. (2009). Measuring cell adhesion forces during the cell cycle by force spectroscopy. *Biointerphases*, 4:27–34.

Weiss, R. J., Esko, J. D., and Tor, Y. (2017). Targeting heparin and heparan sulfate protein interactions. *Org. Biomol. Chem.*, 17:5656–5668.

Werther, M. and Seitz, H. (2008). *Protein-Protein Interaction*. Springer, New York, USA, 1st edition.

White, E. S. and Muro, A. F. (2011). Fibronectin splice variants: understanding their multiple roles in health and disease using engineered mouse models. *IUBMB Life*, 63:538–546.

Wight, T. N. and Merrilees, M. J. (2004). Proteoglycans in atherosclerosis and restenosis: key roles for versican. *Circ. Res.*, 94:1158–1167.

Williams, N. (2010). Prize for the HeLa cell story. *Curr. Biol.*, 20:R1003–R1004.

Wojcikiewicz, E. P., Abdulreda, M. H., Zhang, X., and Moy, V. T. (2006). Force spectroscopy of LFA-1 and its ligands, ICAM-1 and ICAM-2. *Biomacromolecules*, 7:3188–3195.

Woods, A. and Couchman, J. R. (2001). Syndecan-4 and focal adhesion function. *Curr. Opin. Cell Biol.*, 13:578–583.

Woods, A., Longley, R. L., Tumova, S., and Couchman, J. R. (2000a). Syndecan-4 binding to the high affinity heparin-binding domain of fibronectin drives focal adhesion formation in fibroblasts. *Arch. Biochem. Biophys.*, 374:66–72.

Woods, M. L., Cabanas, C., and Shimizu, Y. (2000b). Activation?dependent changes in soluble fibronectin binding and expression of $\beta 1$ integrin activation epitopes in t cells: relationship to t cell adhesion and migration. *Eur. J. Immunol.*, 30:38–49.

Wozniak, M. A., Modzelewska, K., Kwong, L., and Keely, P. J. (2004). Focal adhesion regulation of cell behavior. *Biochim. Biophys. Acta.*, 1692:103–119.

Xie, Z.-L., Shao, S.-L., Lv, J.-W., Wang, C.-H., Yuan, C.-Z., Zhang, W.-W., and Xu, X.-J. (2011). Co-transfection and tandem transfection of HEK293A cells for overexpression and RNAi experiments. *Cell. Biol. Int.*, 35:187–192.

Xu, D. and Esko, J. D. (2014). Demystifying heparan sulfate-protein interactions. *Annu. Rev. Biochem.*, 83:129–157.

Xu, L.-C., Vadillo-Rodriguez, V., and Logan, B. E. (2005). Residence time, loading force, ph, and ionic strength affect adhesion forces between colloids and biopolymer-coated surfaces. *Langmuir*, 21:7591–7500.

Xue, Y., Li, X., Li, H., and Zhang, W. (2014). Quantifying thiol-gold interactions towards the efficient strength control. *Nature Commun.*, 5:4348–4356.

Yamada, K. M., Kennedy, D. W., Kimata, K., and Pratt, R. M. (1980). Characterization of fibronectin interactions with glycosaminoglycans and identification of active proteolytic fragments. *J. Biol. Chem.*, 255:6055–6063.

Yang, W. Y. and Gruebele, M. (2003). Folding at the speed limit. *Nature*, 423:193–197.

Yoshimura, A., Lien, E., Ingalls, R. R., Tuomanen, E., Dziarski, R., and Golenbock, D. (1999). Cutting edge: recognition of Gram-positive bacterial cell wall components by the innate immune system occurs via Toll-like receptor 2. *J. Immunol.*, 163:1–5.

Yue, B. (2014). Biology of the extracellular matrix: An overview. *J. Glaucoma.*, Oct-Nov:S20–S23.

Zhang, H. M., Rao, J. N., Guo, X., Liu, L., Zou, T., Turner, D. J., , and Wang, J.-Y. (2004a). Akt kinase activation blocks apoptosis in intestinal epithelial cells by inhibiting caspase-3 after polyamine depletion. *J. Biol. Chem.*, 279:22539–22547.

Zhang, J.-M. and An, J. (2009). Cytokines, inflammation and pain. *Int. Anesthesiol. Clin.*, 42:27–37.

Zhang, K. and Chen, J. (2012). The regulation of integrin function by divalent cations. *Cell Adh. Migr.*, 6:20–29.

Zhang, X., Craig, S. E., Kirby, H., Humphries, M. J., and Moy, V. T. (2004b). Molecular basis for the dynamic strength of the integrin $\alpha_4\beta_1$/VCAM-1 interaction. *Biophys. J.*, 87:3470–3478.

Zhang, X., Pino, G. M., Shephard, F., Kiss-Toth, E., and Qwarnstrom, E. E. (2012). Distinct control of MyD88 adapter-dependent and Akt kinase-regulated responses by the interleukin (IL)-1RI co-receptor, TILRR. *J. Biol. Chem.*, 287:12348–12352.

Zhang, X., Shephard, F., Kim, H. B., Palmer, I. R., McHarg, S., Fowler, G. J., O'Neil, L. A., Kiss-Toth, E., and Qwarnstrom, E. E. (2010). TILRR, a novel IL-1RI co-receptor, potentiates MyD88 recruitment to control Ras-dependent amplification of NF-κB. *J. Biol. Chem.*, 285:7222–7232.

Zhang, Z., Vuori, K., Reed, J. C., and Ruoslahti, E. (1995a). The $\alpha 5\beta 1$ integrin supports survival of cells on fibronectin and up-regulates Bcl-2 expression. *Proc. Natl. Acad. Sci. USA*, 92:6161–6165.

Zhang, Z., Vuori, K., and Ruoslahti, E. (1995b). The alpha 5 beta 1 integrin supports survival of cells on fibronectin and up-regulates Bcl-2 expression. *PNAS*, 92:6161–6165.

Zhao, W., Lui, S., Cai, M., Xu, H., Jiang, J., and Wang, H. (2013). Detection of carbohydrates on the surface of cancer and normal cells by topography and recognition imaging. *Chem. Comm.*, 49:2980–2982.

Zhao, X., Zhong, Y., Ye, T., Wang, D., and Mao, B. (2015). Discrimination between cervical cancer cells and normal cervical cells based on longitudinal elasticity using atomic force microscopy. *Nanoscale Res. Lett.*, 10:482–489.

Zheng, C., Yin, Q., and Wu, H. (2011). Structural studies of NF-κB signaling. *Cell Res.*, 21:183–195.

Zhu, P., Xiong, W., Rodgers, G., and Qwarnstrom, E. E. (1998). Regulation of interleukin 1 signalling through integrin binding and actin reorganization: disparate effects on NF-kappaB and stress kinase pathways. *Biochem. J.*, 330:975–981.

Zhu, W., Robey, P. G., and Boskey, A. L. (2008). Chapter 9 - The regulatory role of matrix proteins in mineralization of bone. In Marcus, R., Feldman, D., Nelson, D. A., and Rosen, Clifford, J., editors, *Osteoporosis (Third Edition)*, pages 191–240. Academic Press, San Diego.

Appendix A

MATLAB® Code for Quantification of Rupture Forces

The following MATLAB® code, with some slight modifications, was written by Mr. Jamie Blakeman, a fellow PhD student, as part of his PhD project (still ongoing) and therefore credit should go to him. It was used alongside PUNAIS throughout this thesis to quantify rupture forces and effective spring constants on single-molecule unbinding events in AFM force-curves.

$filename = '';$

$startImageNum = 0;$

$endImageNum = 100000;$

try

$y = Curves.(filepath)(:,2);$

$yy = smooth(y);$

$x = Curves.(filepath)(:,1);$

$clearvars\ data\ raw;$

$set(handles.lastlength,'String',filepath);$

```
axes(handles.plotarea);
plot(x,y);
axesop = get(handles.axesauto,'Value');
if axesop == 1
xmin = -0.05e-6;
xmax = 0.3e-6;
ymin = -0.2e-9;
ymax = 0.05e-9;
ylim([ymin ymax])
xlim([xmin xmax])
else
xmin = str2num(get(handles.XMin,'String'));
xmax = str2num(get(handles.XMax,'String'));
ymin = str2num(get(handles.YMin,'String'));
ymax = str2num(get(handles.YMax,'String'));
ylim([ymin ymax])
xlim([xmin xmax])
end
set(handles.plotarea,'YMinorTick','on')
hline(0,'b');
drawnow
[x2 , y2] = ginput;
valuebreak = [x2,y2];
doublesize = size(valuebreak);
lastscansize = num2str(doublesize(1));
readoutstr = strcat('Lastcurvehad','',lastscansize,'event(s)');
```

```
set(handles.txtreadout,'String',readoutstr);
name = strcat(filepath);
libraryofvalues.(name) = valuebreak
global storeForAmmend
storeForAmmend = name;
end

output = evalin('base','output');
LoadingRateValueall = [];
Magnitudeall = [];
ImageNumber = [];
for(ImageNum = 0 : 100000)
ImageNumZeros = sprintf('%04d',ImageNum);
ImageNumStr = num2str(ImageNumZeros);
try filepath = strcat('Image',ImageNumStr); import = output.(filepath);
x1 = import(1);
x2 = import(2);
y1 = import(3);
y2 = import(4);
LoadingRateValue = ((-y1)-(-y2))/((x1)-(x2));
Magnitude = -y1;
LoadingRateValueall = [LoadingRateValueall;LoadingRateValue];
Magnitudeall = [Magnitudeall;Magnitude];
ImageNumber = [ImageNumber;ImageNum];
end
end
T = table(ImageNumber,LoadingRateValueall,Magnitudeall)
```

Appendix B

DSMFS Rupture Force Distributions

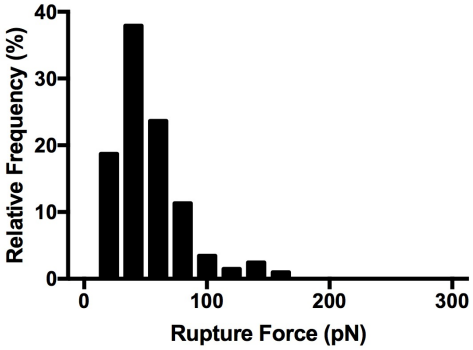

(a) Average rupture force of 43 ± 4 pN corresponding to an average loading rate of 860 ± 50 pNs^{-1}.

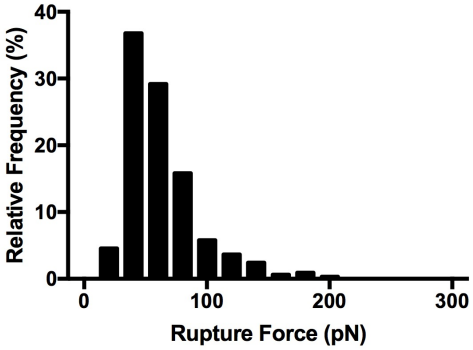

(b) Average rupture force of 51 ± 3 pN corresponding to an average loading rate of 2200 ± 300 pNs^{-1}.

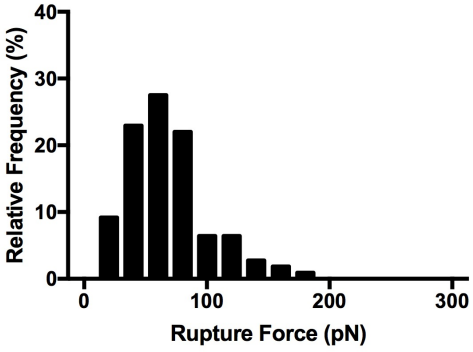

(c) Average rupture force of 59 ± 4 pN corresponding to an average loading rate of 4500 ± 1000 pNs^{-1}.

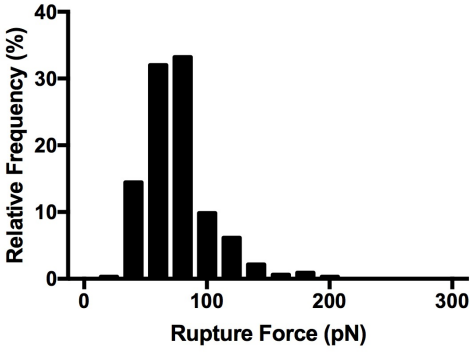

(d) Average rupture force of 70 ± 3 pN corresponding to an average loading rate of 8300 ± 650 pNs^{-1}.

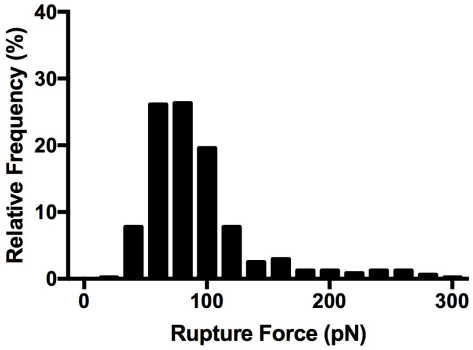

(e) Average rupture force of 77 ± 3 pN corresponding to an average loading rate of 22600 ± 800 pNs^{-1}.

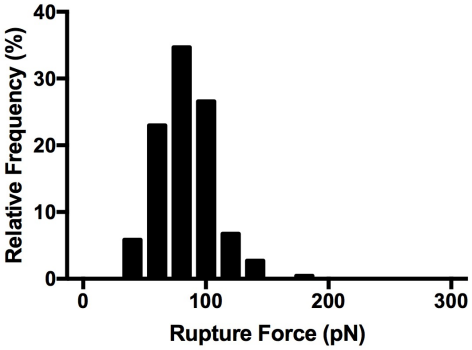

(f) Average rupture force of 82 ± 3 pN corresponding to an average loading rate of 27000 ± 3000 pNs^{-1}.

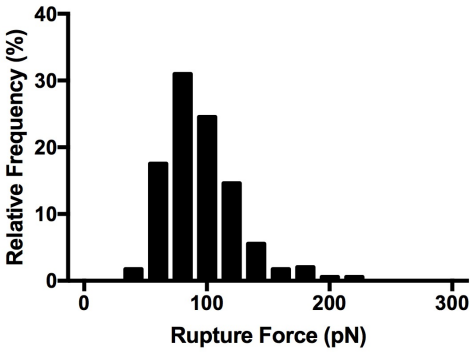

(g) Average rupture force of 89 ± 4 pN corresponding to an average loading rate of 36000 ± 2000 pNs^{-1}.

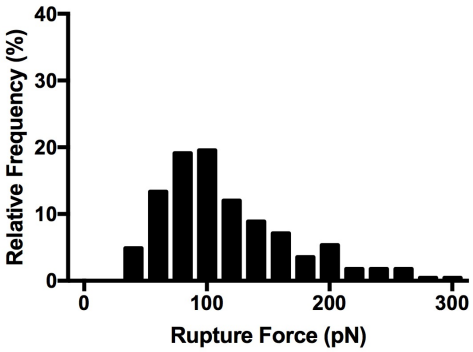

(h) Average rupture force of 96 ± 9 pN corresponding to an average loading rate of 66000 ± 6000 pNs^{-1}.

Fig. B.1 Frequency distributions for extracted rupture forces, taken at different velocities for SDC4-FN unbinding. Modal averages of the rupture force and corresponding loading rate are indicated for each. Included errors correspond to the width of the 95% confidence interval for the fit. SE values for each fit, provided by statistical software package GraphPad, were significantly smaller than the error values (95% confidence interval width) quoted here.

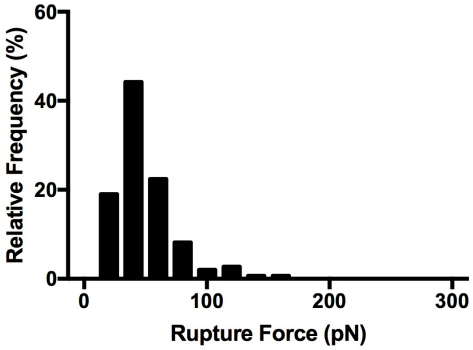

(a) Average rupture force of 34 ± 1 pN corresponding to an average loading rate of 3200 ± 150 pNs^{-1}.

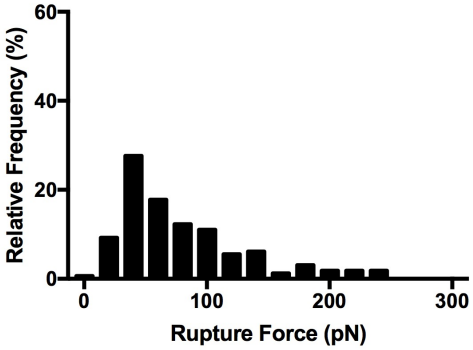

(b) Average rupture force of 43 ± 4 pN corresponding to an average loading rate of 5000 ± 500 pNs^{-1}.

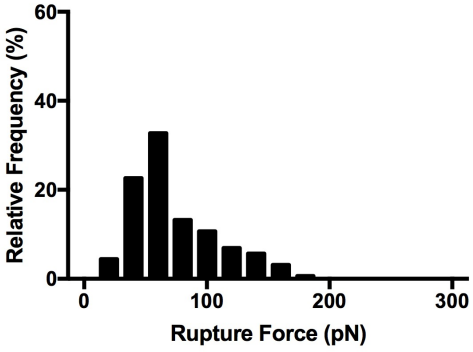

(c) Average rupture force of 58 ± 5 pN corresponding to an average loading rate of 10000 ± 250 pNs^{-1}.

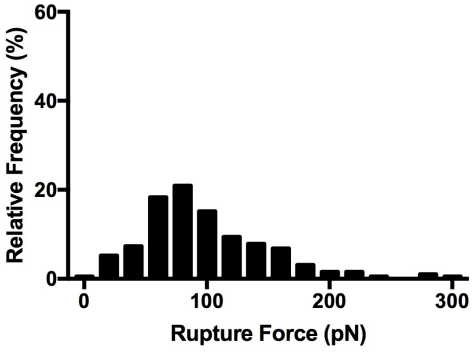

(d) Average rupture force of 83 ± 7 pN corresponding to an average loading rate of 17300 ± 500 pNs^{-1}.

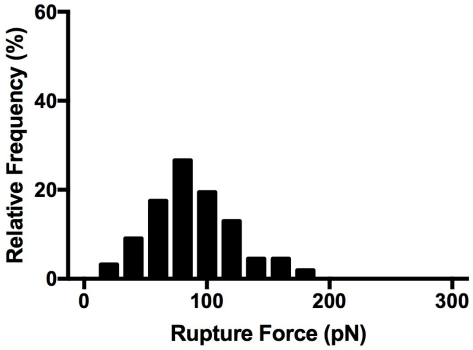

(e) Average rupture force of 84 ± 4 pN corresponding to an average loading rate of 22400 ± 1000 pNs^{-1}.

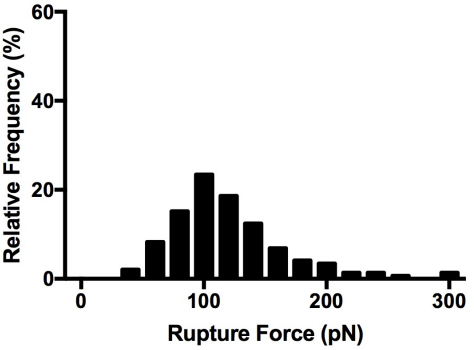

(f) Average rupture force of 99 ± 4 pN corresponding to an average loading rate of 30500 ± 1500 pNs^{-1}.

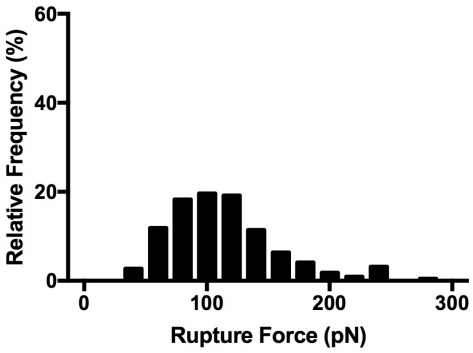

(g) Average rupture force of 106 ± 5 pN corresponding to an average loading rate of 35000 ± 2000 pNs^{-1}.

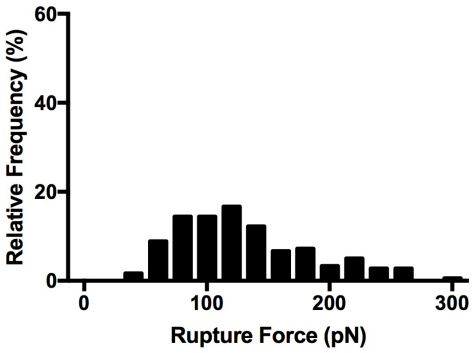

(h) Average rupture force of 112 ± 9 pN corresponding to an average loading rate of 46000 ± 5000 pNs^{-1}.

Fig. B.2 Frequency distributions for extracted rupture forces, taken at different velocities for DCN-FN unbinding. Modal averages of the rupture force and corresponding loading rate are indicated for each. Included errors correspond to the width of the 95% confidence interval for the fit. SE values for each fit, provided by statistical software package GraphPad, were significantly smaller than the error values (95% confidence interval width) quoted here.

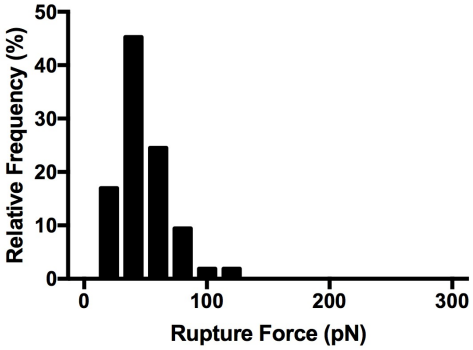

(a) Average rupture force of 38 ± 4 pN corresponding to an average loading rate of 480 ± 80 pNs^{-1}.

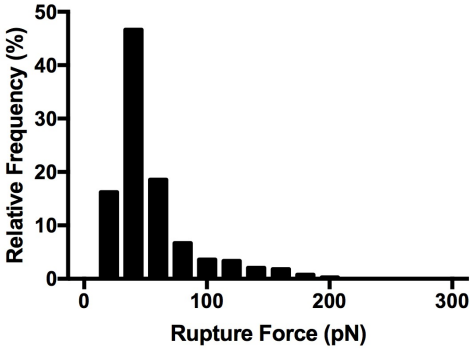

(b) Average rupture force of 41 ± 4 pN corresponding to an average loading rate of 930 ± 110 pNs^{-1}.

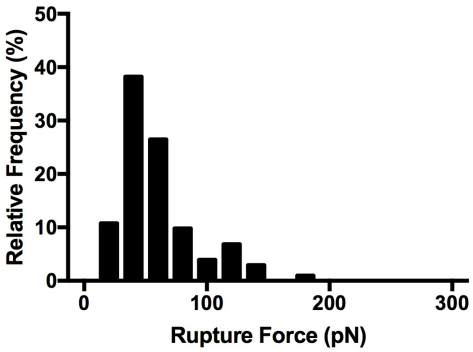

(c) Average rupture force of 46 ± 3 pN corresponding to an average loading rate of 1550 ± 250 pNs^{-1}.

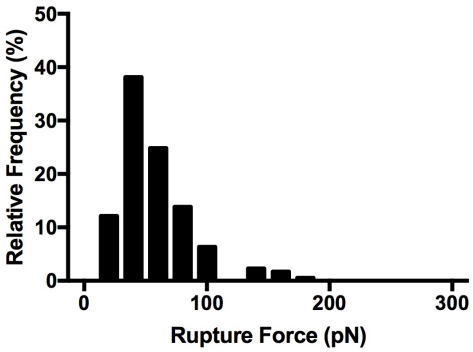

(d) Average rupture force of 47 ± 5 pN corresponding to an average loading rate of 2200 ± 200 pNs^{-1}.

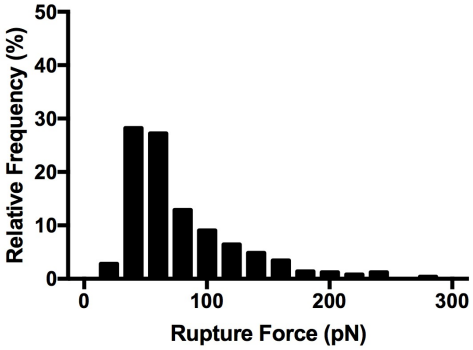

(e) Average rupture force of 49 ± 4 pN corresponding to an average loading rate of 2800 ± 150 pNs^{-1}.

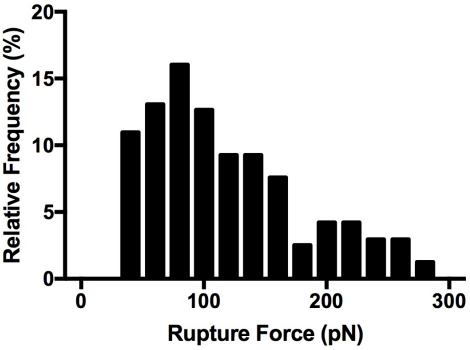

(f) Average rupture force of 72 ± 6 pN corresponding to an average loading rate of 14000 ± 2000 pNs^{-1}.

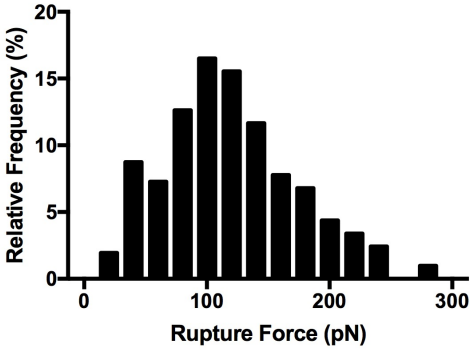

(g) Average rupture force of 106 ± 7 pN corresponding to an average loading rate of 23800 ± 3500 pNs^{-1}.

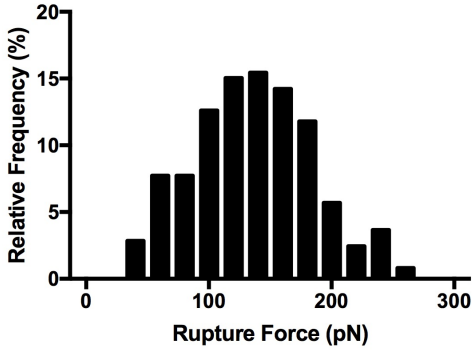

(h) Average rupture force of 133 ± 12 pN corresponding to an average loading rate of 35000 ± 3000 pNs^{-1}.

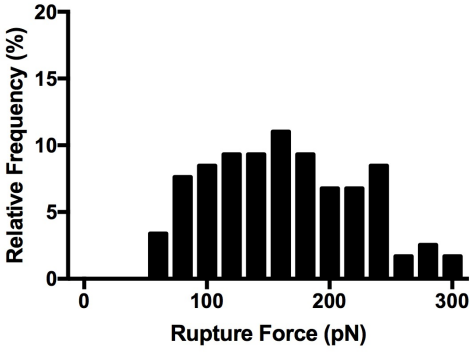

(i) Average rupture force of 155 ± 20 pN corresponding to an average loading rate of 59000 ± 5000 pNs^{-1}.

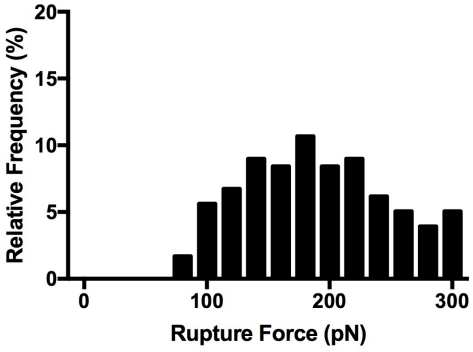

(j) Average rupture force of 185 ± 25 pN corresponding to an average loading rate of 91000 ± 9000 pNs^{-1}.

Fig. B.3 Frequency distributions for extracted rupture forces, taken at different velocities for $\alpha_5\beta_1$-FN unbinding. Modal averages of the rupture force and corresponding loading rate are indicated for each. Included errors correspond to the width of the 95% confidence interval for the fit. SE values for each fit, provided by statistical software package GraphPad, were significantly smaller than the error values (95% confidence interval width) quoted here.

Appendix C

Extracted Modulus Distributions for Individual Cells

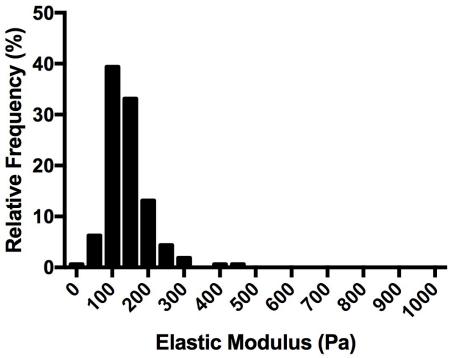

(a) Relative frequency distribution of the extracted elastic modulus for control HeLa cell 1. Described by a standard deviation of 60 Pa and a mean of 138 ± 5 Pa.

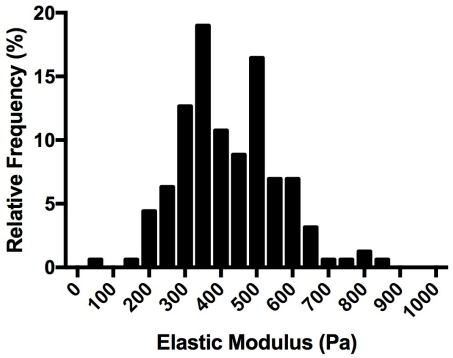

(b) Relative frequency distribution of the extracted elastic modulus for control HeLa cell 2. Described by a standard deviation of 135 Pa and a mean of 421 ± 11 Pa.

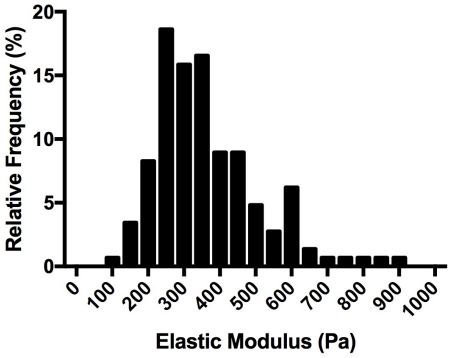

(c) Relative frequency distribution of the extracted elastic modulus for control HeLa cell 3. Described by a standard deviation of 146 Pa and a mean of 365 ± 12 Pa.

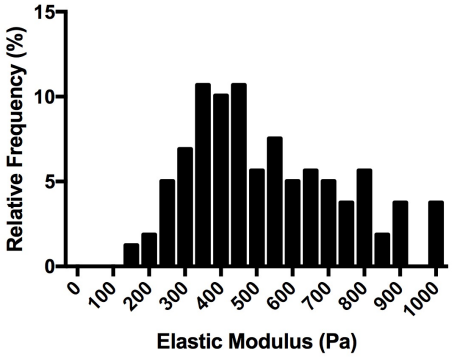

(d) Relative frequency distribution of the extracted elastic modulus for control HeLa cell 4. Described by a standard deviation of 256 Pa and a mean of 563 ± 20 Pa.

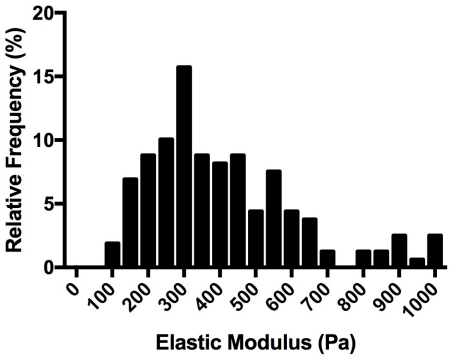

(e) Relative frequency distribution of the extracted elastic modulus for control HeLa cell 5. Described by a standard deviation of 219 Pa and a mean of 417 ± 17 Pa.

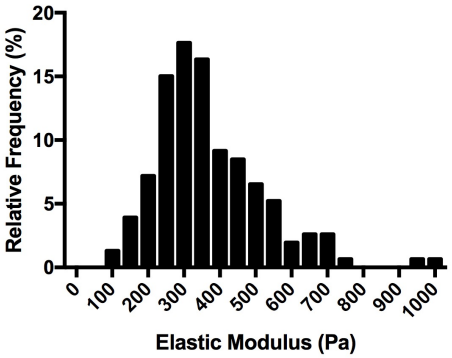

(f) Relative frequency distribution of the extracted elastic modulus for control HeLa cell 6. Described by a standard deviation of 152 Pa and a mean of 370 ± 12 Pa.

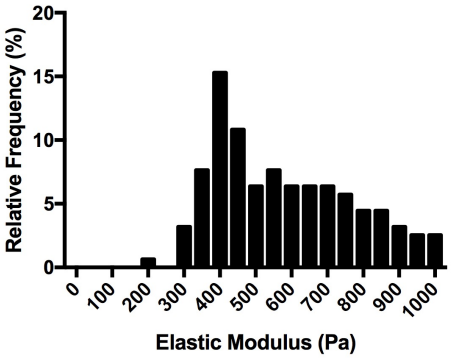

(g) Relative frequency distribution of the extracted elastic modulus for control HeLa cell 7. Described by a standard deviation of 226 Pa and a mean of 612 $\pm$ 18 Pa.

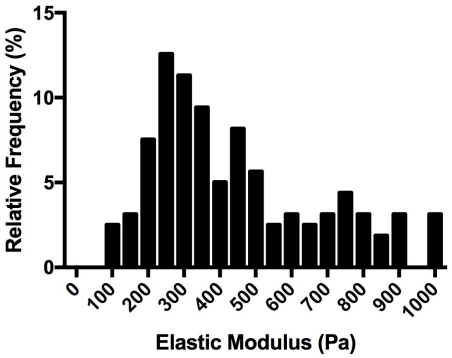

(h) Relative frequency distribution of the extracted elastic modulus for control HeLa cell 8. Described by a standard deviation of 307 Pa and a mean of 504 $\pm$ 24 Pa.

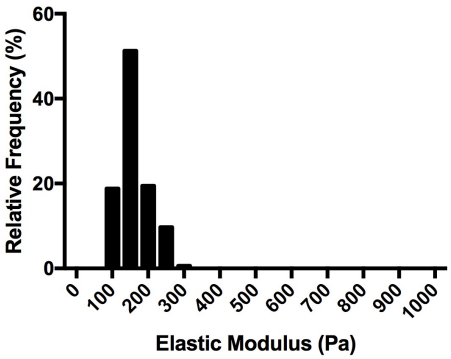

(i) Relative frequency distribution of the extracted elastic modulus for control HeLa cell 9. Described by a standard deviation of 42 Pa and a mean of 162 $\pm$ 3 Pa.

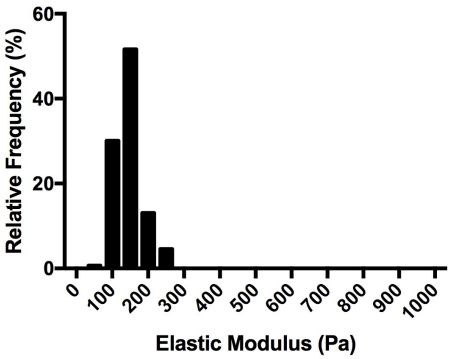

(j) Relative frequency distribution of the extracted elastic modulus for control HeLa cell 10. Described by a standard deviation of 41 Pa and a mean of 146 $\pm$ 3 Pa.

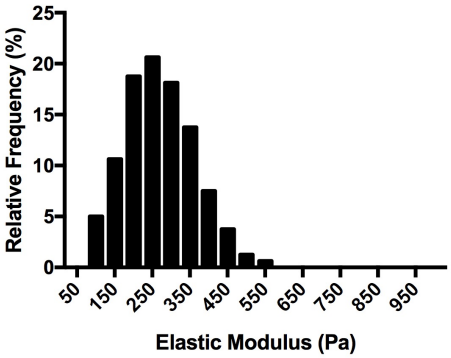

(k) Relative frequency distribution of the extracted elastic modulus for control HeLa cell 11. Described by a standard deviation of 90 Pa and a mean of 268 $\pm$ 7 Pa.

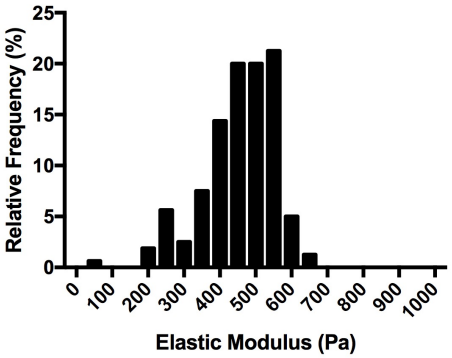

(l) Relative frequency distribution of the extracted elastic modulus for control HeLa cell 12. Described by a standard deviation of 100 Pa and a mean of 455 $\pm$ 8 Pa.

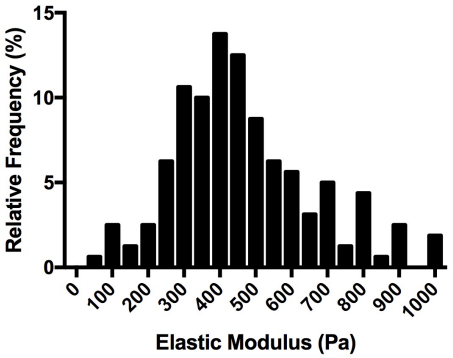

(m) Relative frequency distribution of the extracted elastic modulus for control HeLa cell 13. Described by a standard deviation of 200 Pa and a mean of 471 ± 16 Pa.

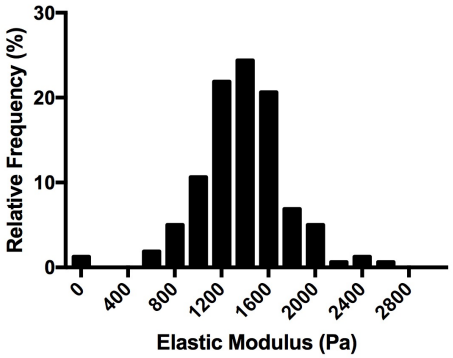

(n) Relative frequency distribution of the extracted elastic modulus for control HeLa cell 14. Described by a standard deviation of 371 Pa and a mean of 1370 ± 29 Pa.

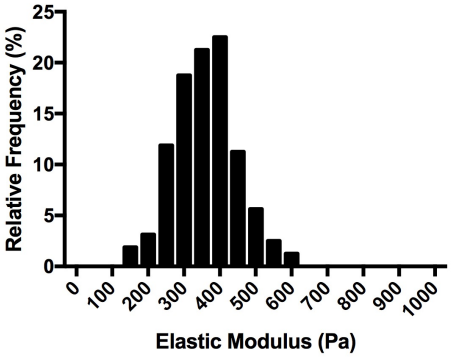

(o) Relative frequency distribution of the extracted elastic modulus for control HeLa cell 15. Described by a standard deviation of 87 Pa and a mean of 360 ± 7 Pa.

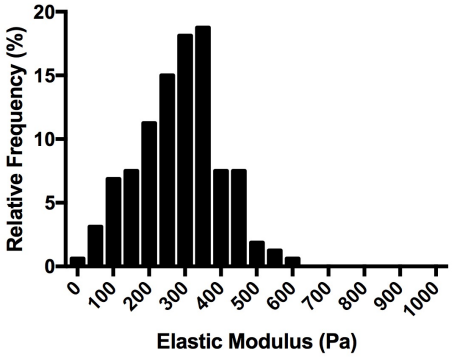

(p) Relative frequency distribution of the extracted elastic modulus for control HeLa cell 16. Described by a standard deviation of 112 Pa and a mean of 283 ± 9 Pa.

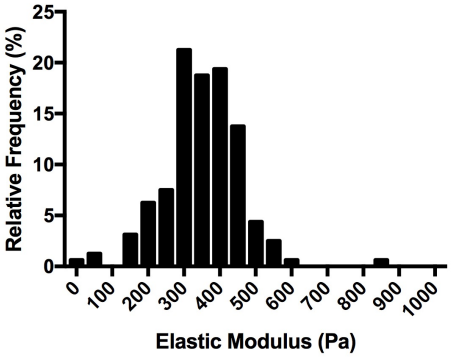

(q) Relative frequency distribution of the extracted elastic modulus for control HeLa cell 17. Described by a standard deviation of 105 Pa and a mean of 352 ± 8 Pa.

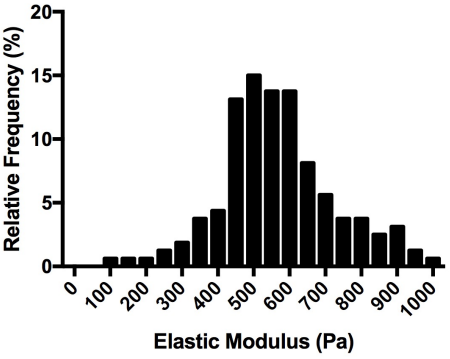

(r) Relative frequency distribution of the extracted elastic modulus for control HeLa cell 18. Described by a standard deviation of 196 Pa and a mean of 586 ± 16 Pa.

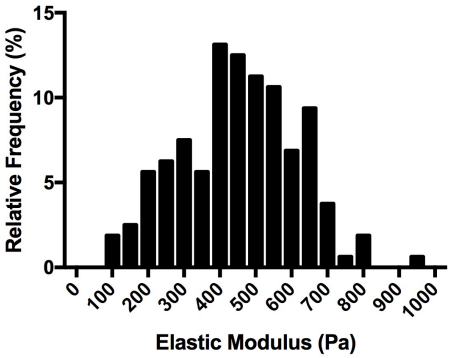

(s) Relative frequency distribution of the extracted elastic modulus for control HeLa cell 19. Described by a standard deviation of 162 Pa and a mean of 452 ± 13 Pa.

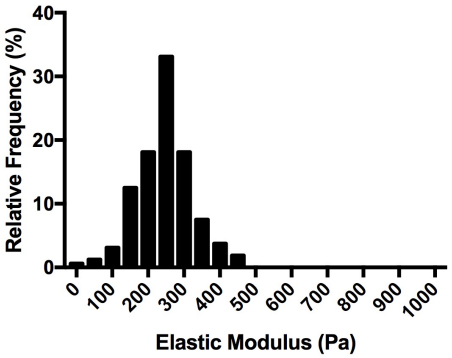

(t) Relative frequency distribution of the extracted elastic modulus for control HeLa cell 20. Described by a standard deviation of 79 Pa and a mean of 246 ± 6 Pa.

Fig. C.1 Relative frequency distributions of extracted elastic moduli extracted over 10 force maps for individual control HeLa cells. Standard deviations and mean ± SEM are indicated for each.

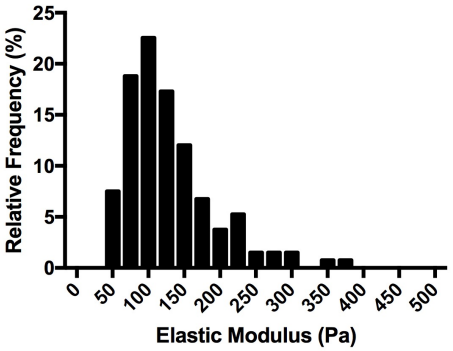

(a) Relative frequency distribution of the extracted elastic modulus for IL-1β stimulated HeLa cell 1. Described by a standard deviation of 63 Pa and a mean of 130 ± 5 Pa.

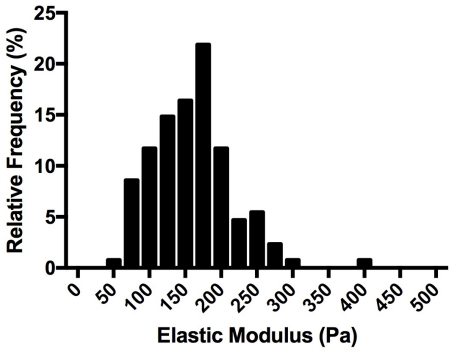

(b) Relative frequency distribution of the extracted elastic modulus for IL-1β stimulated HeLa cell 2. Described by a standard deviation of 56 Pa and a mean of 160 ± 5 Pa.

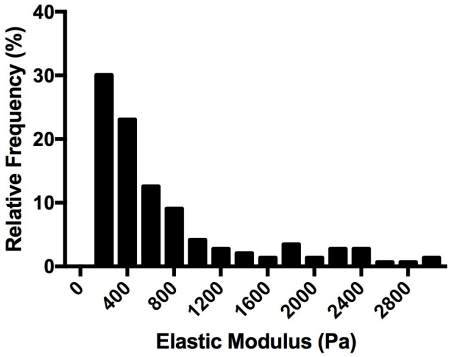

(c) Relative frequency distribution of the extracted elastic modulus for IL-1β stimulated HeLa cell 3. Described by a standard deviation of 748 Pa and a mean of 772 ± 63 Pa.

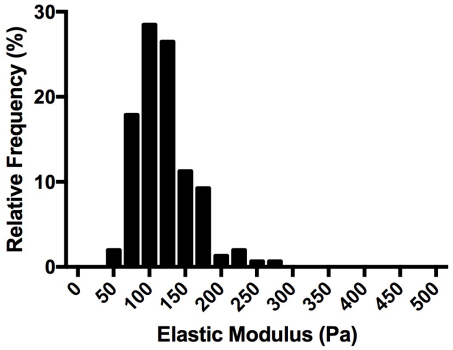

(d) Relative frequency distribution of the extracted elastic modulus for IL-1β stimulated HeLa cell 4. Described by a standard deviation of 40 Pa and a mean of 119 ± 3 Pa.

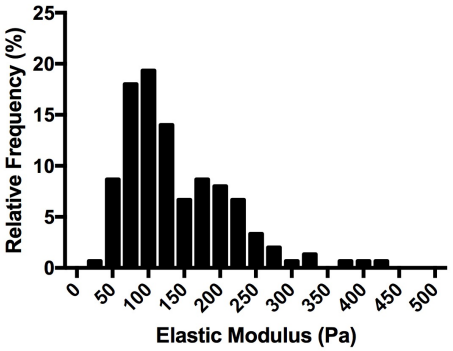

(e) Relative frequency distribution of the extracted elastic modulus for IL-1β stimulated HeLa cell 5. Described by a standard deviation of 74 Pa and a mean of 139 ± 6 Pa.

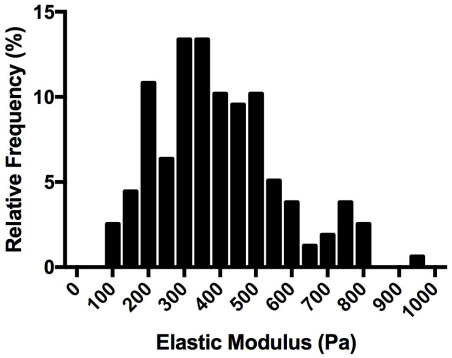

(f) Relative frequency distribution of the extracted elastic modulus for IL-1β stimulated HeLa cell 6. Described by a standard deviation of 173 Pa and a mean of 396 ± 14 Pa.

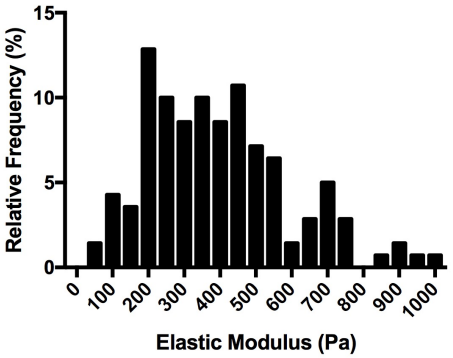

(g) Relative frequency distribution of the extracted elastic modulus for IL-1β stimulated HeLa cell 7. Described by a standard deviation of 204 Pa and a mean of 398 $\pm$ 17 Pa.

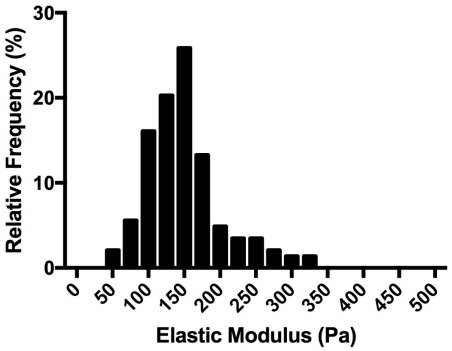

(h) Relative frequency distribution of the extracted elastic modulus for IL-1β stimulated HeLa cell 8. Described by a standard deviation of 53 Pa and a mean of 150 $\pm$ 4 Pa.

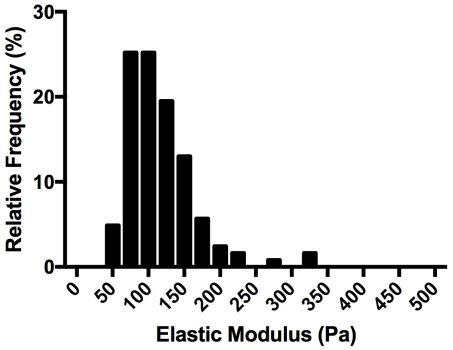

(i) Relative frequency distribution of the extracted elastic modulus for IL-1β stimulated HeLa cell 9. Described by a standard deviation of 48 Pa and a mean of 117 $\pm$ 4 Pa.

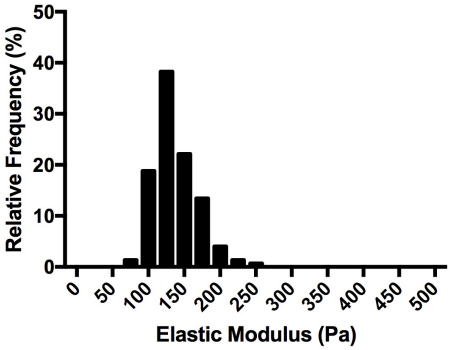

(j) Relative frequency distribution of the extracted elastic modulus for IL-1β stimulated HeLa cell 10. Described by a standard deviation of 31 Pa and a mean of 137 $\pm$ 3 Pa.

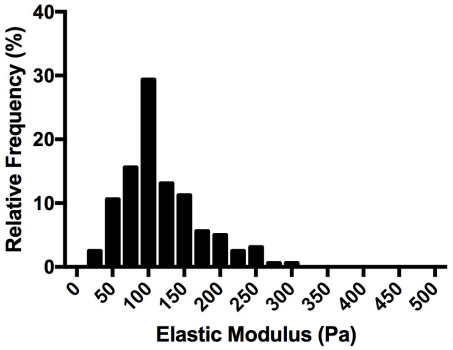

(k) Relative frequency distribution of the extracted elastic modulus for IL-1β stimulated HeLa cell 11. Described by a standard deviation of 54 Pa and a mean of 117 $\pm$ 4 Pa.

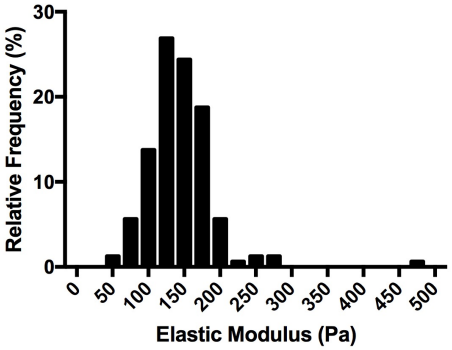

(l) Relative frequency distribution of the extracted elastic modulus for IL-1β stimulated HeLa cell 12. Described by a standard deviation of 46 Pa and a mean of 144 $\pm$ 4 Pa.

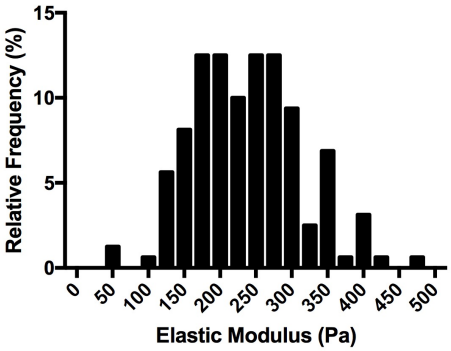

(m) Relative frequency distribution of the extracted elastic modulus for IL-1β stimulated HeLa cell 13. Described by a standard deviation of 79 Pa and a mean of 240 $\pm$ 6 Pa.

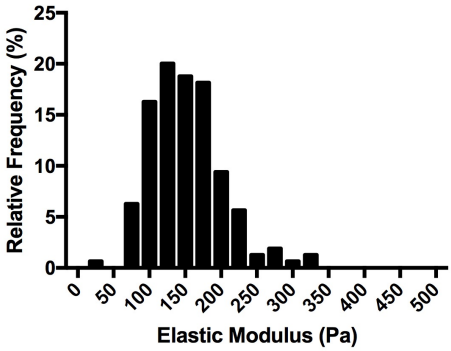

(n) Relative frequency distribution of the extracted elastic modulus for IL-1β stimulated HeLa cell 14. Described by a standard deviation of 52 Pa and a mean of 151 $\pm$ 4 Pa.

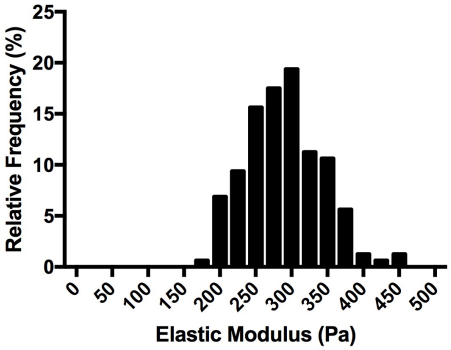

(o) Relative frequency distribution of the extracted elastic modulus for IL-1β stimulated HeLa cell 15. Described by a standard deviation of 53 Pa and a mean of 290 $\pm$ 4 Pa.

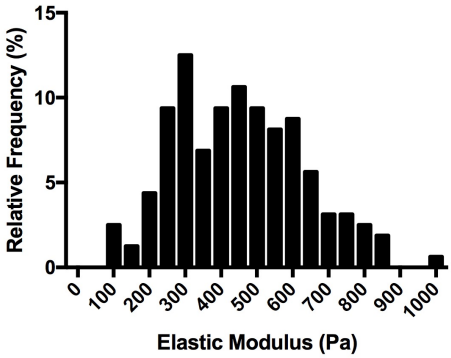

(p) Relative frequency distribution of the extracted elastic modulus for IL-1β stimulated HeLa cell 16. Described by a standard deviation of 182 Pa and a mean of 452 $\pm$ 14 Pa.

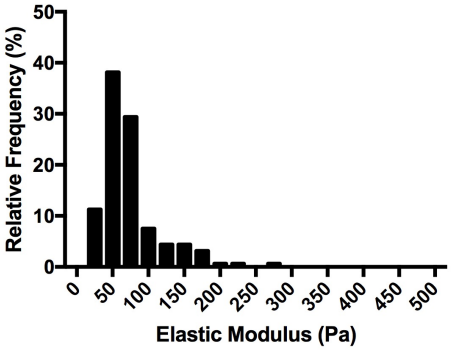

(q) Relative frequency distribution of the extracted elastic modulus for IL-1β stimulated HeLa cell 17. Described by a standard deviation of 40 Pa and a mean of 74 $\pm$ 3 Pa.

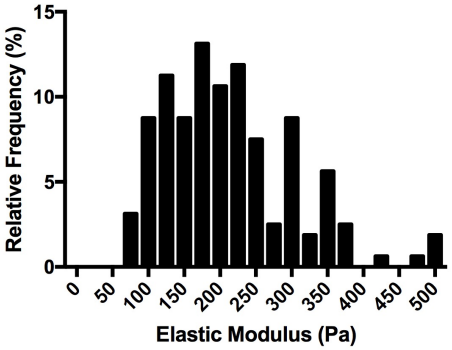

(r) Relative frequency distribution of the extracted elastic modulus for IL-1β stimulated HeLa cell 18. Described by a standard deviation of 94 Pa and a mean of 216 $\pm$ 7 Pa.

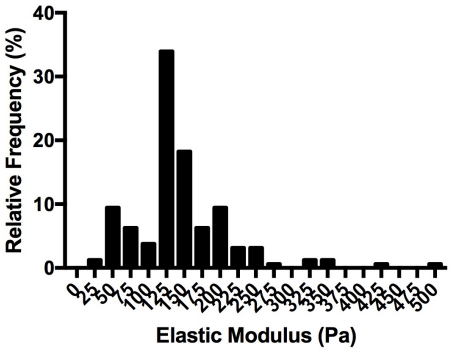

(s) Relative frequency distribution of the extracted elastic modulus for IL-1β stimulated HeLa cell 19. Described by a standard deviation of 76 Pa and a mean of 148 $\pm$ 6 Pa.

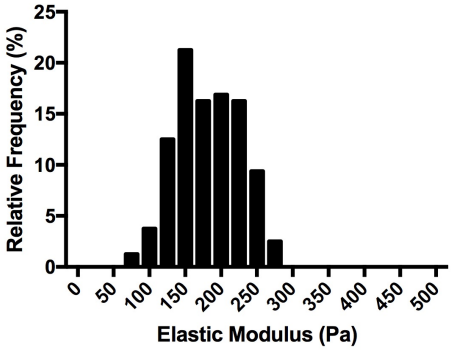

(t) Relative frequency distribution of the extracted elastic modulus for IL-1β stimulated HeLa cell 20. Described by a standard deviation of 45 Pa and a mean of 181 $\pm$ 4 Pa.

Fig. C.2 Relative frequency distributions of extracted elastic moduli extracted over 10 force maps for individual HeLa cells stimulated with 10^{-9} M IL-1β. Standard deviations and mean $\pm$ SEM are indicated for each.

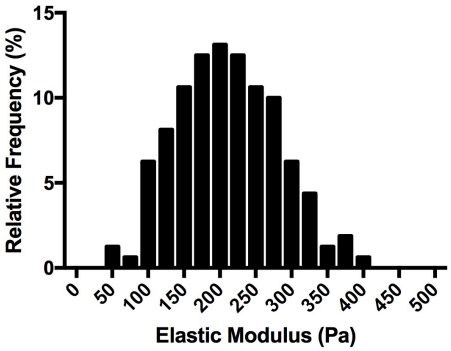

(a) Relative frequency distribution of the extracted elastic modulus for EV transfected HeLa cell 1. Described by a standard deviation of 70 Pa and a mean of 211 $\pm$ 6 Pa.

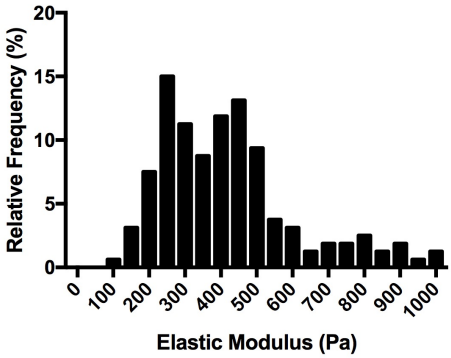

(b) Relative frequency distribution of the extracted elastic modulus for EV transfected HeLa cell 2. Described by a standard deviation of 189 Pa and a mean of 416 $\pm$ 15 Pa.

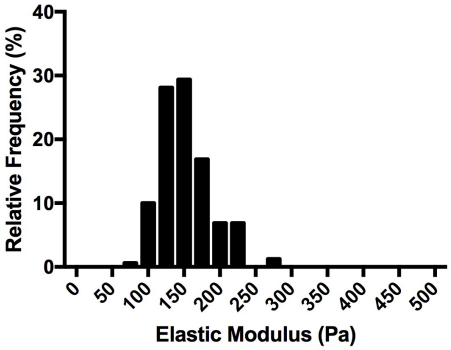

(c) Relative frequency distribution of the extracted elastic modulus for EV transfected HeLa cell 3. Described by a standard deviation of 36 Pa and a mean of 152 $\pm$ 3 Pa.

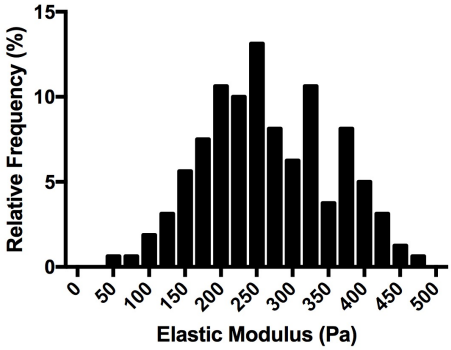

(d) Relative frequency distribution of the extracted elastic modulus for EV transfected HeLa cell 4. Described by a standard deviation of 88 Pa and a mean of 265 $\pm$ 7 Pa.

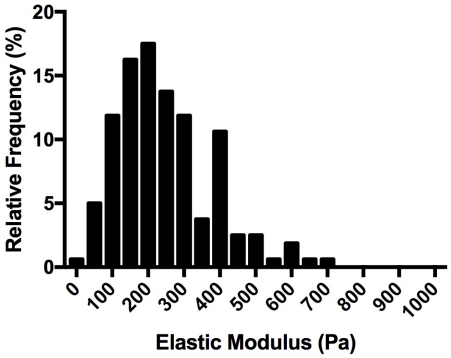

(e) Relative frequency distribution of the extracted elastic modulus for EV transfected HeLa cell 5. Described by a standard deviation of 134 Pa and a mean of 246 $\pm$ 11 Pa.

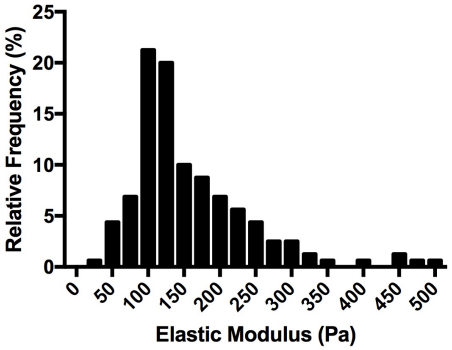

(f) Relative frequency distribution of the extracted elastic modulus for EV transfected HeLa cell 6. Described by a standard deviation of 114 Pa and a mean of 167 $\pm$ 9 Pa.

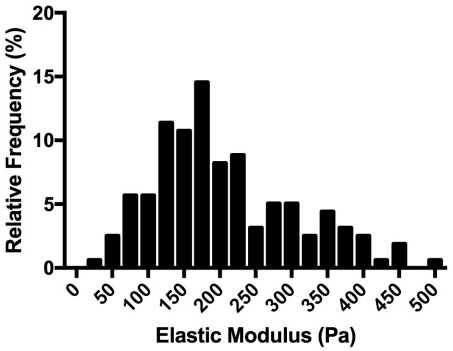

(g) Relative frequency distribution of the extracted elastic modulus for EV transfected HeLa cell 7. Described by a standard deviation of 114 Pa and a mean of 215 $\pm$ 9 Pa.

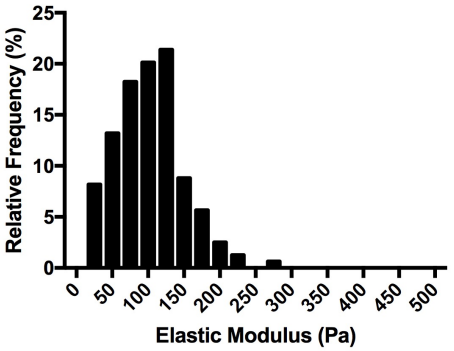

(h) Relative frequency distribution of the extracted elastic modulus for EV transfected HeLa cell 8. Described by a standard deviation of 47 Pa and a mean of 102 $\pm$ 4 Pa.

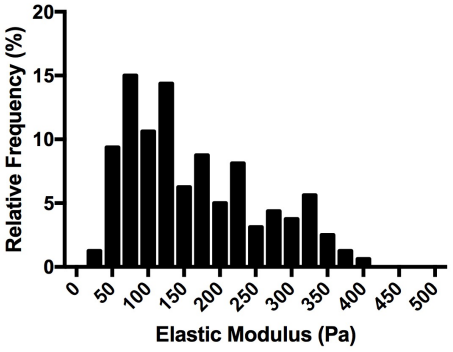

(i) Relative frequency distribution of the extracted elastic modulus for EV transfected HeLa cell 9. Described by a standard deviation of 91 Pa and a mean of 162 $\pm$ 7 Pa.

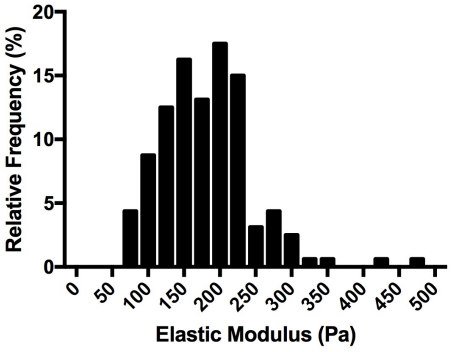

(j) Relative frequency distribution of the extracted elastic modulus for EV transfected HeLa cell 10. Described by a standard deviation of 63 Pa and a mean of 182 $\pm$ 5 Pa.

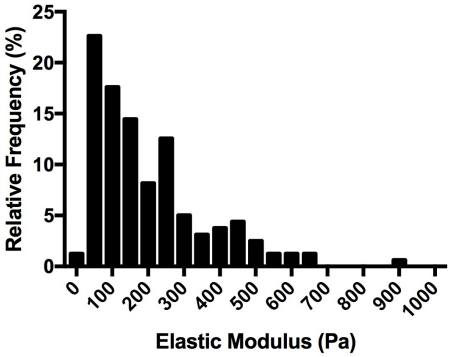

(k) Relative frequency distribution of the extracted elastic modulus for EV transfected HeLa cell 11. Described by a standard deviation of 158 Pa and a mean of 200 $\pm$ 13 Pa.

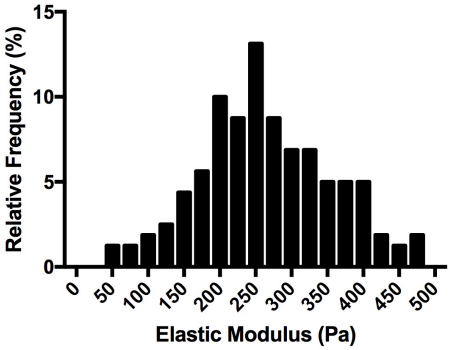

(l) Relative frequency distribution of the extracted elastic modulus for EV transfected HeLa cell 12. Described by a standard deviation of 151 Pa and a mean of 299 $\pm$ 12 Pa.

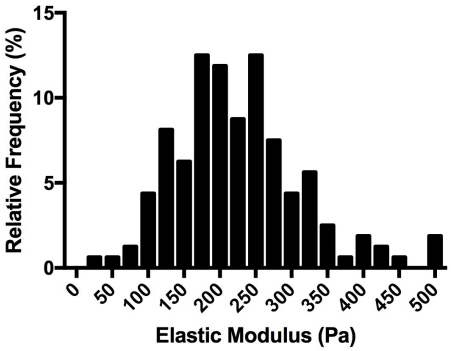

(m) Relative frequency distribution of the extracted elastic modulus for EV transfected HeLa cell 13. Described by a standard deviation of 140 Pa and a mean of 254 $\pm$ 11 Pa.

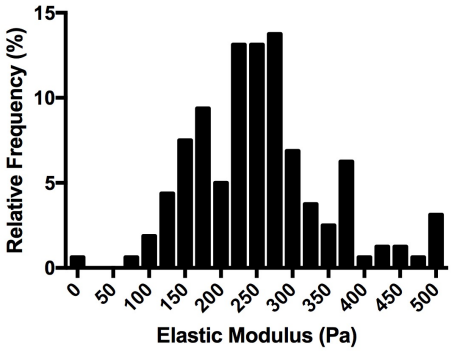

(n) Relative frequency distribution of the extracted elastic modulus for EV transfected HeLa cell 14. Described by a standard deviation of 120 Pa and a mean of 273 $\pm$ 10 Pa.

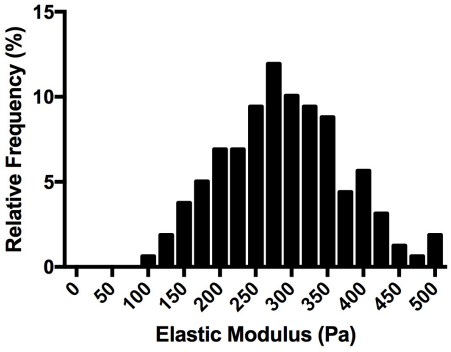

(o) Relative frequency distribution of the extracted elastic modulus for EV transfected HeLa cell 15. Described by a standard deviation of 164 Pa and a mean of 324 $\pm$ 13 Pa.

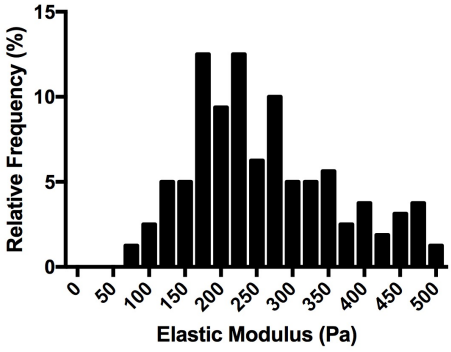

(p) Relative frequency distribution of the extracted elastic modulus for EV transfected HeLa cell 16. Described by a standard deviation of 119 Pa and a mean of 269 $\pm$ 9 Pa.

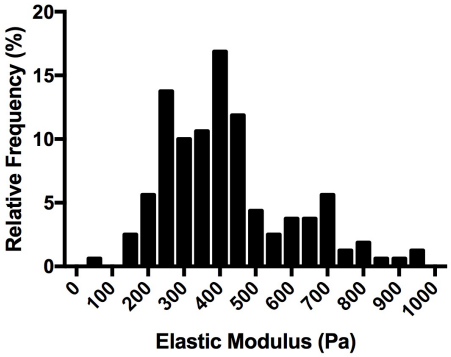

(q) Relative frequency distribution of the extracted elastic modulus for EV transfected HeLa cell 17. Described by a standard deviation of 274 Pa and a mean of 444 $\pm$ 19 Pa.

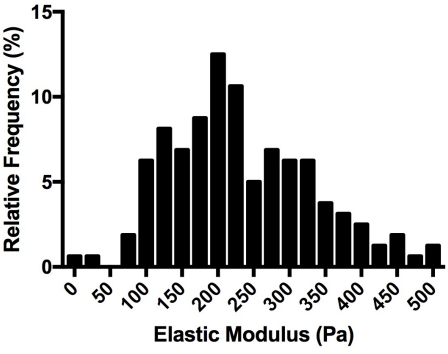

(r) Relative frequency distribution of the extracted elastic modulus for EV transfected HeLa cell 18. Described by a standard deviation of 140 Pa and a mean of 254 $\pm$ 11 Pa.

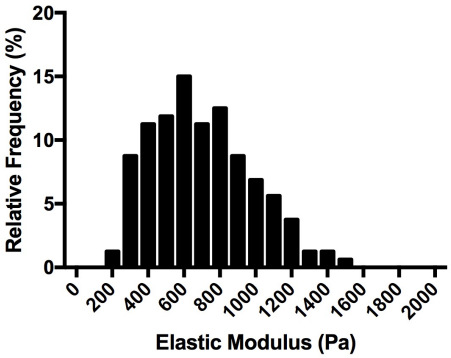

(s) Relative frequency distribution of the extracted elastic modulus for EV transfected HeLa cell 19. Described by a standard deviation of 277 Pa and a mean of 699 $\pm$ 22 Pa.

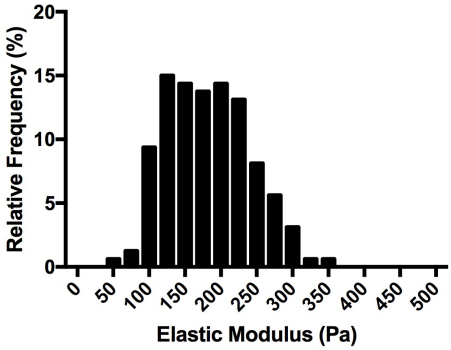

(t) Relative frequency distribution of the extracted elastic modulus for EV transfected HeLa cell 20. Described by a standard deviation of 58 Pa and a mean of 183 $\pm$ 5 Pa.

Fig. C.3 Relative frequency distributions of extracted elastic moduli extracted over 10 force maps for individual HeLa cells transfected with 1.5 μg EV per dish. Standard deviations and mean $\pm$ SEM are indicated for each.

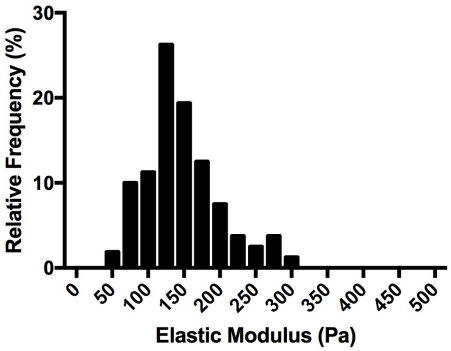

(a) Relative frequency distribution of the extracted elastic modulus for TILRR transfected HeLa cell 1. Described by a standard deviation of 52 Pa and a mean of 140 $\pm$ 4 Pa.

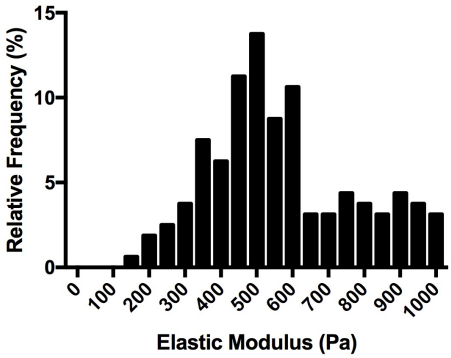

(b) Relative frequency distribution of the extracted elastic modulus for TILRR transfected HeLa cell 2. Described by a standard deviation of 228 Pa and a mean of 591 $\pm$ 18 Pa.

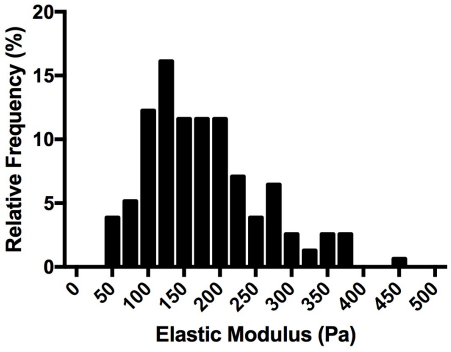

(c) Relative frequency distribution of the extracted elastic modulus for TILRR transfected HeLa cell 3. Described by a standard deviation of 85 Pa and a mean of 180 $\pm$ 7 Pa.

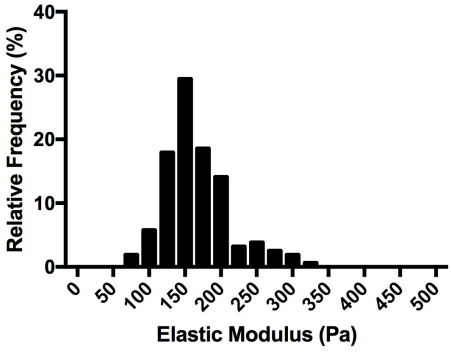

(d) Relative frequency distribution of the extracted elastic modulus for TILRR transfected HeLa cell 4. Described by a standard deviation of 46 Pa and a mean of 166 $\pm$ 4 Pa.

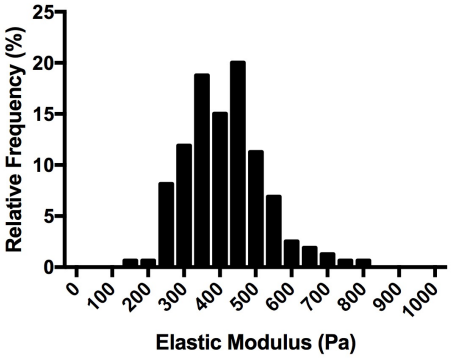

(e) Relative frequency distribution of the extracted elastic modulus for TILRR transfected HeLa cell 5. Described by a standard deviation of 122 Pa and a mean of 414 $\pm$ 9 Pa.

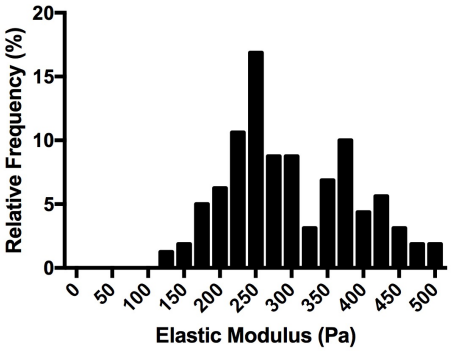

(f) Relative frequency distribution of the extracted elastic modulus for TILRR transfected HeLa cell 6. Described by a standard deviation of 105 Pa and a mean of 310 $\pm$ 8 Pa.

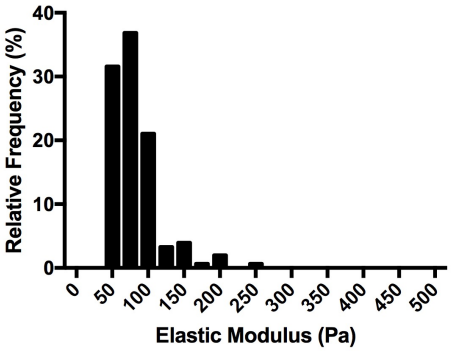

(g) Relative frequency distribution of the extracted elastic modulus for TILRR transfected HeLa cell 7 in. Described by a standard deviation of 34 Pa and a mean of 81 $\pm$ 3 Pa.

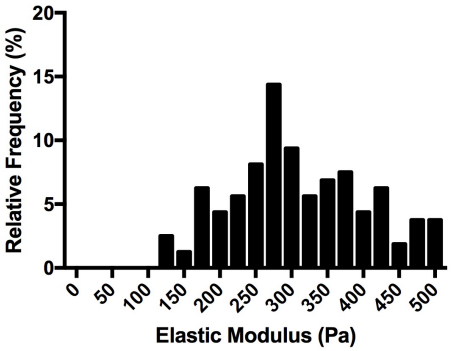

(h) Relative frequency distribution of the extracted elastic modulus for TILRR transfected HeLa cell 8. Described by a standard deviation of 114 Pa and a mean of 330 $\pm$ 9 Pa.

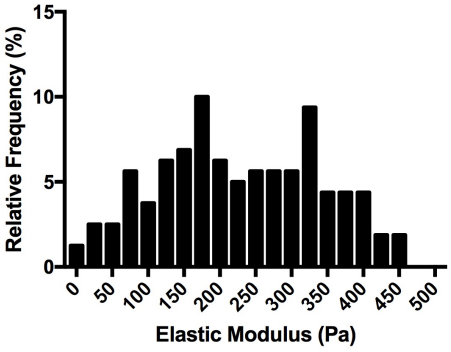

(i) Relative frequency distribution of the extracted elastic modulus for TILRR transfected HeLa cell 9. Described by a standard deviation of 161 Pa and a mean of 258 $\pm$ 13 Pa.

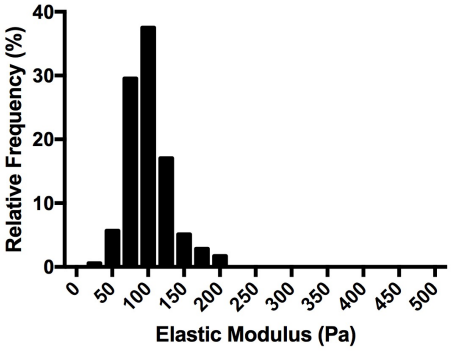

(j) Relative frequency distribution of the extracted elastic modulus for TILRR transfected HeLa cell 10 in. Described by a standard deviation of 29 Pa and a mean of 100 $\pm$ 2 Pa.

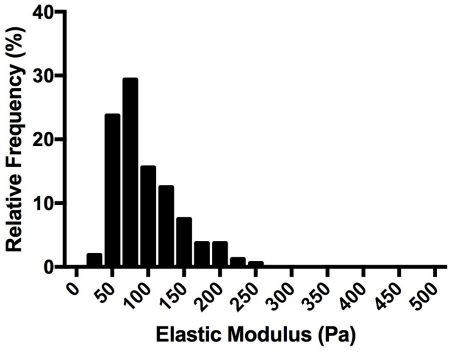

(k) Relative frequency distribution of the extracted elastic modulus for TILRR transfected HeLa cell 11. Described by a standard deviation of 45 Pa and a mean of 95 $\pm$ 4 Pa.

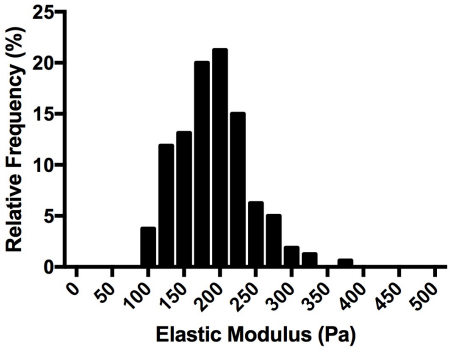

(l) Relative frequency distribution of the extracted elastic modulus for TILRR transfected HeLa cell 12. Described by a standard deviation of 50 Pa and a mean of 190 $\pm$ 4 Pa.

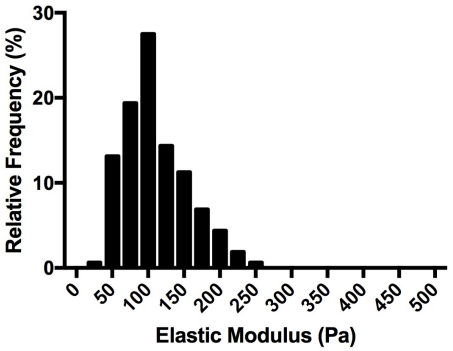

(m) Relative frequency distribution of the extracted elastic modulus for TILRR transfected HeLa cell 13. Described by a standard deviation of 45 Pa and a mean of 110 ± 4 Pa.

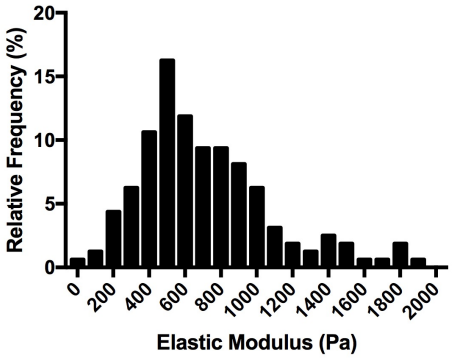

(n) Relative frequency distribution of the extracted elastic modulus for TILRR transfected HeLa cell 14. Described by a standard deviation of 407 Pa and a mean of 733 ± 32 Pa.

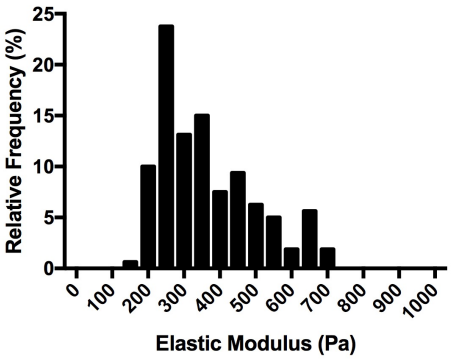

(o) Relative frequency distribution of the extracted elastic modulus for TILRR transfected HeLa cell 15. Described by a standard deviation of 134 Pa and a mean of 363 ± 11 Pa.

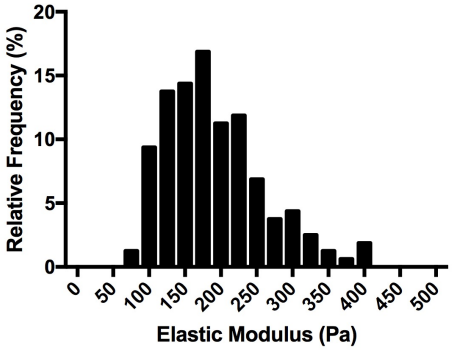

(p) Relative frequency distribution of the extracted elastic modulus for TILRR transfected HeLa cell 16. Described by a standard deviation of 70 Pa and a mean of 191 ± 6 Pa.

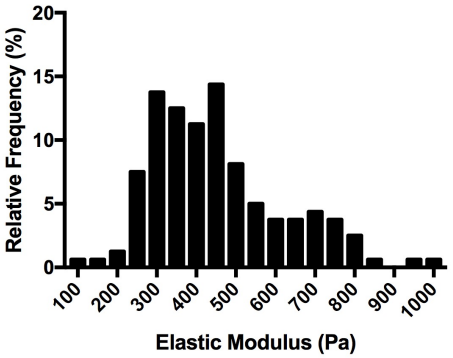

(q) Relative frequency distribution of the extracted elastic modulus for TILRR transfected HeLa cell 17. Described by a standard deviation of 234 Pa and a mean of 491 ± 18 Pa.

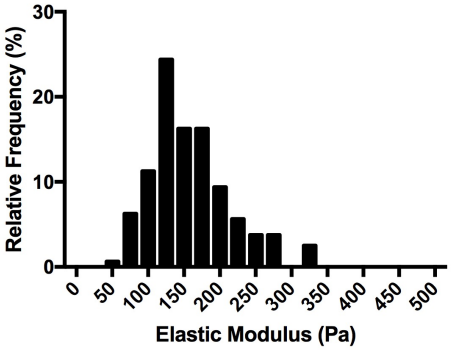

(r) Relative frequency distribution of the extracted elastic modulus for TILRR transfected HeLa cell 18. Described by a standard deviation of 55 Pa and a mean of 159 ± 4 Pa.

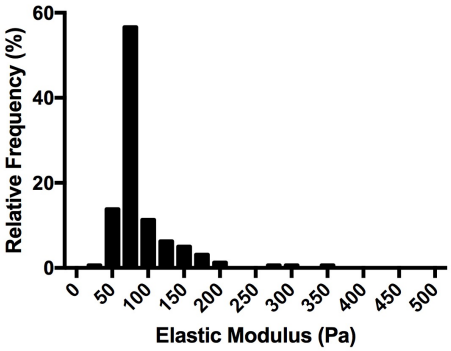

(s) Relative frequency distribution of the extracted elastic modulus for TILRR transfected HeLa cell 19. Described by a standard deviation of 44 Pa and a mean of 89 $\pm$ 3 Pa.

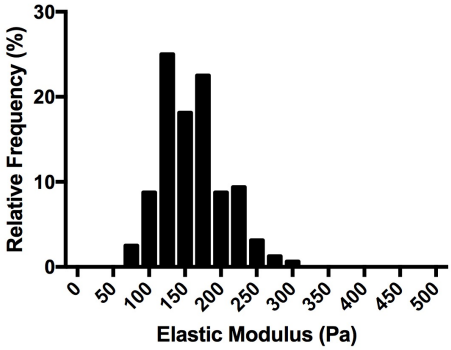

(t) Relative frequency distribution of the extracted elastic modulus for TILRR transfected HeLa cell 20. Described by a standard deviation of 43 Pa and a mean of 160 $\pm$ 3 Pa.

Fig. C.4 Relative frequency distributions of extracted elastic moduli extracted over 10 force maps for individual HeLa cells transfected with 1.5 μg TILRR cDNA per dish. Standard deviations and mean $\pm$ SEM are indicated for each.

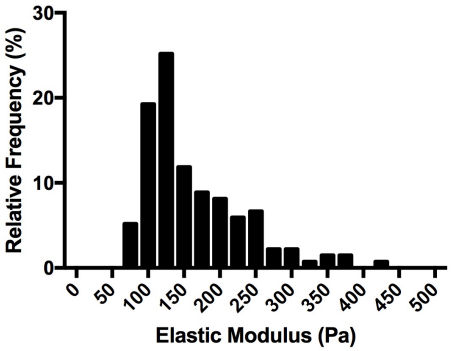

(a) Relative frequency distribution of the extracted elastic modulus for EV transfected and IL-1 stimulated HeLa cell 1. Described by a standard deviation of 71 Pa and a mean of 163 $\pm$ 6 Pa.

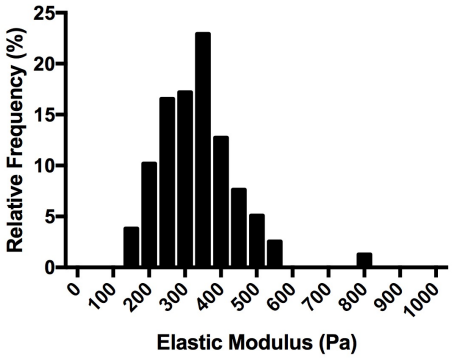

(b) Relative frequency distribution of the extracted elastic modulus for EV transfected and IL-1 stimulated HeLa cell 2. Described by a standard deviation of 108 Pa and a mean of 335 $\pm$ 9 Pa.

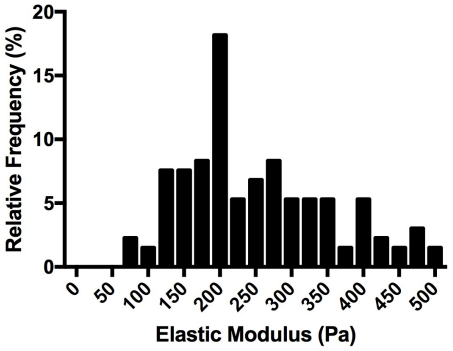

(c) Relative frequency distribution of the extracted elastic modulus for EV transfected and IL-1 stimulated HeLa cell 3. Described by a standard deviation of 113 Pa and a mean of 260 $\pm$ 10 Pa.

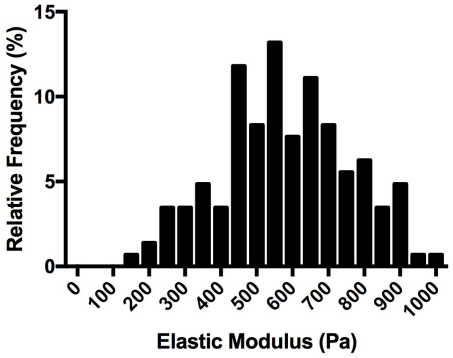

(d) Relative frequency distribution of the extracted elastic modulus for EV transfected and IL-1 stimulated HeLa cell 4. Described by a standard deviation of 184 Pa and a mean of 583 $\pm$ 15 Pa.

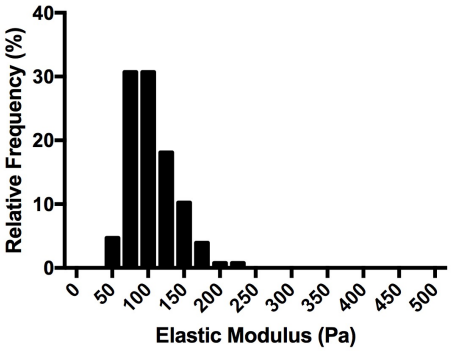

(e) Relative frequency distribution of the extracted elastic modulus for EV transfected and IL-1 stimulated HeLa cell 5. Described by a standard deviation of 32 Pa and a mean of 105 $\pm$ 3 Pa.

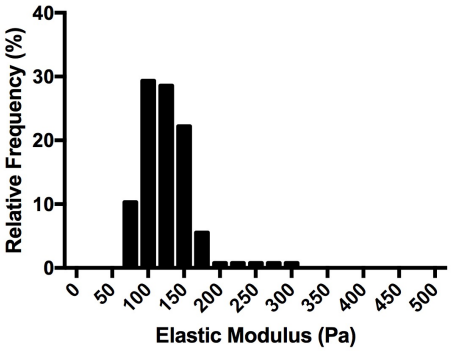

(f) Relative frequency distribution of the extracted elastic modulus for EV transfected and IL-1 stimulated HeLa cell 6. Described by a standard deviation of 36 Pa and a mean of 125 $\pm$ 3 Pa.

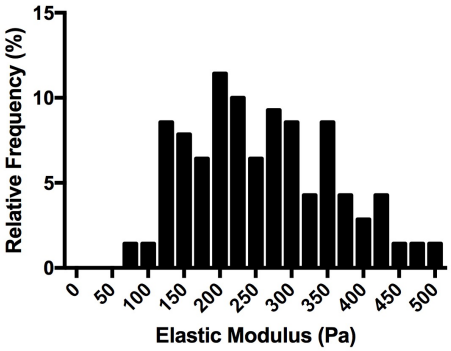

(g) Relative frequency distribution of the extracted elastic modulus for EV transfected and IL-1 stimulated HeLa cell 7. Described by a standard deviation of 99 Pa and a mean of 259 $\pm$ 8 Pa.

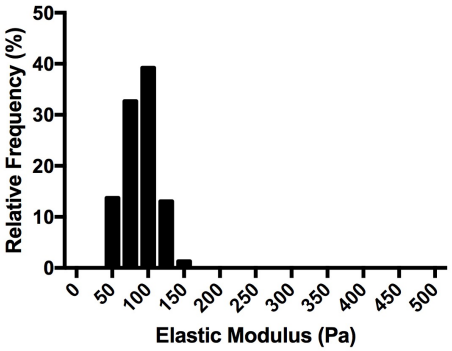

(h) Relative frequency distribution of the extracted elastic modulus for EV transfected and IL-1 stimulated HeLa cell 8. Described by a standard deviation of 21 Pa and a mean of 88 $\pm$ 2 Pa.

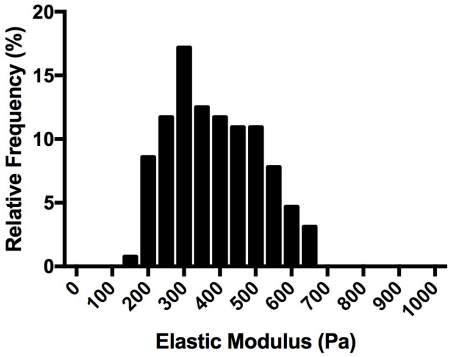

(i) Relative frequency distribution of the extracted elastic modulus for EV transfected and IL-1 stimulated HeLa cell 9. Described by a standard deviation of 123 Pa and a mean of 134 $\pm$ 11 Pa.

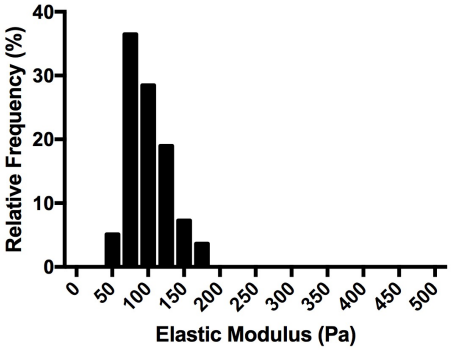

(j) Relative frequency distribution of the extracted elastic modulus for EV transfected and IL-1 stimulated HeLa cell 10. Described by a standard deviation of 29 Pa and a mean of 99 $\pm$ 2 Pa.

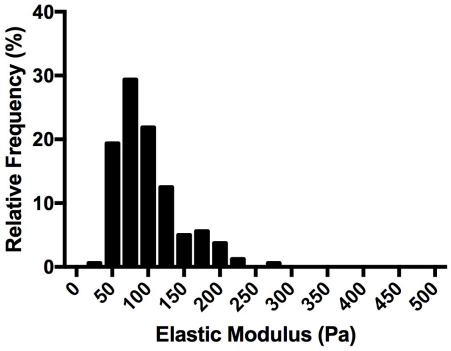

(k) Relative frequency distribution of the extracted elastic modulus for EV transfected and IL-1 stimulated HeLa cell 11. Described by a standard deviation of 44 Pa and a mean of 98 $\pm$ 4 Pa.

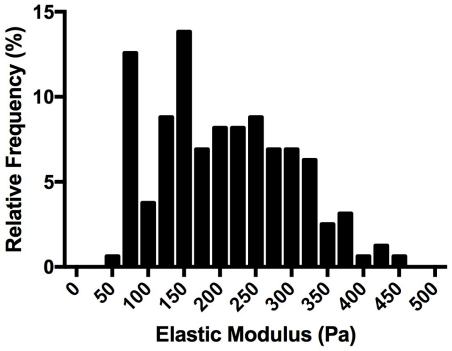

(l) Relative frequency distribution of the extracted elastic modulus for EV transfected and IL-1 stimulated HeLa cell 12. Described by a standard deviation of 92 Pa and a mean of 205 $\pm$ 7 Pa.

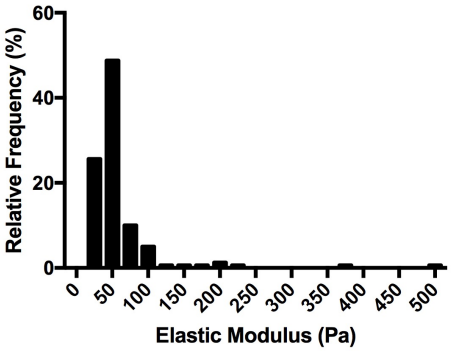

(m) Relative frequency distribution of the extracted elastic modulus for EV transfected and IL-1 stimulated HeLa cell 13. Described by a standard deviation of 160 Pa and a mean of 96 $\pm$ 13 Pa.

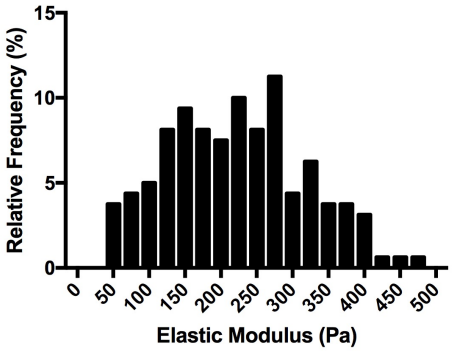

(n) Relative frequency distribution of the extracted elastic modulus for EV transfected and IL-1 stimulated HeLa cell 14. Described by a standard deviation of 104 Pa and a mean of 226 $\pm$ 8 Pa.

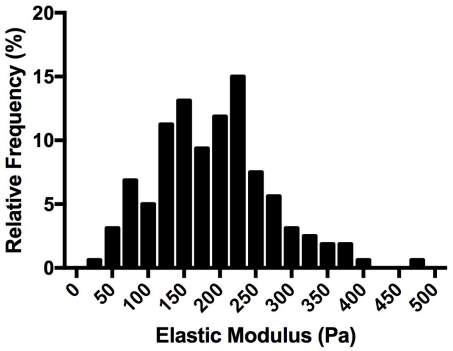

(o) Relative frequency distribution of the extracted elastic modulus for EV transfected and IL-1 stimulated HeLa cell 15. Described by a standard deviation of 80 Pa and a mean of 191 $\pm$ 6 Pa.

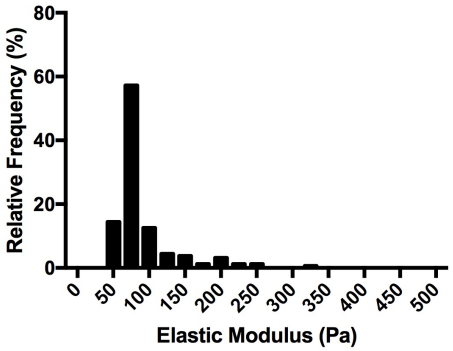

(p) Relative frequency distribution of the extracted elastic modulus for EV transfected and IL-1 stimulated HeLa cell 16. Described by a standard deviation of 44 Pa and a mean of 91 $\pm$ 3 Pa.

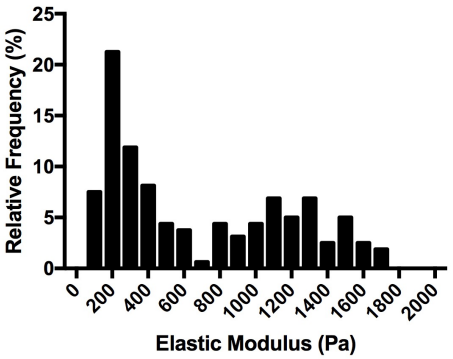

(q) Relative frequency distribution of the extracted elastic modulus for EV transfected and IL-1 stimulated HeLa cell 17. Described by a standard deviation of 500 Pa and a mean of 678 $\pm$ 40 Pa.

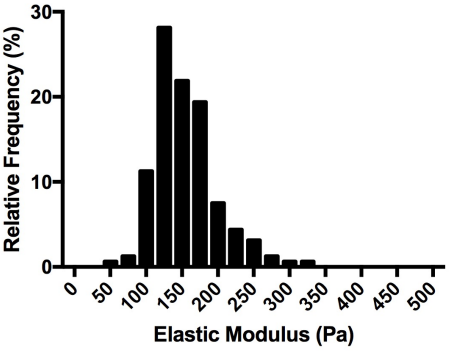

(r) Relative frequency distribution of the extracted elastic modulus for EV transfected and IL-1 stimulated HeLa cell 18. Described by a standard deviation of 43 Pa and a mean of 154 $\pm$ 3 Pa.

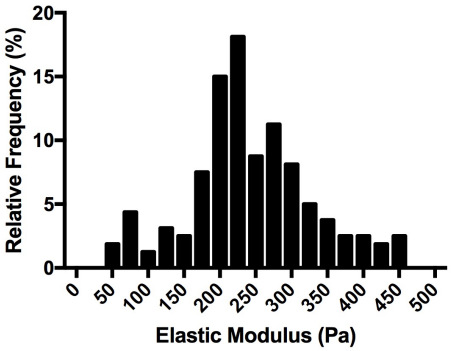

(s) Relative frequency distribution of the extracted elastic modulus for EV transfected and IL-1 stimulated HeLa cell 19. Described by a standard deviation of 85 Pa and a mean of 242 $\pm$ 7 Pa.

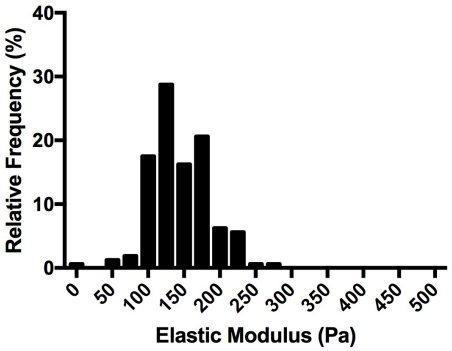

(t) Relative frequency distribution of the extracted elastic modulus for EV transfected and IL-1 stimulated HeLa cell 20. Described by a standard deviation of 41 Pa and a mean of 144 $\pm$ 3 Pa.

Fig. C.5 Relative frequency distributions of extracted elastic moduli extracted over 10 force maps for individual HeLa cells transfected with 1.5 μg EV per dish and stimulated with 10^{-9} M IL-1β. Standard deviations and mean $\pm$ SEM are indicated for each.

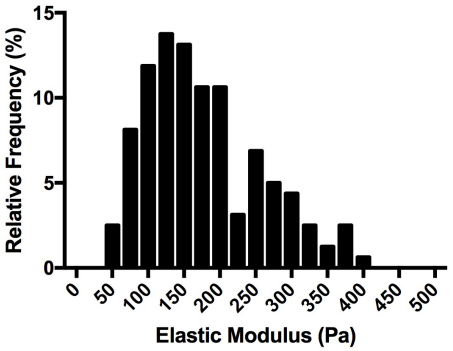

(a) Relative frequency distribution of the extracted elastic modulus for TILRR transfected and IL-1 stimulated HeLa cell 1. Described by a standard deviation of 118 Pa and a mean of 193 $\pm$ 9 Pa.

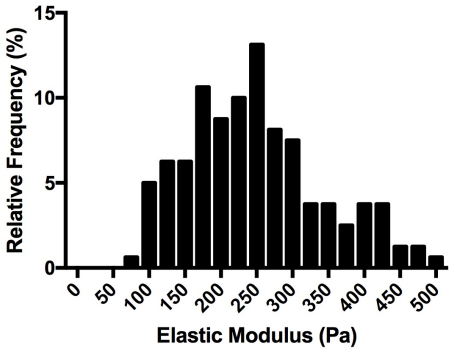

(b) Relative frequency distribution of the extracted elastic modulus for TILRR transfected and IL-1 stimulated HeLa cell 2. Described by a standard deviation of 110 Pa and a mean of 257 $\pm$ 9 Pa.

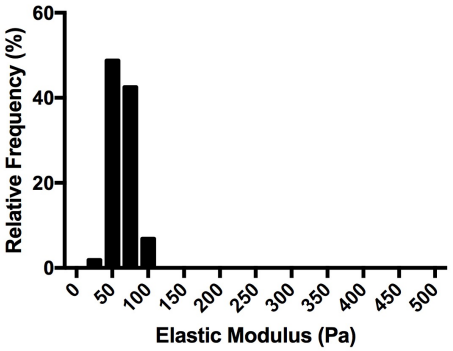

(c) Relative frequency distribution of the extracted elastic modulus for TILRR transfected and IL-1 stimulated HeLa cell 3. Described by a standard deviation of 14 Pa and a mean of 64 $\pm$ 1 Pa.

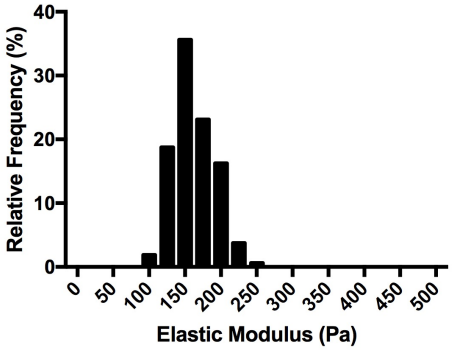

(d) Relative frequency distribution of the extracted elastic modulus for TILRR transfected and IL-1 stimulated HeLa cell 4. Described by a standard deviation of 28 Pa and a mean of 162 $\pm$ 2 Pa.

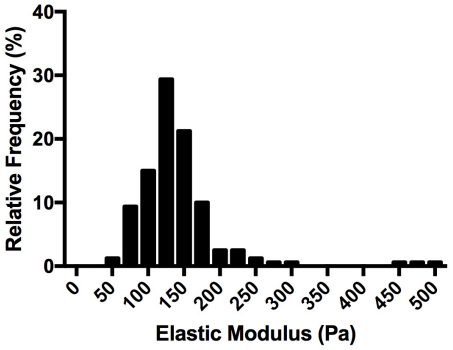

(e) Relative frequency distribution of the extracted elastic modulus for TILRR transfected and IL-1 stimulated HeLa cell 5. Described by a standard deviation of 122 Pa and a mean of 164 $\pm$ 10 Pa.

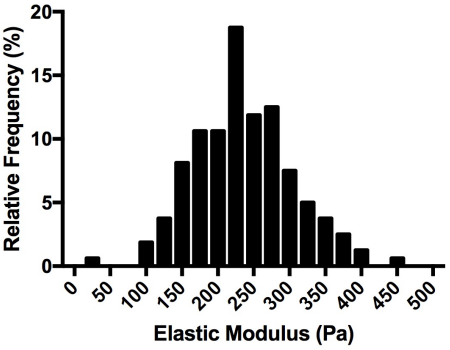

(f) Relative frequency distribution of the extracted elastic modulus for TILRR transfected and IL-1 stimulated HeLa cell 6. Described by a standard deviation of 77 Pa and a mean of 237 $\pm$ 6 Pa.

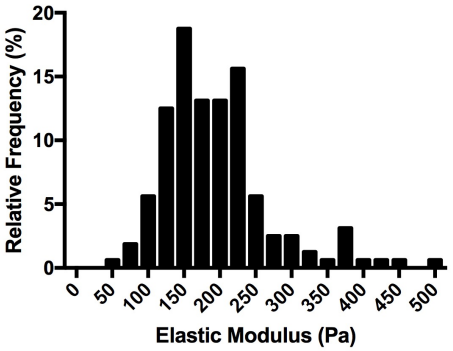

(g) Relative frequency distribution of the extracted elastic modulus for TILRR transfected and IL-1 stimulated HeLa cell 7. Described by a standard deviation of 81 Pa and a mean of 195 $\pm$ 6 Pa.

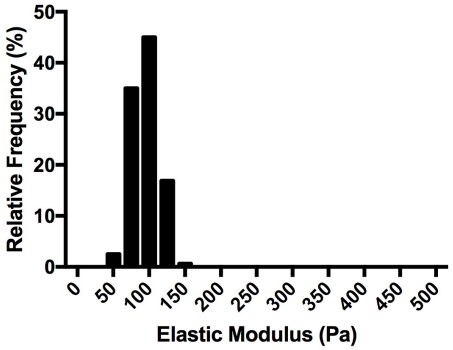

(h) Relative frequency distribution of the extracted elastic modulus for TILRR transfected and IL-1 stimulated HeLa cell 8. Described by a standard deviation of 18 Pa and a mean of 94 $\pm$ 1 Pa.

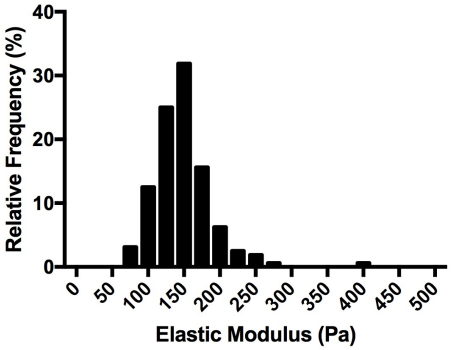

(i) Relative frequency distribution of the extracted elastic modulus for TILRR transfected and IL-1 stimulated HeLa cell 9. Described by a standard deviation of 42 Pa and a mean of 149 $\pm$ 3 Pa.

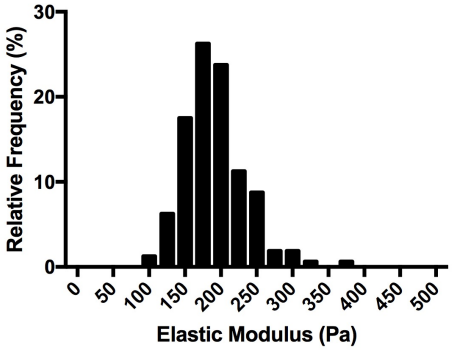

(j) Relative frequency distribution of the extracted elastic modulus for TILRR transfected and IL-1 stimulated HeLa cell 10. Described by a standard deviation of 43 Pa and a mean of 192 $\pm$ 3 Pa.

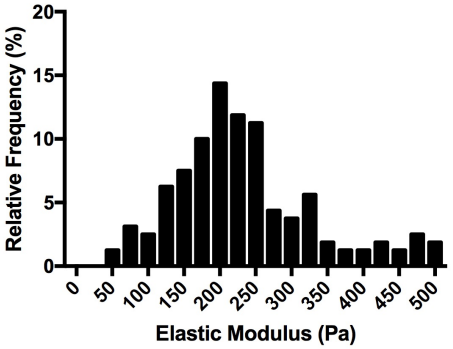

(k) Relative frequency distribution of the extracted elastic modulus for TILRR transfected and IL-1 stimulated HeLa cell 11. Described by a standard deviation of 143 Pa and a mean of 258 $\pm$ 11 Pa.

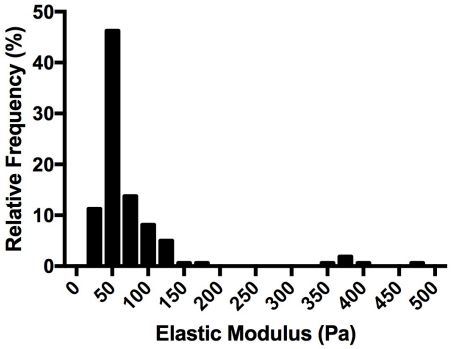

(l) Relative frequency distribution of the extracted elastic modulus for TILRR transfected and IL-1 stimulated HeLa cell 12. Described by a standard deviation of 301 Pa and a mean of 173 $\pm$ 24 Pa.

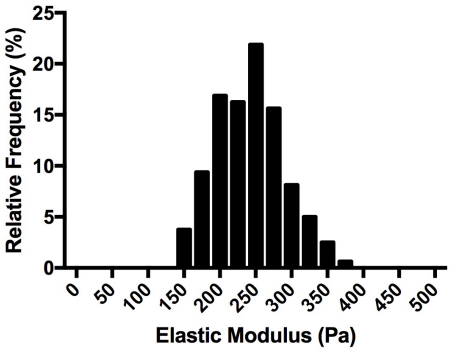

(m) Relative frequency distribution of the extracted elastic modulus for TILRR transfected and IL-1 stimulated HeLa cell 13. Described by a standard deviation of 48 Pa and a mean of 241 $\pm$ 4 Pa.

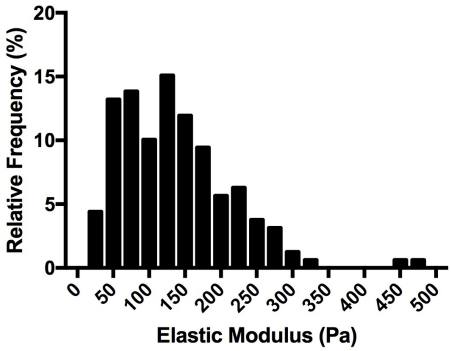

(n) Relative frequency distribution of the extracted elastic modulus for TILRR transfected and IL-1 stimulated HeLa cell 14. Described by a standard deviation of 78 Pa and a mean of 138 $\pm$ 6 Pa.

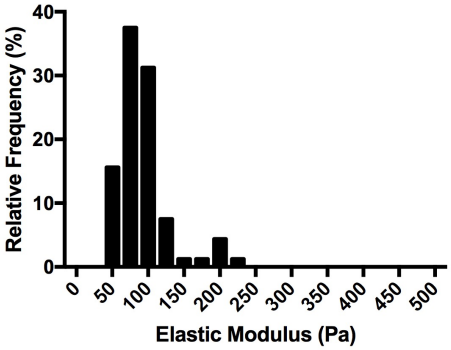

(o) Relative frequency distribution of the extracted elastic modulus for TILRR transfected and IL-1 stimulated HeLa cell 15. Described by a standard deviation of 36 Pa and a mean of 92 $\pm$ 3 Pa.

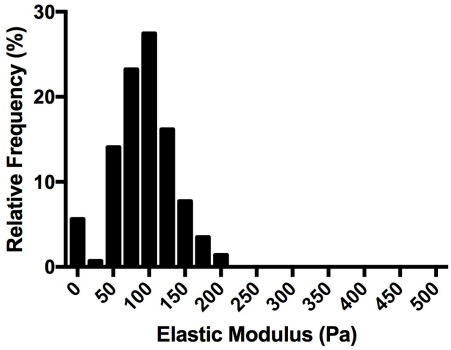

(p) Relative frequency distribution of the extracted elastic modulus for TILRR transfected and IL-1 stimulated HeLa cell 16. Described by a standard deviation of 41 Pa and a mean of 93 $\pm$ 3 Pa.

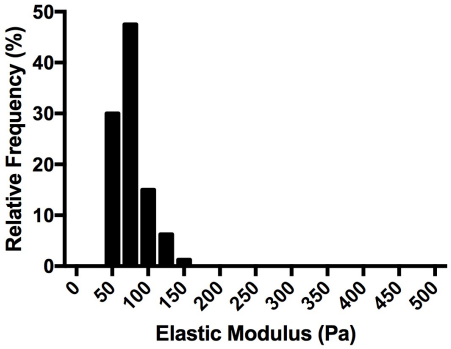

(q) Relative frequency distribution of the extracted elastic modulus for TILRR transfected and IL-1 stimulated HeLa cell 17. Described by a standard deviation of 21 Pa and a mean of 75 $\pm$ 2 Pa.

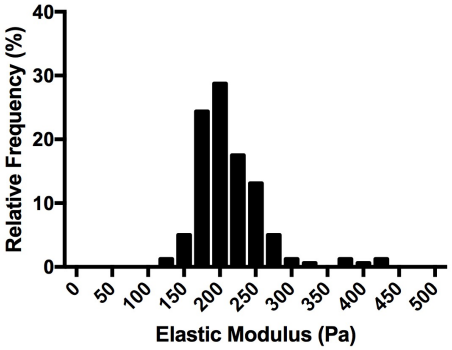

(r) Relative frequency distribution of the extracted elastic modulus for TILRR transfected and IL-1 stimulated HeLa cell 18. Described by a standard deviation of 48 Pa and a mean of 214 $\pm$ 4 Pa.

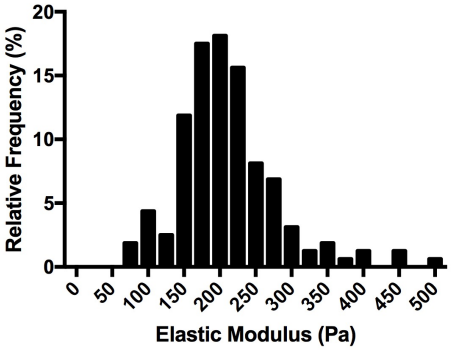

(s) Relative frequency distribution of the extracted elastic modulus for TILRR transfected and IL-1 stimulated HeLa cell 19. Described by a standard deviation of 99 Pa and a mean of 222 $\pm$ 8 Pa.

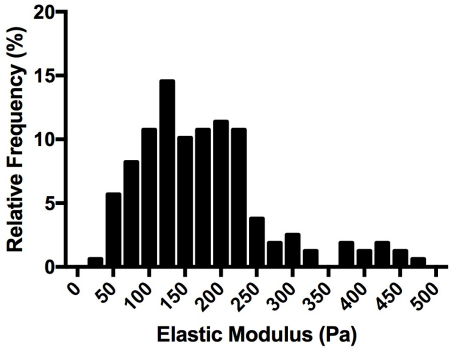

(t) Relative frequency distribution of the extracted elastic modulus for TILRR transfected and IL-1 stimulated HeLa cell 20. Described by a standard deviation of 97 Pa and a mean of 178 $\pm$ 8 Pa.

Fig. C.6 Relative frequency distributions of extracted elastic moduli extracted over 10 force maps for individual HeLa cells transfected with 1.5 μg TILRR cDNA per dish and stimulated with 10^{-9} M IL-1β. Standard deviations and mean $\pm$ SEM are indicated for each.